

**TonB facilitated Unfolding of *Escherichia coli* TonB-dependent Cobalamin  
Transporter BtuB using Electron Paramagnetic Resonance Spectroscopy**

Viranga Wanshanath Wimalasiri

Peradeniya, Sri Lanka

Bachelor of Science (Special Degree) in Chemistry

University of Peradeniya, Peradeniya, Sri Lanka 2017

A Dissertation presented to the Graduate Faculty of the Department of Chemistry  
at The University of Virginia in Candidacy for the Degree of Doctor of Philosophy

Department of Chemistry

The University of Virginia

August 2024

**© Copyright by**

**Viranga Wanshanath Wimalasiri**

**All Rights Reserved**

**August 2024**

## Abstract

The outer membrane (OM) of Gram-negative bacteria such as *Escherichia coli* (*E. coli*) creates an impermeable membrane thus requiring active transport proteins for essential nutrient uptake to ensure bacterial survival. This task is executed by TonB-dependent transporters (TBDTs) that utilize the proton motive force (PMF) of the inner membrane (IM) by coupling with the TonB/ExbB/ExbD complex. BtuB is a TonB-dependent transporter responsible for binding and uptake of Cobalamin (Vitamin B<sub>12</sub>) across the OM, and BtuB is an essential protein for the proper function of human microbiome. Though numerous crystal structures are available for multiple TBDTs, the molecular mechanism of TBDT function is poorly characterized.

Numerous studies have shown that site-directed spin labeling (SDSL) coupled with electron paramagnetic resonance (EPR) spectroscopy is a powerful tool to study structural and functional dynamics of membrane proteins. We have shown that single and double cysteine mutations can be successfully incorporated to BtuB, and spin labeled for continuous wave and pulse EPR spectroscopy. However, labeling cysteine pairs in BtuB in *in-vivo* proves to be challenging as efficient labeling requires the use of a knockout strain where the bacterial periplasmic redox homeostasis is modified.

In in this thesis we begin by examining a knockout strain, which is deficient in the disulfide bond oxidase *dsbA*, and demonstrate that it promotes a much more efficient double spin labeling of pairs of cysteines on both periplasmic and extracellular surfaces for BtuB, when the protein is purified and reconstituted into phospholipid bilayers. Surprisingly, double electron-electron resonance (DEER) experiments in the *dsbA* null strain reveal the presence of intermolecular BtuB-BtuB interactions, which were not previously observed in purified and phospholipid reconstituted

preparations. This is likely a result of the improvement in labeling efficiency of BtuB. Second, we demonstrate that this approach is necessary to perform *in-vivo* double spin labeling of the ferric citrate transporter FecA, and that expression in the *dsbA* null strain also improves the *in-vitro* labeling of FecA. The expression of FecA in the *dsbA* null strain required a two-plasmid transformation that allowed FecA induction with arabinose. As a result of this approach we were able to demonstrate that extracellular loops of FecA execute a different gating behavior in the cell than they do when the protein is purified and reconstituted into a phospholipid bilayer.

In BtuB, a highly conserved N-terminal energy coupling motif termed the Ton box is known to switch from an ordered to a disordered state upon substrate binding, where it extends into the periplasmic space and may interact with the IM protein TonB. This structural change requires the breaking of an ionic interaction between R14 in the core domain and D316 in the BtuB  $\beta$ -barrel. In a second portion of this thesis, we use the *dsbA* null mutant to show that the permanent disruption of this ionic lock results in a greater extension of the Ton box than is observed with substrate addition alone, and that this behavior can be mimicked by the binding of the C-terminal domain of TonB. This structural change may open a pathway for substrate transport. Finally, it is known that an extracellular substrate binding loop, SB3, moves 2 nm toward the periplasmic surface *in-vivo*. We show that this transition can also be observed in an isolated OM preparation when either the R14-D316 ionic lock is disrupted or when TonB C-terminal domain is bound to BtuB Ton box. This indicates that structural transitions that are seen in the intact cell can be observed in an isolated preparation provided that components in the native membrane and protein partners critical for TBDT transport are present.

## Table of Contents

Title	Page
<b>Abstract</b>	<b>III - IV</b>
<b>Table of Contents</b>	<b>V - XI</b>
<b>Table of Figures</b>	<b>XII - XVII</b>
<b>List of Tables</b>	<b>XVIII</b>
<b>Table of Abbreviations</b>	<b>XIX - XXII</b>
<b>Acknowledgements</b>	<b>XXIII - XXVI</b>
<b>Chapter 1: Introduction</b>	<b>1 - 78</b>
1.1 Significance	1 - 4
1.2 Bacterial Physiology	4 - 8
1.3 Bacterial Growth Cycle	8 - 12
1.4 OM Biogenesis	12 - 40
1.4.1 LPS Synthesis and Transport	12 - 20
1.4.2 Lipoprotein Synthesis and Transport	20 - 24
1.4.3 OMP Synthesis and Transport	24 - 40
1.4.3.1 Periplasmic Chaperones	24 - 29
1.4.3.2 Beta-barrel Assembly Machinery (BAM) Complex	29 - 34
1.4.3.3 Disulfide Bond Formation (Dsb) System	34 - 40
1.4.3.3.1 Oxidative Pathway	35 - 38
1.4.3.3.2 Isomerization Pathway	38 - 40
1.5 Outer Membrane Proteins	40 - 43
1.5.1 OM Porins	41 - 43
1.6 TonB-dependent Transporters (TBDTs)	43 - 52

1.6.1 TBDT Expression and Regulation	43 - 45
1.6.2 TBDT Transport of Scarce Nutrients	45 - 46
1.6.3 TBDT Architecture and Function	46 - 50
1.6.3.1 Architecture and Function of FhuA	46 - 47
1.6.3.2 Architecture and Function of FecA	48 - 49
1.6.3.3 Architecture and Function of BtuB	49 - 50
1.6.4 Current knowledge of BtuB and other TBDTs	50 - 52
1.7 TonB/ExbB/ExbD System	53 - 55
1.8 Proposed Mechanisms of TonB-dependent Transport	56
1.9 Specific Aims and Goals for this Thesis	56 - 57
1.10 References	58 - 78
<b>Chapter 2: Materials and Methods</b>	<b>79 - 158</b>
2.1 Materials	79 - 81
2.2 Molecular Biology Techniques	81 - 93
2.2.1 Polymerase Chain Reaction (PCR)	81 - 83
2.2.2 Designing Primers for PCR Reactions	83 - 85
2.2.3 PCR Mutagenesis and Cloning	85 - 87
2.2.4 DNA Plasmid Features	87 - 89
2.2.5 Plasmid DNA Isolation	89
2.2.6 Plasmid DNA Quality and Quantity Determination	90
2.2.7 DNA Sequencing	90 - 91
2.2.8 Analysis of DNA Sequencing Files	91 - 93
2.3 Microbiological Techniques	93 - 101
2.3.1 Importance of Sterile Techniques in Microbiological Experiments	93
2.3.2 Competent Cells	94

2.3.3 Preparation of Competent Cells	94 - 95
2.3.4 DNA Transformation through Heat Shock Treatment	95 - 97
2.3.5 Preservation of Bacterial Strains for Long Term Use	97 - 98
2.3.6 Laboratory Methods for Growing Bacteria	98 - 101
2.3.6.1 Plating Techniques for Bacterial Cultures	99
2.3.6.2 Cell Culturing Methods	100 - 101
2.4 Biophysical and Biochemical Techniques	101 - 110
2.4.1 Protein Overexpression and Purification	101 - 107
2.4.2 Membrane Protein Reconstitution from Detergent into Lipid Systems	108 - 110
2.5 EPR Spectroscopy as a Tool to Examine Protein Systems	111 - 150
2.5.1 Basics of EPR	115 - 125
2.5.1.1 Electron Zeeman Interaction	116 - 120
2.5.1.2 Anisotropy of g value	120 - 122
2.5.1.3 Hyperfine Interaction	122 - 125
2.5.2 CW-EPR for Detection of Nitroxide	125 - 128
2.5.3 Pulse EPR Experiments	128 - 139
2.5.3.1 Laboratory and Rotating Frames for Pulse EPR	128 - 133
2.5.3.2 Relaxation Effects of M through T <sub>1</sub> and T <sub>2</sub>	133 - 136
2.5.3.2.1 Spin Lattice Relaxation Time (T <sub>1</sub> )	133 - 135
2.5.3.2.2 Transverse Relaxation Time (T <sub>2</sub> )	135 - 136
2.5.3.3 Spin Echo and Relaxation	136 - 139
2.5.4 Double Electron-Electron Resonance (DEER) Spectroscopy	139 - 150
2.5.4.1 The DEER Experiment	141 - 146
2.5.4.2 Crucial Factors for a Successful DEER Experiment	146 - 150
2.6 References	151 - 158

<b>Chapter 3. A disulfide chaperone knockout significantly enhances double spin labeling efficiency of BtuB for <i>in-vitro</i> pulse EPR spectroscopy</b>	<b>159 - 181</b>
3.1 Abstract	159
3.2 Introduction	160 - 163
3.3 Materials and Methods	164 - 166
3.3.1 Cell Lines and Plasmids	164
3.3.2 PCR Mutagenesis and OMP Expression	164
3.3.3 OM and Reconstituted BtuB Sample Preparation	165
3.3.4 EPR Measurements	166
3.3.5 Data Processing	166
3.4 Results	167 - 171
3.4.1 Expression in <i>dsbA</i> <sup>-</sup> strain improves the labeling efficiency of BtuB <i>in-vitro</i>	167 - 170
3.4.2 Expression in <i>dsbA</i> <sup>-</sup> strain improves pulse EPR signals for labelled BtuB in both reconstituted and OM preparations	170 - 171
3.5 Discussion	172 - 174
3.6 Future Directions	174
3.7 Supplementary Information	175 - 177
3.8 References	178 - 181
<b>Chapter 4. A disulfide chaperone knockout facilitates efficient double spin labeling of ferric citrate transporter FecA for <i>in-vivo</i> pulse EPR spectroscopy</b>	<b>182 - 203</b>
4.1 Abstract	182 - 183
4.2 Introduction	183 - 185
4.3 Materials and Methods	185 - 188
4.3.1 Cell Lines and Plasmids	185 - 186
4.3.2 PCR Mutagenesis and OMP Expression	186



4.3.3 OM and Reconstituted BtuB Sample Preparation	186 - 187
4.3.4 Whole cell Spin Labeling of FecA	187
4.3.5 EPR Measurements	187 - 188
4.3.6 Data Processing	188
4.4 Results	189 - 195
4.4.1 The use of a DsbA deficient strain facilitates double spin-labeling of FecA <i>in-vivo</i>	189 - 192
4.4.2 DEER signals from FecA <i>in-situ</i> reveal the presence of a conformational gating in an extracellular loop	193 - 195
4.5 Discussion	196 - 197
4.6 Future Directions	197 - 198
4.7 Supplementary Information	198
4.8 References	199 - 203
<b>Chapter 5. The Role of a Conserved Ionic Lock in Transport by the Outer Membrane Cobalamin Transporter BtuB using pulse EPR spectroscopy</b>	<b>204 - 237</b>
5.1 Abstract	204
5.2 Introduction	205 - 209
5.3 Materials and Methods	209 - 213
5.3.1 Cell Lines and Plasmids	209
5.3.2 PCR Mutagenesis and OMP Expression	210
5.3.3 OM and Reconstituted BtuB Sample Preparation	210 - 211
5.3.4 C-terminal TonB fragment (103-239) Expression and Purification	211
5.3.5 EPR Measurements	212
5.3.6 Data Processing	212 - 213
5.4 Results	213 - 218
5.4.1 Disruption of the R14-D316 ionic lock results in a substrate independent extension of the BtuB Ton box in isolated reconstituted systems	213 - 215

5.4.2 Pulse EPR indicates that the Ton box of BtuB in OM preparations undergoes a greater extension in the presence of the ionic lock mutant, or the binding of TonB, than that seen in reconstituted preparations	215 - 218
5.5 Discussion	218 - 223
5.6 Future Directions	223 - 224
5.7 Supplementary Information	225 - 232
5.8 References	233 - 237
<b>Chapter 6. Structural intermediates observed for TonB dependent Cobalamin Transporter BtuB indicating a possible transport mechanism</b>	<b>238 - 271</b>
6.1 Abstract	238 - 239
6.2 Introduction	239 - 243
6.3 Materials and Methods	243 - 246
6.3.1 Cell Lines and Plasmids	243
6.3.2 PCR Mutagenesis and OMP Expression	243 - 244
6.3.3 OM and Reconstituted BtuB Sample Preparation	244
6.3.4 C-terminal TonB fragment (103-239) Expression and Purification	245
6.3.5 EPR Measurements	245 - 246
6.3.6 Data Processing	246
6.4 Results	246 - 255
6.4.1 Disruption of the R14-D316 ionic lock produces minimal changes in the EPR spectra of SB3 in isolated reconstituted systems	246 - 249
6.4.2 Pulse EPR signals observed for OM preparations indicate novel conformations for SB3 not observed in reconstituted preparations when the R14-D316 ionic lock is disrupted or when TonB is bound	249 - 255
6.5 Discussion	255 - 260
6.6 Future Directions	261
6.7 Supplementary Information	262 - 265
6.8 References	266 - 271

<b>Significance of the Research</b>	<b>272 - 277</b>
<b>Appendix</b>	<b>278 - 283</b>
Appendix 1 – Standard Amino Acids	278 - 279
Appendix 2 – <i>E. coli</i> wild type BtuB, FecA, and TonB sequences	280 - 281
2.1 <i>E. coli</i> wild type BtuB amino acid sequence (Uniprot ID P06129)	280
2.2 <i>E. coli</i> wild type FecA amino acid sequence (Uniprot ID P13036)	280 - 281
2.3 <i>E. coli</i> wild type TonB amino acid sequence (Uniprot ID P02929)	281
Appendix 3 - <i>E. coli</i> BtuB and FecA mutations	282 - 283
3.1 <i>E. coli</i> BtuB mutations	282
3.2 <i>E. coli</i> FecA mutations	282 - 283
References	283

## Table of Figures

Figure Title	Page
<b>Chapter 1: Introduction</b>	<b>1 - 78</b>
Figure 1.1 Bacterial Cell Cycle	5
Figure 1.2 Bacterial Chromosome Replication	6
Figure 1.3 Bacterial Growth Curve	11
Figure 1.4 Typical LPS Structure	14
Figure 1.5 Structure of <i>E. coli</i> Rough LPS Core Oligosaccharide	16
Figure 1.6 LPS Transport Machinery Structures	18
Figure 1.7 Synthesis and Transport of Lipoproteins to the inner leaflet of the OM	22
Figure 1.8 Periplasmic Chaperones Skp and SurA Structures	25
Figure 1.9 Periplasmic Chaperones DegP and FkpA Structures	28
Figure 1.10 OMP Assembly and Insertion to OM	30
Figure 1.11 The BAM Complex	31
Figure 1.12 Crystal structures of <i>E. coli</i> Dsb system	37 - 38
Figure 1.13 Crystal structures of OM Porins	42
Figure 1.14 Schematic Diagram of TonB-dependent Transport	44
Figure 1.15 Chemical Structures of Siderophores Synthesized by Bacteria for Iron Acquisition	46
Figure 1.16 Crystal structures of FhuA	47

Figure 1.17 Crystal structures of FecA	48 - 49
Figure 1.18 Crystal structures of BtuB	50
Figure 1.19 Crystal structures of ExbB/ExbD complex	54
Figure 1.20 Crystal structures of TonB and TonB/ExbB/ExbD complex	55
<b>Chapter 2: Materials and Methods</b>	<b>79 - 158</b>
Figure 2.1 DpnI Digestion of DNA	83
Figure 2.2 Primer Design Process for BtuB Periplasmic Turn Residue Q510 to C510 (Q510C)	84
Figure 2.3 Plasmid Map of pAG1 Harboring the wild type <i>btuB</i> Gene	88 - 89
Figure 2.4 Gene sequence of BtuB D6C-Q510C-D316A obtained from Plasmidsaurus translated to its Corresponding Amino Acid Sequence using ExPasy translate	92
Figure 2.5 Alignment of Amino Acid sequences of BtuB in the Isolated plasmid and WT BtuB	92 - 93
Figure 2.6 DNA Transformation through the Heat Shock Method	95 - 96
Figure 2.7 Cellular processes involved in DNA Transformation	97
Figure 2.8 Various plating techniques of Bacterial Cultures on Agar plates	99
Figure 2.9 Membrane solubilization and Membrane Protein Isolation using Detergents	102
Figure 2.10 Structures of distinct types of Detergents	103
Figure 2.11 Schematic diagram of Affinity Chromatography	105
Figure 2.12 Protein Net Charge variability with pH of the Environment	106
Figure 2.13 Elution profile of spin labelled D6C-Q510C (D6R1-Q510R1) using anion-exchange fast-protein liquid chromatography (FPLC)	107
Figure 2.14 Structures of Reconstitution Lipids	108

Figure 2.15 Different types of Lipid-based systems	109
Figure 2.16 Detergent based Lipid Reconstitution of Membrane Proteins	110
Figure 2.17 Different types of Spin Labels used for EPR experiments	113
Figure 2.18 Spin labeling process during MTSL introduction	114
Figure 2.19 Variations in Spin Label behavior as a function of Protein Secondary/Tertiary structure	115
Figure 2.20 Effect on Electronic Spin to an Applied Magnetic field $B_0$	117
Figure 2.21 The precession of the Magnetization Vector (M) along the Rotating Frame	119 - 120
Figure 2.22 Applied Magnetic field (B) orientation with respect to the orientation of the molecule containing paramagnetic center	121
Figure 2.23 Energy diagram for Nitroxide Energy Level splitting with $m_s = \pm 1/2$ and $m_l = \pm 1, 0$ due to Zeeman interaction and Hyperfine coupling	124 - 125
Figure 2.24 Spatial coordinates of the nitroxide bond and their corresponding CW-EPR spectra and calculated g and A tensors	125 - 126
Figure 2.25 Simulated EPR spectra obtained at different Rotation Correlation Times ( $\tau_c$ )	127
Figure 2.26 Experimental EPR spectra obtained for D6R1-Q510R1 BtuB	128
Figure 2.27 Microwave magnetic fields in Laboratory and Rotational frames with Angular frequency $\omega_0$ for Pulse EPR experiments	130
Figure 2.28 Rotation of Magnetization M due to $B_1$ along x-axis and the effect of a $\pi/2$ pulse on Magnetization and its corresponding pulse shape	130 - 131
Figure 2.29 Pulse Phases depending on the orientation of $B_1$ and the corresponding orientation of M	131
Figure 2.30 Microwave Pulse Length obtained by Amplification of a segment of the CW microwave irradiation and its corresponding excitation bandwidth obtained through Fourier Transformation	132
Figure 2.31 FID generation observed in Rotating and Laboratory frames	133
Figure 2.32 Spin-lattice Relaxation effects Net Magnetization	134 - 135
Figure 2.33 Transverse relaxation process where fanning out results in the decrease of Net Magnetization along x-y plane	136

Figure 2.34 Behavior of Magnetization in an Echo Experiment	137
Figure 2.35 Pulse Sequence and behavior of Net Magnetization in a Stimulated and Refocused Echo experiment	139
Figure 2.36 Dipolar interaction between two species with Paramagnetic centers	140
Figure 2.37 Pake Pattern obtained from a FT of dipolar coupling due to Paramagnetic Nitroxide pair	141
Figure 2.38 Fundamental Principle of 4-pulse DEER Experiment	143 - 144
Figure 2.39 Separation of Time Domain trace $V(t)$ to obtain Form Factor $F(t)$ by removing Background Function $B(t)$ to extract Distance Distribution data	146
Figure 2.40 Possible positions for Observer and Pump pulses in the EPR spectra for nitroxide in DEER	147 - 148
Figure 2.41 Optimum conditions for successful DEER experiment	150
<b>Chapter 3. A disulfide chaperone knockout significantly enhances double spin labeling efficiency of BtuB for <i>in-vitro</i> pulse EPR spectroscopy</b>	<b>159 - 181</b>
Figure 3.1 The Disulfide Bond Formation system responsible for Crosslinking pairs of Cysteine residues in OMPs before reaching the OM	163
Figure 3.2 The use of DsbA deficient strain improves the relative labeling efficiency of BtuB in a phospholipid reconstituted preparation	168
Figure 3.3 DEER data from purified reconstituted protein or an outer-membrane preparation are improved using a DsbA deficient strain	171
Figure S3.1 V90R1-T188R1 DEER data from purified reconstituted protein or an outer-membrane preparation are improved using a DsbA deficient strain	175 - 176
Figure S3.2 Substrate induced unfolding of the BtuB Ton box observed in crystal structures	176
Figure S3.3 Substrate induced conformational changes of plug domain of BtuB observed in crystal structures	177
<b>Chapter 4. A disulfide chaperone knockout facilitates efficient double spin labeling of ferric citrate transporter FecA for <i>in-vivo</i> pulse EPR spectroscopy</b>	<b>182 - 203</b>
Figure 4.1 Double spin labeling of FecA <i>in-vivo</i> requires a DsbA deficient strain	190 - 191
Figure 4.2 Plasmid map of pTARA harboring the phage T7 RNA Polymerase (T7 RNAP)gene	192

Figure 4.3 Conformational Gating in the 8/11 Extracellular Loops is dependent upon environment	193 - 194
Figure S4.1 Substrate induced conformational changes of extracellular loops of FecA observed in crystal structures	198
<b>Chapter 5. The role of a conserved ionic lock in transport by the outer membrane cobalamin transporter BtuB using pulse EPR spectroscopy</b>	<b>204 - 237</b>
Figure 5.1 The crystal structures of BtuB with the R14-D316 ionic interaction	208
Figure 5.2 The cleavage of R14-D316 ionic lock results in extension of BtuB Ton box in a phospholipid reconstituted preparation	214
Figure 5.3 DEER data for D6R1-I305R1 obtained from an outer-membrane preparation	216 - 217
Figure 5.4 DEER data for D6R1-I305R1-D316A obtained from purified reconstituted protein or an outer-membrane preparation	217 - 218
Figure S5.1 DEER data for D6R1-Q510R1 obtained from an outer-membrane preparation	225 - 226
Figure S5.2 DEER data for D6R1-Q510R1-D316A obtained from purified reconstituted protein or an outer-membrane preparation	226 - 227
Figure S5.3 DEER data for V10R1-Q510R1 obtained from an outer-membrane preparation	227 - 228
Figure S5.4 DEER data for V10R1-Q510R1-D316A obtained from purified reconstituted protein or an outer-membrane preparation	228 - 229
Figure S5.5 Substrate induced conformational changes of plug domain of D6R1-I305R1 BtuB observed in crystal structures	229
Figure S5.6 Substrate induced conformational changes of plug domain of D6R1-Q510R1 BtuB observed in crystal structures	230
Figure S5.7 Substrate induced conformational changes of plug domain of V10R1-Q510R1 BtuB observed in crystal structures	231
Figure S5.8 DEER data D6R1-Q510R1 obtained in the intact cell	232
<b>Chapter 6. Structural intermediates observed for TonB dependent cobalamin transporter BtuB indicating a possible transport mechanism</b>	<b>238 - 271</b>
Figure 6.1 The cleavage of R14-D316 ionic lock exhibit minute structural changes of BtuB in a phospholipid reconstituted preparation	248
Figure 6.2 DEER data for V90R1-I305R1 obtained from an outer-membrane preparation	250 - 251
Figure 6.3 DEER data for V90R1-I305R1-D316A obtained from purified reconstituted protein or an outer-membrane preparation	251 - 252



Figure 6.4 DEER data for V90R1-I305R1 obtained from purified reconstituted protein in POPC liposomes	253
Figure 6.5 DEER data for V90R1-I305R1 obtained from purified reconstituted protein in DLPC liposomes	254
Figure S6.1 DEER data for V90R1-Q510R1 obtained from an outer-membrane preparation	262 - 263
Figure S6.2 DEER data for V90R1-Q510R1-D316A obtained from purified reconstituted protein or an outer-membrane preparation	263 - 264
Figure S6.3 Substrate induced conformational changes of plug domain of V90R1-I305R1 BtuB observed in crystal structures	264
Figure S6.4 Substrate induced conformational changes of plug domain of V90R1-Q510R1 BtuB observed in crystal structures	265

## List of Tables

<b>Table Title</b>	<b>Page</b>
<b>Chapter 2: Materials and Methods</b>	<b>79 - 158</b>
Table 2.1 Initial and final concentrations of reagents required for a PIPE PCR experiment	86 - 87
Table 2.2 PIPE PCR steps, temperature conditions, and the time durations used for all BtuB and FecA mutation experiments	87
<b>Appendix</b>	<b>278 - 283</b>
Table 3.1 <i>E. coli</i> BtuB primers with their corresponding melting temperatures (T <sub>m</sub> ) and PCR annealing temperatures	282
Table 3.2 <i>E. coli</i> FecA primers with their corresponding melting temperatures (T <sub>m</sub> ) and PCR annealing temperatures	282 - 283

## Table of Abbreviations

(p)ppGpp	Guanosine Pentaphosphate
AFM	Atomic Force Microscopy
AMP	Ampicillin
ATP	Adenosine Triphosphate
BAM	$\beta$ -barrel Assembly Machinery
BtuB	B-twelve uptake protein B
CD	Circular Dichroism
CFU	Colony Forming Unit
CMC	Critical Micelle Concentration
CN-Cbl	Cyanocobalamin (Vitamin B <sub>12</sub> )
Cryo-EM	Cryo-Electron Microscopy
CW	Continuous Wave
Cys	Cysteine
DC	Direct Current
DEER	Double Electron-Electron Resonance
DegP	Serine Endoprotease
DLPC	1,2-dilauroyl-sn-glycero-3-phosphocholine
DNA	Deoxyribonucleic Acid
Dsb	Disulfide Bond
DTT	Dithiothreitol
<i>E. coli</i>	<i>Escherichia Coli</i>
ECF	Exo-Cytoplasmic Function
EPR	Electron Paramagnetic Resonance

ESEEM	Electron Spin Echo Envelope Modulation
FecA	Ferric dicitrate binding protein A
FhuA	Ferric hydroxamate uptake protein A
FID	Free Induction Decay
FKBP	FK506 Binding Protein
FkpA	FkpB binding protein A
FPLC	Fast Protein Liquid Chromatography
FT	Fourier Transform
Fur	Ferric Uptake Regulator
GST	Glutathione transferase
HDX-MS	Hydrogen-Deuterium Exchange Mass Spectrometry
IM	Inner Membrane
IMPACT	Intein-mediated Purification with an Affinity Chitin-binding Tag
IPTG	isopropyl $\beta$ -D-thiogalactopyranoside
ITC	Isothermal Calorimetry
Kdo	3-deoxy-D-manno-oct-2-ulosonic acid
LB	Luria-Bertani/Lysogeny Broth
Lol	Lpp Transport Pathway
LOS	Lipooligosaccharides
Lpp	Lipoprotein
LPS	Lipopolysaccharide
Lpt	LPS Transport Machinery
LUMO	Lowest Unoccupied Molecular Orbital
M9	Minimal Media
MBP	Maltose Binding Protein

MD	Molecular Dynamics
MK	Menaquinone
MMM	Multiscale Modeling of Macromolecules
MTSL	S-(1-oxyl-2,2,5,5-tetramethyl-2,5-dihydro-1H-pyrrol-3-yl)methyl methanesulfonylthioate
MWCO	Molecular Weight Cut Off
NADPH	Nicotinamide Adenine Dinucleotide Phosphate
NMR	Nuclear Magnetic Resonance
O/N	Overnight
OD <sub>600</sub>	Optical Density at 600 nm Wavelength
OG	n-octyl- $\beta$ -D-glucopyranoside
OM	Outer Membrane
OmpA	Outer membrane protein A
OmpC	Outer membrane protein C
OmpF	Outer membrane protein F
OMPs	Outer Membrane Proteins
PCD	Programmed Cell Death
PCR	Polymerase Chain Reaction
PEG	Polyethylene glycol
PG	Phosphatidyl glycerol
pI	Isoelectric point
PIPE	Polymerase Incomplete Primer Extension
PMF	Proton Motive Force
POPC	1-palmitoyl-2-oleoyl-sn-glycero-3-phosphocholine
POTRA	Polypeptide Transport Associated
PPI	Protein-Protein Interactions

PTM	Post Translational Modification
RNA	Ribonucleic Acid
RNS	Reactive Nitrogen Species
ROS	Reactive Oxygen Species
RT	Room Temperature
SB3	Substrate Binding Loop 3
SCC	Single Cell Colony
SDS	Sodium Dodecyl Sulphate
SDSL	Site-directed Spin Labeling
Skp	Seventeen-kilodalton Protein
SNR	Signal-to-Noise Ratio
SOMO	Single Occupied Molecular Orbital
SRT	Shot-Repetition Time
SurA	Survival Protein A
T7 RNAP	T7 Ribonucleic Acid Polymerase
TBDTs	TonB-dependent Transporters
TPR	Tetratricopeptide Repeat
Trx	Thioredoxin
UQ	Ubiquinone
WT	Wild Type

## Acknowledgement

First, I am forever thankful to Professor David S. Cafiso, who gave me the opportunity to pursue my graduate studies in the field of Biochemistry. In the beginning, I did not possess the necessary knowledge to understand the underlying biochemical and biophysical concepts that are required to embark Dave's research. Nonetheless, he welcomed me to his group with open arms, providing assurance that I have the capability to be successful. He was a wonderful advisor, granting me ample time to learn and expand my knowledge in biochemical, biophysical principles and EPR spectroscopy while raising his expectations of me higher and higher every day. The ultimate result of his mentoring and support is this thesis. By being a great supervisor, he assisted me in deepening my understanding on membrane proteins and EPR spectroscopy, as well as becoming an experienced researcher in membrane biochemistry. For all that, THANK YOU SO MUCH DAVE.

Thank you to all the current members in Cafiso group, Monika Wieliniec, Akosua Poma Ofosuhene, and Dr. Abigail Graham as well as the former members of the Cafiso group, Dr. Thushani Nilaweera, Dr. David Nyenhuis, Dr. Sarah Bentley-Nyenhuis, Kinga Jurczak, Matthew Blewett, Jacob Staley, Dr. Qian Liang and Dr. Vanessa Bijak. I am fortunate to have joined the Cafiso group at the correct time. To have unlimited support and fruitful companionship from my dear friends, Monika, Kinga, Matt, Poma and Abigail allowed me to be successful in the Cafiso Lab. I also cannot forget the support given by Natasha Dodamgoda, who joined the Cafiso Lab as a first-year UVA undergraduate student assisting me with molecular biology experiments, Kinga Jurczak for her immense support on one of my thesis projects, and Monika Wieliniec for supporting me with EPR experiments at the end of my graduate career to complete my work on time. Thank you so much Monika, Kinga and Natasha.

I cannot begin to thank my wonderful mentor Dr. Thushani Nilaweera, my Sri Lankan elder-sister (or as I call in Sinhalese, “Thushani Akki”) in the Cafiso Lab. In the beginning of my graduate research, I did not bear any knowledge related to molecular biology and biochemical techniques. While being insanely patient with my mistakes, you taught me basic concepts of molecular biology while nurturing me in skills and techniques related to molecular biology and biochemistry until I became confident enough to do experiments on my own. Your wonderful mentoring skills have generated a well experienced researcher in molecular biology and biochemistry, and a mentor to many more researchers in the Cafiso Lab. Thank you so much Thushani Akki. Also, I am immensely grateful to my wonderful EPR teacher Dr. David Nyenhuis for having many helpful discussions related to EPR spectroscopy and personally training me to be proficient in CW and Pulse EPR instrumentation.

I am ecstatic to have a wonderful advisor like Professor Robert K. Nakamoto, who was continuously supervising me and providing insight for my research. His humor and smile always lighted up the Cafiso Lab and he never runs out of ideas nor suggestions for any question that I have. He was always kind enough to provide his bacterial strains and plasmids along with his ideas that improved my research immensely. Thank you so much Bob. Also, I would like to thank my thesis committee members Prof. Andreas Gahlmann, Prof. Donald Hunt, Prof. Robert K. Nakamoto, and Prof. Jetze Tepe for the support and guidance throughout my PhD Candidacy Examination, 4<sup>th</sup> Year Research Seminar and the final Thesis Dissertation. I would also like to thank Susie Marshall, Sage Bradburn, and Amy Cabell for all their support throughout the years as the Graduate Student Coordinator.

The first year of my graduate student life at UVA was quite a challenge as I was attempting to fit into the Chemistry Department and be more communicative with the graduate student body.



My true outgoing self was able to thrive thanks to the events organized by our former Director of Graduate Studies Prof. Brent Gunnoe with chemistry graduate students as well as our graduate student organizations at the Chemistry department. Thank you Brent, Chemistry L.E.A.D, Chemistry Graduate Student Council for providing me with opportunities to overcome my fear of communication. Thinking back, it was the best way for me to gain the needed communication skills, networks and to gain friendships at the most appropriate timeline. I also wish to give a special shout out to my wonderful Sri Lankan community at Charlottesville for creating a second home that I can always count on if I needed support. The togetherness of the Sri Lankan graduate student community that increased exponentially throughout the years allowed us to create our own organization at UVA and exhibit our culture and heritage to UVA community. Thank you so much all of you.

Besides all these wonderful people, I would like to express my heartfelt gratitude to those who were always close to my heart providing endless support and love. I would like to thank my parents from the bottom of my heart, specially my mother Prof. Swarna Wimalasiri who inspired me to follow my PhD research in biochemistry, while giving her unconditional love, support, sacrifice and blessings in each step of my life. That has made me the successful scientist and human being that I am today. Thank you mom and I love you so much. I would also like to extend my thanks to my wonderful big brother, Dr. Pubudu Wimalasiri who took care of me when I was little until I was independent once I started my graduate career at UVA. Your love, guidance and support helped me get through tough times. For that, I thank you and I love you so much. Finally, I would like to thank my special star, the love of my life, my wonderful wife Oshani Wanasinghe who was always with me through thick and thin. She was always there for me lifting me up in every moment that I needed inspiration to work hard. Overall, you made me a better researcher with lots of

courage and dedication to be a pillar for the advancement of science. I would not have made it through this journey without your unconditional love, support and guidance. Thank you so much honey and I love you always. This thesis is my gift for all the sacrifices you all have made for me.

# **Chapter 1: Introduction**

## 1.1 Significance

To ensure their survival, bacteria are capable of rapid adaptation to the continuously variable microenvironment. Where pathogenic bacteria are concerned, this trait can lead to multi drug resistant organisms that can be harmful for the host in question. It is apparent that most of these pathogenic bacteria are Gram-negative, where their architecture consists of an extra outer membrane (OM) apart from the cytoplasmic/inner membrane (IM). This unique OM is an asymmetric bilayer composed of phospholipids present in the inner leaflet and lipopolysaccharides (LPS) present in the outer leaflet creating an impermeable barrier for both hydrophilic and hydrophobic compounds. Furthermore, the OM is a host to various outer membrane proteins (OMPs) that provide robust, antibiotic resistant and adaptable properties, active transport, enzymatic activity, and various critical functions required for bacterial survival<sup>1-6</sup>. Compounds greater than 600 Da of molecular size cannot diffuse through the outer membrane; therefore, *Escherichia coli* (*E. coli*) and other Gram-negative bacteria obtain various essential nutrients such as vitamin B<sub>12</sub>, carbohydrates, and metal complexes through the OM using OM active transporter proteins of high affinity and specificity<sup>1-6</sup>. One special class of transporters are the TonB-dependent transporters (TBDTs), which uptake essential nutrients by utilizing the proton motive force (PMF) present in the IM by coupling to IM protein complex TonB/ExbB/ExbD, which will be focused on detail in this dissertation.

TBDTs have been extensively studied to elucidate their structural and functional dynamics through many molecular biology, biochemical, biophysical and analytical techniques. Multiple crystallographic structures have been obtained at atomic resolution under different experimental

conditions as well as numerous *in-vitro* experiments such as OM isolations, and lipid bilayer reconstitutions have been done to investigate structural dynamics, transition states, and allosteric behavior involved in TBDT transport. Though protein crystallography provides us with a three-dimensional representation of the protein structure, the structure is static, and knowledge of the dynamic transitions that may take place are poorly characterized. Furthermore, reagents used during the crystallization process tend to trap proteins with bound substates that are more compact in structure, thereby limiting the observation of states that are more extended and dynamic<sup>1</sup>.

Fluorescence labeling based experiments have also been extensively used to study proteins in isolated and intact cell systems. This technique can be implemented by the attachment of a fluorophore to the protein of interest or through specific antibody based binding techniques to attach fluorescent molecules to proteins for study. Though it is an important technique, the large size of many fluorophores limits the resolution and accuracy of structural changes that can be determined and makes it difficult to identify subtle changes in protein dynamics. Also, it is crucial to clear away any natural fluorophores that may interfere with the introduced fluorophore substrates. Therefore, ample interest have been shown for site-directed spin labeling (SDSL) coupled with electron paramagnetic resonance (EPR) to study OMPs as it can be easily implemented and can provide sensitive information regarding structural and functional dynamics of proteins. With respect to fluorescence techniques, SDSL utilizes small nitroxide spin labels used for EPR, therefore quite sensitive to subtle changes in protein structure and dynamics<sup>5,7</sup>.

This dissertation focuses on employing SDSL coupled with EPR to study OMPs expressed in Gram-negative bacteria (*E. coli*). EPR experiments can be implemented for both *in-vitro* and *in-vivo* systems with the assistance of nitroxide spin labels attached through cysteines introduced to OMP of interest through molecular biological approaches followed by the subsequent use of

continuous wave (CW) and pulse EPR techniques. The main goal for this work is to elucidate the structural dynamics involved in active transport of TBDTs using the *E. coli* Cobalamin (Vitamin B<sub>12</sub>) transporter BtuB. The molecular mechanism of active transport of cobalamin through BtuB is still debated in the scientific community. There are numerous pathways for TBDT function that has been proposed, but these are generally poorly supported by direct experimental evidence. Through the use of EPR as a tool to study BtuB in both isolated (*in-vitro*) and intact cell (*in-vivo*) systems, we have discovered novel transitions that are only observed in intact systems but are not present in isolated systems<sup>7</sup>.

Gram-negative bacterial OMP sequences exhibit the presence of nil or even number of cysteines since all available free cysteines are crosslinked before final folding and insertion into the OM. This is executed by the disulfide bond formation (Dsb) system present in the periplasmic space and IM. Consecutive cysteines in OMPs are crosslinked by Dsb oxidase *dsbA* and is re-energized to its oxidized form by IM protein *dsbB*. If the disulfide crosslinks require isomerization, it is executed by Dsb isomerase *dsbC* and is re-energized to its original oxidized form by IM protein *dsbD*<sup>7</sup>. Previous studies have shown that by using a knockout of *dsbA*, double cysteines with uncrosslinked thiols in BtuB can be expressed and labelled with nitroxide spin labels in intact cells<sup>7,8</sup>. The *dsbA*<sup>-</sup> strain has shown higher labeling efficiencies of cysteine double mutants *in-vitro* compared to the wild-type strain<sup>8</sup>. As an extension of improved spin labeling efficiency for other TBDTs, assistance of T7 RNA polymerase containing plasmid pTARA yields remarkable labeling efficiencies for the Ferric Citrate transporter FecA. Also, EPR experiments have shown that substrate binding to the extracellular surface shifts the equilibrium of an energy coupling segment termed the Ton box of BtuB towards an extended or disordered state<sup>5</sup>. Disrupting a conserved ionic lock (R14/D316) between the protein beta-barrel and the core of the protein

eliminates this substrate-dependent coupling and shifts the Ton box equilibrium towards an unfolded state<sup>9</sup>, and this state can be mimicked by the binding of a C-terminal domain of TonB.

These findings have shown that application of EPR to investigate structural and functional dynamics of TBDTs in Gram-negative bacteria is quite effective and dependable and it can be used to further advance on future research regarding OMPs of interest.

## 1.2 Bacterial Physiology

There are intriguing mechanisms involving various biomolecules such as proteins, lipids, and nucleic acids that govern the life of microorganisms in diverse habitats. Adapting to different environments through regulation of key cellular mechanisms by specific activation or deactivation of genes determines their natural survival and cell proliferation. Understanding bacterial physiology unveils the fundamental principles that support life at the cellular level.

Bacteria undergo constant regulation of cellular processes for survival based on the variability of environmental conditions around them. Changes in temperature, availability of nutrients, and the bacterial density levels are detected by microorganisms and result in downstream signaling to control gene expression to thereby increase or decrease specific biomolecule production. These changes in cellular processes can affect the overall bacterial cell cycle where we observe faster doubling cycles in nutrient rich media and slower doubling cycles in nutrient deficient media.

The traditional bacterial cell cycle is divided into three main stages. They are namely period B, C, and D where period B represent the time between division of a new bacterial cell and the initiation of chromosome DNA replication, period C represent the time period from initiation of chromosome DNA replication up to termination, and period D represent the time frame between chromosome DNA replication termination up to cell division<sup>10</sup> (see Figure 1.1).

In organisms such as *E. coli*, cell replication originates at the origin of a single circular chromosome, replicates bi-directionally along the circumference of the chromosome and terminates at the opposite end of the origin. However, the chromosome remains in an exceptionally ordered state and it is defined as nucleoid<sup>11</sup>. The first step in cell division is proposed to be the polymerization of the tubulin-like protein FtsZ, forming a ring-like structure (Z ring) closer to the cytoplasmic membrane. The rod-shaped structure of *E. coli* translates the cell division site to the midpoint of the cell while being perpendicular to the long axis of the cell. The ring constriction results in two daughter cells which are half the length of the mother cell and are morphologically and genetically identical<sup>12</sup>. Throughout cell division, the Z ring has prevailed, and it serves as a scaffold to recruit downstream components. It is also crucial in the synthesis, shape, and location of the division septum<sup>13</sup>.

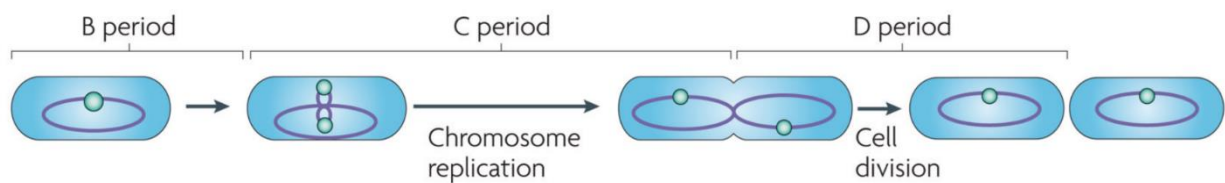


Figure 1.1 Bacterial Cell Cycle. During each cycle bacteria undergoes three stages (period B, C, D) to achieve successful chromosome replication and cell division. Figure was taken from Wang, J. D., & Levin, P. A. (2009). Metabolism, cell growth and the bacterial cell cycle. *Nature reviews. Microbiology*, 7(11), 822–827.

Under an increase in nutrient availability and rich growth conditions, a decrease in mass doubling times but a constant C & D period can be observed which results in chromosome replication and segregation requiring more time than the mass doubling time<sup>14</sup>. To overcome this circumstance, cells execute multiple chromosome replications before the end of previous

replication round resulting in multiple rounds of replications (two, four and up to eight) occurring simultaneously. This phenomenon is identified as the “multi-fork replication”<sup>15</sup> (Figure 1.2). *E. coli* mechanism for multi-fork replication shows that slow growth replication exhibits a single round of replication per cycle where fast growth replication exhibit multiple rounds of replication per cycle<sup>14</sup>.

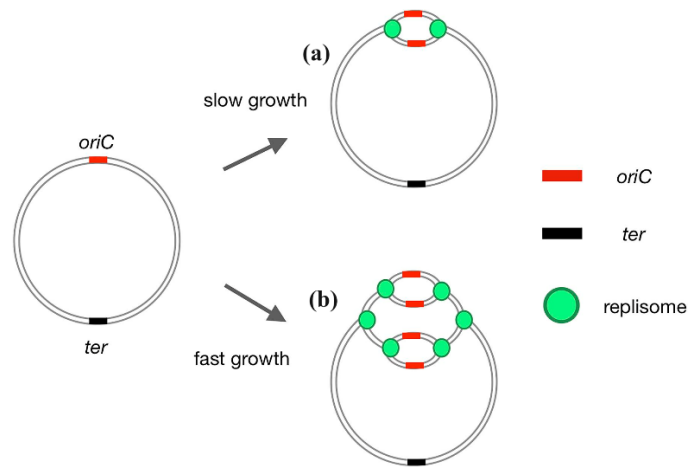


Figure 1.2 Bacterial Chromosome Replication. (a) in slow growth conditions where mass doubling time  $> C$  &  $D$  period, single chromosome replication where two copies near *oriC* is observed. (b) in fast growth conditions where mass doubling time  $\leq C$  &  $D$  period, multiple chromosome replication occurs close to *oriC*. However, multi-fork replication guarantees completion of at least one genome before cell division to ensure identical genome characteristics of daughter cells. Figure was taken from Trojanowski, D., Hołowka, J., & Zakrzewska-Czerwińska, J. (2018). Where and When Bacterial Chromosome Replication Starts: A Single Cell Perspective. *Frontiers in microbiology*, 9, 2819.

Chromosomal DNA undergoes three steps for a single replication round which are initiation, elongation, and termination. The metabolic control of bacterial cell division is controlled by nutrient dependent activity of DnaA, a protein in AAA+ family of ATPases. DnaA binds directly



with regions of *oriC* rich in A and T allowing it to unwind thereby initiating DNA chromosome replication. Thus, the rate at which DNA chromosome replication occurs rests solely on the levels of DnaA present in the cell. *E. coli* DnaA expression is mainly regulated by the small nucleotides guanosine tetraphosphate and guanosine pentaphosphate, (p)ppGpp. Synthesis of (p)ppGpp can be induced by either carbon starvation or by amino acid starvation through the enzymes SpoT hydrolase and RelA synthase respectively<sup>17</sup>. Apart from (p)ppGpp regulation of DnaA, chromosome replication can also be mediated by SeqA based DnaA regulation where SeqA preferentially binds to *oriC* which are hemimethylated thereby disrupting the DnaA-*oriC* interactions<sup>18</sup>.

Once the cells are matured after chromosome replication to a size equal to that of two daughter cells, cell division is initiated. As mentioned previously, FtsZ constructs its Z ring by interacting with the cell membrane where ZipA, an essential protein for cell division, provides assistance<sup>13</sup>. However, attaining mature cell size is crucial before cell division which is primarily dependent on carbon availability in rapidly growing bacteria. In the presence of high carbon conditions, UDP-glucose synthesis takes place where glucose-6-phosphate from glycolysis pathway acts as a precursor. The synthesized UDP-glucose interacts with the bifunctional diacylglycerol glucosyltransferase UgtP which in turn interacts with FtsZ thereby delaying Z-ring formation followed by cell division until cells reach optimum maturity. This process is crucial as increased carbon availability results in multi-fork replication thus regulation of cellular size is crucial to accommodate for higher chromosome DNA levels in the cell. In contrast, low carbon conditions do not present these cellular mechanisms and an overall reduction in cell size is observed<sup>19</sup>.

As with all living organisms, bacterial cells undergo cellular aging and apoptosis as time progresses. Bacterial cell growth and progression is directly proportional to the nutrient levels and

as they are consumed and depleted, cells will undergo a switch in behavior to a state of survival from their usual reproduction. As nutrients such as carbon and amino acid sources are drained, cells will increase RelA and SpoT activity, thereby an increase in (p)ppGpp will be observed.

Furthermore, cell division occurring at mid cell allows the daughter cells to have one old pole and one new pole. Interestingly, in Gram-negative bacteria the outer membrane proteins reside in the poles as time progresses due to protein-protein interactions with protein complexes already residing in the poles through a diffusion and capture mechanism. As the number of old poles inherited by progenitor cells increases due to cellular reproduction, the OMP levels in bacteria also increases. Also, the freshly synthesized peptidoglycan is absent in the cell poles as they reside mainly in the side walls therefore over time, the older poles become less adaptive to the environment than the newer poles resulting in cellular death rather than survival<sup>20</sup>.

### 1.3 Bacterial Growth Cycle

Bacteria will mostly encounter oligotrophic environments in nature, which force them to evolve under conditions of fluctuating nutrient availability. A lack of nutrients for growth will allow bacteria to deviate from a steady growth phase to a stationary phase which will allow them to survive under harsh environmental conditions without further exhausting limited resources<sup>21,22</sup>. It is further estimated that almost 60% of earth's biomass is composed of resting microorganisms where the lack of essential nutrients has allowed them to remain in the stationary phase<sup>23</sup>. Bacteria also have adapted unique strategies to maintain the cells viable for a prolonged period of time without any energy yielding substrates. This is known as starvation survival. Many Gram-positive bacteria construct dormant spores as a response mechanism against starvation. Though their methodology is different, both Gram-negative and Gram-positive bacteria have the ability to resume growth when nutrients become available for them and exhaust the nutrients up to a point

where they will have to enter a stationary phase to survive. This alteration continues depending on the nutrient levels leading cells to a feast and famine lifestyle<sup>22,24</sup>. Bacterial growth is considered to be an increase in cell number in a population which happens via cell growth and division. Plotting the viability of *Escherichia Coli* cells which is measured as CFU ml<sup>-1</sup> (CFU - Colony Forming Units) with rich media at 37 °C has revealed a characteristic growth pattern which is composed of five distinct phases<sup>25</sup>. They are lag phase, log or exponential phase, stationary phase, death phase and long-term stationary phase. There are several factors such as the species and growth conditions that may change some minor aspects such as the length of the lag phase, time required to attain stationary phase and the total number of cells in the bacterial population.

Cells experience the lag phase when they are first introduced into a different nutritional environment. Here, the metabolic reprogramming of cells takes place which allows them to develop in their current environment. The length of the lag phase is determined by the bacterial species utilized for the experiment, the shifting of the environmental parameter, and the time limit in which the cells have undergone starving conditions<sup>26</sup>. Once these cells have adapted to their current environment, they initiate their growth and division in an exponential manner which is the exponential phase or log phase. The growth rate of bacterial population is defined by the number of doublings per hour. These cells asexually divide by binary fission at a constant rate. This rate is mainly controlled by the environmental conditions where nutrient-poor conditions will result in a low rate and nutrient-rich conditions will result in a high rate. During this phase, there are several conditions that must be satisfied. First, all intrinsic parameters measured as population averages such as mean volume, density, and composition of the cells must remain constant. Second, all extrinsic parameters should increase exponentially such as the optical density of the culture and the number of cells, DNA, RNA, and protein per milliliter. Finally, the composition, temperature

and pH of the medium should remain constant within the cells' detection limits<sup>27</sup>. As cells grow exponentially, they deplete the nutrient stocks available for growth and will then reach the stationary phase. Here, no increase in cell number is observed. In Gram-negative bacteria, the starvation condition triggers a sigma factor RpoS (RNA Polymerase,  $\sigma_s$ ) which controls around 10% of *E. coli* genes which prepare the cells to survive in harsh conditions<sup>28,29</sup>. This stress response provides protection against temperature stress and osmotic stress<sup>30,31</sup>. In the stationary phase, the cultures accumulate waste products due to bacterial metabolism and then enter the death phase. Here, the number of live cells decreases exponentially, and the pattern of the exponential phase is reversed. It has been found that *E. coli* enters the death phase in Luria-Bertani (LB) media after incubation for 3 days<sup>25</sup>. It has been proposed that programmed cell death (PCD) occurs in order to provide nutrients for the remaining live cells to survive but it has not been authenticated. Around 90 - 99% of the population will die during this phase and provide their nutrients to the exhausted media for the survivors, which can retain the viability in a constant manner for months or even years. This is known as the long-term stationary phase<sup>24</sup>. Successive rounds of growth advantage in stationary phase phenotypes, mutants with better ability to search for nutrients than the parental strain. But the balance between dying and growing cells provides a dynamic equilibrium where the final output is the stable viability of the bacterial population<sup>25</sup>.

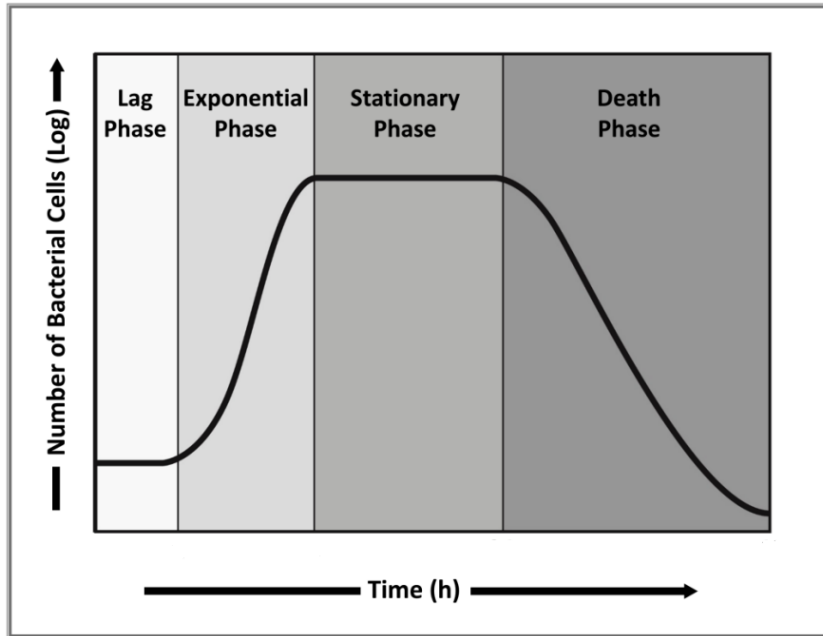


Figure 1.3 Bacterial growth curve. The lag phase represents the period at which bacterial cells adapt to the newly introduced environment and initiates cellular reproduction. The log phase represents the period where cells are functioning at optimum capacity where the number of cells double with each doubling cycle. The steady phase represents the period where nutrients are depleted, and waste accumulation begins to effect cellular function therefore replication is hindered, and ultimately cellular death occurs. Figure was taken from T Garrison, A., & W Huigens III, R. (2017). Eradicating bacterial biofilms with natural products and their inspired analogues that operate through unique mechanisms. *Current topics in medicinal chemistry*, 17(17), 1954-1964.

Furthermore, it is crucial to understand that these five phases have been derived from laboratory cultures utilizing a model organism. The times for each of the phases in nature is unknown but it will probably depend on the species and the environment in which that species is present<sup>25</sup>. Many studies have been carried out for *E. coli* physiology with cultures in steady-state growth (log or exponential phase). The period for *E. coli* in LB media in an exponential phase is

estimated to end when the optical density at 600 nm (OD<sub>600</sub>) is between 0.600 and 1.000 (OD<sub>600</sub> of 1.000 = 5 x 10<sup>8</sup> cells/ml). Cells in this OD range seem to vary widely in physiological state. However, a more focused study on *E. coli* K-12 strain MG1655<sup>32</sup> in LB media has indicated that the average cell mass begins to decrease at an OD<sub>600</sub> of 0.300 which marks the decrease of growth rate and thereby the end of exponential phase<sup>33</sup>.

When studying structural and functional changes in native intact systems, it is crucial to understand the state of the cells to validate the reliability of results obtained. For example, cells present in an overnight culture and a 4 – 6hr culture have different functional capabilities depending on the media used and the level of nutrition available for harvest. Cell cultures obtained at early log phase (OD<sub>600</sub> of 0.300) will have a higher percentage of healthy cells, which can be utilized for functional studies in native systems, than do cell cultures obtained at mid log phase (OD<sub>600</sub> of 0.600). This is because of the accumulation of a significant percentage of old poles and the limited availability of nutrients<sup>34</sup>. In contrast, overnight cultures are 14 – 16hr growth cultures where the cells will be in the late stationary phase, where cell growth no longer takes place, and where the accumulation of old poles and the number of lysed cells will be significantly increased due to rapid exhaustion of nutrients. Therefore, structural and functional studies using overnight cell cultures might not provide accurate information regarding intact systems compared to cells obtained at early log phase. These cells are metabolically healthy and functionally active, thereby providing much more reliable information regarding function.

## 1.4 OM Biogenesis

### 1.4.1 LPS Synthesis and Transport

Gram-negative bacteria such as *Escherichia Coli* (*E. coli*) consist of two membranes namely the outer membrane (OM) and the inner membrane (IM). The OM is a unique asymmetric bilayer

where the inner leaflet is composed of phospholipids and the majority of the outer leaflet is composed lipopolysaccharides (LPS). LPS is a highly negatively charged molecule which projects into the cell exterior providing antibiotic resistant properties to the cell while increasing membrane stability and decreasing membrane permeability. This enhances the integrity of the OM while providing antibiotic resistant properties to the bacteria<sup>1</sup>. This OM is also the environment where lipoproteins and integral membrane proteins called outer membrane proteins (OMPs) reside. There is an elaborate protein machinery, which is responsible for synthesis and transport of these LPS, lipoproteins, and OMPs to the OM for active function.

LPS is a crucial molecule for Gram negative outer membrane rigidity and stability. LPS majorly contributes to the structural integrity of the OM and it provides an overall negative charge to the surface of the bacteria for higher stability. LPS is a very unique molecule, whose structure is fully decoded mainly in Gram-negative species, and it consist of three main structural domains: Lipid A, Core Oligosaccharide and O-antigen (Figure 1.3). The O-antigen is a highly variable unit of LPS composed of repeating oligosaccharide units<sup>1,36-38</sup>. Lipid A is the hydrophobic long chain moiety that anchors LPS into the outer leaflet of the outer membrane. In *E. coli* and many *Enterobacteriaceae*, lipid A is a glucosamine disaccharide, phosphorylated at the 1 and 4' position and consist of six acyl chains attached by an ester bond (3 and 3' positions) and an amide linkage (2 and 2' positions)<sup>38</sup>. The most conserved portion of LPS is lipid A but there can be variations among chain length and the number of acyl chains across different species<sup>39</sup>. The lipid A is covalently linked to the core oligosaccharide which is further divided to inner and outer core. The inner core remains conserved among different isolates of the same species but the outer core is variable. The inner core consist of atleast one residue of 3-deoxy-D-manno-oct-2-ulosonic acid (Kdo) which links it to lipid A and usually also L-glycero-D-manno-heptose (heptose)<sup>40</sup>. The O-

antigen is composed of repeating units containing one to six residues, and it is the surface-exposed moiety responsible for immunogenic properties of LPS (Figure 1.4). The O-antigen is the most variable portion of LPS and it is used as a characteristic feature for strain classification based on different serological properties<sup>38</sup>. *E coli* strains which are unable to produce the O-antigen are known as “rough” strains whereas the wild-type strains which can produce O-antigens are known as “smooth” strains. These gram-negative species with LPS composed of only lipid A and core oligosaccharides are defined as lipooligosaccharides (LOS). The O-antigen is not produced in *E. coli* K12 derivatives due to a mutation in the *rfb* locus in which the genes responsible for O-antigen biosynthesis is clustered<sup>41</sup>.

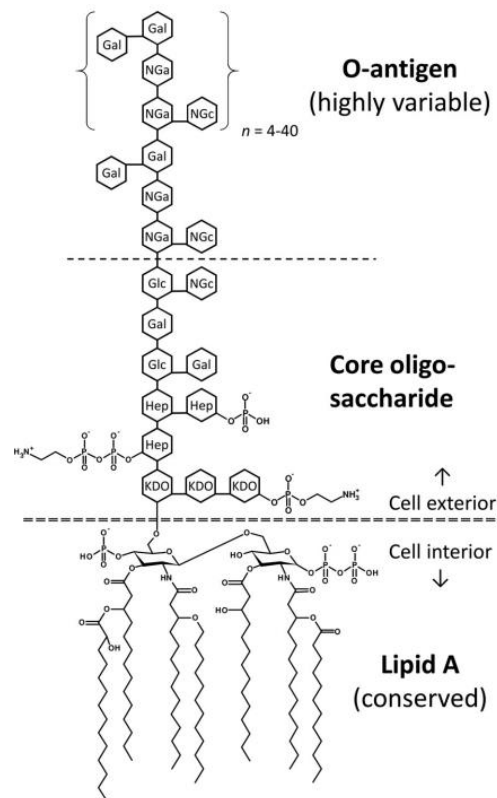


Figure 1.4 Typical LPS structure. It consists of a conserved lipid A buried in the OM, core oligosaccharide, and a highly variable O-antigen based on the bacterial strain. Figure was taken



from Raman, R., Raper, M. A., Hahn, E., & Schilke, K. F. (2017). Enhanced capture of bacteria and endotoxin by antimicrobial WLBU2 peptide tethered on polyethylene oxide spacers. *Biointerphases*, 12(5).

Biosynthesis of LPS is complex process requiring many different cellular compartments with spatial and temporal coordination of several independent pathways which converge to synthesize the full LPS molecule. The synthesis of lipid A with the Kdo residues of the inner core (Kdo<sub>2</sub>-lipid A moiety) occurs in the cytoplasm and at the inner leaflet of the IM. This is known as the “Raetz pathway” which is extensively characterized and shown to be conserved among Gram-negative bacteria<sup>38,39</sup>.

The core oligosaccharide can be sub-divided into a more conserved inner core and a variable outer core (Figure 1.4). The inner core contains Kdo and L-glycero-D-manno-heptose (heptose) groups. The outer core, though it is variable, is composed of a series of hexoses. In *E. coli* K-12, the addition of the two Kdo groups by WaaA is followed by a sequential addition of two heptose residues by WaaC and WaaF which extends the inner core where ADP-L-glycero-D-manno-heptose acts as the donor substrate for this reaction<sup>43</sup>.

The outer core extension initiates with an addition of a glucose group to the second heptose in the inner core mediated by WaaG using UDP-glucose as the donor. This glucose group is further extended by adding another glucose group and a galactose group independently from their UDP bound donors by WaaO and WaaB, respectively. WaaO activity is shown to have a dependence towards divalent cations during glucose addition<sup>44</sup>. The final glucose is added to the outer core by enzyme WaaJ whose activity depends on WaaB. The last step in the outer core synthesis is an addition of a heptose group by WaaU glycosyltransferase to the final glucose group added by WaaJ.

This heptose acts as the acceptor of the O-antigen once the lipid A-core moiety has been translocated to the outer leaflet of the IM.

The O-antigen, which as mentioned before is the most surface exposed component of LPS, has a high structural diversity where many distinct groups have been identified for *E. coli* alone. The *E. coli* K-12 strains are unique, and they do not produce O-antigen due to an ancestral mutation that has inactivated the O-antigen synthesis pathway<sup>45</sup>. The O-antigen consists of repeating oligosaccharide units, which are varied so that the size from molecule to molecule varies dramatically. Unlike the rest of the LPS molecule, the O-antigen is synthesized separately where it is built on a lipid carrier molecule, undecaprenyl phosphate (Und-P) in a stepwise manner and then transferred to the core oligosaccharide of the LPS molecule bound to the periplasmic face of IM<sup>46,47</sup>.

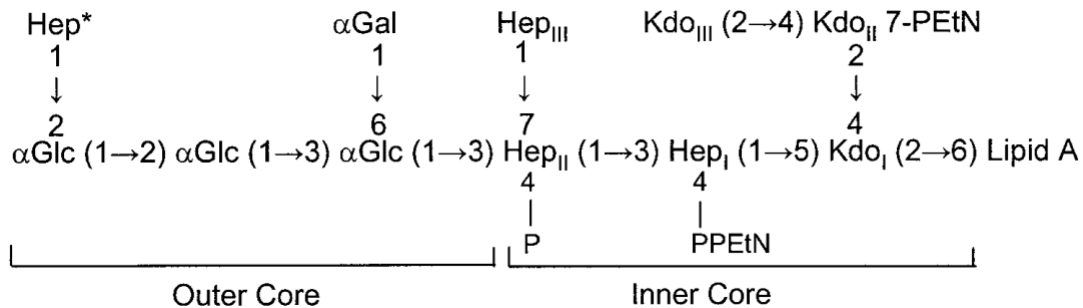


Figure 1.5 Structure of *E. coli* rough LPS core oligosaccharide. It consists of a conserved inner core and a variable outer core. Figure was taken from Nikaido, H. (2003). Molecular basis of bacterial outer membrane permeability revisited. *Microbiology and molecular biology reviews*, 67(4), 593-656.

LPS transport begins at the inner membrane where the completed lipid A-core moiety, which is docked in the inner leaflet of the IM, is fit for translocation across the IM by the MsbA ABC

transporter. This process will translocate lipid A-core moiety to the periplasmic face of the IM where the O-antigen ligation to this complex is mediated by WaaL ligase. After O-antigen binding to the lipid A-core moiety to complete the LPS molecule, it must be extracted from the periplasmic face of the IM, transported across the periplasmic surface to the OM, and finally be transported through the OM to the outer leaflet of OM against a concentration gradient, which is a challenging process considering the chemical nature of LPS. For this process, seven essential proteins span the entire cell envelope, and utilize the energy from ATP hydrolysis in the cytoplasm to transport LPS from IM to the OM<sup>48,49</sup>. The Lipopolysaccharide transport proteins LptABCDEFGH physically interact to convert chemical energy to mechanical work through conformational changes in their structure for LPS transport. After MsbA flips the LPS to the periplasmic face of IM and O-antigen binds to complete the LPS molecule, the second ABC transporter LptB<sub>2</sub>FG uses energy derived from ATP hydrolysis to detach LPS from the IM leaflet and push it towards the periplasmic bridge made by LptC, LptA and N-terminal domain of LptD<sup>50,51</sup>. The LptD/LptE complex constructed at the OM then finally mediates LPS final assembly in the outer leaflet of the OM<sup>52</sup> (Figure 1.6).

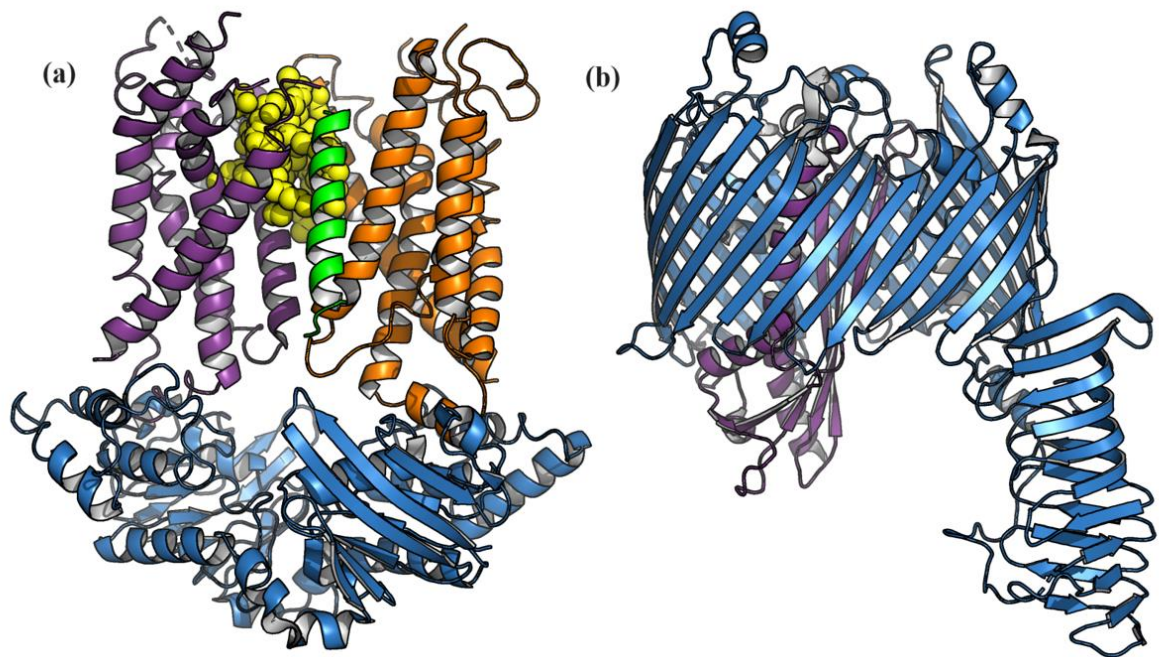


Figure 1.6 LPS transport machinery structures. (a) **LptB<sub>2</sub>FGC** complex with bound LPS fragment (yellow spheres) (PDB ID 6S8N) (b) **LptDE** complex where **LptD** is forming the beta barrel while **LptE** forms a core domain and occludes the barrel.  $\beta$ -jellyroll like structure is formed by LptD N-terminus (PDB ID 4Q35). Crystal structures were obtained from Protein Data Bank (<https://www.rcsb.org/>) and protein structures were generated from PyMOL Molecular Graphics System version 3.0.3.

The Lpt complex, which catalyzes this process, is a multiprotein machinery that uses energy from ATP hydrolysis to move these LPS molecules to the OM after successfully detaching from the IM. The energy is obtained by LptB<sub>2</sub>FG, an ABC transporter which couples the detaching of LPS from IM with the ATP hydrolysis. LptB<sub>2</sub>FG is tetramer with a dimer of LptB and two polytopic proteins LptF and LptG<sup>53</sup>. Also, LptB<sub>2</sub>FG maintains a stable association with LptC, an IM protein with a transmembrane helix and a large periplasmic domain folded into a  $\beta$ -jellyroll<sup>54</sup>.

In the current model for LptB<sub>2</sub>FG mediated LPS transport, the LptB dimer exhibits an open conformation in the nucleotide-free state. Upon ATP binding, LptB monomers shift closer followed by conformational changes transmitted to LptF and LptG through the coupling helices. This induces an opening of the lateral gate between one of the TM1-TM5 interfaces of LptFG allowing LPS to enter the internal cavity. After LPS is released from LptB<sub>2</sub>FG transporter, it reaches the periplasmic domain of LptC. This domain consists of a series of antiparallel  $\beta$ -jellyroll domains, which has a hydrophobic region that is suggested to maintain the acyl chains of LPS during its transit through the periplasm<sup>55</sup>. LptA, and the periplasmic domain of LptD consist of  $\beta$ -jellyroll fold and these domains of LptC, LptA, and LptD align in a head to tail manner to further extent the hydrophobic groove across the periplasm. This LptCAD orientation is suggested to form a bridge across the periplasm through which LPS can travel to reach OM<sup>56</sup>. After LPS reaches the OM, in order to maintain asymmetry of the OM, the efficient insertion of LPS into the outer leaflet of OM while avoiding insertion at the inner leaflet is crucial. The OM  $\beta$ -barrel protein LptD and the lipoprotein LptE controls this step<sup>57</sup>. LptD is an OM protein belonging to the Lpt family with a C-terminal transmembrane 26 stranded  $\beta$ -barrel domain similar to TonB-dependent transporters (TBDTs/22  $\beta$ -strands) and a N-terminal periplasmic domain which is connected by two non-consecutive disulfide bonds<sup>58</sup>. The interior of LptD is hydrophilic and is postulated to interact with the core oligosaccharides and O-antigen during transport. The membrane-associated component of LptD is large, where the H-bonding is between  $\beta$ -strands 1 ( $\beta$ 1) and 26 ( $\beta$ 26) and a small gap will be constructed when the H-bonding is disrupted. It is proposed that after LPS arrives at the  $\beta$ -jellyroll domain of LptD, the acyl chains of LPS are directly deposited into the OM through the small gap that is present between the periplasmic domain and the  $\beta$ -barrel domain of LptD. Considering the tilt angle at N-terminus  $\beta$ 1 ( $30^\circ$ ) and C-terminus  $\beta$ 26 ( $67^\circ$ ), it is assumed that the

small gap of LptD may provide a degree of opening of the  $\beta$ -barrel between  $\beta 1$  and  $\beta 26$  to allow lateral passing of the hydrophobic portion of LPS through the LptD lumen out into the OM. Overall, this mechanism of the Lpt complex in LPS transport to the OM is known as the “PEZ Model”<sup>55</sup>.

#### 1.4.2 Lipoprotein (Lpp) Synthesis and Transport

Another major component of the OM are lipoproteins which make a significant contribution to the integrity of the cell envelope structure. Lipoproteins present in Gram-negative bacteria contain a common lipid structure which anchors the protein to the membrane but it is highly diverse in terms of structure, function and sequence. Lipoprotein synthesis begins in the cytoplasm and it is then modified with lipids at the outer leaflet of the inner membrane (IM) followed by translocation and insertion into the OM. Lipoproteins are synthesized with a signal sequence which allows them to be transferred across the IM by the SEC translocon. The Cys residue between the mature protein and the signal sequence is strictly conserved in all lipoproteins. This Cys residue is surrounded by a partially conserved sequence Leu(Ala/Val)-Leu-Ala(Ser)-Gly(Ala)-Cys which is known as the “lipobox” and is recognized by lipid-modifying enzymes. This modification occurs at the outer leaflet of the IM when a diacylglycerol is added to the sulfhydryl group (-SH) of Cys by phosphatidylglycerol/prolipoprotein diacylglyceryl transferase (Lgt). This reaction is followed by the cleavage of the signal peptide near the Cys residue by a special lipoprotein signal peptidase (signal peptidase II/Lsp). Lastly, a fatty acid translocation from phospholipids to the amino group of the Cys residue occurs by membrane-bound phospholipid/apolipoprotein transacylase (Lnt) (Figure 1.7). Though all lipoproteins mature in the periplasmic side of IM, some will be targeted for trafficking to the OM while the others will remain in the IM. The targeting signals for these lipoproteins are encoded within the protein sequence while heterologous proteins can be targeted

to the OM via a fusion with the N-terminal sequence of the OM lipoproteins<sup>59</sup>. *E. coli* lipoprotein studies indicate that lipoproteins have a quite simple and elegant OM targeting signal where the identification of the second amino acid (+2) adjacent to the lipidated Cys determines the localization of the lipoprotein.

The major route that grants Lpp access to the OM is the Lol pathway (Figure 1.7). It consists of components in each part of the cell envelope. The IM contains LolCD<sub>2</sub>E, an ATP-binding cassette transporter which extracts matured Lpp from the IM, which should be present in the periplasmic side of the OM, while retaining the lipoproteins, which should be present in the periplasmic side of the IM. The soluble chaperone LolA in the periplasm obtains the Lpp transferred from LolCD<sub>2</sub>E. The inner leaflet of OM contains a lipoprotein LolB, which receives the Lpp shuttled to the OM by LolA and anchors them to the inner leaflet of the OM<sup>34,60</sup>. However, recent studies have shown that under the conditions where both LolA and LolB are deleted, the trafficking of Lpp to the OM still takes place indicating that there might be another unknown pathway of Lpp transport. Further studies are essential to fully understand how Lpp is shuttled to OM<sup>61</sup>.

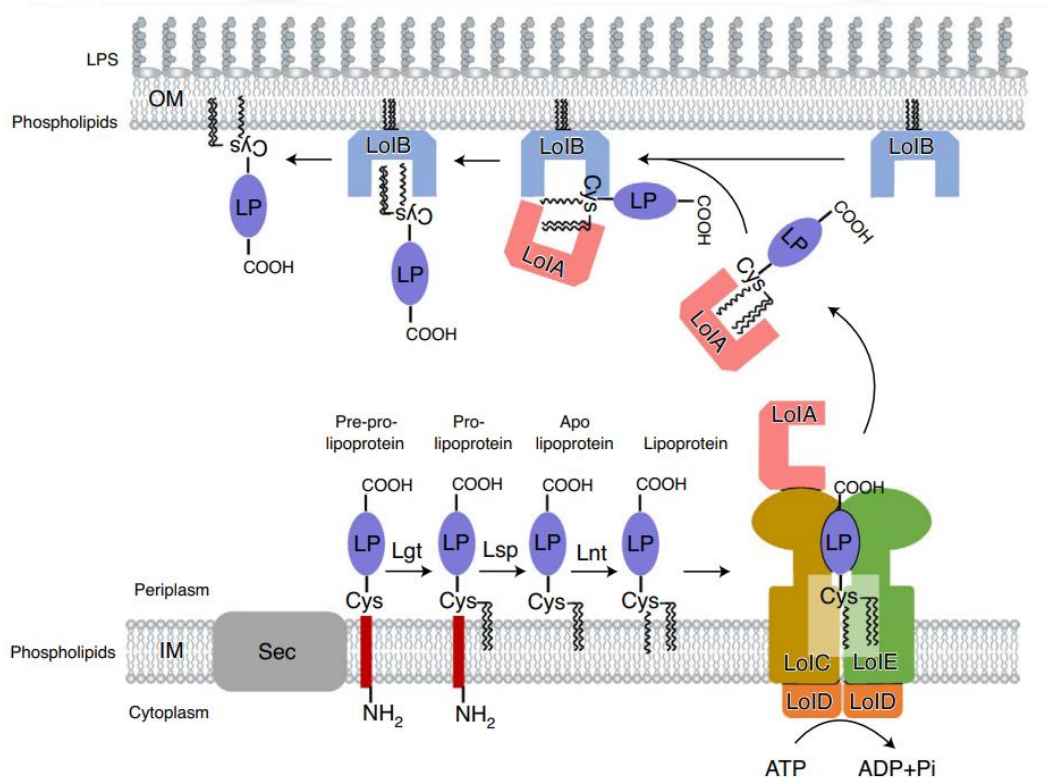


Figure 1.7 Synthesis and transport of lipoproteins to the inner leaflet of the OM. The lipoprotein precursors are bound to chaperone LolA through LolCD<sub>2</sub>E ABC transporter, translocated to the OM where it meets LolB through mouth-to-mouth interaction to transfer Lpp to LolB and finally inserted to the OM. Figure was taken from Tang, X., Chang, S., Zhang, K., Luo, Q., Zhang, Z., Wang, T., Qiao, W., Wang, C., Shen, C., Zhang, Z., Zhu, X., Wei, X., Dong, C., Zhang, X., & Dong, H. (2021). Structural basis for bacterial lipoprotein relocation by the transporter LolCDE. *Nature structural & molecular biology*, 28(4), 347–355.

Lipoprotein interaction with IM LolCD<sub>2</sub>E indicates that Lpp primarily interacts with LolE. LolC do not interact with Lpp though it also contains a hydrophobic cavity similar to LolE. Hence, the key role of LolC is to recruit LolA to the IM complex<sup>63,64,65</sup>. Both LolC and LolE contain a similar periplasmic domain however LolA can be captured by the LolC loop which was recently



discovered by a co-crystallization study<sup>64</sup>. With these findings, it was proposed that LolE takes in the Lpp from the membrane and LolC takes in the periplasmic chaperone LolA. LolD is the ATPase that provides energy for the LolCD<sub>2</sub>E complex, and it is proposed that the energy derived may be required to perform the energetically unfavorable extraction of the acyl chains from the IM bilayer. However, recent *in-vitro* studies indicate that the initial ATP binding induces an alteration in the LolCD<sub>2</sub>E-Lpp complex which makes the Lpp removable in the presence of detergent. Therefore, it is assumed that the energy derived from ATP hydrolysis may be important for the next steps, which release Lpp from the complex and transfers it to LolA, thereby resetting the LolCD<sub>2</sub>E complex for the next Lpp<sup>66</sup>.

LolA is obtained by LolC via a “hook-and-pad interaction.” Here, the solvent exposed  $\beta$ -hairpin loop, which extends from the LolC periplasmic domain, is the hook and the three residues in the LolC periplasmic domain where LolA binds is the pad. Both interact with the LolC  $\beta$ -hairpin loop and the three residues in the periplasmic domain are required for binding LolA<sup>64</sup>. LolA is an incomplete  $\beta$ -barrel with an enclosed hydrophobic cavity composed of aromatic residues<sup>67</sup>. A sequence homology is shared between the periplasmic domains of LolA and LolC where the Lpp transfer is assumed to occur by the lining of the hydrophobic cavities in a mouth-to-mouth orientation. Crosslinking analysis reveals that the entrance region of the LolA cavity interacts with LolC and the periplasmic regions of LolC and LolE (around 200 residues) exhibit sequence similarity with LolA (around 182 residues), therefore similar hydrophobic cavities maybe present in LolC and LolE. It is proposed that the function of LolA includes the shielding of the acyl chains in Lpp from the aqueous periplasm and transport across to the OM. However, the *E. coli* LolA structural data indicates that its hydrophobic cavity is insufficient to accommodate all three acyl chains of Lpp<sup>67</sup>. An alternate proposal for Lpp binding to LolA indicates that some acyl chains

might bind to the hydrophobic patches present on the LolA surface<sup>68</sup>. After LolA shuttles Lpp in the periplasm towards the OM, LolB that is docked into the inner leaflet of the OM receives Lpp from LolA in a mouth-to-mouth manner through a connection between their hydrophobic cavities, and the ultimate step of Lpp trafficking is executed by anchoring Lpp to the OM<sup>69</sup>.

### 1.4.3 OMP Synthesis and Transport

All OMPs follow a similar mechanism of synthesis and transport. These OMPs are initially synthesized at the ribosome in cytoplasmic space and are then transported to the OM. After OMP synthesis at the ribosome, these OMPs then transverse the IM in their unfolded state utilizing a small pore in the center of SecYEG translocon (4). The OMP precursors are delivered to the SecYEG translocon by the SecAB chaperones in their unfolded state with an N-terminal signal peptide which is cleaved by periplasmic peptidases upon delivery to the Sec translocon (5). Upon arriving to the periplasmic surface, the aqueous environment will trigger these unfolded proteins to aggregate and thereby misfold. This process is prevented by periplasmic chaperones where they interact with the unfolded OMP precursors, escort them through the periplasmic surface, and deliver them to the OM where the  $\beta$ -barrel assembly machinery complex (BAM complex) correctly folds and inserts them into the OM<sup>70</sup>.

#### 1.4.3.1 Periplasmic chaperones

Due to the fact that spontaneous protein folding is a rapid and an error prone process, the newly synthesized unfolded proteins use periplasmic chaperones to reach their final conformational state. In *E. coli*, there are three particular periplasmic chaperones namely SurA, Skp, and DegP specifically responsible for transporting OMPs through the periplasm to the OM.

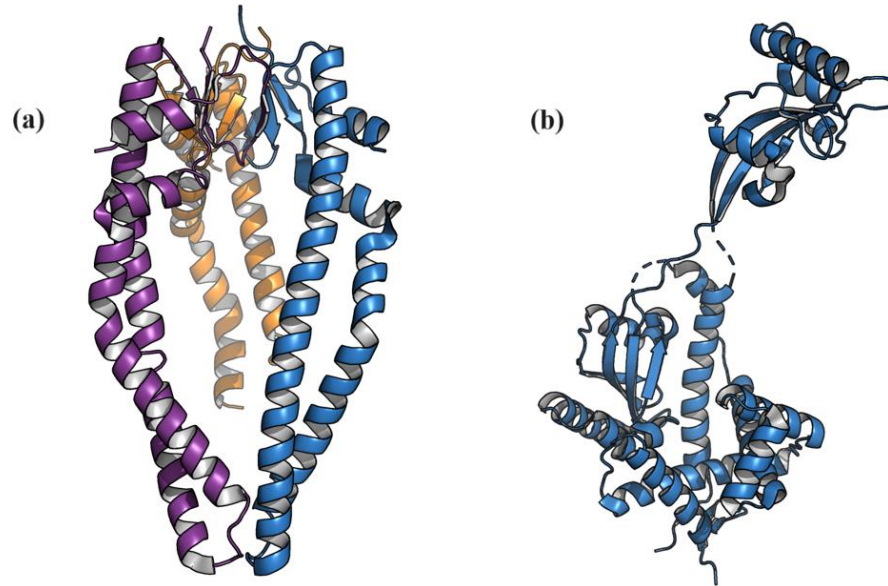


Figure 1.8 Periplasmic chaperones Skp and SurA structures. (a) Crystal structure of trimeric chaperone Skp (PDB ID 1SG2) (b) Crystal structure of SurA (PDB ID 1M5Y). Crystal structures were obtained from Protein Data Bank (<https://www.rcsb.org/>) and protein structures were generated from PyMOL Molecular Graphics System version 3.0.3.

SurA is a periplasmic chaperone identified as a survival factor in stationary phase cells. The primary function of SurA includes the folding and periplasmic shuttling of OMPs<sup>71</sup>. SurA consists of a higher affinity towards peptide sequences with higher aromatic residues, which contains the motif Ar-X-Ar motif where Ar is an aromatic residue and X is a polar residue. This pattern is common in OMPs as amphipathic  $\beta$ -strands are generally characterized by alternating hydrophobic and hydrophilic residues. The Ar-X-Ar motif is prevalent at the periplasmic turns of OMPs since aromatic residues tend to cluster at the end of  $\beta$ -strands that form  $\beta$ -barrels. Furthermore SurA shows a higher affinity towards unfolded OMPs than unfolded soluble or folded proteins<sup>72</sup>. Crystal structures show four main domains in SurA, a N-terminal domain which doesn't have any known structural homology, two central domains consist of conserved parvulin fold observed in many

PPIases (P1 and P2), and a short C-terminal domain that forms a long  $\alpha$ -helix followed by a short  $\beta$ -strand<sup>73</sup>. The P2 domain of SurA which has the PPIase activity forms a satellite domain which is around 30 Å removed from the other domains. The other domains together forms the core of the protein.

Skp, also known as seventeen kilodalton protein is another periplasmic chaperone which stabilizes OMPs during their passage through the periplasmic surface. Skp interacts with unfolded OMPs as they are released from the Sec translocon<sup>74</sup>. The binding of Skp allows the hydrophobic, aggregation prone OMPs to remain stable while shuttling through the periplasm. Skp is also proposed to assist insertion of OMPs to the OM or to the BAM complex. It has also been shown that Skp and LPS together is sufficient to allow  $\beta$ -barrel OMPs to enter the OM<sup>75</sup>. Skp forms a stable trimer which binds substrate in a strict 1:1 ratio. Crystal structures indicate that the Skp trimer has a “jellyfish” like structure with a central  $\beta$ -barrel “body” trimerization domain to which each subunit donates 4  $\beta$ -strands and a long straggly  $\alpha$ -helical tentacles to grasp substrates<sup>76</sup>. The three subunits superimpose to form a rigid hydrophobic core but the tentacles are highly flexible with hinge loops at the position where they connect with the body. The  $\alpha$ -helical arms have an overall positive charge on the outer surface that is assumed to interact with LPS, and the hydrophobic patches on the inside surface is assumed to interact with hydrophobic substrates. The arms form a central cavity large enough to hold an OM pore, with different size proteins being accommodated by the flexibility of the hinges<sup>76</sup>. Both SurA and Skp achieve similar tasks with different methods. Both SurA and Skp shuttle OMPs to the OM in their unfolded state.

DegP is the *E. coli* periplasmic chaperone belonging to the high temperature requirement (HtrA) family of proteins which is able to survive at elevated temperatures. This is mediated by two functions, which are a chaperone activity and an protease activity. The chaperone activity

rescues slightly misfolded proteins and the protease activity induces a rapid degradation of irretrievably misfolded proteins<sup>77</sup>. At low temperatures (around 28 °C) the chaperone activity is prominent but as the temperature increases, the protease activity becomes prominent. DegP is critical for survival above 37 °C or under conditions of stress such as when chaperone SurA is knocked out or OMPs are overexpressed<sup>78</sup>. The DegP monomer is composed of three domains: a protease domain present at the N-terminus, which is homologous to the trypsin family of serine proteases, and two consecutive PSD95, DlgA, ZO-1 (PDZ) domains at the C-terminus where PDZ is the common module that is involved in mediating protein-protein interactions. The smallest active unit is a DegP trimer (DegP<sub>3</sub>), with hydrophobic interactions between the protease domain forming the interface while the PDZ domains sticks out with a highly flexible orientation from the sides<sup>79</sup>. This trimer is present under conditions of both high protease and chaperone activity, and is thought to be a major form at elevated temperatures; whereas at lower temperatures, these trimers associate to make larger complexes depending on the nature and presence of substrate<sup>80</sup>. The most common form of DegP in the absence of substrate is a hexamer (DegP<sub>6</sub>) mediated by the PDZ domains. Structural data further indicates that the main purpose of the oligomerization of DegP is to regulate substrate access to the protease domains. Although the hexamer is the most stable form in the absence of substrate, formation of 12-mer or 24-mer can be observed in the presence of denatured protein. Addition of a denatured substrate such as a lysozyme, casein or albumin causes multiplication of DegP<sub>6</sub> into DegP<sub>12</sub> or DegP<sub>24</sub> followed by a slow return to the DegP<sub>6</sub> state<sup>80</sup>. However, it is understood that the proposed chaperone role for DegP where the formation of hydrophobic cage in which they can fold into their final conformation is dissimilar to the models proposed for SurA and Skp which do not fold their substrates to preserve the folding energy for membrane insertion.

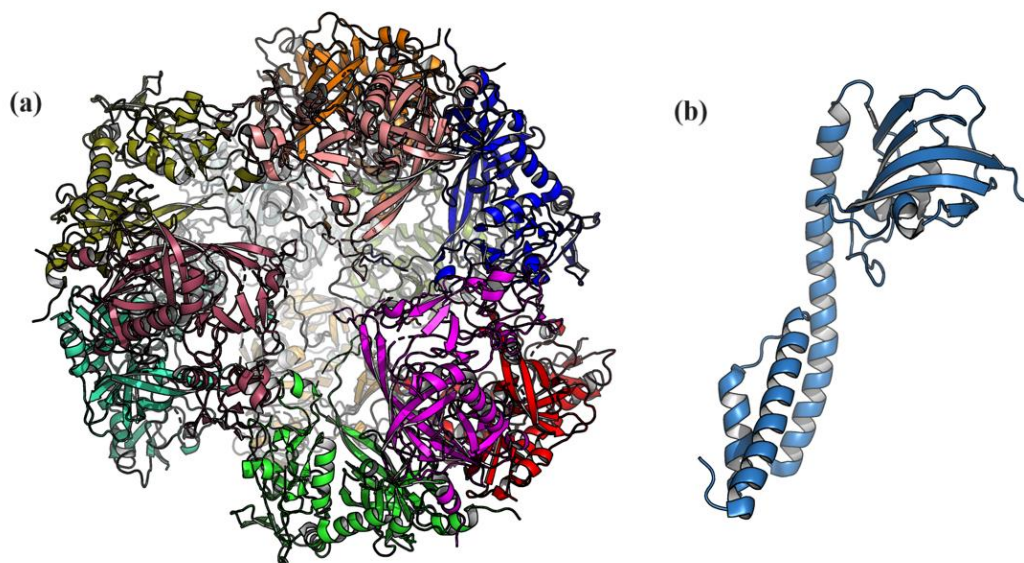


Figure 1.9 Periplasmic chaperones DegP and FkpA structures. (a) Crystal structure of DegP dodecamer (DegP<sub>12</sub>) (PDB ID 2ZLE) (b) Crystal structure of FkpA monomer. (PDB ID 1Q6U). Crystal structures were obtained from Protein Data Bank (<https://www.rcsb.org/>) and protein structures were generated from PyMOL Molecular Graphics System version 3.0.3.

Apart from SurA, there are three other proteins with proline cis-trans isomerase activity in *E. coli* which are FkpA, PpiA and PpiD. Among these three proteins, FkpA belongs to the FK506-binding protein (FKBP) family which is sensitive to the immunosuppressant FK506, and it is shown to maintain both chaperone and PPIase functions<sup>81</sup>. Apart from PPIase activity, FkpA is also shown to assist with folding of several soluble proteins, including recombinantly expressed single chain antibody fragments. Structural data indicates that FkpA forms a stable homodimer where each monomer contains two distinct domains, where there is a high degree of flexibility in the orientations of the two domains. The N-terminal domain is made up of three long  $\alpha$ -helices which entwine to form the dimer interface whereas the C-terminus homologous to FKBP are present at the end of the molecule which contains the PPIase activity<sup>82</sup>. NMR studies of the residues of C-

terminal domains show major chemical shifts in the presence of model substrates with the distance and the orientation between the two domains changing to accommodate different substrates. However, there are suggestions that FkpA preferentially binds to oligomerized proteins to prevent further aggregation, and there seems to be no specific binding pocket on the interaction surface that might select specific amino acid sequences or three dimensional motifs. These studies further indicate that FkpA might be a more general chaperone with the ability to bind to many different substrates provided that they present exposed hydrophobic patches to the environment.

#### 1.4.3.2 Beta-barrel assembly machinery (BAM) complex

After chaperones transport native unfolded OMPs to the outer membrane, the BAM complex obtains these OMPs, folds them into their native configuration and inserts them to the OM (Figure 1.10). In *E. coli*, the BAM complex is composed of five components BamA, B, C, D and E. BamA is composed of an N-terminal periplasmic domain containing five polypeptide transport associated (POTRA) domains (P1-P5) and a C-terminal 16 stranded  $\beta$ -barrel domain. Further studies have indicated that the interaction of BamA with its other components is mediated by the POTRA domains and that BamA requires a lateral opening mediated by  $\beta$ -strand 1 and 16 into the membrane for function<sup>84,85</sup>. BamB is a lipoprotein which is attached to the periplasmic side of the OM by the N-terminal lipid anchor. It is composed of an eight-bladed  $\beta$ -propeller where each propeller is composed of four antiparallel  $\beta$ -strands composed of WD40-like repeats. BamB is also wider in one edge compared to the other giving a protein an overall wedge shape<sup>86,87</sup>. BamC is composed of an unstructured

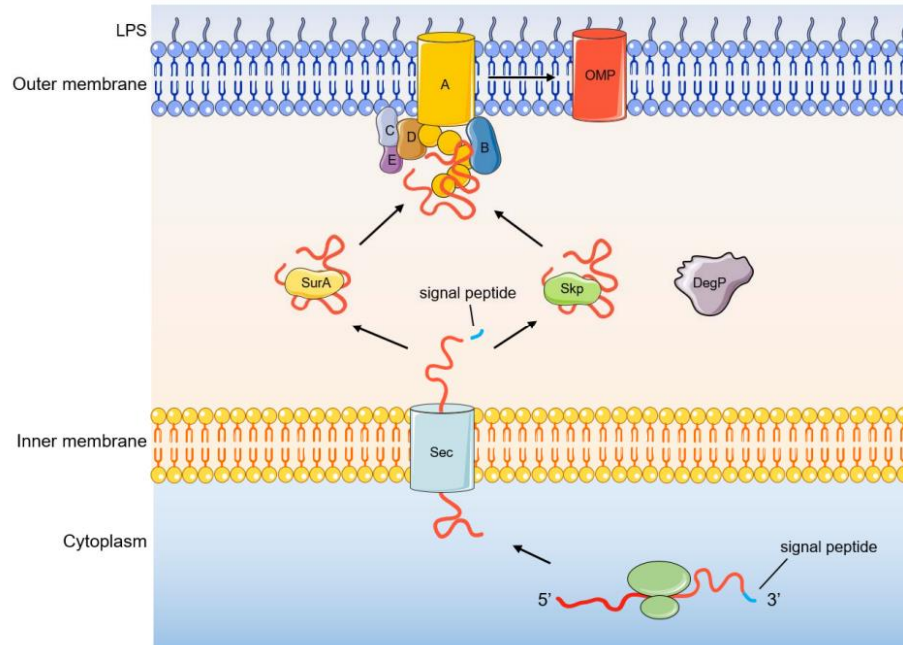


Figure 1.10 OMP Assembly and insertion to OM. Once the peptides are translocated to the periplasmic space through SecYEG translocon, periplasmic chaperones transport these unfolded proteins to the BAM complex where they are properly folded to  $\beta$ -barrel architecture and inserted to the OM. Figure was taken from Xu, Q., Guo, M., & Yu, F. (2023).  $\beta$ -Barrel Assembly Machinery (BAM) Complex as Novel Antibacterial Drug Target. *Molecules (Basel, Switzerland)*, 28(9), 3758.

N-terminal domain with two helix-grip domains. Further *in-vivo* studies have shown that the helix-grip domains are surface exposed in *E. coli*<sup>88,89</sup>. BamD is composed of five tetratricopeptide repeat (TPR) domains, and it has been suggested that BamD has a role in BamA activation and interaction with substrate<sup>90,91</sup>. BamE is composed of an  $\alpha\beta\beta\beta$  fold and it has been shown to further assist the interaction between BamA and BamD<sup>92,93</sup> (Figure 1.11). Though structures of the BAM components have been solved, the mechanism of  $\beta$ -barrel folding and insertion into the OM is yet known. After discovery of BAM complex, it was shown that both BamB and BamD interact with BamA via its POTRA domains<sup>94</sup>. Also some studies have indicated that the POTRA domains



interact with the substrate before insertion into the OM<sup>95</sup>. The junction site that closes the barrel in BamA where  $\beta 1$  and  $\beta 16$  are present was found to be shorter, which resulted in a thin hydrophobic belt. Also, it was apparent in crystal structures that  $\beta 16$  was partially deviated from  $\beta 1$  where it was in a bent conformation that was pointing towards the lumen of the barrel<sup>96</sup>. This data indicated that there might be a lateral gate present in BamA which provides access to the OM during biogenesis<sup>97</sup>. Furthermore, an exit pore was discovered that was proposed to mediate the extracellular loop formation of OMPs<sup>96</sup>.

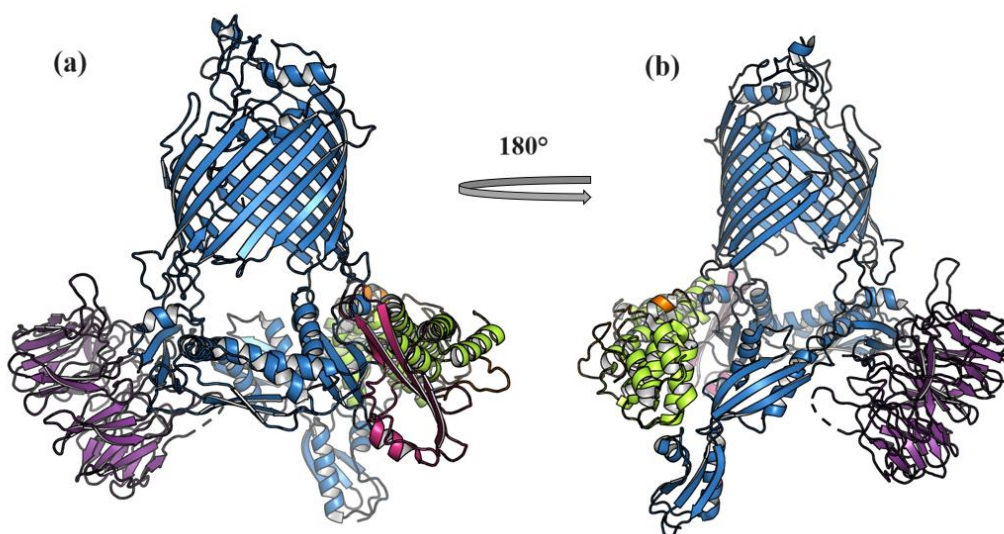


Figure 1.11 The BAM complex. Crystal structure (a) front view (b) rear view of BAM Complex (PDB ID 5D00). BAM Complex is composed of five components. They are **BamA**, **BamB**, **BamC**, **BamD**, and **BamE**. Crystal structures were obtained from Protein Data Bank (<https://www.rcsb.org/>) and protein structures were generated from PyMOL Molecular Graphics System version 3.0.3.

Many crystal structure studies have been carried out to identify the function of components in the BAM complex. Crystal structure studies of a fusion between P3, P4, and P5 of BamA with

BamB indicated that BamB binds to P3 in proximity to the linker with P2. This interaction is assumed to regulate the conformational changes in the POTRA domains that were observed between P2 and P3 previously<sup>95</sup>. A crystal structure of a fusion between P4 and P5 with BamD indicated that TPR3 and TPR4 of BamD initiated the primary interactions with P5 of BamA. Though it is suggested that BamD may activate BamA for function, the true effect of BamD binding to BamA remains unclear<sup>98</sup>. Recent crystal structures indicated that BamC was found to interact with BamD however the helix grip domains were found in various states along the periplasmic side of the complex. In addition, BamE was found to interact with TPR4 and TPR5 of BamD and also with P5 of BamA which may indicate that BamE enhances the interaction between BamD and BamA<sup>99,100</sup>. Also, TPR1 and TPR2 of BamD were found to interact with P1 and P2 of BamA which may indicate the stabilization of a ring-like structure along the periplasmic portion of the BAM complex. Though this ring conformation is found to be essential for OMP biogenesis, the mechanism as to which it contributes to OMP biogenesis of BAM complex has not been elucidated<sup>101</sup>. Further studies on BamD interactions with POTRA domains of BamA indicated that only the interaction with P5 is consistent with observations *in-vivo*. This suggests that the interactions between P1 and P2 found in crystal structures might be artifacts<sup>94</sup>. Most recently, the structural data obtained have provided evidence for substantial conformational changes in BamA. There, four conformational states are observed for the POTRA domains. Two states out of four were present for structures that lacked BamB in which P1 and P2 underwent a shift of ~30 Å from each other with P5, which is located directly under the barrel domain of BamA, thereby closing access to the luminal domain of the barrel<sup>101</sup>. A third confirmation state in the cryo-EM structure without BamB indicated slight shifts of P1 and P2<sup>102</sup>. The fourth state was observed for complex with BamB, and indicated all POTRA domains shifting ~40 Å, thereby locating P5 away from

BamA and enabling access to the luminal domain of the barrel. POTRA domains of BamA were initially discovered to be dynamic, and the BAM complex itself is considered to be dynamic. Therefore, the observed conformational states may be due to binding of BAM associated substrate or crystallization artefacts. X-ray crystal structures further indicated that the different states observed for BamA is BamB dependent, where BamA consists of a classical barrel domain with a fully formed junction site that is known as the inward-open conformation in the presence of BamB<sup>101</sup>. In the absence of BamB, BamA undergoes a major structural change where the first half of the barrel domain is rotated by 45° starting with  $\beta$ 1 and ending with  $\beta$ 9. The extracellular loops 1 (L1), L2 and L3 fully opening along the exit pore, also known as the outward-open conformation<sup>103</sup>. Recent cryo-EM structures also indicate an outward-open conformation in the absence of BamB<sup>102</sup>. As a consequence of outward-open conformation, the H-bonding between  $\beta$ 1 and  $\beta$ 16 gets disrupted completely. Also, BamE was found to interact specifically with phosphatidylglycerol (PG) and enhance OMP insertion into liposomes, and it was discovered that the lipid binding site overlaps with the BamD binding site. Therefore, PG can be recruited by BamE for membrane insertion of OMPs. From all the structural data obtained, it is been speculated that the roles of BamB and BamC-D-E may be to regulate the cycling of BamA from inward-open to outward-open conformations, inspite of the dynamic conformational changes observed for BamA and the POTRA domains. These conformational changes does have the ability to support the OMP biogenesis by directly threading nascent OMPs to the OM or further priming the membrane for insertion of OMPs<sup>104</sup>.

Due to the fact that  $\beta$ -sheets are amphipathic, having a hydrophobic interface on one side and hydrophilic interface on the other,  $\beta$ -barrels do not have the ability to be fully membrane integrated prior to closure of the barrel. This leads to the proposal of two models for BAM function known as

the “budding model” and the “BamA assisted model”. In the “budding model”, the  $\beta$ -strands of the OMPs are templated at the open BamA forming a BamA/OMP hybrid barrel. Once all the strands are formed, the OMP barrel closes and buds off BamA into the OM. This is supported by initial structural data indicating a poor H-bonding between  $\beta 1$  and  $\beta 16$ . In addition, the BamA barrel has a low thermodynamic stability compared to other  $\beta$ -barrels, and a melting temperature of 37 °C indicates that BamA is highly dynamic at physiological temperature. This weakened H-bonding led to the assumption that the BamA barrel can be opened laterally, exposing unpaired  $\beta$ -strands where this opening can create sites for  $\beta$ -strand templating of an incoming OMP, which can obtain access to the gate by first being threaded through the lumen of BamA<sup>97</sup>. In the case of “BamA assisted model”, the folding of OMPs to  $\beta$ -barrels is initiated on the periplasmic side of the OM followed by integration as one unit into the outer membrane by the BAM complex. A main feature of  $\beta$ -barrel proteins is their high free energy of folding, and their ability to fold *in-vitro* in the presence of a thin lipid bilayer<sup>105</sup>. Biophysical studies indicate that a denatured OMP first binds to the membrane surface followed by a transition step where the  $\beta$  hairpins starts to form and penetrate the membrane in a coordinated manner. This type of spontaneous folding can occur only in thin membranes composed of short acyl chains lipids above the temperature of phase transition<sup>106</sup>. Native *E. coli* lipids such as phosphatidylglycerol (PG) and phosphatidylethanolamine (PE) do not alone support OMP folding, therefore it is assumed that the BAM complex reduces the kinetic barrier to membrane insertion by constructing a defect or stabilizing a transition state for the OMP at the OM<sup>107</sup>. Crystal structures further indicated that the barrel domain is 9-12 Å thick next to its seam therefore, it may cause a membrane defect or a hydrophobic mismatch between the membrane and aromatic rings of BamA.

#### 1.4.3.3 Disulfide bond formation (Dsb) system

#### 1.4.3.3.1 Oxidative Pathway

Biosynthetic disulfide linkage formation is a crucial step for maturation of secreted proteins in both eukaryotic and prokaryotic cells. These covalent disulfide linkages are constructed between two free thiol (-SH) groups present in cysteine (Cys) residues in the protein backbone. This crosslinking helps stabilize secreted proteins; however incorrect pairing of cysteines will result in a protein fold that differs from its native configuration. *E. coli* DsbA (DsbA analogs in other bacteria) is a 21 kDa monomeric protein present in the periplasm which catalyzes oxidative disulfide crosslinking (S-S) between cysteine residues. However, several factors have to be considered for oxidative protein folding by DsbA. The majority of crosslinks occur between consecutive Cys residues in the presence of DsbA. Here, DsbA will bind to the first Cys present in the peptide travelling through SecYEG and induce a covalent crosslink between the first and the second Cys entering the periplasm to create a disulfide linkage. Hence, the crosslinking will depend on the rate of export of the polypeptide to the periplasm. It is possible to observe almost consistent consecutive S-S linkages during co-translational export (slow export pathway). However, this will vary during post-translational export (fast export pathway) as it is about ten times faster than co-translational export. Here, S-S crosslinking induced after complete polypeptide has been exported into the periplasm can be consecutive and non-consecutive. DsbA is an oxidoreductase enzyme belonging to thioredoxin family having Cys-X-X-Cys (X – any amino acid) motif in their active site. This motif present in the disulfide bonded form can undergo a thiol-disulfide exchange reaction<sup>108</sup>. After oxidation of DsbA to induce S-S linkages in the secreted protein, DsbA will be reduced. This will then be re-oxidized by inner membrane (IM) protein DsbB to its native active state where it can again catalyze crosslinking and so forth. Therefore, DsbB acts as a DsbA maintenance protein having six Cys residues from which four are essential for re-

oxidation of DsbA. In general, disulfide bonds can be oxidized to create S-S linkages, reduced by the addition of dithiothreitol (DTT), and be isomerized by DsbC/DsbD complexes.

Bacterial oxidative folding is best characterized for *E. coli* K12. Here, DsbA/DsbB protein complex is responsible for the S-S linking (Figure 1.12a). Here, highly oxidative DsbA with a red-ox potential of -122 mV is the key enzyme that directly interacts with the protein that is folding. The active site Cys-X-X-Cys motif for *E. coli* K12 is Cys30-Pro31-His32-Cys33 (CPHC)<sup>108</sup>. DsbA Cys30 has a pKa of 3.5 in its reduced form and will be present in the thiolate form at physiological pH. Surprisingly, the reduced dithiolate form of DsbA is more stable than the oxidized S-S form of the enzyme by  $3.6 \pm 1.4$  kcal/mol. This energy difference results in reduction of the disulfide of DsbA and oxidation of its substrates. A network of interactions via the Cys30 thiolate side chain helps stabilize the reduced form of DsbA over its oxidized form. Thiol-disulfide exchange was proposed to proceed with two steps where the first step involves a nucleophilic attack on the surface exposed Cys30 by a Cys from substrate protein followed by a second step where the second Cys of the substrate attacks the first Cys of substrate which is linked with Cys30 of DsbA. This results in an S-S linked substrate and production of reduced DsbA. Overall, this is considered to be a bimolecular nucleophilic substitution reaction ( $S_N^2$ )<sup>110</sup>.

After the production of reduced DsbA, re-oxidation of DsbA in the bacterial periplasm is required for completion of catalytic cycle. The IM performs this re-oxidation using protein DsbB. DsbB consists of four transmembrane helices connected by two periplasmic domains. The four essential Cys residues are present in the 2 periplasmic domains (Cys41 and Cys44 in N-terminal periplasmic loop P1, Cys104 and Cys130 in the C-terminal periplasmic loop P2) (Figure 1.12a). Mutation experiments have shown that Cys30 of DsbA interacts with Cys104 of P2 to introduce a mixed disulfide. Electron flow would be from DsbA to first Cys104-Cys130 in P2 of DsbB

followed by Cys41-Cys44 in P1 of DsbB<sup>111,112</sup>. Finally, the electrons will flow to quinones and to the respiratory chain for oxygen production. In aerobic oxidative folding, the quinone co-factor of DsbB is ubiquinone (UQ) and Menaquinone (MK) for anaerobic oxidative folding. It is observed that the quinone binding is crucial for the DsbA oxidizing function of DsbB and further studies have suggested that the oxidation of DsbA by DsbB occurs via several concerted disulfide exchange reactions<sup>113</sup>. Structural models of DsbB: DsbA inter-loop complexes reveal a straight-line arrangement of six redox-active Cys. The standard redox potentials for DsbB are much lower than that of DsbA (-210 mV for Cys41-Cys44 in P1 and -220 mV for Cys104-Cys130 in P2 compared to -122 mV for DsbA) and the periplasmic loop of DsbB containing Cys104 and Cys130 has been shown to undergo rapid conformational changes induced by DsbA during the reaction. These conformational changes with the disulfide rearrangements are assumed to facilitate the energetically unfavorable electron transfer from DsbA to DsbB<sup>114</sup>.

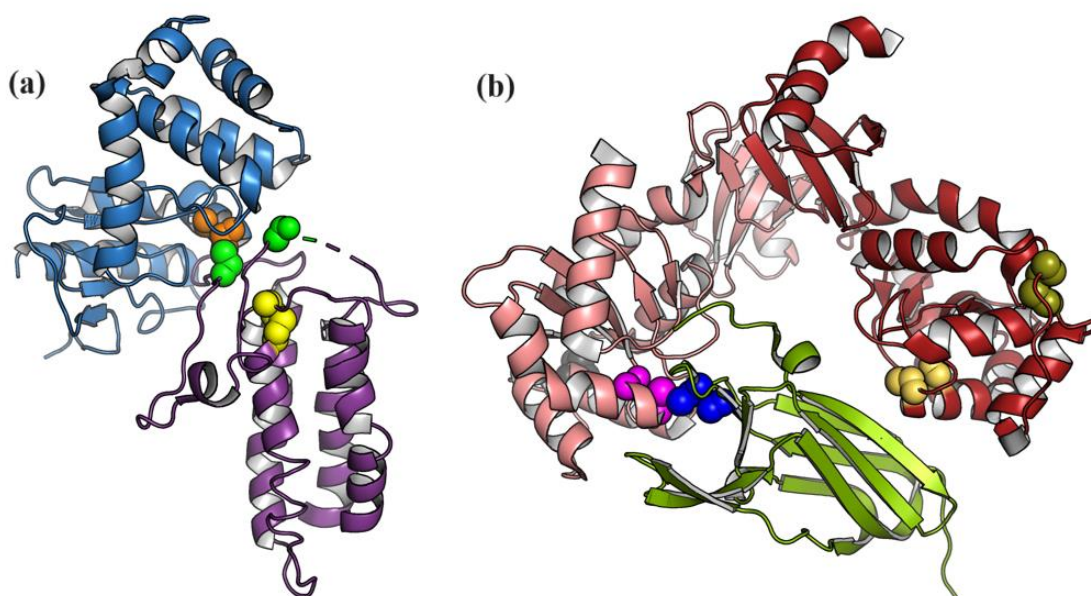


Figure 1.12 Crystal structures of *E. coli* Dsb system. (a) **DsbA/DsbB** Complex (PDB ID 2ZUP) (b) **DsbC/DsbC/DsbD $\alpha$**  Complex (PDB ID 1JZD). DsbA is responsible for crosslinking free

cysteines in OMPs and DsbB is responsible for the re-energizing of DsbA. **DsbA** consist of **Cys30-Cys33** pair, **DsbB** consist of **Cys41-Cys44** and **Cys104-Cys130** pairs. The dimeric form of DsbC in V-shaped structure (**DsbC-DsbC**) consists of Cys98-Cys101 and Cys141-Cys163 pairs (**C98-C101** and **C141-C163** in **DsbC**) (**C98-C101** and **C141-C163** in **DsbC**), and **DsbD<sub>α</sub>** consist of **Cys103-Cys109**. Crystal structures were obtained from Protein Data Bank (<https://www.rcsb.org/>) and protein structures were generated from PyMOL Molecular Graphics System version 3.0.3.

#### 1.4.3.3.2 Isomerization Pathway

Certain consecutive disulfide bonds catalyzed by DsbA might not allow for proper folding. This fault is corrected by the redox isomerase DsbC, which catalyzes the cleavage of incorrect disulfide linkages and allows for rearrangement to the native conformation. This reaction will result in the oxidation of DsbC<sup>115</sup>. For proteins with an odd number of cysteine (Cys) residues, another crucial component DsbG is present in the periplasmic domain to prevent oxidation of non-disulfide bond forming cysteine residues to sulfenic acid<sup>34</sup>. Both DsbC and DsbG are reduced and re-energized for active function by the transmembrane protein DsbD (Figure 1.12b).

DsbC is a V-shaped 2 x 23 kDa homodimer belonging to the thioredoxin (Trx) family. The N-terminus contains a dimerization domain connected via a linker  $\alpha$ -helix to the C-terminal domain, which contains the Trx domain Cys98-Gly99-Tyr100-Cys101 as its active site. The two Cys residues in DsbC are in a reduced form in the active state. The dimeric form of DsbC is found to be crucial for its function. Here, the active site of DsbC is sterically protected from unwanted oxidations from DsbB by remaining as a dimer. As a result, DsbC can function as an oxidant of secreted proteins in the periplasm. Electrochemically, DsbC has a redox potential of -130 mV which is slightly lower than DsbA (-120 mV). The model proposed for DsbC function involves initiation by a nucleophilic attack by Cys98 in the Trx domain to construct a mixed disulfide



between DsbC and the substrate. The latter reaction is proposed to have two possibilities. In one reaction pathway, the secondary reaction includes an attack from Cys in the substrate to the mixed disulfide thereby generating a more stable disulfide bond in the substrate and fully restoring the reduced form of DsbC, which exhibits the true isomerase function. The second reaction pathway includes an attack from Cys101 in DsbC to the mixed disulfide, constructing a reduced disulfide and an oxidized DsbC. This pathway allows DsbA to re-oxidize the substrate to form the correct disulfide, but here DsbC acts as a reductase rather than an isomerase. In both proposed mechanisms, the reduced form of DsbC is crucial for initiating the reaction to repair an incorrect disulfide bond<sup>117,118</sup>. Furthermore, DsbC consists of a chaperone activity that permits binding to unfolded proteins, which does not require the active site cysteines unlike DsbA<sup>119</sup>.

For the continuous function of the Dsb isomerization pathway, both DsbC and DsbG must remain in the reduced active state. This is done by the transmembrane protein DsbD. DsbD is a 59 kDa protein with three domains: An N-terminal periplasmic domain DsbD<sub>α</sub> having an immunoglobulin-like fold, a hydrophobic core domain DsbD<sub>β</sub> with 8 transmembrane segments, and a C-terminal periplasmic domain DsbD<sub>γ</sub> with a thioredoxin-like fold<sup>119,120</sup>. Each of these domains have a pair of Cys that are crucial for the activity of DsbD. As DsbC and DsbG are reduced by DsbD, DsbD gets oxidized. Oxidized DsbD is reduced by cytoplasmic thioredoxin A (TrxA), which then becomes oxidized. Oxidized TrxA is then reduced by thioredoxin reductase (TrxB), so that the electrons to reduce DsbC and DsbG originate from NADPH<sup>121</sup>.

TrxA initiates the electron flow from the cytoplasm by reducing the disulfide linkage between Cys163 and Cys285 (Cys163-Cys285) in the DsbD<sub>β</sub> domain while being oxidized to construct the disulfide linkage between Cys32 and Cys35 (Cys32-Cys35) in TrxA. DsbD<sub>β</sub> domain has an hourglass-like structure with inverted symmetry where the Cys163 is cytoplasmic-proximal and

Cys285 is periplasmic-proximal. This conformation of DsbD $\beta$  allows communication with TrxA from cytoplasmic side and DsbD $\gamma$  from periplasmic side<sup>122</sup>. The conformation of DsbD $\beta$  remains static between its oxidized and reduced forms, however some structure-based mechanisms might be present for opening the channel for TrxA to be in direct contact with DsbD $\beta$  during electron transport. Then, the electron flow proceeds from DsbD $\beta$  domain by reducing the disulfide linkage between Cys461 and Cys464 (Cys461-Cys464) in C-terminal periplasmic domain DsbD $\gamma$  domain while being oxidized to construct Cys163-Cys285 linkage in DsbD $\beta$  domain. Consequently, the electron flow proceeds from DsbD $\gamma$  domain by reducing the disulfide linkage between Cys103 and Cys109 (Cys103-Cys109) in the N-terminal periplasmic domain DsbD $\alpha$  while being oxidized to construct Cys461-Cys464 linkage in DsbD $\gamma$  domain. Finally, the electron flow concludes with the DsbD $\alpha$  domain being oxidized to construct Cys103-Cys109 linkage while reducing either Cys98-Cys101 of DsbC or Cys109-Cys112 of DsbG in order to convert them to their active state<sup>123</sup>.

### 1.5 Outer membrane proteins

Almost all of the OMPs present in Gram-negative bacteria are composed of 8-24 antiparallel  $\beta$ -stranded barrels where the first and last beta strand are bound by hydrogen bonding to complete the barrel architecture. The amino acids connecting these beta strands form long loops on the extracellular side and short turns from the periplasmic side. They are classified according to their structure which can be monomeric (OmpA)(Figure 1.13c) with long extracellular loops or trimeric (OmpC, OmpF)(Figure 1.13a,d). These porins facilitate diffusion of solutes with molecular mass less than 600 Da. Substrate specific channels such as LamB (Figure 1.13b), or substrate specific active transporters such as TonB dependent transporters (TBDTs) with an N-terminal core domain are responsible for uptaking compounds greater than 600 Da against a concentration gradient (discussed in Chapter 1.6)<sup>1</sup>.

### 1.5.1 OM Porins

A substantial fraction of OMPs belong to this category. For *E. coli*, there are three main trimeric porins. They are OmpF and OmpC which prefer cationic molecules and PhoE which prefers anionic molecules<sup>124</sup>. These channels have an hourglass type structure where the narrowest part is known as the “constriction region”. The constriction region of *E. coli* OmpF is roughly circular with a diameter of 6.5 – 7.0 Å whereas this region in OmpC has a diameter of 5.5 – 6.0 Å. This region is formed by extracellular loop 3 (L3), which composed of 35 residues that fold inwards to generate a narrow sized pore. Also, L3 sets up an electric field across the constrictor region which is caused by a line of positively charged residues on the barrel wall that lie opposite to negatively charged residues. This field orients water molecules inside the porin and make it size and shape dependent for hydrophobic molecules to pass through the constrictor region<sup>124</sup>. In *E. coli*, OmpF is required for the translocation of the bacteriocidal proteins colicin A and colicin E3 across the OM. Porins also facilitate the translocation of antibiotics and β-lactams, such as penicillins and carbapenems enter the cell through porins. Closely related enterobacteriaceae of *E. coli* have homologs of porins such as OmpF and OmpC.

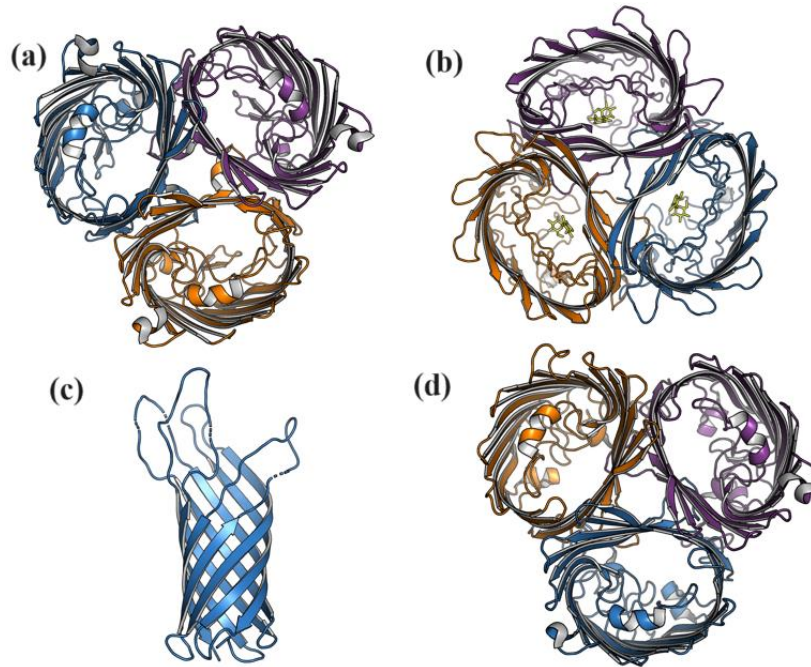


Figure 1.13 Crystal structures of OM porins. (a) periplasmic side view of trimeric porin OmpF (PDB ID 3K19) (b) periplasmic side view of trimeric porin LamB with glucose moieties (yellow) (PDB ID 1MPQ) (c) side view of monomeric OmpA (PDB ID 1BXW) (d) periplasmic side view of trimeric porin OmpC (PDB ID 2XG6). Crystal structures were obtained from Protein Data Bank (<https://www.rcsb.org/>) and protein structures were generated from PyMOL Molecular Graphics System version 3.0.3.

OmpA is a highly conserved multi-functional outer membrane protein present in E coli, and is a receptor for bacteriocins such as colicin U, colicin L, and bacteriocin 28b as well as bacteriophages such as M1 and K3. OmpA consist of two allelic forms where there are dissimilar residues present in loop 2 and 3. These forms are namely *ompA1* and *ompA2*<sup>125</sup> where *ompA2* is less sensitive to a variety of bacteriophages<sup>126</sup>. Structural studies have suggested that during temperature stress, OmpA might convert from a conventional 8 stranded  $\beta$ -barrel into a 16 stranded barrel ion channel with the assistance of the very long c-terminal domain present in the periplasm.

Here the Glu52-Arg138 salt bridge in the 8  $\beta$ -stranded form is cleaved to create a new interaction between Glu52 and Lys 82 in the C-terminal domain to create the 16  $\beta$ -stranded form<sup>126</sup>.

Furthermore, OmpA performs the critical role of regulating maintenance of outer membrane integrity whereas OmpF holds the role of antibiotic transport through the OM. OmpC consist of both characteristics of OmpA and OmpF<sup>127</sup>.

## 1.6 TonB-dependent Transporters (TBDTs)

Compounds greater than 600 Da cannot diffuse through the OM (via the porins), and there are substrate specific active transport proteins that uptake essential compounds against a concentration gradient. Since there are not any energy driven processes such as ATP hydrolysis or proton motive force (PMF) in the OM, these transporter proteins couple with the inner membrane protein complex TonB/ExbB/ExbD to extract energy from the PMF in the IM for active transport (Figure 1.14). Hence, these OMPs are known as TonB dependent transporters (TBDTs). These TBDTs are responsible for uptake of nutrients such as vitamin B<sub>12</sub>, iron, nickel, and copper complexes, complex carbohydrates, and bacteriophages.

### 1.6.1 TBDT Expression and Regulation

*E. coli* express seven (7) TBDTs. They are Fiu, FepA and Cir which uptakes ferric (Fe<sup>3+</sup>) catecholate siderophores, FhuA and FhuE which uptakes Fe<sup>3+</sup> hydroxamate siderophores, FecA which uptakes citrate form of Fe<sup>3+</sup> and BtuB which uptakes cyano-cobalamin (CNCbl) (Vitamin B<sub>12</sub>). There are multiple TBDTs for iron acquisition likely due to its essential nature for cell survival. Among these and other transporters, the regulation of TBDT expression is quite diverse. It is of utmost importance to regulate cellular iron levels due to its toxicity at elevated levels and potential to create reactive radicals<sup>128</sup>. *E. coli* have Fur (Ferric Uptake Regulator) which is a ferric

siderophore transcriptional repressor<sup>129</sup>. In the presence of elevated levels of iron, Fur interacts with DNA sequences using Fe<sup>2+</sup> as a cofactor creating a conformation named “Fur box”. This inhibits expression of genes responsible for iron transporters. In the presence of low iron levels, Fur cannot bind to DNA<sup>130</sup>.

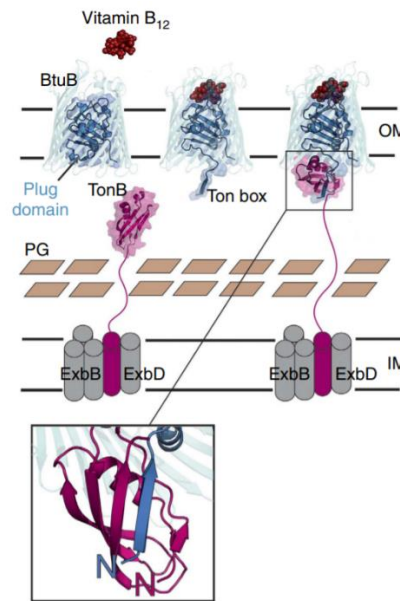


Figure 1.14 Schematic diagram of TonB-dependent transport<sup>127</sup>. Inner membrane protein complex TonB/ExbB/ExbD extremely sensitive to the PMF of IM derives energy and provides it to the OMPs by coupling to the TBDTs through TonB to initiate active transport of essential nutrients against a concentration gradient. Figure was taken from Hickman, S. J., Cooper, R. E. M., Bellucci, L., Paci, E., & Brockwell, D. J. (2017). Gating of TonB-dependent transporters by substrate-specific forced remodelling. *Nature communications*, 8, 14804.

TBDT expression can also be regulated by Extra-Cytoplasmic Function (ECF)  $\sigma$  factors and there are anti  $\sigma$ -factors that suppress them. The expression of the *fecABCDE* genes for ferric citrate transport are under control of the  $\sigma$  factor FecI. In the presence of substrate, signal transduction through FecA in the OM initiates an interaction between the periplasmic N-terminus of FecA and the C-terminus of FecR in the IM. This interaction results in transmission of a signal

from FecR through IM to FecI which guides RNA polymerase for transcription<sup>131</sup>. Surprisingly, FecR is the anti  $\sigma$ -factor to the FecA expression  $\sigma$ -factor FecI<sup>132</sup>.

Another approach by cells to regulate TBDT expression is through a riboswitch. A riboswitch is a small mRNA element that is found in the 5'-untranslated region (5'-UTR) of the mRNA that can be induced by a ligand to regulate transcription in cis-fashion<sup>133</sup>. The 5' end of the *btuB* mRNA gene contains such a riboswitch which is activated in the presence of adenosyl-cobalamin, a byproduct formed during vitamin B<sub>12</sub> metabolism<sup>134</sup>.

TBDT expression can also be regulated by small RNAs (sRNA). Hfq is an RNA chaperone which can induce RNA-RNA interactions between its binding constituents<sup>135</sup>. The mRNAs of *cirA*, *fepA*, and *fecA* bind to Hfq whereas the sRNAs OmrA and OmrB can also positively bind and induce RNA-RNA interactions thereby repressing RNA transcription<sup>136,137</sup>.

### 1.6.2 TBDT transport of scarce nutrients

Iron is required for essential processes such as bacterial growth, metabolism, ATP synthesis and DNA replication. Although it is a very crucial element for survival, iron in free form can catalyze a cascade of undesirable reactions resulting in the formation of reactive oxygen and nitrogen species (ROS/RNS) inducing cell toxicity. Therefore, iron is generally bound to proteins (heme, transferrin, ferritin) for stability and transport. This also reduces the bioavailability of iron to be scavenged by bacteria. Therefore, bacteria have synthesized unique biomolecules to harvest and transport iron. One such method is the synthesis of siderophores. Siderophores are small organic molecules (catechol, hydroxamate, citrate) synthesized by bacteria that consist of a remarkably high affinity for Fe<sup>2+</sup> and Fe<sup>3+</sup> (Figure 1.15) by the presence of multiple chelating groups. Another unique way of iron uptake is by synthesis of TBDTs which recognize iron

transport proteins present in the host environment and extract iron from the transport protein for uptake<sup>138</sup>.

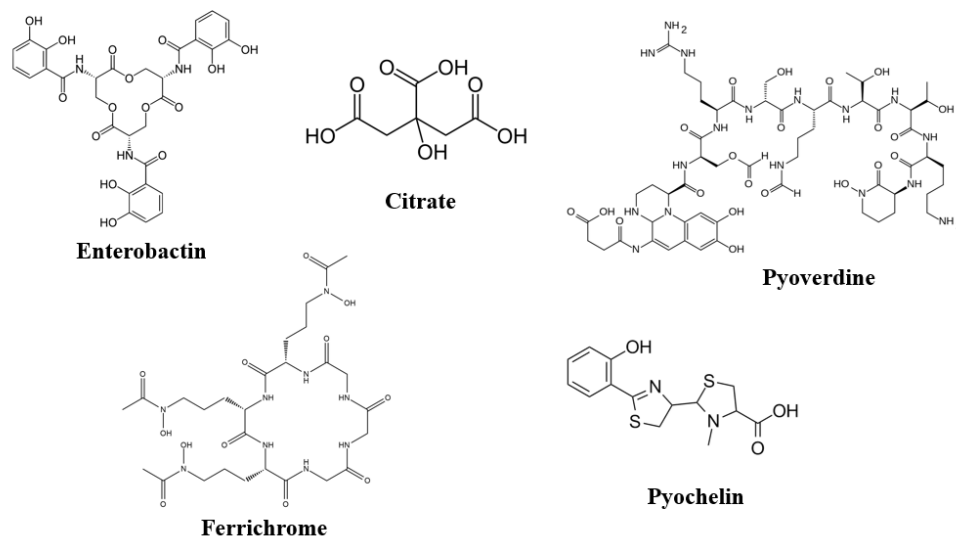


Figure 1.15 Chemical structures of siderophores synthesized by bacteria for iron acquisition.

### 1.6.3 TBDT architecture and function

TBDTs are structurally homologous with the C-terminus folded into a 22-stranded  $\beta$ -barrel and the N-terminus forming a globular core-domain (plug domain) to occlude the interior of the barrel. The antiparallel  $\beta$ -strands are connected by long loops from the extracellular side and by short turns from the periplasmic side. The extracellular surface of the  $\beta$ -barrel is composed of long loops, postulated to be crucial for substrate binding during active transport. The core domain must undergo a structural rearrangement to allow transport of substrates to the periplasmic space.

#### 1.6.3.1 Architecture and function of FhuA

*E. coli* FhuA is the active transporter that uptakes iron in the form of ferrichrome. FhuA is also responsible for uptake of bacteriocins such as colicin M and bacteriophages such as T1, T5 and  $\Phi 80$ <sup>139</sup>. According to the crystal structures, the FhuA N-terminal core (plug) domain is formed



from residues 1-161 whereas residues 162-723 forms the 22 stranded  $\beta$ -barrel. FhuA interior has two main pockets outlined by the plug domain, a large pocket from the extracellular side and a small pocket from the periplasmic side (Figure 1.16a). During substrate binding, multitude of substrate induced conformational changes occur in the protein where some of the extracellular loops of the barrel and core domain shift from the extracellular side but a significant extension of the N-terminal core domain where the switch helix (residues 24-29) unwinds into the periplasm. Residues 7-13 represents the Tonbox of FhuA which is observed to be interacting with C-terminus of TonB (Figure 1.16b) upon substrate binding<sup>140</sup>.

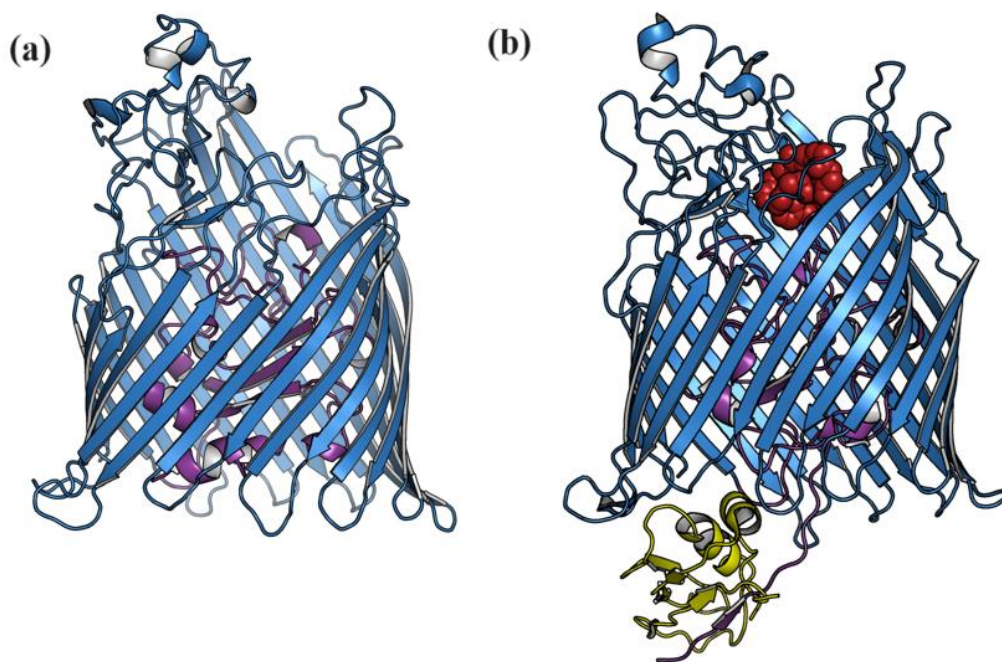


Figure 1.16 Crystal structures of FhuA. (a) Apo state of FhuA (PDB ID 1BY3) (b) **Ferrichrome** bound FhuA with C-terminus of **TonB** (PDB ID 2GRX). The **plug domain** is occluding the  **$\beta$ -barrel** pore and the **TonB-Tonbox** interaction is observed. Crystal structures were obtained from Protein Data Bank (<https://www.rcsb.org/>) and protein structures were generated from PyMOL Molecular Graphics System version 3.0.3.

### 1.6.3.2 Architecture and function of FecA

*E. coli* FecA is the active transporter that uptakes iron in the form of ferric citrate. According to the crystal structures, the FecA core domain is formed from residues 80-221 whereas residues 222-741 forms the 22 stranded  $\beta$ -barrel. Residues 1-80 of FecA represents the periplasmic N-terminal flexible region which signals to the IM FecR depending on the ligand status of FecA. The N-terminus of FecA is not resolved in the crystal structures. During substrate binding, a significant substrate induced conformational changes occur in the extracellular loops of the barrel domain where an  $\alpha$ -helix of loop seven (L7) (residues 516-535) and loop eight (L8) (residues 562-581) unwinds and translates 11 Å and 15 Å towards the center of the protein indicating a gating motion respectively. Residues 56-63 represents the Tonbox of FecA which is not present in the crystal structure<sup>141</sup>.

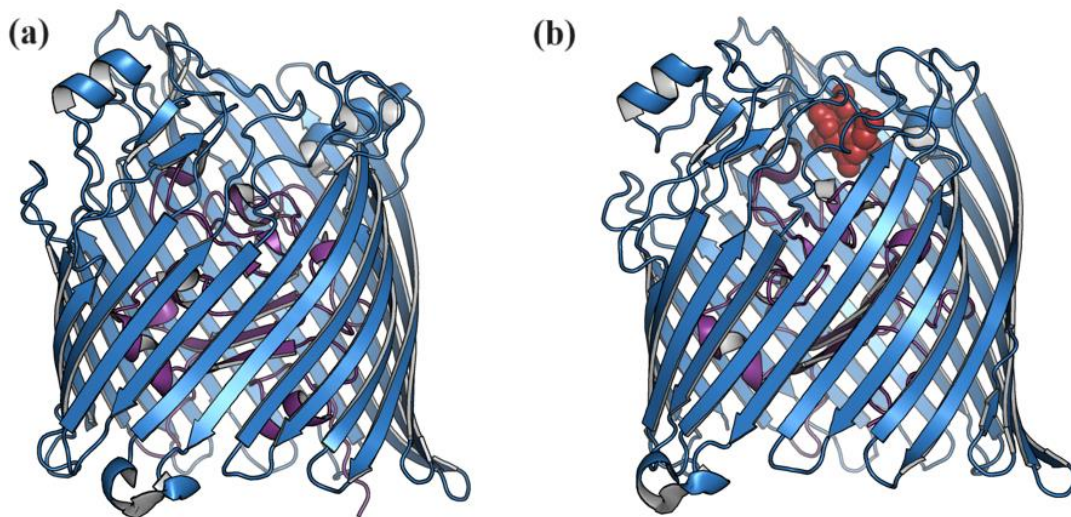


Figure 1.17 Crystal structures of FecA. (a) Apo state of FecA (PDB ID 1KMO) (b) **Ferric Citrate** bound FecA (PDB ID 1KMP). The **plug domain** occluding the pore of the  **$\beta$ -barrel**. Crystal

structures were obtained from Protein Data Bank (<https://www.rcsb.org/>) and protein structures were generated from PyMOL Molecular Graphics System version 3.0.3.

### 1.6.3.3 Architecture and function of BtuB

*E. coli* BtuB is the active transporter that uptakes cyanocobalamin (CN-Cbl) (Vitamin B<sub>12</sub>), E colicins (E2, E3), A colicins, and bacteriophage BF23. BtuB has been crystallized under different conditions as apo state (PDB ID 1NQE), apo state with bound calcium (Ca<sup>2+</sup>) (PDB ID 1NQG) (Figure 1.18a), CN-Cbl and Ca<sup>2+</sup> bound (PDB ID 1NQH), CN-Cbl, Ca<sup>2+</sup> and TonB C-terminus (PDB ID 2GSK) (Figure 1.18b), colicin E2 bound (PDB ID 1UJW), and colicin E3 bound (PDB ID 2YSU) states. The BtuB core domain is formed from residues 1-136 whereas residues 137-594 form the 22 stranded  $\beta$ -barrel. Compared to the iron transporters, BtuB is about 60-100 residues smaller due to the presence of shorter extracellular loops and smaller core domain. BtuB doesn't have a switch helix but it does contain the Tonbox (residues 6-12) in its N-terminus. The crystal structures indicate that the presence of Ca<sup>2+</sup> stabilizes loop 2 (L2), 3 (L3), and 4 (L4) where the affinity (K<sub>D</sub>) of BtuB for Ca<sup>2+</sup> is 0.3 nM. BtuB has an "aspartate cage" formed through D179, D193, D195, D230, and D241 from L2 and L3 which supports two Ca<sup>2+</sup> ions with 4 Å separation<sup>142,143</sup>. The presence of CN-Cbl with Ca<sup>2+</sup> induces a direct interaction between substrate and L3 and L4. However, BtuB does not exhibit a gating motion of the extracellular loops as the iron transporters indicate in their structures. Surprisingly, the extension of Tonbox was also not observed in the presence of Ca<sup>2+</sup> and CN-Cbl in the crystal structures, which contradicted the data that our lab observed through Electron Paramagnetic Resonance (EPR) experiments<sup>5</sup>. But, it has been determined that the state of Tonbox is altered and forced to fold in the presence of precipitants or osmolytes such as polyethylene glycols (PEG) used during the crystallization process. The

Tonbox extension is however observed when BtuB is co-crytallised with  $\text{Ca}^{2+}$ , CN-Cbl and the C-terminus of TonB<sup>L44</sup> (Figure 1.18b) where the Ton box must be extended to interact with TonB.

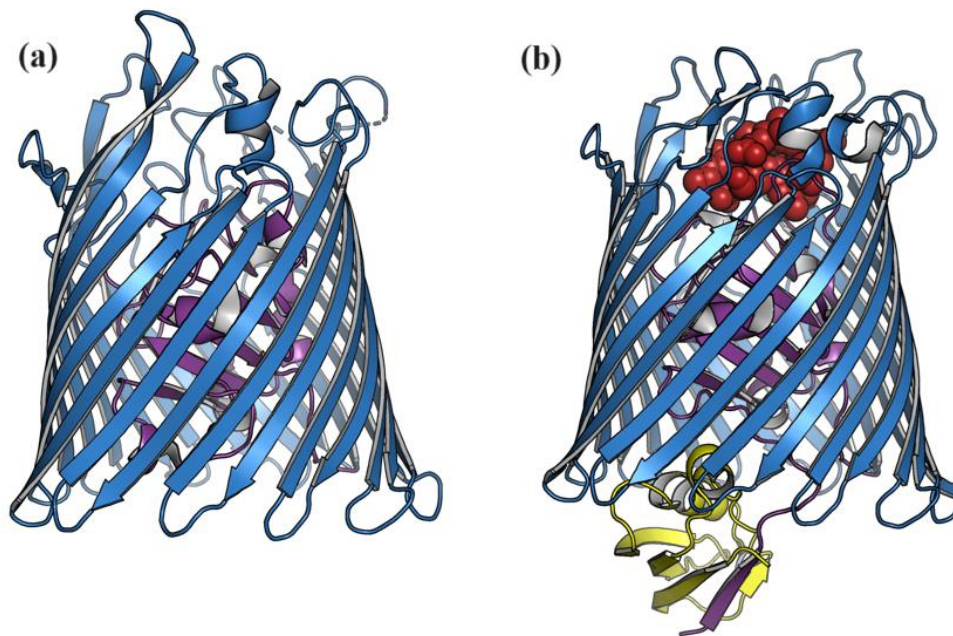


Figure 1.18 Crystal structures of BtuB. (a) Apo state of BtuB (PDB ID 1NQG) (b) **CN-Cbl** bound BtuB with C-terminus of **TonB** (PDB ID 2GSK). The **plug domain** is occluding the  **$\beta$ -barrel** pore and the **TonB-Tonbox** interaction is observed. Crystal structures were obtained from Protein Data Bank (<https://www.rcsb.org/>) and protein structures were generated from PyMOL Molecular Graphics System version 3.0.3.

#### 1.6.4 Current knowledge of BtuB and other TBDTs

In addition to the protein crystal structures, various chemical biology, biochemical and biophysical techniques have been implemented to study the structural and functional dynamics of TBDTs to gain understanding of the mechanism of active transport. TBDTs present in pathogenic bacteria can harvest essential nutrients such as iron from the hosts in which they reside. Thus, understanding the TBDT transport mechanism has become important for understanding bacterial

survival, and they are potential targets for new antibiotics as they are unique to Gram-negative bacteria. The development of drugs that can be recognized by and delivered through TBDTs to target bacterial have also generated substantial interest in the field of biotechnology.

Currently, TBDTs are known to exhibit a substrate induced conformational change, which likely allows TBDTs to couple to the IM protein TonB to execute active transport. Loop deletion studies of BtuB indicated that removing L8 and L10 resulted in resistance for phage BF23, deletion of L7 affected the binding of colicin E3 whereas loop deletions had no effect on colicin E1 binding indicating that colicin binding is different than BF23 binding. CN-Cbl binding was also severely affected by loop deletions<sup>145</sup>. EPR experiments on OM isolations and lipid reconstitutions of BtuB indicated that the energy coupling segment, or Ton box, unfolded 20 – 30 Å into the periplasm upon substrate binding<sup>5</sup>. It was also shown that a crucial ionic lock between R14 in the core domain and D316 in the barrel domain (R14-D316) is disrupted during Tonbox unfolding thereby acting as a molecular switch<sup>9</sup>. MD-simulation data of substrate binding to BtuB has indicated that Ca<sup>2+</sup> binding occurs prior to CN-Cbl binding and that it enhances CN-Cbl binding by around 1000-fold. Furthermore, simulations indicate that L7 and L8 interact with CN-Cbl which is not observed in the crystal structures<sup>146</sup>. The interaction between the C-terminus of TonB with Ton box translates a signal to the extracellular surface of the protein to partially dissociate bound substrate so that the transporter can initiate migration of substrate through the protein<sup>147,148</sup>. Also, a specific Ton box orientation is required for the binding of TonB<sup>149</sup>. Earlier studies of BtuB in the intact cell were utilized to validate the dynamics of the extracellular loop movements of BtuB observed in isolated systems<sup>150</sup>. These experiments validated the observations regarding the loop movements of BtuB in isolated native and reconstituted systems<sup>151</sup>. Also, the standard K-12 derived strain was unsuccessful in double spin labeling pairs of cysteines due to the presence of an active Dsb system.

A mutant bacterial strain where the disulfide oxidase *dsbA* and its re-energizer *dsbB* is absent (*dsbA*<sup>-</sup> or *dsbB*<sup>-</sup> strain) resulted in efficient double spin labelling in both extracellular and periplasmic side of BtuB in the intact cell for continuous wave (CW) and pulse EPR experiments<sup>7</sup> as well as in the isolated native and reconstituted systems<sup>8</sup>. Intact cell experiments utilizing single and double cysteine mutations using Double Electron-Electron Resonance (DEER) spectroscopy displayed distance distributions indicating supramolecular assembly of BtuB to create OMP islands. This effect seems to be mediated by specific interfaces on the opposite sides of the barrel domain of BtuB where a high concentration of aromatic residues is present<sup>152</sup>. Further experiments on the extracellular loops in the intact cells indicated that the BtuB extracellular loops behaves differently in the native environment than they do in isolated native or reconstituted systems where they are more structured, and the binding of substrate does little to no changes in loop structure<sup>153</sup>. Most recent study of BtuB in the intact cell indicates that the substrate binding loop 3 (SB3) of the core domain undergoes a significant conformational transition when the R14-D316 ionic lock is disrupted, and the substrate is present. As mentioned previously, disruption of R14-D316 can result in extension of the Tonbox to the periplasmic space mimicking the binding of TonB. In the presence of both conditions, SB3 is displaced by about 20 Å towards the periplasmic side of BtuB. Interestingly, this observation is not observed when BtuB is reconstituted into a phospholipid bilayer system indicating the importance of membrane contribution and energetics involved in the overall function of OMPs<sup>154</sup>. As a result of these experiments, there was a crucial need to explore possible ways in which we can observe unique BtuB conformational changes observed in the intact cell in the isolated systems as well (Discussed in detail in Chapters 3,5,6).

## 1.7 TonB/ExbB/ExbD system

The TonB/ExbB/ExbD system is the molecular machinery that is present in the IM of Gram-negative bacteria and is responsible for assisting in active transport of nutrients through TBDTs. This complex utilizes the proton gradient across the IM as the energy source where ExbB/ExbD complex harness the energy of the PMF and provide it to TonB unit which couples with TBDTs in the OM.

The overall structure of TonB includes a N-terminal transmembrane helix which anchors TonB to the IM, a highly conserved C-terminal domain which is responsible for coupling with TBDTs and a proline rich linker which connects these two domains and consist of the length necessary for the C-terminus to reach the OM. This C-terminus then interacts with the Ton box of TBDTs to form a very stable complex and it is postulated that the energy derived and provided to TonB alters the structure of the core domain of TBDTs after binding to the Ton box to allow passage for substrates<sup>147,155</sup>.

The stoichiometry of the ExbB/ExbD complex has been widely debated for multiple years. However recent structural data obtained through protein crystallography, mass spectrometry and cryo-electron microscopy techniques support the 5:2 ratio of the ExbBD complex where ExbB is forming a pentameric pore with high hydrophobicity circling a dimer of ExbD helices<sup>156,157</sup> (Figure 1.19). It is also observed that a structural homology with ExbBD ratio is present with the IM flagellar motors MotAB and PomAB sensitive to proton and sodium gradient in the IM respectively<sup>158</sup>. The periplasmic domains of ExbB and MotB are not present in the high-resolution structures due to their high flexibility. Furthermore, a complete structure of TonB/ExbB/ExbD complex has not yet been observed.

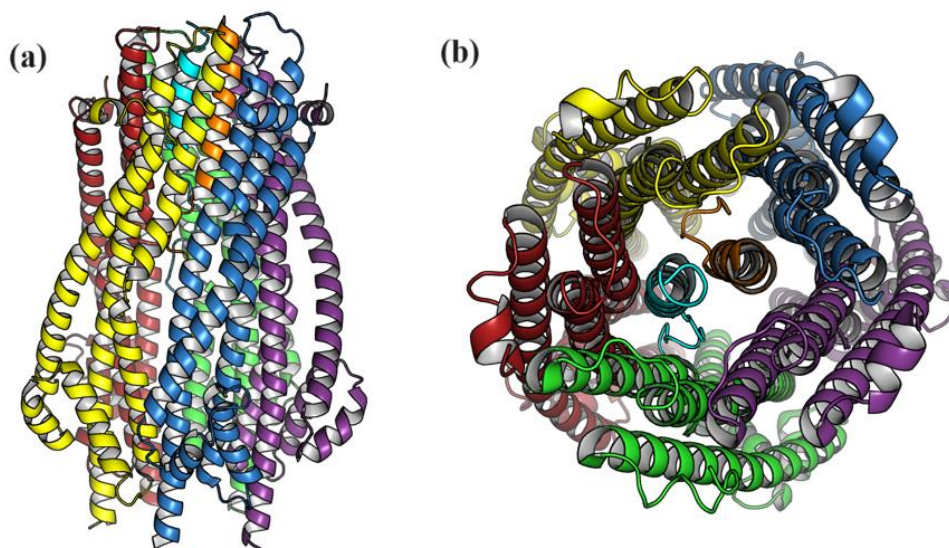


Figure 1.19 Crystal structures of ExbB/ExbD complex. (a) side view of transmembrane domain (b) top view of ExbB/ExbD complex (PDB ID 6YTI). The ExbD dimer (**ExbD1**, **ExbD2**) is present in the hydrophobic core constructed by the ExbB pentamer (**ExbB1**, **ExbB2**, **ExbB3**, **ExbB4**, **ExbB5**). Crystal structures were obtained from Protein Data Bank (<https://www.rcsb.org/>) and protein structures were generated from PyMOL Molecular Graphics System version 3.0.3.

Experimental studies on the periplasmic domains of ExbD and TonB have concluded that the C-terminus of TonB prefers a dimerized state, though the physical importance of this formation is not well understood (Figure 1.20b). Furthermore, it has been observed that the two periplasmic domains of ExbD exhibit a dimeric state and a structure have been identified where a fragment of TonB is interacting in between the two ExbD domains<sup>159</sup> (Figure 1.20a). The locality of TonB in the TonB/ExbB/ExbD complex has not been fully elucidated however structural data of the ExbB/ExbD complex suggest that the transmembrane domain of TonB does not reside in the interior of the ExbB pentamer.



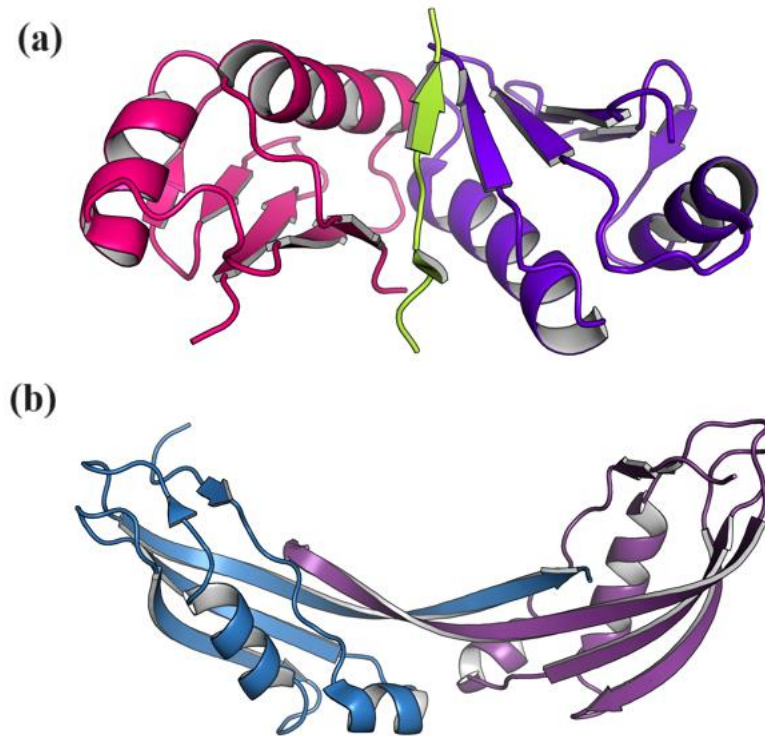


Figure 1.20 Crystal structures of TonB and TonB/ExbB/ExbD complex. (a) periplasmic domains of ExbD dimer (**ExbD1**, **ExbD2**) (residues 61-134) interacting with **TonB** binding motif (residues 43-51) (PDB ID 8P9R) (b) Dimerized form of TonB C-terminus (**TonB1**, **TonB2**) (PDB ID 1U07). Crystal structures were obtained from Protein Data Bank (<https://www.rcsb.org/>) and protein structures were generated from PyMOL Molecular Graphics System version 3.0.3.

Considering both TonB and ExbD consist of periplasmic linker regions responsible for connecting the transmembrane and periplasmic domains, it can be postulated that interactions between TonB binding motif and ExbD dimer through the linker regions may occur during active transport<sup>159</sup>.

## 1.8 Proposed mechanisms of TonB-dependent transport

Currently, there are two proposed mechanisms for TonB-dependent transport, which are known as the “pulling model” and the “rotating model.” Both proposals indicate that TonB coupled to the ExbB/ExbD complex in the energized IM exerts a mechanical force through its C-terminal domain to the OMP of interest via the TonB-Ton box interaction. The pulling model states that TonB exerts a pulling motion to the N-terminus of the OMP, inducing a partial or full unfolding of the hatch domain, resulting in passage for substrate transport. Studies on the BtuB hatch domain have shown significant hydrophilic interactions between interfacial waters, thereby reducing the energetic barrier for hatch domain movement inside the barrel domain<sup>160</sup>. Also, a modest force on the N-terminus of the hatch domain resulted in a significant conformational change by hatch domain unfolding, which was observed experimentally and through computational techniques<sup>127,160</sup>. The rotating model is fundamentally based on the structural and functional similarity of the ExbB/ExbD complex coupled with TonB to the flagellar motors MotAB and PomAB<sup>158</sup>. The Rotational Surveillance and Energy Transfer (ROSET) model postulates that the rotational motion present during proton pumping by ExbB/ExbD is transferred to its associated partner TonB. Once TonB is bound to Ton box of OMP, the constantly present rotational kinetic energy triggers conformational dynamics where a rearrangement of the hatch domain allows passage for substrate transport<sup>161</sup>.

## 1.9 Specific aims and goals of this thesis

Previous studies have indicated that BtuB double-spin labeling to examine structural and functional dynamics is not possible in the energized intact cells in the standard K-12 derived strain but is possible with strain including a knockout in the Dsb system responsible for crosslinking pairs of cysteines<sup>7</sup>. Double-spin labeling isolated BtuB preparations in K-12 derived strain is

limited but possible under certain conditions<sup>5</sup>. We aim to compare BtuB double-labeling efficiencies with the Dsb knockout strain and K-12 derived strain under several experimental conditions to identify the best isolated system for BtuB studies. Also, BtuB *in-vivo* experiments have been made possible using the Dsb knockout strain but extending this study to include other TBDTs (FecA, FhuA, FepA) is of utmost importance. Therefore, we aim to explore the possibility of efficient double spin-labeling of the Ferric citrate transporter FecA, which has not been possible in the standard BL21(DE3) strain for DEER studies. Studies of BtuB in cells have exhibited novel conformational dynamics that were not observed in isolated preparations. Therefore, it is advantageous to be able to study TBDTs in intact cells whenever possible. Previous BtuB studies R14-D316 ionic interaction between the hatch and barrel domains act as a molecular switch to regulate the configuration of the Ton box<sup>9</sup>. Furthermore, a substrate-dependent conformational change where the Ton box expands 20 – 30 Å into the periplasm is observed through DEER measurements<sup>5</sup>. However, studies regarding the dependency of Ton box expansion to the substrate (CNCbl), TonB, and R14-D316 disruption have not been thoroughly evaluated. We aim to explore the factors affecting the unfolding of the Ton box and the extent of Ton box expansion under different experimental conditions to gain insight into the necessary components required to initiate transmembrane signaling of BtuB. Further BtuB studies have shown a possible shift of substrate binding loop 3 (SB3) towards the periplasm in cells when the ionic lock is disrupted but is not observed in the isolated systems<sup>155</sup>. Also, possible shifts in other parts of the hatch domain during this shift are yet to be explored. We aim to understand the shift of SB3 by double spin labeling across the protein to identify possible directional shifts through the barrel domain of BtuB. This information will be vital in identifying the initial steps involved in a possible transport mechanism.

## 1.10 References

1. Nikaido, H. (2003). Molecular basis of bacterial outer membrane permeability revisited. *Microbiology and molecular biology reviews*, 67(4), 593-656.
2. Shroll, R. M., & Straatsma, T. P. (2002). Molecular structure of the outer bacterial membrane of *Pseudomonas aeruginosa* via classical simulation. *Biopolymers: Original Research on Biomolecules*, 65(6), 395-407.
3. Nagle, J. F., & Tristram-Nagle, S. (2000). Structure of lipid bilayers. *Biochimica et Biophysica Acta (BBA)-Reviews on Biomembranes*, 1469(3), 159-195.
4. Balusek, C., & Gumbart, J. C. (2016). Role of the native outer-membrane environment on the transporter BtuB. *Biophysical Journal*, 111(7), 1409-1417.
5. Xu, Q., Ellena, J. F., Kim, M., & Cafiso, D. S. (2006). Substrate-dependent unfolding of the energy coupling motif of a membrane transport protein determined by double electron-electron resonance. *Biochemistry*, 45(36), 10847-10854.
6. Rocque, W. J., Coughlin, R. T., & McGroarty, E. J. (1987). Lipopolysaccharide tightly bound to porin monomers and trimers from *Escherichia coli* K-12. *Journal of bacteriology*, 169(9), 4003-4010.
7. Nilaweera, T. D., Nyenhuis, D. A., Nakamoto, R. K., & Cafiso, D. S. (2019). Disulfide chaperone knockouts enable in vivo double spin labeling of an outer membrane transporter. *Biophysical Journal*, 117(8), 1476-1484.
8. Wimalasiri, V. W., Nilaweera, T. D., & Cafiso, D. S. (2021). Disulfide Chaperone Knockouts Facilitate Double Spin Labelling of an Outer Membrane Transporter For in Vitro EPR Studies. *Biophysical Journal*, 120(3), 72a-73a.

9. Wang, J. D., & Levin, P. A. (2009). Metabolism, cell growth and the bacterial cell cycle. *Nature Reviews Microbiology*, 7(11), 822-827.
10. Johnson, A., & O'Donnell, M. (2005). Cellular DNA replicases: components and dynamics at the replication fork. *Annu. Rev. Biochem.*, 74(1), 283-315..
11. Harry, E., Monahan, L., & Thompson, L. (2006). Bacterial cell division: the mechanism and its precision. *International review of cytology*, 253, 27-94.
12. Adams, D. W., & Errington, J. (2009). Bacterial cell division: assembly, maintenance and disassembly of the Z ring. *Nature Reviews Microbiology*, 7(9), 642-653.
13. Cooper, S., & Helmstetter, C. E. (1968). Chromosome replication and the division cycle of *Escherichia coli* Br. *Journal of molecular biology*, 31(3), 519-540.
14. Yoshikawa, H., O'Sullivan, A., & Sueoka, N. (1964). Sequential replication of the *Bacillus subtilis* chromosome, III. Regulation of initiation. *Proceedings of the National Academy of Sciences*, 52(4), 973-980.
15. Trojanowski, D., Hołowka, J., & Zakrzewska-Czerwińska, J. (2018). Where and when bacterial chromosome replication starts: a single cell perspective. *Frontiers in Microbiology*, 9, 2819.
16. Zyskind, J. W., & Smith, D. W. (1992). DNA replication, the bacterial cell cycle, and cell growth. *Cell*, 69(1), 5-8.
17. Kaguni, J. M. (2006). DnaA: controlling the initiation of bacterial DNA replication and more. *Annu. Rev. Microbiol.*, 60(1), 351-371.
18. Donachie, W. D., & Begg, K. J. (1989). Cell length, nucleoid separation, and cell division of rod-shaped and spherical cells of *Escherichia coli*. *Journal of bacteriology*, 171(9), 4633-4639.

19. Laloux, G., & Jacobs-Wagner, C. (2014). How do bacteria localize proteins to the cell pole?. *Journal of cell science*, 127(1), 11-19.
20. Morita, R. Y. (1997). *Bacteria in Oligotrophic Environments*. Springer.
21. Kolter, R., Siegele, D. A., & Tormo, A. (1993). The stationary phase of the bacterial life cycle. *Annual review of microbiology*, 47, 855-875.
22. Gray, J. V., Petsko, G. A., Johnston, G. C., Ringe, D., Singer, R. A., & Werner-Washburne, M. (2004). "Sleeping beauty": quiescence in *Saccharomyces cerevisiae*. *Microbiology and molecular biology reviews*, 68(2), 187-206.
23. Almiron, M., Link, A. J., Furlong, D., & Kolter, R. (1992). A novel DNA-binding protein with regulatory and protective roles in starved *Escherichia coli*. *Genes & development*, 6(12b), 2646-2654.
24. Finkel, S. E. (2006). Long-term survival during stationary phase: evolution and the GASP phenotype. *Nature Reviews Microbiology*, 4(2), 113-120.
25. Pin, C., & Baranyi, J. (2008). Single-cell and population lag times as a function of cell age. *Applied and environmental microbiology*, 74(8), 2534-2536.
26. Lacour, S., & Landini, P. (2004).  $\sigma$ S-dependent gene expression at the onset of stationary phase in *Escherichia coli*: function of  $\sigma$ S-dependent genes and identification of their promoter sequences. *Journal of Bacteriology*, 186(21), 7186-7195.
27. Weber, H., Polen, T., Heuveling, J., Wendisch, V. F., & Hengge, R. (2005). Genome-wide analysis of the general stress response network in *Escherichia coli*:  $\sigma$ S-dependent genes, promoters, and sigma factor selectivity. *Journal of bacteriology*, 187(5), 1591-1603.

28. Givskov, M., Eberl, L., Møller, S., Poulsen, L. K., & Molin, S. (1994). Responses to nutrient starvation in *Pseudomonas putida* KT2442: analysis of general cross-protection, cell shape, and macromolecular content. *Journal of Bacteriology*, *176*(1), 7-14.
29. Jenkins, D. E., Chaisson, S. A., & Matin, A. (1990). Starvation-induced cross protection against osmotic challenge in *Escherichia coli*. *Journal of bacteriology*, *172*(5), 2779-2781.
30. Fishov, I., Zaritsky, A., & Grover, N. B. (1995). On microbial states of growth. *Molecular microbiology*, *15*(5), 789-794.
31. Bachmann, B. J. (1996). Derivations and genotypes of some mutant derivatives of *Escherichia coli* K-12. *Escherichia coli and Salmonella typhimurium cellular and molecular biology*, 2460.
32. Sezonov, G., Joseleau-Petit, D., & d'Ari, R. (2007). *Escherichia coli* physiology in Luria-Bertani broth. *Journal of bacteriology*, *189*(23), 8746-8749.
33. Nilaweera, T. D. (2018). Exploring BtuB in *Escherichia coli* via a new direct spin labeling approach and electron paramagnetic resonance spectroscopy (*Doctoral Thesis Dissertation*). University of Virginia, Charlottesville, USA.
34. T Garrison, A., & W Huigens III, R. (2017). Eradicating bacterial biofilms with natural products and their inspired analogues that operate through unique mechanisms. *Current topics in medicinal chemistry*, *17*(17), 1954-1964.
35. Bertani, B., & Ruiz, N. (2018). Function and biogenesis of lipopolysaccharides. *Ecosal plus*, *8*(1), 10-1128.
36. Bos, M. P., Robert, V., & Tommassen, J. (2007). Biogenesis of the gram-negative bacterial outer membrane. *Annu. Rev. Microbiol.*, *61*(1), 191-214.

37. Raetz, C. R., & Whitfield, C. (2002). Lipopolysaccharide endotoxins. *Annual review of biochemistry*, 71(1), 635-700.
38. Raetz, C. R., Reynolds, C. M., Trent, M. S., & Bishop, R. E. (2007). Lipid A modification systems in gram-negative bacteria. *Annu. Rev. Biochem.*, 76(1), 295-329.
39. Holst, O. (2007). The structures of core regions from enterobacterial lipopolysaccharides— an update. *FEMS microbiology letters*, 271(1), 3-11.
40. Liu, D., & Reeves, P. R. (1994). Presence of different O antigen forms in three isolates of one clone of Escherichia coli. *Genetics*, 138(1), 7-10.
41. Raman, R., Raper, M. A., Hahn, E., & Schilke, K. F. (2017). Enhanced capture of bacteria and endotoxin by antimicrobial WLBU2 peptide tethered on polyethylene oxide spacers. *Biointerphases*, 12(5), 05G603.
42. Gronow, S., Brabetz, W., & Brade, H. (2000). Comparative functional characterization in vitro of heptosyltransferase I (WaaC) and II (WaaF) from Escherichia coli. *European journal of biochemistry*, 267(22), 6602–6611.
43. Qian, J., Garrett, T. A., & Raetz, C. R. (2014). In vitro assembly of the outer core of the lipopolysaccharide from Escherichia coli K-12 and Salmonella typhimurium. *Biochemistry*, 53(8), 1250–1262.
44. Stevenson, G., Neal, B., Liu, D., Hobbs, M., Packer, N. H., Batley, M., Redmond, J. W., Lindquist, L., & Reeves, P. (1994). Structure of the O antigen of Escherichia coli K-12 and the sequence of its rfb gene cluster. *Journal of bacteriology*, 176(13), 4144–4156.
45. Whitfield C. (2006). Biosynthesis and assembly of capsular polysaccharides in Escherichia coli. *Annual review of biochemistry*, 75, 39–68.



46. Jann, B., Reske, K., & Jann, K. (1975). Heterogeneity of lipopolysaccharides. Analysis of polysaccharide chain lengths by sodium dodecylsulfate-polyacrylamide gel electrophoresis. *European journal of biochemistry*, *60*(1), 239–246.
47. Chng, S. S., Gronenberg, L. S., & Kahne, D. (2010). Proteins required for lipopolysaccharide assembly in *Escherichia coli* form a transenvelope complex. *Biochemistry*, *49*(22), 4565–4567.
48. Ruiz, N., Gronenberg, L. S., Kahne, D., & Silhavy, T. J. (2008). Identification of two inner-membrane proteins required for the transport of lipopolysaccharide to the outer membrane of *Escherichia coli*. *Proceedings of the National Academy of Sciences of the United States of America*, *105*(14), 5537–5542.
49. Dong, H., Zhang, Z., Tang, X., Paterson, N. G., & Dong, C. (2017). Structural and functional insights into the lipopolysaccharide ABC transporter LptB<sub>2</sub>FG. *Nature communications*, *8*(1), 222.
50. Freinkman, E., Okuda, S., Ruiz, N., & Kahne, D. (2012). Regulated assembly of the transenvelope protein complex required for lipopolysaccharide export. *Biochemistry*, *51*(24), 4800–4806.
51. Freinkman, E., Chng, S. S., & Kahne, D. (2011). The complex that inserts lipopolysaccharide into the bacterial outer membrane forms a two-protein plug-and-barrel. *Proceedings of the National Academy of Sciences of the United States of America*, *108*(6), 2486–2491.
52. Narita, S., & Tokuda, H. (2009). Biochemical characterization of an ABC transporter LptBFGC complex required for the outer membrane sorting of lipopolysaccharides. *FEBS letters*, *583*(13), 2160–2164.

53. Tran, A. X., Dong, C., & Whitfield, C. (2010). Structure and functional analysis of LptC, a conserved membrane protein involved in the lipopolysaccharide export pathway in *Escherichia coli*. *The Journal of biological chemistry*, 285(43), 33529–33539.
54. Okuda, S., Sherman, D. J., Silhavy, T. J., Ruiz, N., & Kahne, D. (2016). Lipopolysaccharide transport and assembly at the outer membrane: the PEZ model. *Nature reviews. Microbiology*, 14(6), 337–345.
55. Dong, H., Xiang, Q., Gu, Y., Wang, Z., Paterson, N. G., Stansfeld, P. J., He, C., Zhang, Y., Wang, W., & Dong, C. (2014). Structural basis for outer membrane lipopolysaccharide insertion. *Nature*, 511(7507), 52–56.
56. Wu, T., McCandlish, A. C., Gronenberg, L. S., Chng, S. S., Silhavy, T. J., & Kahne, D. (2006). Identification of a protein complex that assembles lipopolysaccharide in the outer membrane of *Escherichia coli*. *Proceedings of the National Academy of Sciences of the United States of America*, 103(31), 11754–11759.
57. Botos, I., Majdalani, N., Mayclin, S. J., McCarthy, J. G., Lundquist, K., Wojtowicz, D., Barnard, T. J., Gumbart, J. C., & Buchanan, S. K. (2016). Structural and Functional Characterization of the LPS Transporter LptDE from Gram-Negative Pathogens. *Structure (London, England : 1993)*, 24(6), 965–976.
58. Yamaguchi, K., Yu, F., & Inouye, M. (1988). A single amino acid determinant of the membrane localization of lipoproteins in *E. coli*. *Cell*, 53(3), 423–432.
59. Okuda, S., & Tokuda, H. (2011). Lipoprotein sorting in bacteria. *Annual review of microbiology*, 65, 239–259.

60. Grabowicz, M., & Silhavy, T. J. (2017). Redefining the essential trafficking pathway for outer membrane lipoproteins. *Proceedings of the National Academy of Sciences of the United States of America*, *114*(18), 4769–4774.
61. Tang, X., Chang, S., Zhang, K., Luo, Q., Zhang, Z., Wang, T., Qiao, W., Wang, C., Shen, C., Zhang, Z., Zhu, X., Wei, X., Dong, C., Zhang, X., & Dong, H. (2021). Structural basis for bacterial lipoprotein relocation by the transporter LolCDE. *Nature structural & molecular biology*, *28*(4), 347–355.
62. Mizutani, M., Mukaiyama, K., Xiao, J., Mori, M., Satou, R., Narita, S., Okuda, S., & Tokuda, H. (2013). Functional differentiation of structurally similar membrane subunits of the ABC transporter LolCDE complex. *FEBS letters*, *587*(1), 23–29.
63. Kaplan, E., Greene, N. P., Crow, A., & Koronakis, V. (2018). Insights into bacterial lipoprotein trafficking from a structure of LolA bound to the LolC periplasmic domain. *Proceedings of the National Academy of Sciences of the United States of America*, *115*(31), E7389–E7397.
64. Okuda, S., & Tokuda, H. (2009). Model of mouth-to-mouth transfer of bacterial lipoproteins through inner membrane LolC, periplasmic LolA, and outer membrane LolB. *Proceedings of the National Academy of Sciences of the United States of America*, *106*(14), 5877–5882.
65. Ito, Y., Kanamaru, K., Taniguchi, N., Miyamoto, S., & Tokuda, H. (2006). A novel ligand bound ABC transporter, LolCDE, provides insights into the molecular mechanisms underlying membrane detachment of bacterial lipoproteins. *Molecular microbiology*, *62*(4), 1064–1075.

66. Takeda, K., Miyatake, H., Yokota, N., Matsuyama, S., Tokuda, H., & Miki, K. (2003). Crystal structures of bacterial lipoprotein localization factors, LolA and LolB. *The EMBO journal*, *22*(13), 3199–3209.
67. Remans, K., Pauwels, K., van Ulsen, P., Buts, L., Cornelis, P., Tommassen, J., Savvides, S. N., Decanniere, K., & Van Gelder, P. (2010). Hydrophobic surface patches on LolA of *Pseudomonas aeruginosa* are essential for lipoprotein binding. *Journal of molecular biology*, *401*(5), 921–930.
68. Matsuyama, S.i, Yokota, N., & Tokuda, H. (1997). A novel outer membrane lipoprotein, LolB (HemM), involved in the LolA (p20)-dependent localization of lipoproteins to the outer membrane of *Escherichia coli*. *The EMBO journal*, *16*(23), 6947–6955.
69. Konovalova, A., Kahne, D. E., & Silhavy, T. J. (2017). Outer Membrane Biogenesis. *Annual review of microbiology*, *71*, 539–556.
70. Tormo, A., Almirón, M., & Kolter, R. (1990). *surA*, an *Escherichia coli* gene essential for survival in stationary phase. *Journal of bacteriology*, *172*(8), 4339–4347.
71. Hennecke, G., Nolte, J., Volkmer-Engert, R., Schneider-Mergener, J., & Behrens, S. (2005). The periplasmic chaperone SurA exploits two features characteristic of integral outer membrane proteins for selective substrate recognition. *The Journal of biological chemistry*, *280*(25), 23540–23548.
72. Bitto, E., & McKay, D. B. (2002). Crystallographic structure of SurA, a molecular chaperone that facilitates folding of outer membrane porins. *Structure (London, England : 1993)*, *10*(11), 1489–1498.
73. Harms, N., Koningstein, G., Dontje, W., Muller, M., Oudega, B., Luirink, J., & de Cock, H. (2001). The early interaction of the outer membrane protein phoE with the periplasmic

- chaperone Skp occurs at the cytoplasmic membrane. *The Journal of biological chemistry*, 276(22), 18804–18811.
74. Bulieris, P. V., Behrens, S., Holst, O., & Kleinschmidt, J. H. (2003). Folding and insertion of the outer membrane protein OmpA is assisted by the chaperone Skp and by lipopolysaccharide. *The Journal of biological chemistry*, 278(11), 9092–9099.
75. Korndörfer, I. P., Dommel, M. K., & Skerra, A. (2004). Structure of the periplasmic chaperone Skp suggests functional similarity with cytosolic chaperones despite differing architecture. *Nature structural & molecular biology*, 11(10), 1015–1020.
76. Clausen, T., Southan, C., & Ehrmann, M. (2002). The HtrA family of proteases: implications for protein composition and cell fate. *Molecular cell*, 10(3), 443–455.
77. Mogensen, J. E., & Otzen, D. E. (2005). Interactions between folding factors and bacterial outer membrane proteins. *Molecular microbiology*, 57(2), 326–346.
78. Krojer, T., Garrido-Franco, M., Huber, R., Ehrmann, M., & Clausen, T. (2002). Crystal structure of DegP (HtrA) reveals a new protease-chaperone machine. *Nature*, 416(6879), 455–459.
79. Krojer, T., Sawa, J., Schäfer, E., Saibil, H. R., Ehrmann, M., & Clausen, T. (2008). Structural basis for the regulated protease and chaperone function of DegP. *Nature*, 453(7197), 885–890.
80. Arié, J. P., Sassoon, N., & Betton, J. M. (2001). Chaperone function of FkpA, a heat shock prolyl isomerase, in the periplasm of *Escherichia coli*. *Molecular microbiology*, 39(1), 199–210.
81. Saul, F. A., Arié, J. P., Vulliez-le Normand, B., Kahn, R., Betton, J. M., & Bentley, G. A. (2004). Structural and functional studies of FkpA from *Escherichia coli*, a cis/trans

- peptidyl-prolyl isomerase with chaperone activity. *Journal of molecular biology*, 335(2), 595–608.
82. Xu, Q., Guo, M., & Yu, F. (2023).  $\beta$ -Barrel Assembly Machinery (BAM) Complex as Novel Antibacterial Drug Target. *Molecules (Basel, Switzerland)*, 28(9), 3758.
83. Noinaj, N., Kuszak, A. J., Gumbart, J. C., Lukacik, P., Chang, H., Easley, N. C., Lithgow, T., & Buchanan, S. K. (2013). Structural insight into the biogenesis of  $\beta$ -barrel membrane proteins. *Nature*, 501(7467), 385–390.
84. O'Neil, P. K., Rollauer, S. E., Noinaj, N., & Buchanan, S. K. (2015). Fitting the Pieces of the  $\beta$ -Barrel Assembly Machinery Complex. *Biochemistry*, 54(41), 6303–6311.
85. Noinaj, N., Fairman, J. W., & Buchanan, S. K. (2011). The crystal structure of BamB suggests interactions with BamA and its role within the BAM complex. *Journal of molecular biology*, 407(2), 248–260.
86. Kim, K. H., & Paetzel, M. (2011). Crystal structure of Escherichia coli BamB, a lipoprotein component of the  $\beta$ -barrel assembly machinery complex. *Journal of molecular biology*, 406(5), 667–678.
87. Webb, C. T., Selkrig, J., Perry, A. J., Noinaj, N., Buchanan, S. K., & Lithgow, T. (2012). Dynamic association of BAM complex modules includes surface exposure of the lipoprotein BamC. *Journal of molecular biology*, 422(4), 545–555.
88. Kim, K. H., Aulakh, S., Tan, W., & Paetzel, M. (2011). Crystallographic analysis of the C-terminal domain of the Escherichia coli lipoprotein BamC. *Acta crystallographica. Section F, Structural biology and crystallization communications*, 67(Pt 11), 1350–1358.

89. Sandoval, C. M., Baker, S. L., Jansen, K., Metzner, S. I., & Sousa, M. C. (2011). Crystal structure of BamD: an essential component of the  $\beta$ -Barrel assembly machinery of gram-negative bacteria. *Journal of molecular biology*, *409*(3), 348–357.
90. Dong, C., Hou, H. F., Yang, X., Shen, Y. Q., & Dong, Y. H. (2012). Structure of Escherichia coli BamD and its functional implications in outer membrane protein assembly. *Acta crystallographica. Section D, Biological crystallography*, *68*(Pt 2), 95–101.
91. Kim, K. H., Kang, H. S., Okon, M., Escobar-Cabrera, E., McIntosh, L. P., & Paetzel, M. (2011). Structural characterization of Escherichia coli BamE, a lipoprotein component of the  $\beta$ -barrel assembly machinery complex. *Biochemistry*, *50*(6), 1081–1090.
92. Knowles, T. J., Browning, D. F., Jeeves, M., Maderbocus, R., Rajesh, S., Sridhar, P., Manoli, E., Emery, D., Sommer, U., Spencer, A., Leyton, D. L., Squire, D., Chaudhuri, R. R., Viant, M. R., Cunningham, A. F., Henderson, I. R., & Overduin, M. (2011). Structure and function of BamE within the outer membrane and the  $\beta$ -barrel assembly machine. *EMBO reports*, *12*(2), 123–128.
93. Wu, T., Malinverni, J., Ruiz, N., Kim, S., Silhavy, T. J., & Kahne, D. (2005). Identification of a multicomponent complex required for outer membrane biogenesis in Escherichia coli. *Cell*, *121*(2), 235–245.
94. Kim, S., Malinverni, J. C., Sliz, P., Silhavy, T. J., Harrison, S. C., & Kahne, D. (2007). Structure and function of an essential component of the outer membrane protein assembly machine. *Science (New York, N.Y.)*, *317*(5840), 961–964.
95. Ni, D., Wang, Y., Yang, X., Zhou, H., Hou, X., Cao, B., Lu, Z., Zhao, X., Yang, K., & Huang, Y. (2014). Structural and functional analysis of the  $\beta$ -barrel domain of BamA from

- Escherichia coli. *FASEB journal : official publication of the Federation of American Societies for Experimental Biology*, 28(6), 2677–2685.
96. Noinaj, N., Kuszak, A. J., Balusek, C., Gumbart, J. C., & Buchanan, S. K. (2014). Lateral opening and exit pore formation are required for BamA function. *Structure (London, England : 1993)*, 22(7), 1055–1062.
97. Ricci, D. P., Hagan, C. L., Kahne, D., & Silhavy, T. J. (2012). Activation of the Escherichia coli  $\beta$ -barrel assembly machine (Bam) is required for essential components to interact properly with substrate. *Proceedings of the National Academy of Sciences of the United States of America*, 109(9), 3487–3491.
98. Bergal, H. T., Hopkins, A. H., Metzner, S. I., & Sousa, M. C. (2016). The Structure of a BamA-BamD Fusion Illuminates the Architecture of the  $\beta$ -Barrel Assembly Machine Core. *Structure (London, England : 1993)*, 24(2), 243–251.
99. Noinaj, N., Gumbart, J. C., & Buchanan, S. K. (2017). The  $\beta$ -barrel assembly machinery in motion. *Nature reviews. Microbiology*, 15(4), 197–204.
100. Gu, Y., Li, H., Dong, H., Zeng, Y., Zhang, Z., Paterson, N. G., Stansfeld, P. J., Wang, Z., Zhang, Y., Wang, W., & Dong, C. (2016). Structural basis of outer membrane protein insertion by the BAM complex. *Nature*, 531(7592), 64–69.
101. Iadanza, M. G., Higgins, A. J., Schiffrin, B., Calabrese, A. N., Brockwell, D. J., Ashcroft, A. E., Radford, S. E., & Ranson, N. A. (2016). Lateral opening in the intact  $\beta$ -barrel assembly machinery captured by cryo-EM. *Nature communications*, 7, 12865.
102. Bakelar, J., Buchanan, S. K., & Noinaj, N. (2016). The structure of the  $\beta$ -barrel assembly machinery complex. *Science (New York, N.Y.)*, 351(6269), 180–186.



103. Rigel, N. W., Ricci, D. P., & Silhavy, T. J. (2013). Conformation-specific labeling of BamA and suppressor analysis suggest a cyclic mechanism for  $\beta$ -barrel assembly in *Escherichia coli*. *Proceedings of the National Academy of Sciences of the United States of America*, *110*(13), 5151–5156.
104. Kleinschmidt J. H. (2015). Folding of  $\beta$ -barrel membrane proteins in lipid bilayers - Unassisted and assisted folding and insertion. *Biochimica et biophysica acta*, *1848*(9), 1927–1943.
105. Danoff, E. J., & Fleming, K. G. (2015). Membrane defects accelerate outer membrane  $\beta$ -barrel protein folding. *Biochemistry*, *54*(2), 97–99.
106. Gessmann, D., Chung, Y. H., Danoff, E. J., Plummer, A. M., Sandlin, C. W., Zaccai, N. R., & Fleming, K. G. (2014). Outer membrane  $\beta$ -barrel protein folding is physically controlled by periplasmic lipid head groups and BamA. *Proceedings of the National Academy of Sciences of the United States of America*, *111*(16), 5878–5883.
107. Dutton, R. J., Boyd, D., Berkmen, M., & Beckwith, J. (2008). Bacterial species exhibit diversity in their mechanisms and capacity for protein disulfide bond formation. *Proceedings of the National Academy of Sciences of the United States of America*, *105*(33), 11933–11938.
108. Bocian-Ostrzycka, K. M., Grzeszczuk, M. J., Banaś, A. M., & Jagusztyn-Krynicka, E. K. (2017). Bacterial thiol oxidoreductases - from basic research to new antibacterial strategies. *Applied microbiology and biotechnology*, *101*(10), 3977–3989.
109. Daniels, R., Mellroth, P., Bernsel, A., Neiers, F., Normark, S., von Heijne, G., & Henriques-Normark, B. (2010). Disulfide bond formation and cysteine exclusion in gram-positive bacteria. *The Journal of biological chemistry*, *285*(5), 3300–3309.

110. Hatahet, F., Boyd, D., & Beckwith, J. (2014). Disulfide bond formation in prokaryotes: history, diversity and design. *Biochimica et biophysica acta*, 1844(8), 1402–1414.
111. Landeta, C., Boyd, D., & Beckwith, J. (2018). Disulfide bond formation in prokaryotes. *Nature microbiology*, 3(3), 270–280.
112. Früh, V., Zhou, Y., Chen, D., Loch, C., Ab, E., Grinkova, Y. N., Verheij, H., Sligar, S. G., Bushweller, J. H., & Siegal, G. (2010). Application of fragment-based drug discovery to membrane proteins: identification of ligands of the integral membrane enzyme DsbB. *Chemistry & biology*, 17(8), 881–891.
113. Zhou, Y., Cierpicki, T., Jimenez, R. H., Lukasik, S. M., Ellena, J. F., Cafiso, D. S., Kadokura, H., Beckwith, J., & Bushweller, J. H. (2008). NMR solution structure of the integral membrane enzyme DsbB: functional insights into DsbB-catalyzed disulfide bond formation. *Molecular cell*, 31(6), 896–908.
114. Rozhkova, A., Stirnimann, C. U., Frei, P., Grauschopf, U., Brunisholz, R., Grütter, M. G., Capitani, G., & Glockshuber, R. (2004). Structural basis and kinetics of inter- and intramolecular disulfide exchange in the redox catalyst DsbD. *The EMBO journal*, 23(8), 1709–1719.
115. Zapun, A., Missiakas, D., Raina, S., & Creighton, T. E. (1995). Structural and functional characterization of DsbC, a protein involved in disulfide bond formation in *Escherichia coli*. *Biochemistry*, 34(15), 5075–5089.
116. Kadokura, H., & Beckwith, J. (2010). Mechanisms of oxidative protein folding in the bacterial cell envelope. *Antioxidants & redox signaling*, 13(8), 1231–1246.
117. Liu, X., & Wang, C. C. (2001). Disulfide-dependent folding and export of *Escherichia coli* DsbC. *The Journal of biological chemistry*, 276(2), 1146–1151.

118. Cho, S. H., Porat, A., Ye, J., & Beckwith, J. (2007). Redox-active cysteines of a membrane electron transporter DsbD show dual compartment accessibility. *The EMBO journal*, 26(15), 3509–3520.
119. Rozhkova, A., Stirnimann, C. U., Frei, P., Grauschopf, U., Brunisholz, R., Grütter, M. G., Capitani, G., & Glockshuber, R. (2004). Structural basis and kinetics of inter- and intramolecular disulfide exchange in the redox catalyst DsbD. *The EMBO journal*, 23(8), 1709–1719.
120. Rietsch, A., Bessette, P., Georgiou, G., & Beckwith, J. (1997). Reduction of the periplasmic disulfide bond isomerase, DsbC, occurs by passage of electrons from cytoplasmic thioredoxin. *Journal of bacteriology*, 179(21), 6602–6608.
121. Inaba K. (2009). Disulfide bond formation system in Escherichia coli. *Journal of biochemistry*, 146(5), 591–597.
122. Rozhkova, A., & Glockshuber, R. (2008). Thermodynamic aspects of DsbD-mediated electron transport. *Journal of molecular biology*, 380(5), 783–788.
123. Pagès, J. M., James, C. E., & Winterhalter, M. (2008). The porin and the permeating antibiotic: a selective diffusion barrier in Gram-negative bacteria. *Nature reviews. Microbiology*, 6(12), 893–903.
124. Krishnan, S., & Prasadarao, N. V. (2012). Outer membrane protein A and OprF: versatile roles in Gram-negative bacterial infections. *The FEBS journal*, 279(6), 919–931.
125. Smith, S. G., Mahon, V., Lambert, M. A., & Fagan, R. P. (2007). A molecular Swiss army knife: OmpA structure, function and expression. *FEMS microbiology letters*, 273(1), 1–11.

126. Choi, U., & Lee, C. R. (2019). Distinct Roles of Outer Membrane Porins in Antibiotic Resistance and Membrane Integrity in *Escherichia coli*. *Frontiers in microbiology*, *10*, 953.
127. Hickman, S. J., Cooper, R. E. M., Bellucci, L., Paci, E., & Brockwell, D. J. (2017). Gating of TonB-dependent transporters by substrate-specific forced remodelling. *Nature communications*, *8*, 14804.
128. Imlay, J. A., Chin, S. M., & Linn, S. (1988). Toxic DNA damage by hydrogen peroxide through the Fenton reaction in vivo and in vitro. *Science (New York, N.Y.)*, *240*(4852), 640–642.
129. Bagg, A., & Neilands, J. B. (1987). Ferric uptake regulation protein acts as a repressor, employing iron (II) as a cofactor to bind the operator of an iron transport operon in *Escherichia coli*. *Biochemistry*, *26*(17), 5471–5477.
130. Hantke K. (1981). Regulation of ferric iron transport in *Escherichia coli* K12: isolation of a constitutive mutant. *Molecular & general genetics : MGG*, *182*(2), 288–292.
131. Härle, C., Kim, I., Angerer, A., & Braun, V. (1995). Signal transfer through three compartments: transcription initiation of the *Escherichia coli* ferric citrate transport system from the cell surface. *The EMBO journal*, *14*(7), 1430–1438.
132. Ochs, M., Veitinger, S., Kim, I., Welz, D., Angerer, A., & Braun, V. (1995). Regulation of citrate-dependent iron transport of *Escherichia coli*: *fecR* is required for transcription activation by *FecI*. *Molecular microbiology*, *15*(1), 119–132.
133. Kadner R. J. (1978). Repression of synthesis of the vitamin B12 receptor in *Escherichia coli*. *Journal of bacteriology*, *136*(3), 1050–1057.

134. Nou, X., & Kadner, R. J. (2000). Adenosylcobalamin inhibits ribosome binding to *btuB* RNA. *Proceedings of the National Academy of Sciences of the United States of America*, *97*(13), 7190–7195.
135. Valentin-Hansen, P., Eriksen, M., & Udesen, C. (2004). The bacterial Sm-like protein Hfq: a key player in RNA transactions. *Molecular microbiology*, *51*(6), 1525–1533.
136. Guillier, M., & Gottesman, S. (2008). The 5' end of two redundant sRNAs is involved in the regulation of multiple targets, including their own regulator. *Nucleic acids research*, *36*(21), 6781–6794.
137. Noinaj, N., Guillier, M., Barnard, T. J., & Buchanan, S. K. (2010). TonB-dependent transporters: regulation, structure, and function. *Annual review of microbiology*, *64*, 43–60.
138. Page M. G. P. (2019). The Role of Iron and Siderophores in Infection, and the Development of Siderophore Antibiotics. *Clinical infectious diseases : an official publication of the Infectious Diseases Society of America*, *69*(Suppl 7), S529–S537.
139. Bonhivers, M., Plançon, L., Ghazi, A., Boulanger, P., le Maire, M., Lambert, O., Rigaud, J. L., & Letellier, L. (1998). FhuA, an *Escherichia coli* outer membrane protein with a dual function of transporter and channel which mediates the transport of phage DNA. *Biochimie*, *80*(5-6), 363–369.
140. Pawelek, P. D., Croteau, N., Ng-Thow-Hing, C., Khursigara, C. M., Moiseeva, N., Allaire, M., & Coulton, J. W. (2006). Structure of TonB in complex with FhuA, *E. coli* outer membrane receptor. *Science (New York, N.Y.)*, *312*(5778), 1399–1402.

141. Ferguson, A. D., Chakraborty, R., Smith, B. S., Esser, L., van der Helm, D., & Deisenhofer, J. (2002). Structural basis of gating by the outer membrane transporter FecA. *Science (New York, N.Y.)*, 295(5560), 1715–1719.
142. Chimento, D. P., Mohanty, A. K., Kadner, R. J., & Wiener, M. C. (2003). Substrate-induced transmembrane signaling in the cobalamin transporter BtuB. *Nature structural biology*, 10(5), 394–401.
143. Chimento, D. P., Kadner, R. J., & Wiener, M. C. (2003). The Escherichia coli outer membrane cobalamin transporter BtuB: structural analysis of calcium and substrate binding, and identification of orthologous transporters by sequence/structure conservation. *Journal of molecular biology*, 332(5), 999–1014.
144. Shultis, D. D., Purdy, M. D., Banchs, C. N., & Wiener, M. C. (2006). Outer membrane active transport: structure of the BtuB:TonB complex. *Science (New York, N.Y.)*, 312(5778), 1396–1399.
145. Fuller-Schaefer, C. A., & Kadner, R. J. (2005). Multiple extracellular loops contribute to substrate binding and transport by the Escherichia coli cobalamin transporter BtuB. *Journal of bacteriology*, 187(5), 1732–1739.
146. Xu, Q., Ellena, J. F., Kim, M., & Cafiso, D. S. (2006). Substrate-dependent unfolding of the energy coupling motif of a membrane transport protein determined by double electron-electron resonance. *Biochemistry*, 45(36), 10847–10854.
147. Lukasik, S. M., Ho, K. W., & Cafiso, D. S. (2007). Molecular basis for substrate-dependent transmembrane signaling in an outer-membrane transporter. *Journal of molecular biology*, 370(5), 807–811.

148. Gumbart, J., Wiener, M. C., & Tajkhorshid, E. (2009). Coupling of calcium and substrate binding through loop alignment in the outer-membrane transporter BtuB. *Journal of molecular biology*, 393(5), 1129–1142.
149. Freed, D. M., Lukasik, S. M., Sikora, A., Mokdad, A., & Cafiso, D. S. (2013). Monomeric TonB and the Ton box are required for the formation of a high-affinity transporter-TonB complex. *Biochemistry*, 52(15), 2638–2648.
150. Sikora, A., Joseph, B., Matson, M., Staley, J. R., & Cafiso, D. S. (2016). Allosteric Signaling Is Bidirectional in an Outer-Membrane Transport Protein. *Biophysical journal*, 111(9), 1908–1918.
151. Cadieux, N., Bradbeer, C., & Kadner, R. J. (2000). Sequence changes in the ton box region of BtuB affect its transport activities and interaction with TonB protein. *Journal of bacteriology*, 182(21), 5954–5961.
152. Joseph, B., Sikora, A., Bordignon, E., Jeschke, G., Cafiso, D. S., & Prisner, T. F. (2015). Distance Measurement on an Endogenous Membrane Transporter in E. coli Cells and Native Membranes Using EPR Spectroscopy. *Angewandte Chemie (International ed. in English)*, 54(21), 6196–6199.
153. Joseph, B., Sikora, A., & Cafiso, D. S. (2016). Ligand Induced Conformational Changes of a Membrane Transporter in E. coli Cells Observed with DEER/PELDOR. *Journal of the American Chemical Society*, 138(6), 1844–1847.
154. Nyenhuis, D. A., Nilaweera, T. D., Niblo, J. K., Nguyen, N. Q., DuBay, K. H., & Cafiso, D. S. (2020). Evidence for the Supramolecular Organization of a Bacterial Outer-Membrane Protein from In Vivo Pulse Electron Paramagnetic Resonance Spectroscopy. *Journal of the American Chemical Society*, 142(24), 10715–10722.

155. Nyenhuis, D. A., Nilaweera, T. D., & Cafiso, D. S. (2020). Native Cell Environment Constrains Loop Structure in the *Escherichia coli* Cobalamin Transporter BtuB. *Biophysical journal*, *119*(8), 1550–1557.
156. Nilaweera, T. D., Nyenhuis, D. A., & Cafiso, D. S. (2021). Structural intermediates observed only in intact *Escherichia coli* indicate a mechanism for TonB-dependent transport. *eLife*, *10*, e68548.
157. Sarver, J. L., Zhang, M., Liu, L., Nyenhuis, D., & Cafiso, D. S. (2018). A Dynamic Protein-Protein Coupling between the TonB-Dependent Transporter FhuA and TonB. *Biochemistry*, *57*(6), 1045–1053.
158. Celia, H., Noinaj, N., & Buchanan, S. K. (2020). Structure and Stoichiometry of the Ton Molecular Motor. *International journal of molecular sciences*, *21*(2), 375.
159. Zinke, M., Lejeune, M., Mechaly, A., Bardiaux, B., Boneca, I. G., Delepelaire, P., & Izadi-Pruneyre, N. (2024). Ton motor conformational switch and peptidoglycan role in bacterial nutrient uptake. *Nature communications*, *15*(1), 331.
160. Gumbart, J., Wiener, M. C., & Tajkhorshid, E. (2007). Mechanics of force propagation in TonB-dependent outer membrane transport. *Biophysical journal*, *93*(2), 496–504.
161. Klebba P. E. (2016). ROSET Model of TonB Action in Gram-Negative Bacterial Iron Acquisition. *Journal of bacteriology*, *198*(7), 1013–1021.



## **Chapter 2 – Materials and Methods**

### 2.1 Materials

The pAG1 plasmid encoding wild type (WT) *btuB* gene was generously provided by late Prof. Robert J. Kadner, School of Medicine, University of Virginia. The pET22b plasmid encoding WT *tonB* fragment (residues 103-239) was kindly provided by Prof. Robert K. Nakamoto, School of Medicine, University of Virginia. The pIS711 plasmid encoding WT *fecA* gene downstream of the phage T7 gene 10 promoter was generously provided by Prof. Volkmar Braun, University of Tübingen, Tübingen, Germany. The pTARA plasmid encoding the T7 polymerase under control of the araBAD promoter was obtained from Addgene, Watertown, MA.

*E. coli* strain RK5016 (-*argH*, -*btuB*, -*metE*) was generously provided by late Prof. Robert J. Kadner, School of Medicine, University of Virginia. *E. coli* strain RI90 carrying the *dsbA* null mutation system (*araD139 Δ(araABC-leu)7679 galU galK Δ(lac)X74 rpsL thi phoR Δara714 leu+ dsbA:: Kanr*) was kindly provided by Coli Genetic Stock Center, Yale University (New Haven, CT) and was used for BtuB expression. *E. coli* strains T7 express *LysY/I<sup>q</sup>* competent cells were obtained from New England Biolabs (Ipswich, MA) and was used for TonB expression. *E. coli* strain BL21(DE3) cells were obtained from Agilent Technologies (Santa Clara, CA) which lacks OM porins such as OmpA, OmpC, LamB and was used for FecA expression. *E. coli* Top10 competent cells was obtained from IBA Life Sciences (Göttingen, Germany) and was used for plasmid propagation.

The DNA Primers used for Polymerase Incomplete Primer Extension (PIPE) mutagenesis were obtained from Integrated DNA Technologies (Coralville, IA). PfuUltra high fidelity DNA polymerase enzyme was obtained from Agilent Technologies (Santa Clara, CA). DpnI digestion

enzyme was obtained from New England Biolabs (Ipswich, MA). GeneJET Plasmid Miniprep Kit was obtained from ThermoFisher Scientific (Waltham, MA). Sarkosyl ( $C_{15}H_{28}NNaO_3$ ), 0.5M ethylenediaminetetraacetic acid (EDTA) ( $C_{10}H_{16}N_2O_8$ ), ammonium sulphate( $(NH_4)_2SO_4$ ), sodium citrate dihydrate ( $C_6H_5Na_3O_7 \cdot 2H_2O$ ), and magnesium chloride ( $MgCl_2$ ) were obtained from Fisher Scientific (Waltham, MA). Tryptone and Yeast Extract were obtained from IBI Scientific (Dubuque, IA). Deoxyribonucleotide triphosphate (dNTP), HEPES (Free Acid) ( $C_8H_{18}N_2O_4S$ ), and sodium chloride (NaCl) were obtained from Bio Basic (Amherst, NY). Agar was obtained from BD Biosciences (San Jose, CA). Dibasic potassium phosphate ( $K_2HPO_4$ ), monobasic potassium phosphate ( $KH_2PO_4$ ), chloramphenicol ( $C_{11}H_{12}Cl_2N_2O_5$ ), dithiothreitol (DTT) ( $C_4H_{10}O_2S_2$ ), and n-octyl- $\beta$ -D-glucopyranoside (OG) ( $C_{14}H_{28}O_6$ ) were obtained from Chem Impex (Wood Dale, IL). Glycerol ( $C_3H_8O_3$ ), aprotinin ( $C_{284}H_{432}N_{84}O_{79}S_7$ ) and leupeptin hemisulfate ( $C_{20}H_{38}N_6O_4 \cdot 0.5H_2SO_4$ ) were obtained from Research Products International (Mt Prospect, IL). Calcium chloride ( $CaCl_2$ ) was obtained from Acros Organics (Geel, Belgium). Magnesium sulphate ( $MgSO_4$ ), d-glucose ( $C_6H_{12}O_6$ ) and thiamine hydrochloride ( $C_{12}H_{18}Cl_2N_4OS$ ) were obtained from Sigma-Aldrich (Saint Louis, MO). L-methionine ( $C_5H_{11}NO_2S$ ) and L-arginine ( $C_6H_{14}N_4O_2$ ) were obtained from Caisson Labs (Smithfield, UH). L-(+)-arabinose ( $C_5H_{10}O_5$ ) was obtained from EMD Millipore (Billerica, MA). Ampicillin sodium salt ( $C_{16}H_{18}N_3NaO_4S$ ) was obtained from Cayman Chemical Company (Ann Arbor, MI). Tris Amino ( $C_4H_{11}NO_3$ ) was obtained from VWR Scientific (Batavia, IL). 4-benzenesulfonyl fluoride hydrochloride (AEBSF) ( $C_8H_{10}FNO_2S \cdot HCl$ ) and isopropyl  $\beta$ -D-thiogalactopyranoside (IPTG) ( $C_9H_{18}O_5S$ ) were obtained from Gold Bio (Saint Louis, MO). Imidazole ( $C_3H_4N_2$ ) was obtained from GFS Chemicals (Columbus, OH). S-(1-oxyl-2,2,5,5-tetramethyl-2,5-dihydro-1H-pyrrol-3-yl)methyl methanesulfonothioate (MTSL) ( $C_{10}H_{18}NO_3S_2$ ) and benzonase nuclease enzyme were obtained

from Santa Cruz Biotechnology (Dallas, TX). HiTrap® Q High Performance (Q-HP) columns were obtained from GE Healthcare (Chicago, IL) and were used for BtuB and FecA purification through ion-exchange chromatography. Profinity™ IMAC Ni-charged resin was obtained from Bio Rad (Des Plaines, IL) and was used for 6xHis tag TonB fragment (103-239 residues) purification. 1-palmitoyl-2-oleoyl-sn-glycero-3-phosphocholine (POPC) (C<sub>42</sub>H<sub>82</sub>NO<sub>8</sub>P) and 1,2-dilauroyl-sn-glycero-3-phosphocholine (DLPC) (C<sub>32</sub>H<sub>64</sub>NO<sub>8</sub>P) were obtained from Avanti Polar Lipids (Alabaster, AL) and was used in lipid reconstitution.

For EPR experiments, d<sub>8</sub>-glycerol (≥ 98% D) (C<sub>3</sub>D<sub>8</sub>O<sub>3</sub>) and Ferric citrate (C<sub>6</sub>H<sub>5</sub>FeO<sub>7</sub>) were obtained from Sigma-Aldrich (Saint Louis, MO) whereas Cyanocobalamin (Vitamin B<sub>12</sub>) (C<sub>63</sub>H<sub>88</sub>CoN<sub>14</sub>O<sub>14</sub>P) was obtained from Research Products International (Mt Prospect, IL). Round Boro Glass Tubing (0.6mm ID x 0.84mm OD) and Clear Fused Quartz Tubing (1.10mm ID x 1.60mm OD) were obtained from VitroCom (Mount Lakes, NJ) and were used for CW-EPR and pulse-EPR (DEER) experiments, respectively.

## 2.2 Molecular Biology Techniques

Numerous biochemical and biophysical techniques have been utilized to study native and mutant proteins at the molecular and cellular level. However, to study these proteins, they have to be successfully transformed/cloned into their appropriate expression vectors and mutants need to be generated based on site-directed mutagenesis. Therefore, accuracy and success at the DNA level is imperative for these studies.

### 2.2.1 Polymerase Chain Reaction (PCR)

PCR is a fundamental technique in molecular biology, and it is the first step needed to synthesize and amplify novel DNA sequences of interest. PCR involves denaturing the DNA

followed by renaturing of short deoxyribonucleic acid (DNA) or ribonucleic acid (RNA) with the assistance of an enzyme at a specific temperature<sup>1</sup>. This thesis work used PCR extensively to create mutants of *btuB* and *fecA* genes encoding BtuB and FecA, respectively. PCR process is composed of three (3) major steps. They are denaturation, annealing, and elongation. During the denaturation step, the template DNA is denatured at 95 °C. The annealing step involves the binding of introduced primers with the template DNA<sup>2</sup>. The elongation step is where the DNA polymerase (Pfu DNA polymerase enzyme isolated from *Pyrococcus furiosus*) elongates the DNA primers annealed to the template DNA thereby completing the gene sequence<sup>3</sup>. This process continues for multiple cycles and finally the samples are held at 4 °C.

Once DNA amplification is complete, removal of the template DNA through enzymatic digestion is possible depending on the type of PCR. This process utilizes a restriction enzyme such as DpnI endonuclease which recognizes methylated sites in double stranded DNA and cleaves from the specific site 5'-GmATC-3' from the DNA sequence<sup>4,5</sup> (Figure 2.1a). During PCR amplification, the template DNA consists of methylated sites whereas the amplified DNA is unmethylated. Thus, DpnI removes the template DNA which is no longer required.

Next step is the analysis of DNA samples through agarose DNA gel electrophoresis. This process involves the migration of negatively charged DNA towards the positively charged anode. The extent of migration depends on the size of the amplified DNA, agarose concentration, and particularly the DNA conformation. This allows us to identify properly amplified DNA which can be used for the next steps. Here, fluorescent intercalating dyes (Ex: SYBR Gold) can be used to stain DNA fragments which can then be detected under UV light<sup>6</sup>. Interestingly, after gel bands have been visualized (Figure 2.1b), the DNA sample introduced to the gel can be recovered using organic chemical-based DNA extraction methods<sup>7</sup>.

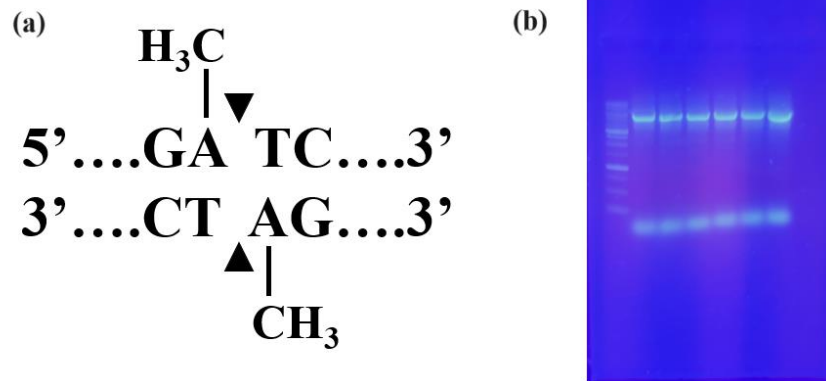


Figure 2.1 DpnI digestion of DNA. (a) DpnI endonuclease recognition site in methylated DNA. The cleavage site is denoted by solid (black)  $\Delta$  symbol<sup>5</sup> (b) Agarose gel with a successful PCR amplification. The fluorescent band on the top represents amplified plasmid and band at the bottom represents DNA primer dimers occurring due to forward and reverse primer interactions.

### 2.2.2 Designing primers for PCR reactions

To obtain the desired PCR product, careful selection of DNA sequence for the primer is crucial as it determines the efficient annealing of the primer to template DNA which will then be successfully amplified during the PCR process. To design a primer with positive potential for successful PCR amplification, there are certain conditions that can be utilized as guidelines. They are as follows. (i). It is best to have a primer which has 18-36 nucleotides. Short primers can result in non-specific amplification and long primers can result in ineffective screening and annealing to the template DNA during the annealing period. (ii). It is optimal to have a GC content of 40 – 60% when it comes to base composition. (iii). It is desirable to have the primer melting temperature in the range of 64 – 68 °C with no significant temperature changes between the primer pairs.

However, this parameter cannot be fully manipulated as the melting temperature varies with the GC content of the primer selected (Figure 2.2).

### BtuB Q510C Primers

**Original BtuB Sequence**

```
cagcaggtgaaataaccagctcgactggcagttgtatgacttcgactgggggtattacttat
Q Q V K Y Q L D W Q L Y D F D W G I T Y
```

**Mutated Sequence (Residue of interest converted to a cysteine with the appropriate codons)**

```
cagcaggtgaaataaccagctcgactggcgcttgtatgacttcgactgggggtattacttat
Q Q V K Y Q L D W C L Y D F D W G I T Y
```

**Selected Forward Primer**

```
cagcaggtgaaataaccagctcgactggcgcttgtatgacttcgactgggggtattacttat
Q Q V K Y Q L D W C L Y D F D W G I T Y
```

5'- CCA GCT CGA CTG G**TGC**TT GTA TGA CTT CGA C -3'

**Complementary Reverse Primer\***

5'- GTC GAA GTC ATA CAA **GCA** CCA GTC GAG CTG G -3'

\*Reverse Primer can be obtained by analyzing the selected forward primer with IDT OligoAnalyzer Tool

Figure 2.2 Primer design process for BtuB periplasmic turn residue Q510 to C510 (Q510C)

Once the site to be mutated has been chosen, the primer design protocol included obtaining the genome sequence of BtuB (and FecA for Chapter 4) using Uniprot website<sup>8</sup> (Uniprot ID P06129 for BtuB and ID P13036 for FecA), followed by a conversion of this sequence to its corresponding amino acid sequence using ExPASy translate<sup>9</sup>. By aligning these two sequences, we can obtain the corresponding three (3) nucleotide codon for each amino acid (Figure 2.2). This thesis work was based solely on point mutations on residues to either cysteine (C) or alanine (A). The selection of forward (5' to 3') primer was performed in such a way that the point mutation resides at the center of the selected primer while each side of the mutation having 14 - 16 nucleotides (33 - 35 nucleotides total) which can allow the primer to be properly oriented to the template DNA during annealing. Once the forward primer is selected, OligoAnalyzer Tool in

Integrated DNA Technologies (IDT)<sup>10</sup> was used to obtain the complementary reverse primer in the 5' to 3' direction. OligoAnalyzer Tool also provides the GC content and melting temperatures of the selected primer as well.

### 2.2.3 PCR mutagenesis and cloning

There are many ways in which DNA cloning can occur. PCR based cloning involves amplifying a fragment of DNA while introducing restriction sites to the 5' and 3' end of the fragment which can be recognized by a secondary plasmid digested with the same restriction sites, thereby proper orientation and insert into the digested plasmid to create a new plasmid with inserted DNA fragment. In contrast, an enzyme free cloning technique is polymerase incomplete primer extension (PIPE) based cloning where the vector PIPE (V-PIPE) and insert PIPE (I-PIPE) anneals with the assistance of the primer ends with overlapping sequences present in both 5' and 3' ends<sup>11</sup>. A transformation to competent cells will result in the ligation of the ends by *E. coli* enzymes to create the new plasmid. Similarly, we have implemented PIPE mutagenesis to synthesize our DNA constructs. In this process the synthesized primers have overlapping sequences along with the point mutation so that the primers can anneal to the template DNA efficiently. The double strand will then be extended by DNA polymerase enzyme to synthesize amplified DNA plasmid.

For this thesis work, pAG1 plasmid encoding the WT *btuB* gene was utilized to create the mutations D6C-Q510C, and V90C-T188C for Chapter 3. The pIS711 plasmid encoding the WT *fecA* gene was utilized to create the mutation Q528C-T666C for Chapter 4. The pAG1 plasmid encoding the WT *btuB* gene was utilized to create the mutations D6C-I305C, D6C-I305C-D316A, D6C-Q510C-D316A, V10C-Q510C, V10C-Q510C-D316A for Chapter 5 and V90C-I305C, V90C-I305C-D316A, V90C-Q510C, V90C-Q510C-D316A for Chapter 6.

The PCR samples were prepared according to the recipe provided in Table 2.1 and the annealing temperatures for PCR reaction protocol (Table 2.2) were determined based on the melting temperatures of the constructed primers used for the particular reaction (Appendix 3). After DpnI digestion, 1% agarose gel was used for DNA electrophoresis.

The successfully amplified samples were transformed to *E. coli* Top10 Competent Cells according to the instructions provided by the manufacturer (Section 2.3.4), plated on lysogeny broth (LB) media containing 100µg/ml ampicillin (AMP) agar plates, and incubated overnight (O/N) at 37 ° C. The single cell colonies (SCC) present on agar were inoculated into culture tubes with 5 mL LB Media and 5 µL of 100mg/mL AMP which was grown overnight (O/N) to obtain cell pellets which were lysed to isolate DNA plasmid according to manufacturer instructions (2.2.5). The isolated plasmids were sent to Azenta Life Sciences<sup>12</sup> or Plasmidsaurus<sup>13</sup> to obtain complete sequences which were then analyzed to verify the presence of the point mutation of interest.

Reagent	Stock Concentration	Volume for PCR	Final Concentration in individual tube
Template DNA	3 ng/µL	1 µL	0.06 ng/µL
10X Pfu Turbo Reaction Buffer	10X	5 µL	1X
Pfultra High Fidelity DNA Polymerase (200 mM Tris-HCl [pH 8.8 at 25 ° C], 100 mM (NH <sub>4</sub> ) <sub>2</sub> SO <sub>4</sub> , 100 mM KCl, 1% (v/v) Triton X-100, 1 mg/mL BSA <sup>14</sup> )	2.5 U/µL	1 µL	0.05 U/µL
dNTPs	10 mM	1 µL	0.2 mM
Forward Primer	10 µM	5 µL	1 µM
Reverse Primer	10 µM	5 µL	1 µM
ddH <sub>2</sub> O	-	32 µL	<i>To bring final volume of PCR tube to 50 µL</i>



Table 2.1 Initial and final concentrations of reagents required for a PIPE PCR experiment

PCR Process	Temperature Condition (° C)	Time Duration (xx mins:yy sec)
Initial Denaturation	95	03:00
Subsequent Denaturation	95	00:30
Annealing	*	00:45
Elongation	68	10:00
Repeat	<i>Back to Subsequent Denaturation Step</i>	<i>20 times</i>
Final Elongation	68	05:00
Hold	4	<i>Indefinitely</i>

Table 2.2 PIPE PCR steps, temperature conditions, and the time durations used for all BtuB and FecA mutation experiments. \*Annealing temperature range selected was based on the melting temperature of the primers used for the experiments (see Appendix 3, Table 3.1 and 3.2).

#### 2.2.4 DNA plasmid features

Several key factors in the plasmid determine its ability to be accepted into specific cells, its ability to express protein of interest, and subsequent processes such as protein purification (Figure 2.3). (i) All plasmids contain an origin of replication (*ori*) where plasmid self-replication initiates. (ii) Selective marker genes such antibiotic (ampicillin, chloramphenicol, kanamycin) resistant genes (AmpR – ampicillin resistant) are used to identify transformed versus non-

transformed cells. (iii) Multiple restriction sites after the promoter (multiple cloning sites or MCS) where they can be cleaved using specific enzymes and new DNA of interest inserted through ligation during cloning experiments. These MCS can also have sequence tags such as His tags which is quite useful during protein purification techniques such as affinity chromatography. (iv) Some plasmids can be encoded with repressor genes that can inhibit transcription of the gene of interest and can be regulated by repressor molecules (Ex: pAG1 plasmid encoding the wild type *btuB* gene contains an ampicillin resistant gene *AmpR* which allows the growth and propagation of the plasmid in the presence of ampicillin antibiotic). However, not all plasmids have this property, and the presence of leaky promoters can lead to continuous expression of genes during cell growth<sup>15,16</sup>.

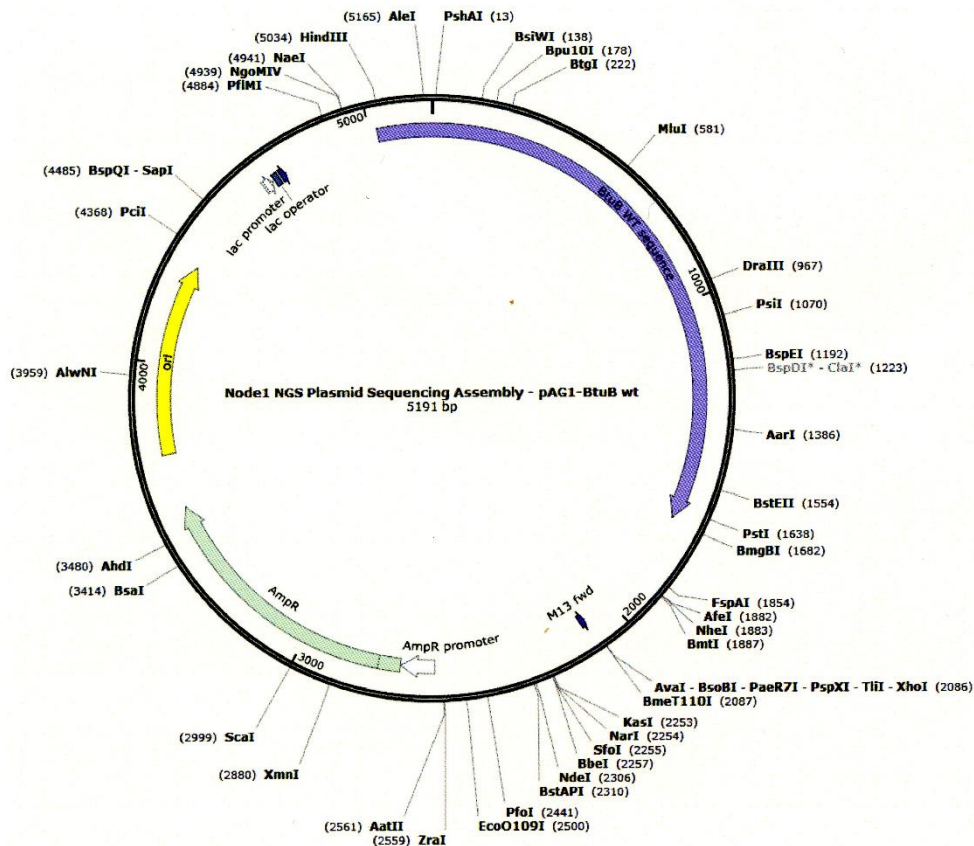


Figure 2.3 Plasmid map of pAG1 harboring the wild type *btuB* gene. It also contains ampicillin resistant (AmpR) gene which allows plasmid propagation in cells in the presence of ampicillin antibiotic.

Plasmid compatibility and plasmid replication competition are encountered when cells are introduced with multiple plasmids. The expression of two incompatible plasmids will eventually result in the expression of one plasmid at the expense of the other. Therefore, measures must be taken to select plasmids from distinct groups during multiple plasmid expression.

### 2.2.5 Plasmid DNA isolation

DNA plasmids obtained through PCR mutagenesis have a low copy number, therefore plasmid amplification using competent cells is required. The DNA plasmid isolated from these competent cells can be used as template DNA in further PCR experiments, can be used as a vector in cloning experiments, and can be used for DNA sequencing. It can also be used for DNA transformation to further amplify plasmid or to cell lines for expression after confirming plasmid content through DNA sequencing.

Isolation of plasmid samples with high purity and high yield is crucial for downstream molecular biology and microbiology experiments. The plasmid isolation process involves growing competent cells containing plasmid of interest O/N at 37 °C followed by DNA isolation using a standard isolation kit and protocol<sup>17</sup>. The cell culture volume affects the amount of plasmid generated through isolation where the plasmid yield of a mini-prep (1 - 5 mL culture) can be up to 40 ug whereas a giga-prep (2.5 – 5L) can yield up to 15 mg<sup>18</sup>.

### 2.2.6 Plasmid DNA quality and quantity determination

Before utilizing isolated DNA for protein expression or downstream PCR mutagenesis, DNA quality indicators must be determined to gain insight about the integrity and quality. DNA absorbs UV-light at a wavelength of 260 nm therefore UV absorbance spectroscopy can be utilized for this process. Interestingly, RNA also absorbs UV radiation at 260 nm as well. The absorbance ratio between 260 nm and 280 nm ( $A_{260/280}$ ) provides insight to DNA purity.  $A_{260/280}$  value of 1.8 represents pure DNA, a value of 2.0 represents pure RNA, and  $A_{260/280} \leq 1.6$  can indicate the presence of proteins, phenols or other contaminants that absorb closer to 280 nm. The absorbance ratio between 260 nm and 230 nm ( $A_{260/230}$ ) is used to identify the contribution of solvent contamination to DNA impurity and as a secondary marker for DNA purity.  $A_{260/230}$  value of 2.0 – 2.2 represents pure DNA whereas  $A_{260/230} \leq 1.8$  indicates contamination due to proteins, guanidine HCl (used in DNA purification), phenols, carbohydrates and lipids<sup>19</sup>.

### 2.2.7 DNA sequencing

DNA sequencing is used to verify that the plasmid contains the correct gene of interest. Sequencing allows us to determine whether a mutation was successfully added to the gene of interest, whether unwanted mutations generated in the gene of interest that can later be corrected back to the WT, whether correct insertion of gene into the plasmid vector has occurred in cloning experiments. Gene sequencing industries use a version of Sanger sequencing where they anneal the amplified DNA to an oligonucleotide primer and then extend it using a polymerase using a mixture of dNTPs and chain terminating di-dNTPs (ddNTPs). By regulating the ddNTP concentrations, the chain elongations will selectively terminate yielding fragments that can easily be separated by gel electrophoresis and analyzed to obtain the DNA sequence of the DNA sample. Recently, a long-read sequencing methodology known as nanopore sequencing has been

introduced by industries which utilized nanometer size pores in a polymer membrane with an applied electrical current. As the DNA passes through the pore, the change in ion flux can be used as a marker thereby identifying DNA sequences without any fragmentation<sup>21,22</sup>. Our lab utilizes Azenta Life Sciences (South Plainfield, NJ) which uses Sanger sequencing or Plasmidsaurus (Eugene, OR) which uses long read sequencing technology.

#### 2.2.8 Analysis of DNA sequencing files

After analysis, Azenta Life Sciences provides the sequence file and the trace file whereas Plasmidsaurus provides the sequence file, trace file, and the plasmid map based on the sequence, which can be visualized using SnapGene<sup>23</sup>. The sequence file contains the gene sequence that was identified by analysis whereas the trace file provides a chromatogram which shows each base pair based on a specific color due to the unique fluorescence of each ddNTP. For sequence analysis, we use the gene sequence and obtain the corresponding amino acid sequence using ExPASy translate tool. This tool provides three (3) possible reading frames each for 5' to 3' and 3' to 5' ends. For sequence results obtained using Azenta Life Sciences, we study the 5' to 3' frames if we sent our isolated DNA plasmid with the forward primer of the WT template and 3' to 5' frames if the reverse primer is sent. For sequence results obtained from Plasmidsaurus, we study the 5' to 3' reading frames (Figure 2.4). The open reading frames present in the 5' to 3' (or 3' to 5') reading frames are used to obtain the amino acid sequence of the analyzed sample. This amino acid sequence is aligned with the WT amino acid sequence using NCBI Blast<sup>24</sup> to verify the presence of the introduced mutation(s) (Figure 2.5). If the sequence results indicate inadequate quality such as short open reading frames or protein fragmentation observed in plasmid maps, a repeat of the DNA isolation step or possible repeat of PCR experiment is recommended.

**5' Frame 2**

```

KKPPLPAVVCLPDQELPTLFPKVTGFSRAQIPNTVLLV-P-LGHHFKNSVAPPTYLALLLILLPVAAASGDKSCLTGLDSRR-LPDKAQR
SG-TGGSCQTPSLERTTYTELRYLQREL-ESATLPEGRKADRYPVSGRVGTGERTRELPGGNAWYLYSPVGFRLH-LERRFL-CSSGGR
SLWKNASNAAFRLFLAFCWPFAMHFFPALSPDSVDNRITAFE-ADTARRSRTERSESVSEEAERPIRKPPLPARWPIH-CSWHDRFP
DWKAGSERNAINV-S-LTH-A-PQALHFMLPARMLCGIVSG-QFHTGNSYDHDYEFLEFVSYVWTVTCYNL-HPLAGPVS--GIQCESGADA
QR-GKVR-LRYADTAIRWEVIIS-YLRYPSPKPEDLPANVASGSHHRVILMKPAASFFYCGCFTMIKKASLLTACSVTAFSAWAQDTSPC
TLVVVTANRFEQPRSTVLAPTTVVTRQDIDRWQSTSVNDVLRRLPGVDITQNGSGQLSSIIFIRGTNASHVLVLDIGVRLNLAGVSGSAD
LSQFPIALVQRVEYIRGPRSAVYGSDAIGGVVNIITTRDEPGTEISAGWGSNSYQNYDVSTQQQLGDKTRVTLGLDGYAHTHGYDVVAYG
NTGTQAOQTDNDGFLSKTYGALEHNFTDAWSGFVRGYGDNRNTYDAYSPGSPLLDTRKLYSQSWDAGLRYNGELIKSQLITSYSHSK
DYNYPHYGRYDSSATLDEMKQYTVQWANNVIVGHGSIGAGVWQKQTTTTPGTGYVEDGYDQRNTGIYLTGLQVGDFTFEGAARSDDN
SQFGRHGTQTSAGWEFIEGYRFIASYGTSYKAPNLGQLYGFYGNPNLDPEKSKQWEGAFEGLTAGVNWRIISGYRNDVSDLIDYDDHTL
KYNEGKARIKGVEATANFDTGPLTHTVSYDYVDARNAITDTPLLRRAKQVKYQLDWCLYDFDWGITYQYLGTRYDKDYSSYPYQTVK
MGGVSLWDLAVAYPVVTSHLTVRGKIANLFDKDYETVYGYQTAGREYTLSGSYTF-TTSHRAGV-LRRWVVGL-RDPQDGCGRHDRVVD
SGSK-RSEQDWAAAKAVQCSSENGCA-KLHQRI-R-QHAIVTGDAVGMDDIPQEARQYRHNQAYAYSIQDGAEDDDERIVRFHTRCLT
ALAI-L--TTALKLELGTGRRTTS-LGKFWRYPT-SPCSTSPFRQLA--RRGPHRSPFPTVAQPEWRMAPDAVFSFYASVRYFTPHMV
HSQYNLL-CRIVKPAPTANTR-RALTGLSAPGIRLQTSCDRLRELVSEVFTVITETRETKPRDTPPIIG-CHDNNGFLDVRWHFSG
KCARNPYLFIFLNTFKYVSAHETITLINASIILKKEEYEYSTFFPCRPYSLFCGILPSCFCSPRNAGESKRC-RSVGCTSGLHRTGSQQR
-DP-EFSPRTFSNDEHF-SSAMWRGIIPY-RRARATRSPHTLFSE-LG-VLTSHRKASYGWHDSKRIMQCCHNHE--HCGQLTSDNDR
RTEGANRFFAQHGGSCNSP-SLGTGAE-SHTKRRA-HHDACSNGNNVAQTINWRTYSSFPATINRLDGGG-SCRTTSALGPSGWLVYC
--IWSR-AWVSRYHCSTGARW-ALPYRSYLHDGESGNYG-TK-TDR-DRCLTD-ALVTVRPSLLIYTLD-FKTSFLI-KDLGEDPF--S
HDQNPLT-VFVPLSVRRRKDQRIFLRSFFSARNLLAN

```

Figure 2.4 Gene sequence of BtuB D6C-Q510C-D316A obtained from Plasmidsaurus translated to its corresponding amino acid sequence using ExPasy translate. 5' to 3' reading frame is considered and the open reading frame is highlighted in red.

(a) Query 1 MIKKASLLTACSVTAFSAWAQDTS~~P~~DLVVVTANRFEQPRSTVLAPTTVVTRQDIDRWQST 60  
Sbjct 11 MIKKASLLTACSVTAFSAWAQDTS~~P~~DLVVVTANRFEQPRSTVLAPTTVVTRQDIDRWQST 70

(b) Query 301 YGRYDSSATLDEM~~KQY~~TVQWANNVIVGHGSIGAGV~~DWQKQ~~TTTTPGTGYVEDGYDQRNTGI 360  
Sbjct 311 YGRYDSSATLDEM~~KQY~~TVQWANNVIVGHGSIGAGV~~AWQKQ~~TTTTPGTGYVEDGYDQRNTGI 370

(c) Query 481 IKGVEATANFDTGPLTHTVSYDYVDARNAITDTPLLRRAKQVKYQLDW~~Q~~LYDFDWGITY 540  
Sbjct 491 IKGVEATANFDTGPLTHTVSYDYVDARNAITDTPLLRRAKQVKYQLDW~~C~~LYDFDWGITY 550

Figure 2.5 Alignment of amino acid sequences of BtuB in the isolated plasmid (from ExPasy Translate) and WT BtuB (Uniprot ID P06129). The WT BtuB sequence is the “Query” whereas the mutated BtuB sequence is the “Subject.” We can observe successful mutations of (a) **D6** to **C6** (**D6C**) (b) **D316** to **A316** (**D316A**) (c) **Q510** to **C510** (**Q510C**). Note that the BtuB signaling

sequence (residues 1-20) is present in the sequencing results as it is only cleaved during protein expression.

## 2.3 Microbiological techniques

After verifying the point mutations introduced to the gene of interest through DNA sequencing, the vectors are transformed into suitable protein expression systems. There are many expression systems utilized for protein expression such as *E. coli* and insect cells. For this thesis work, *E. coli* expression systems were utilized. Microbiological techniques are utilized to introduce DNA vectors to the microbial expression systems and induce protein expression.

### 2.3.1 Importance of sterile techniques in microbiological experiments

A pervasive species such as microbes can easily contaminate materials and instruments utilized for microbiological experiments. This condition is known as “sepsis,” and preventive measures can be taken to avoid such contamination possibilities. These measures are known as “aseptic techniques,” and they can be as simple as disinfecting working area or minimizing the contact of nutrient containing liquid media and agar plates by the use of a sterile field created by the updraft of a Bunsen burner flame<sup>25</sup>. Remarkably effective sterilization techniques include autoclaving, oven sterilization, and filter sterilization. For materials and equipment that can withstand elevated temperatures, autoclaving or oven sterilization is recommended. Autoclaving is performed at hot temperatures (121 °C) and pressures (15 psi). The time of autoclave is dependent on the volume of media and the autoclaving load. For metal objects and glassware, a dry heat sterilization technique such as oven sterilization (121 °C – 170 °C) can be used up to about two (2) hours. For flammable and heat sensitive materials (antibiotics, sugars, amino acids), it is recommended to use filter sterilization using a 0.22 µm pore filter<sup>26</sup>.

### 2.3.2 Competent cells

Competent cells possess the ability for direct incorporation of foreign DNA with high efficiency. Cells that are less competent (most common *E. coli* strains) must be upgraded to a high competency state to achieve efficient DNA incorporation. Therefore, *E. coli* cells are first converted to a more competent state and genes of interest are introduced through DNA transformation. Heat shock treatment and electroporation are the two main approaches utilized for DNA transformation. Depending on the method of DNA transformation, preparation of competent cells can vary. For this thesis work, heat shock treatment-based DNA transformation was used, therefore cell competency was upgraded to specifically account for this treatment.

### 2.3.3 Preparation of competent cells

Proper use of sterile techniques is crucial to obtain competent cells with high efficiency and negative contamination as antibiotics are not utilized in the process of preparation. It is always preferred to use a single-cell colony (SCC) from a freshly streaked antibiotic free plate for the small-scale pre-culture (5 - 10 mL) grown O/N. The main-culture (usually about 200ml) is inoculated with the pre-culture at 1:100 ratio and grown until mid-log phase ( $OD_{600}$  around 0.4 – 0.6). It is vital to harvest cells before they reach late-log early-stationary phase to ensure good health of bacteria for efficient transformation<sup>27</sup>. Following cell harvest, cell preparation is varied based on the DNA transformation method and all protocols are followed in ice. For electroporation-based transformation protocol, cells are washed with ice-cold water to remove any possible components that can interfere with electroporation, resuspended in 10% glycerol, and stored at -80 °C until transformation. For heat-shock based transformation protocol, cells are first incubated with 100 mM  $MgCl_2$ , then with 100 mM  $CaCl_2$  in 15% glycerol and stored at -80 °C in 50  $\mu$ L aliquots until transformation. The incubation with  $MgCl_2$  and  $CaCl_2$  neutralizes the negative charge of the



phospholipid bilayer allowing the DNA to migrate closer to the cell and it also increases membrane permeability<sup>27</sup>. The shelf life of competent cells at -80 °C is about 6 – 12 months, after which time their competency is reduced.

#### 2.3.4 DNA Transformation through heat-shock treatment

Competent cell viability is crucial to maintain during the transformation process to achieve successful incorporation of the gene of interest into the cell. Therefore, all reactions and procedures are performed on ice. First the competent cells are thawed on ice, isolated DNA is introduced (minimum of about 100 ng) into the cells. The mixture is gently mixed by tapping and allowed to incubate on ice for 30 mins. For heat shock treatment, the cells are incubated at 42 °C for 30 – 45 s and quickly incubated on ice for at least 2 mins (Figure 2.6). This process allows the isolated DNA to permeate through the cell membrane into the cell without cellular destruction<sup>28</sup> (Figure 2.7a). Electroporation involves providing a short-term high voltage electric field which induces short-term membrane pores to uptake DNA into cell<sup>29</sup>.

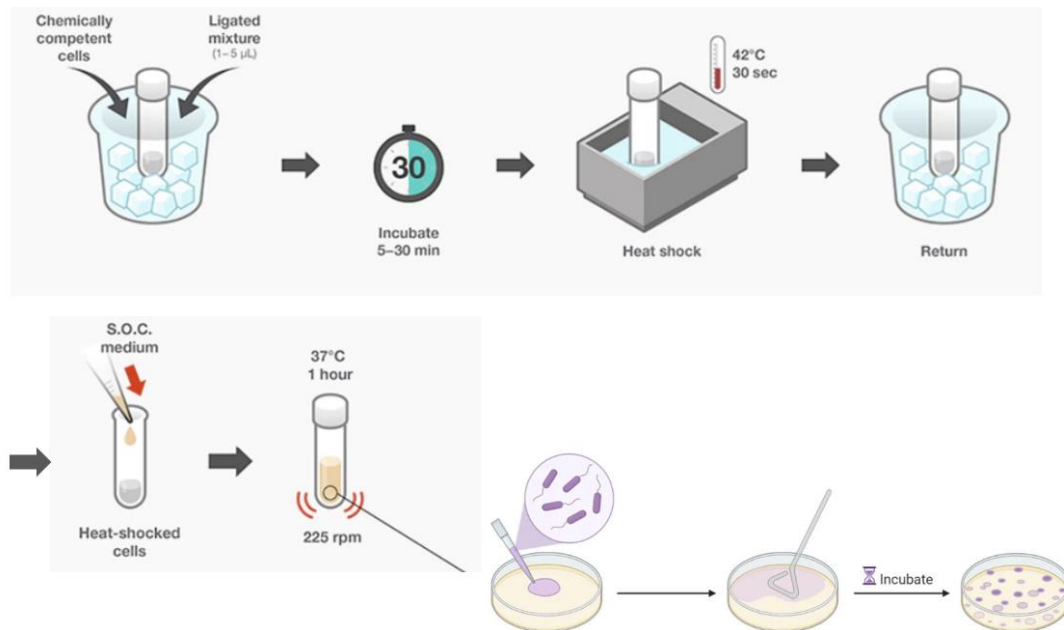


Figure 2.6 DNA transformation through the heat shock method. The steps involve DNA introduction to competent cells followed by incubation, heat shock treatment, secondary incubation, recovery using super optimal broth with catabolite repression (SOC) media and plating in LB agar plate containing specific compounds to identify successfully transformed cells (Ex: pAG1 plasmid encoding *btuB* gene consist of an ampicillin resistant gene (AmpR) therefore plated in LB agar containing 100 ug/mL ampicillin plates). Figures are taken from [https://static.igem.org/mediawiki/2021/c/c7/T--UPF\\_Barcelona--heat-shock\\_transf.pdf](https://static.igem.org/mediawiki/2021/c/c7/T--UPF_Barcelona--heat-shock_transf.pdf) (Accessed on 23<sup>rd</sup> May 2024) and <https://microbenotes.com/spread-plate-technique/> (Accessed on 23<sup>rd</sup> May 2024).

After heat shock treatment, the cells are allowed to recover by growth in antibiotic free media, which initiates cellular reproduction and plasmid amplification (Figure 2.7b). During the recovery step, SOC Media containing 0.5% yeast extract, 2% tryptone, 10 mM NaCl, 2.5 mM KCl, 10 mM MgCl<sub>2</sub>, 10 mM MgSO<sub>4</sub> and 20 mM glucose is added and incubated at 37 °C shaking at 225 rpm for about one (1) hour. Finally, a portion or complete cell sample is plated in a LB agar plate containing antibiotic(s) to obtain successfully transformed cells<sup>28</sup> (Figure 2.6).

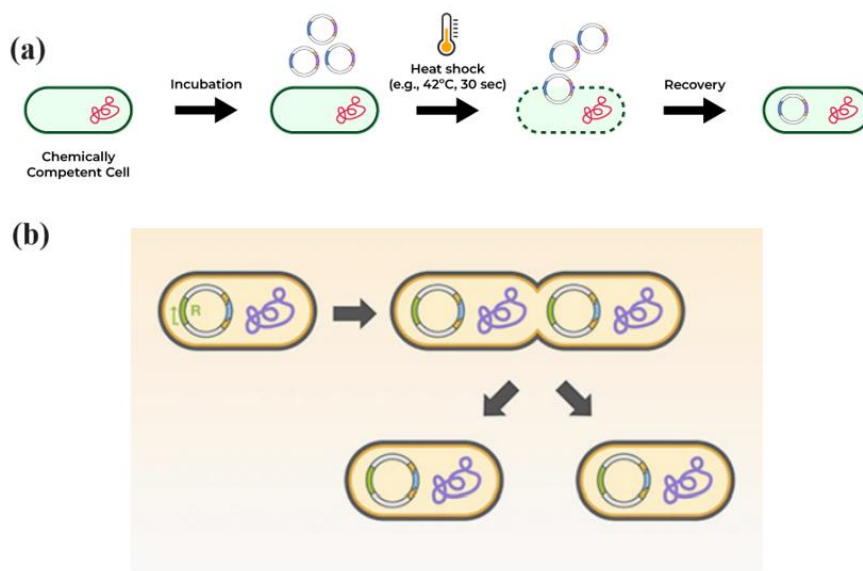


Figure 2.7 Cellular processes involved in DNA transformation. (a) After DNA introduction and incubation, heat shock treatment induces membrane permeability of DNA into the cell. (b) During the recovery step, cellular reproduction results in DNA amplification thereby production of cells resistant to antibiotic (Ex: pAG1 plasmid amplification results in cells resistant to ampicillin). Figures are taken from <https://www.geeksforgeeks.org/cbse-class-12-biotechnology-principles-and-processes-competent-host-for-transformation-with-recombinant-dna/> (Accessed on 23<sup>rd</sup> May 2024) and [https://static.igem.org/mediawiki/2021/c/c7/T--UPF\\_Barcelona--heat-shock\\_transf.pdf](https://static.igem.org/mediawiki/2021/c/c7/T--UPF_Barcelona--heat-shock_transf.pdf) (Accessed on 23<sup>rd</sup> May 2024).

### 2.3.5 Preservation of bacterial strains for long term use

Cryoprotectants such as glycerol can be used to preserve bacterial cells for long term use at  $-80\text{ }^{\circ}\text{C}^{30}$ . For subsequent protein expression and purification, bacterial cells which encode our gene of interest are grown starting from a SCC obtained from an agar plate. There are two ways of approaching this stage. One is to perform a DNA transformation each time, and the other is to prepare a bacterial stock (glycerol stock) for the mutant protein(s) of interest followed by storage

of the stock for future use. Creating stock eliminates the step of DNA transformation to competent cells each time the expression of a specific mutant protein of interest is required. These stocks can last several years and can be used at any point, therefore ensuring aseptic techniques during glycerol stock preparation is vital to avoid possible contamination.

Glycerol stock preparation begins with inoculating a small culture in the presence of antibiotic (around 5 mL LB media with 100 µg/mL ampicillin for BtuB mutants and with extra 25 µg/mL of chloramphenicol for FecA in *dsbA*<sup>-</sup>/pTARA) with a SCC from an agar plate containing mutant protein cells of interest and growing at optimum growth temperature (37 °C for *E. coli*) until mid-log phase where the cells are healthy and active (about 5 - 6 hr). Aliquot 500 µL of cell culture to a sterile cryovial tube with screw cap, mix with a 1:1 ratio of 50% glycerol (500 µL), and store it at -80 °C. It is important to ensure that the stock does not thaw out while using for inoculation at room temperature to ensure viability. Thus, whenever glycerol stocks are being used, it should be transported and kept in dry ice to avoid thawing.

For this thesis work, mutants in BtuB verified by sequencing were transformed to *E. coli* RK5016 and *dsbA*<sup>-</sup> cells. Sequence verified FecA mutants were transformed to *E. coli* BL21(DE3), *dsbA*<sup>-</sup>, and *dsbA*<sup>-</sup>/pTARA (*dsbA*<sup>-</sup> cell line with previously introduced pTARA plasmid encoding T7 RNAP) cells. SCCs from an agar plate was used to make glycerol stocks and stored at -80 °C for future use.

### 2.3.6 Laboratory methods for growing bacteria

There are many ways in which bacteria can be grown in the laboratory. This can include growing in solid agar media, in a semi-solid agar media where there is a significant decrease in agar percentage, and in a liquid media. It is critical to select the media containing the necessary

nutrients required for proper bacterial protein expression and propagation. Cell lines with specific marker genes such as antibiotic-resistant genes should be grown in the presence of the relevant antibiotic apart from the other required nutrients and vice versa.

### 2.3.6.1 Plating techniques for bacterial cultures

Isolating SCCs requires bacterial cultures to be grown on solid or semi-solid agar-based media with the essential nutrients and selective reagents to identify cells incorporation the genes of interest. For this purpose, LB media-based agar plates containing 1% tryptone, 0.5% yeast, 1% NaCl and 2% Agar are used. SCCs can be obtained from culture media by spreading evenly on a plate. SCCs can also be obtained from a streaked plate using a glycerol stock or by restriking a SCC from a spread plate<sup>25</sup> (Figure 2.8).

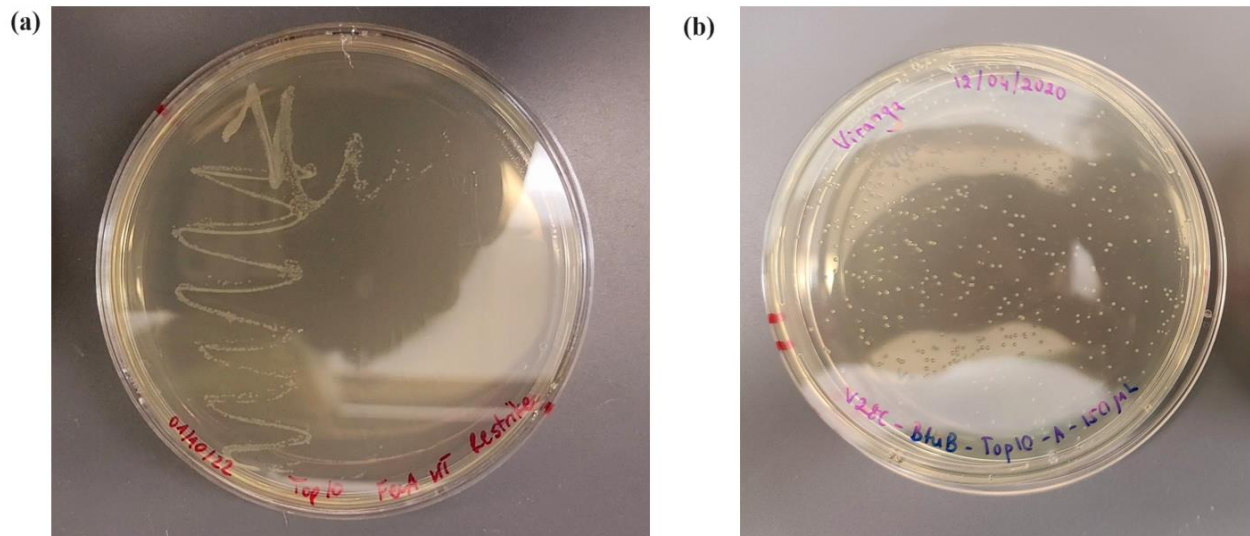


Figure 2.8 Various plating techniques of bacterial cultures on agar plates. (a) A streaked plate from a glycerol stock or restrike of a SCC (b) An evenly spread plate using liquid bacterial culture.

### 2.3.6.2. Cell culturing methods

For protein expression and purification purposes, cells are grown in liquid cultures. There are three methods to grow bacterial cells for various applications. They are batch cultures, semi fed-batch culture, and few-batch culture. For this thesis work, batch cultures were utilized. Furthermore, different culture media was used to grow cells depending on their ultimate application. To amplify DNA plasmids, prepare competent cells, and to express proteins in the presence of nutrient rich conditions, LB media was used. However, for protein expression under the absence of certain nutrients, media that satisfy the minimum conditions required for cell growth was utilized. This is called minimal (M9) media and was extensively used to over express BtuB and FecA in the absence of vitamin B<sub>12</sub> and ferric citrate, respectively. M9 media is composed of 100 mM phosphate buffer, 8 mM (NH<sub>4</sub>)<sub>2</sub>SO<sub>4</sub> and 2 mM sodium citrate. The nutrients added to complete the media for cell culture growth were 0.2% w/v glucose, 0.1% w/v methionine, 0.1% w/v arginine, 150mM thiamine hydrochloride, 3 mM MgSO<sub>4</sub>, and 300 mM CaCl<sub>2</sub>. Both FecA and BtuB gene containing plasmids contains the AmpR gene therefore the cells were grown in the presence of 100 mg/mL ampicillin. For this thesis, *in-vitro* cell culture work was performed using 1 L of 1X M9 cultures whereas *in-vivo* experiments were done using 250 mL of 1X M9 cultures.

During *in-vitro* preparations, the preculture was inoculated with a SCC or a portion of a glycerol stock and grown O/N in a shaking incubator at 37 °C (optimum temperature for *E. coli* growth). The main cultures were inoculated with the preculture and grown at 37 °C in a shaking incubator and inducing agents were added for protein overexpression. The incubation temperature can be reduced to avoid protein aggregation in cells when it is required but plasmids with leaky promoters will continue to grow during the complete growth time regardless of the temperature.

After adequate cell density is present, cells are harvested by pelleting and used for protein purification and downstream experiments.

## 2.4 Biophysical and biochemical techniques

### 2.4.1 Protein overexpression and purification

In general, *E. coli* is the most widely used expression system for proteins as it exhibits rapid growth capabilities therefore massive quantities of proteins are produced. However, it is important to understand that proteins with possible post-translational modifications (PTMs) are best expressed in mammalian or yeast cell vectors as they have the enzymatic machinery that may be required to add these modifications. Also, *E. coli* vectors could express proteins that are non-native and potentially toxic to the bacteria, therefore cell viability should be monitored during the expression, and the expression regulated if necessary to ensure the survival of the cells during protein synthesis. To overcome this situation, genes can be encoded with repressors to inhibit growth of several proteins until proper induction takes place, or signaling sequences may be introduced that direct protein insertion into the periplasm. Proteins that require disulfide crosslinking enter the periplasmic space where the oxidation of cysteines is conducted by the Dsb system (Chapter 1), and OMPs need to be translocated to the periplasm to be chaperoned to the OM for folding and insertion through the BAM complex (Chapter 1). Furthermore, an uninduced protein expression system for OMP expression is recommended as accelerated expression of OMPs can affect the OM biogenesis<sup>31,32</sup>.

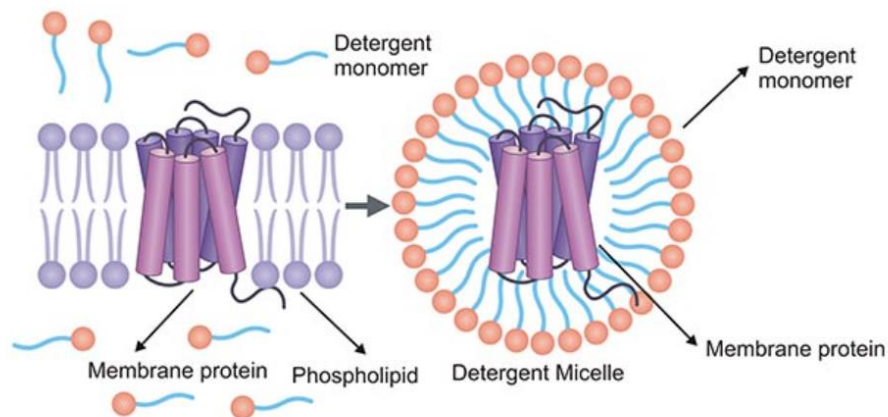


Figure 2.9 Membrane solubilization and membrane protein isolation using detergents. Detergents can disrupt the membrane composition thereby releasing the membrane protein from its bilayer environment into a detergent micelle where it can reside through interactions between the protein and the hydrophobic tails of detergent monomers. Figure was taken from <https://www.cusabio.com/Transmembrane/The-Nature-of-Detergent-and-Its-Application-in-Membrane-Proteins.html> (Accessed on 24th May 2024)

For this thesis work, primary attention was given to study OMPs in an isolated system (*in-vitro*) where protein purification is mainly governed by the individual properties of the target protein such as its charge, size and affinity. Soluble proteins can easily be obtained and purified from the cell lysate after cell lysis and removal of cellular debris. For membrane proteins (OM and IM), the membrane responsible for harboring the protein of interest must be first be isolated and detergents may then be required to solubilize the membrane and purify the protein of interest. Detergents form micelles in which these proteins can reside throughout the purification process (Figure 2.9).



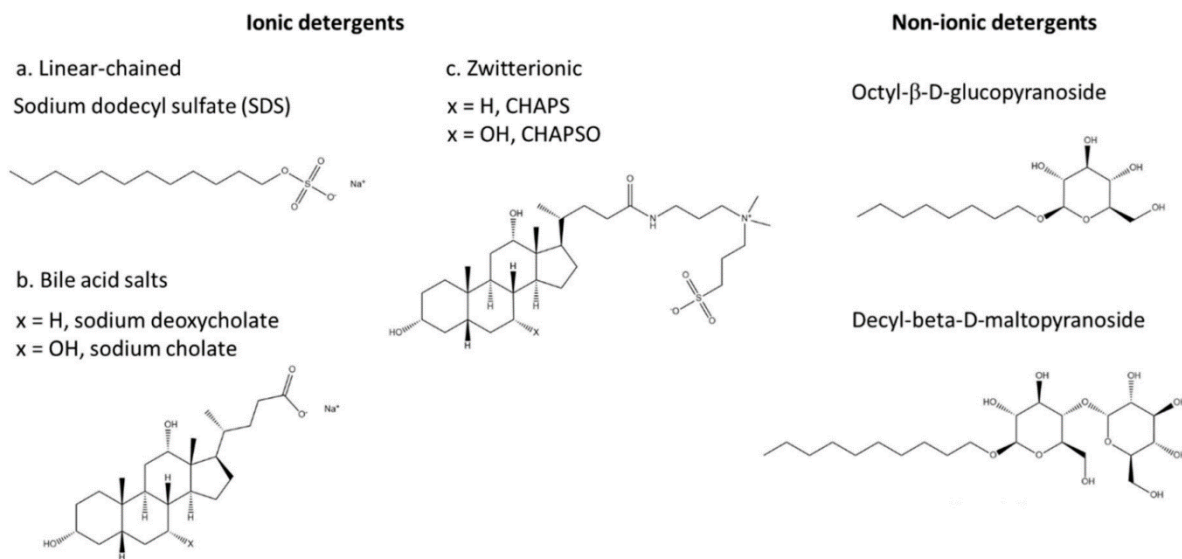


Figure 2.10 Structures of distinct types of detergents. Detergents can be ionic or non-ionic. Ionic detergents can break down to linear-chained, zwitterionic or bile acid salts. Figure was taken from Danko, K., Lukasheva, E., Zhukov, V. A., Zgoda, V., & Frolov, A. (2022). Detergent-Assisted Protein Digestion-On the Way to Avoid the Key Bottleneck of Shotgun Bottom-Up Proteomics. *International journal of molecular sciences*, 23(22), 13903.

There are two (2) main categories of detergents. They are (i) ionic and (ii) non-ionic detergents. Ionic detergents can be further categorized as (a) linear-chained (b) zwitter-ionic and (c) bile acid salts (Figure 2.10). The type of detergent used should be based on the target protein for purification. Strong ionic detergents such as sodium dodecyl sulphate (SDS) can sometimes denature proteins whereas detergents such as n-octyl-β-D-glucopyranoside are mild or non-denaturing and can solubilize membrane proteins without inducing structural deformities<sup>33,34</sup>. Once the proteins are solubilized using detergents, they can be purified using chromatographic techniques.

There are many types of chromatographic techniques that can be used to purify proteins. Proteins can be purified through (i) size-exclusion chromatography where proteins are separated

by size, (ii) chromatofocusing where proteins are purified based on their iso-electric point (pI), (iii) affinity chromatography where protein purification utilize reversible binding of proteins to immobilized ligands, and (iv) ion-exchange chromatography where protein isolation is performed based on the surface charge at a given pH point. For this work, affinity chromatography was used to purify His<sub>6</sub> tag TonB (103-239) fragment and ion-exchange chromatography to purify BtuB and FecA.

In affinity chromatography, DNA vectors containing affinity tags (Ex: 6xHis tags) introduced to the protein of interest can aid late-stage protein purification steps significantly. Separate types of resins are available based on the tag introduced to the protein of interest: (i) Maltose binding proteins (MBP) tag-based proteins can be purified using amylose resins, (ii) Glutathione transferase (GST) tag-based proteins can be purified using glutathione resins, (iii) and His-tag based proteins can be purified using metal-based resins such as Ni<sup>2+</sup> (Ni<sup>2+</sup>-nitrilotriacetic acid or Ni<sup>2+</sup>-NTA), Co<sup>2+</sup>, or Cu<sup>2+</sup> (Figure 2.11). Here, after His tag protein is bound to the resin and unwanted proteins are removed through a wash step, addition of a competing chelating agent such as imidazole will result in the release of His-tag protein from the resin, which can then be eluted. These tags can later be cleaved (Ex: TEV protease for His tag removal from proteins) after purification to obtain a tag-free protein for downstream experiments<sup>35</sup>. An alternate method to avoid the extra step of tag removal can be achieved using an intein-mediated purification with an affinity chitin-binding tag (IMPACT). Once the tag associated protein is bound to chitin resin, a thiol containing reagent (DTT) or pH adjustment from 8.5 to 6.0 will result in the cleavage of protein from the tag and eluted<sup>36</sup>.

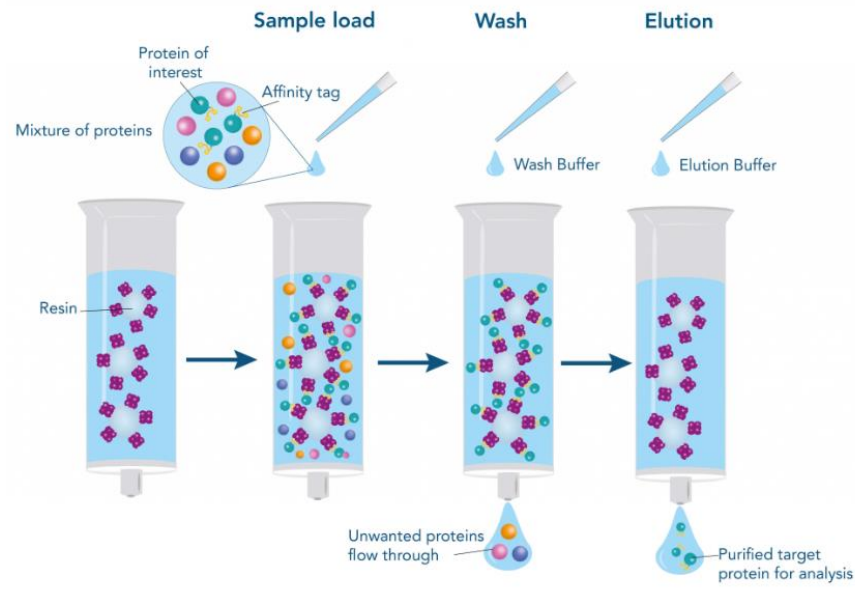


Figure 2.11 Schematic diagram of affinity chromatography. **Target protein** with **affinity tag** is bound to the **resin**. Additional washes with wash buffer remove the unwanted proteins and elution buffer elutes target protein purified from unwanted proteins. Figure was taken from <https://www.iba-lifesciences.com/applications/protein-affinity-chromatography/> (Accessed on 24<sup>th</sup> May 2024)

In ion chromatography, surface charge of the purifying protein of interest becomes the key factor in the purification process. When the pH of the buffer is higher than the pI of the protein, the protein will have a net negative charge and will bind to positively charged resins for anion-exchange based purification, whereas at a pH lower than pI of the protein, the protein will have an overall positive charge and will bind to negatively charged resins for cation-exchange based purification (Figure 2.12).

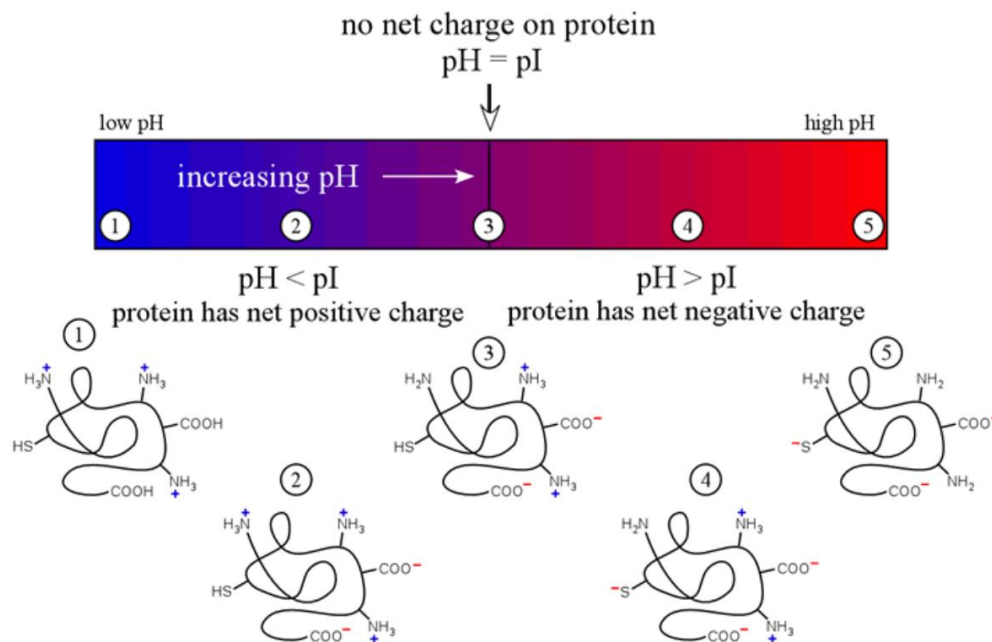


Figure 2.12 protein net charge variability with pH of the environment. pH < pI will result in net positive charge on protein of interest whereas pH > pI will result in net negative charge of the protein of interest. pH = pI will result in net zero charge of the protein of interest. Figure was taken from [https://guweb2.gonzaga.edu/faculty/cronk/CHEM245pub/protein\\_methods.html](https://guweb2.gonzaga.edu/faculty/cronk/CHEM245pub/protein_methods.html) (Accessed on 24th May 2024)

The overall net charge of protein for ion-exchange chromatography is decided based on the overall stability of the protein of interest and other proteins present in the sample. For BtuB and FecA purification, anion-exchange chromatography was used where there is a net negative charge on the proteins of interest. The most used resins for anion exchange chromatography are quaternary ammonium salt (Q) resins or diethylaminoethyl (DEAE) resins whereas sulfopropyl (S) and carboxymethyl (CM) resins are commonly used for cation exchange chromatography<sup>37</sup>. Q and S are strong ion-exchange resins with a wide pH range whereas DEAE and CM are weak ion exchange resins with narrow pH range. The elution profile of BtuB and FecA purification through

anion exchange involves the introduction of the protein sample to the resin followed by initial elution of unbound protein and introduced spin label in the flowthrough by addition of wash buffer. Introduction of elution buffer containing high salt (NaCl) concentration gradient induces protein elution where salt anions ( $\text{Cl}^-$ ) replace bound protein (Figure 2.13). The purified BtuB and FecA in OG micelles are then introduced to lipid vesicles through reconstitution.

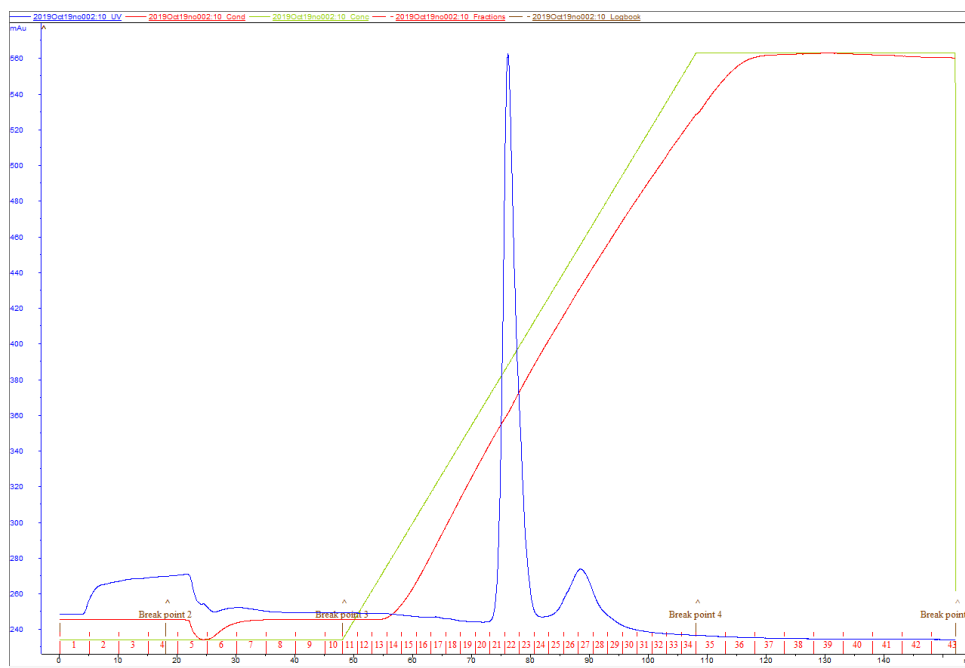


Figure 2.13 Elution profile of spin labelled D6C-Q510C (D6R1-Q510R1) using anion-exchange fast-protein liquid chromatography (FPLC). The **UV absorbance** trace indicates the elution profile where initial increase in absorbance is due to unwanted proteins and unbound spin label being released from the column. When the **elution buffer** is introduced in a gradient up to 100% and increase in the **conductance** trace is observed as well as the elution of bound protein from the resin.

## 2.4.2 Membrane protein reconstitution from detergent into lipid systems

Protein reconstitution into lipid-based system is performed by replacing the detergent molecules in micelles incorporating proteins of interest with lipid molecules. Lipids have similar architecture to that of detergents where they are composed of a hydrophilic head group and a hydrophobic tail group. The structural features of the lipid tail group govern the overall packing thereby the rigidity/fluidity properties of lipid membranes (Figure 2.14).

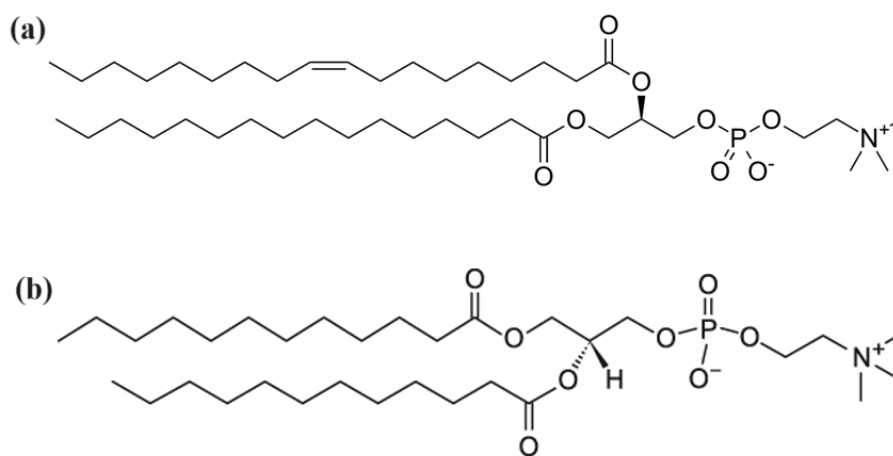


Figure 2.14 Structures of reconstitution lipids. (a) 1-palmitoyl-2-oleoyl-sn-glycero-3-phosphocholine (POPC) and (b) 1,2-dilauroyl-sn-glycero-3-phosphocholine (DLPC). Liposomes created by POPC are tightly packed whereas more fluidic liposomes are formed with DLPC. Structures were taken from <https://avantilipids.com/> (Accessed on 24<sup>th</sup> May 2024).

There are multiple lipid systems that can be used to study membrane proteins such as lipid monolayers, supported lipid bilayers, liposomes and nano-discs<sup>38</sup> (Figure 2.15). To introduce proteins into lipid systems, either direct incorporation of protein to liposomes or detergent mediated approach to introduce proteins to liposomes can be followed. The detergent mediated approach involves an initial step of lipid solubilization in detergent to create a homogeneous

detergent/lipid mixture. This mixture is added to the protein-detergent mixture to form an isotropic protein-lipid-detergent solution.

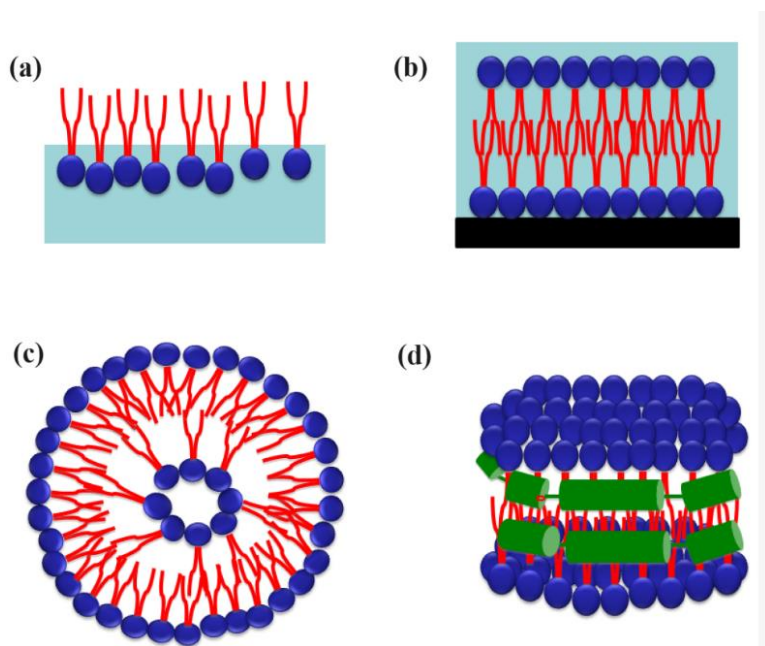


Figure 2.15 Different types of lipid-based systems. (a) lipid monolayer (b) supported lipid bilayer (c) liposome (d) lipid nano-disc. Figure was taken from Shen, H. H., Lithgow, T., & Martin, L. (2013). Reconstitution of membrane proteins into model membranes: seeking better ways to retain protein activities. *International journal of molecular sciences*, 14(1), 1589–1607.

Next step is the removal of detergent from protein-lipid-detergent solution to allow protein-lipid interactions to take place and construct proteoliposomes. This state can be achieved either by diluting the sample solution to decrease the detergent concentration below its critical micelle concentration (CMC) so that detergent micelles will be disrupted allowing the lipids to interact with proteins or to perform a gradual removal of detergent from the solution mixture allowing lipids to form liposomes and incorporate proteins<sup>39</sup>.

Dialysis, chromatographic techniques, and adsorption to hydrophobic resins are methodologies that can be utilized to gradually remove detergents and induce proteoliposome formation. For detergents with high CMC, dialysis is recommended whereas for low CMC detergents, bio-beads (hydrophobic resins) are recommended (Figure 2.16). Dialysis involves performing a buffer exchange using detergent-free buffer during a scope of multiple days to fully remove detergent from the sample mixture as it requires ample time for detergent equilibration with the buffer. Removal of detergents using bio-beads is a rapid process. Once the detergent removal is complete, the beads can be removed from the sample mixture by filtration or centrifugation<sup>40</sup>.

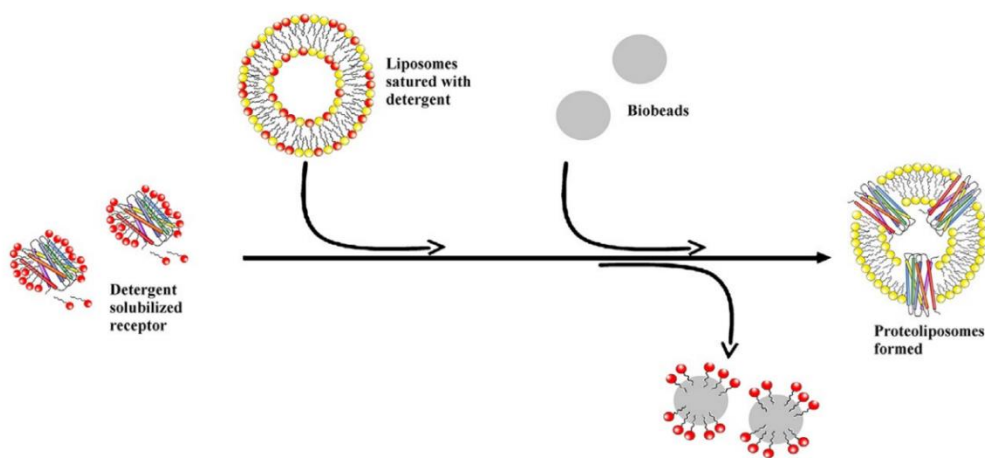


Figure 2.16 Detergent based lipid reconstitution of membrane proteins. Proteins dissolved in detergent micelles are introduced with a lipid-detergent mixture followed by removal of detergent by bio-beads or dialysis (or both) to induce proteoliposome formation. Figure was taken from Goddard, A. D., Dijkman, P. M., Adamson, R. J., dos Reis, R. I., & Watts, A. (2015). Reconstitution of membrane proteins: a GPCR as an example. In *Methods in enzymology* (Vol. 556, pp. 405-424). Academic Press.



## 2.5 EPR spectroscopy as a tool to examine protein systems

X-ray crystallography, Cryo-Electron Microscopy (Cryo EM), circular dichroism (CD), isothermal calorimetry (ITC), nuclear magnetic resonance (NMR), hydrogen-deuterium exchange mass spectrometry (HDX-MS) are a few of the many techniques that are utilized to study structural and functional properties of proteins in the molecular and atomic level<sup>41</sup>. However, size limitations and stability concerns in different native and non-native lipid systems have limited the application of some techniques for certain biological and biomolecular studies. In contrast, recent improvements in electron paramagnetic resonance (EPR) techniques have allowed one to perform experiments on large biomolecules such as membrane proteins, protein complexes, and soluble proteins with high accuracy<sup>42,43</sup>. Unlike techniques such as high-resolution NMR, EPR does not require that the macromolecule rapidly tumble on the spectroscopic time scale, thereby overcoming any size limitation. The method detects paramagnetic centers, which are exceedingly rare in biological systems, which are selectively introduced into the protein. Therefore, methodologies have been devised to introduce artificial paramagnetic centers to the system so they can be studied without any background interference due to native paramagnetic entities in system<sup>44</sup>.

In the EPR field known as spin-labeling, paramagnetic centers are introduced into proteins of interest, and this can be performed using several approaches. These include: (i) Site-directed spin labeling (SDSL), where a residue of interest can be converted to cysteine and then reacted with a thiol specific spin-label<sup>45</sup>. If the protein of interest contains reactive native cysteines, the cysteines must be converted to alanine or serine (structurally similar to cysteine) to avoid background labeling and to ensure conservation of structural features due to DNA mutation. (ii) Spin labeling through click-chemistry approaches<sup>46</sup>. (iii) Intein-mediated protein ligation (IPL)

approach to synthesize protein fragments containing EPR sensitive spin labels<sup>47</sup>. (iv) Unnatural amino acid mutagenesis to incorporate an amino acid which is photoactivatable or can be fluorescently labeled. *E. coli* biosynthetic machinery was found to tolerate synthesis of unnatural amino acids which resembles natural amino acids<sup>48</sup>. This thesis utilized SDSL where BtuB and FecA sites of interest were converted to cysteine using site-directed mutagenesis at the DNA stage, followed by expression in a suitable vector and protein purification and finally spin labeled using EPR specific thiol containing label which can crosslink with cysteine in protein to attach spin label to the site of interest.

Spin labeling generally involves the use of nitroxide spin labels, which may have a number of different functional groups (Figure 2.17) where the paramagnetic center ( $R_2NO$ ) resides on the nitroxide bond<sup>49</sup>. Methanethiosulfonate (MTSL) (R1) is the most commonly used nitroxide spin label for EPR experiments due to its smaller size, its structural resemblance to tryptophan, its high reactivity and selectivity to thiol containing residues (cysteines) (Figure 2.18). Spin label attached EPR spectroscopy provides insight into local secondary structure and tertiary interactions<sup>50</sup> (Figure 2.19) and dynamics of protein backbone such as different conformational states present in protein structure. Proteins with more than one spin label can be used in pulse EPR experiments where the distance between two spins can be measured if it is in the range of 20 – 80 Å. The spin labeling step involves the addition of excess spin label so that all cysteines are derivatized with spin label followed by removal of excess spin label through a washing step(s). Then, the spin labeled proteins are prepared for CW and/or pulse EPR experiments.

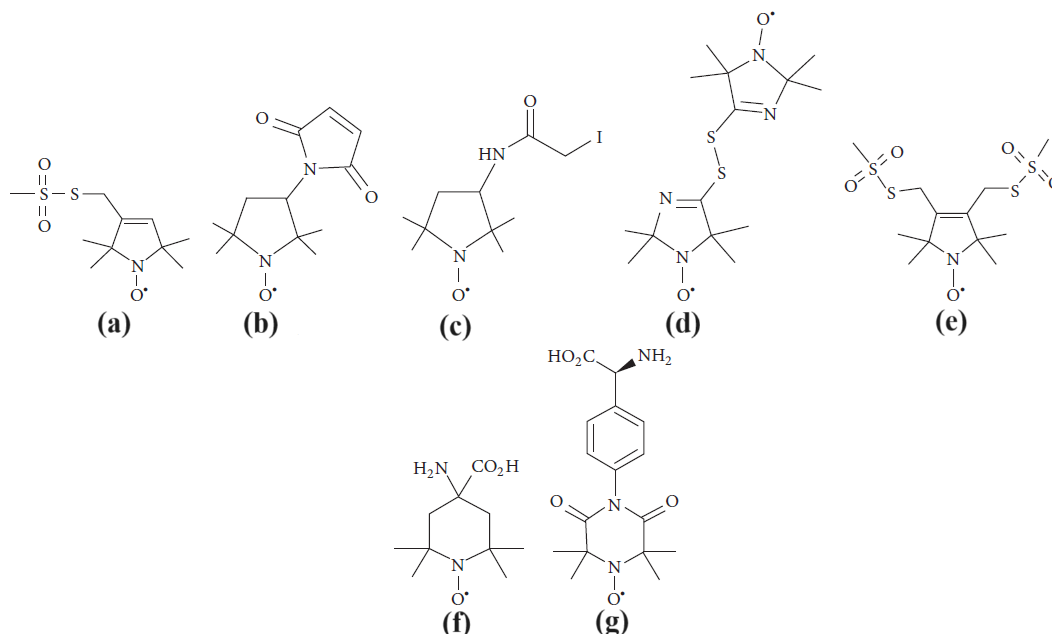


Figure 2.17 Different types of spin labels used for EPR experiments. (a) S-(1-oxyl-2,2,5,5-tetramethyl-2,5-dihydro-1H-pyrrol-3-yl)methyl methanesulfonylthioate (MTSL) (R1 Label). (b) Maleimide spin label (MSL) N-(1-oxyl-2,2,6,6-tetramethyl-4-piperidinyl)maleimide (MAP Label). (c) Iodoacetamide spin label (ISL) 3-(2-iodoacetamido)-2,2,5,5-tetramethylpyrrolidine-1-oxyl (Iodoacetamido PROXYL) (IAP Label). (d) bis(1-oxyl-2,2,5,5-tetramethyl-3-imidazolin-4-yl) disulfide (IDSL) (V1 Label). (e) bifunctional spin label (BSL) (RX Label), (f) 2,2,6,6-tetramethyl-N-oxyl-4-amino-4-carboxylic acid (TOAC), and (g) 4-(3,3,5,5-tetramethyl-2,6-dioxo-4-oxypiperazin-1-yl)-l-phenylglycine (TOPP). Figure was taken from Sahu, I. D., & Lorigan, G. A. (2018). Site-Directed Spin Labeling EPR for Studying Membrane Proteins. *BioMed research international*, 2018, 3248289.

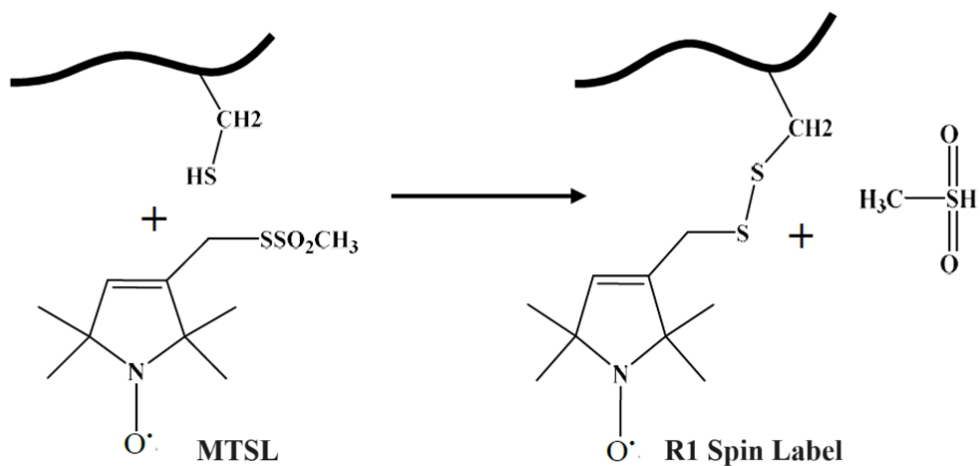


Figure 2.18 Spin labeling process during MTSL introduction. The methanesulfothionate group of MTSL reacts with the thiol group of cysteine to create a disulfide crosslink between MTSL and Cys to create R1 spin label. Figure was taken from Nilaweera, T. D. (2018). Exploring BtuB in *Escherichia coli* via a new direct spin labeling approach and electron paramagnetic resonance spectroscopy (Doctoral Thesis Dissertation). University of Virginia, Charlottesville, USA.

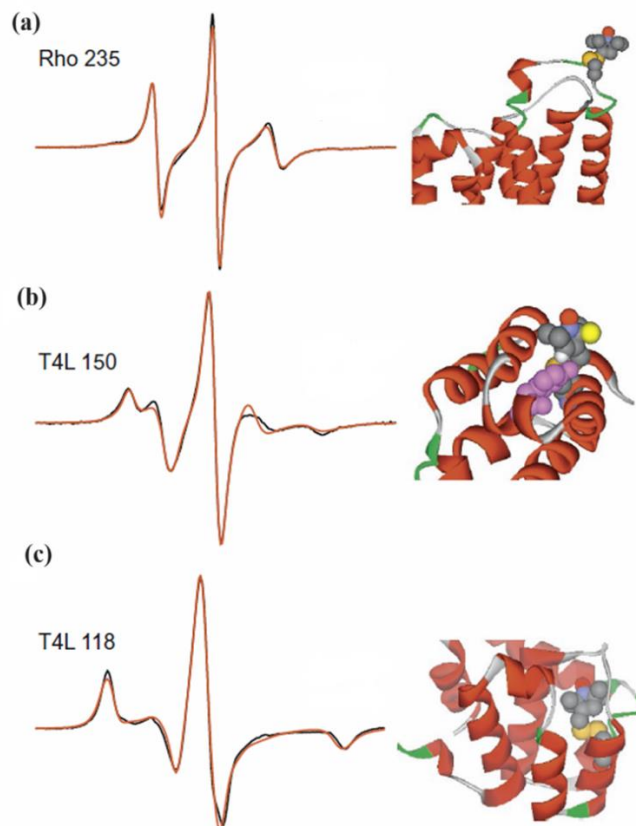


Figure 2.19 Variations in spin label behavior as a function of protein secondary/tertiary structure. (a) Highly mobile spectra observed for highly disordered portion of Rhodopsin. (b) H-bond interaction with a nearby tyrosine reduces spin label mobility at site 150 of T4L (c) An immobilized line shape observed for spin label buried inside the protein backbone at site 118 of T4L. Figure was taken from Altenbach, C., Lopez, C. J., Hideg, K., & Hubbell, W. L. (2015). Exploring structure, dynamics, and topology of nitroxide spin-labeled proteins using continuous-wave electron paramagnetic resonance spectroscopy. In *Methods in Enzymology* (Vol. 564, pp. 59-100). Academic Press.

### 2.5.1 Basics of EPR

For an explanation of fundamental EPR concepts, a basic single electron system can be used. EPR is used to measure energy differences between discrete energy levels, which result from

the interaction of an electron magnetic moment with an external magnetic field. An isolated electron in a force-free environment behaves as if it is spinning; it has an intrinsic angular momentum denoted as “spin” (S) (Figure 2.20a). Because it is charged, this angular momentum results in an induced dipolar magnetic field with a magnetic moment ( $\mu$ ) given by,

$$\mu = h\gamma_e S = -g\beta_e S \quad (\text{Eq 2.1})$$

where  $h$  is the planck constant ( $6.62607015 \times 10^{-34}$  J/Hz),  $\gamma_e$  is the electron gyromagnetic ratio,  $\beta_e$  is the Bohr magnetron ( $\beta_e = e\hbar/2m_e$  where the reduced planck constant  $\hbar = h/2\pi$ ,  $m_e$  and  $e$  are the mass and charge of an electron respectively) ( $\beta_e = 9.274 \times 10^{-24}$  J/T), and  $g$  is the electronic g-factor. For a free electron, the g-value ( $g_e$ ) is exactly 2.0023193043617(15) computed with the assistance of quantum electrodynamics<sup>51</sup>.

#### 2.5.1.1 Electron Zeeman Interaction

When a free electron is exposed to an external magnetic field ( $B_o$ ), energy state splitting occurs due to the *Zeeman Effect*. This results in the formation of two energy states depending on the electron spin quantum number ( $m_s$ ) (Figure 2.20b). The paramagnetic electron will experience a low energy state when the magnetic moment aligns ( $m_s = -1/2$ ) with the applied magnetic field, and a high energy state when the moment lies against ( $m_s = +1/2$ ) the applied field (Figure 2.20c). The difference between the energy states depends on  $B_o$  and it is given by,

$$E = \mu \times B_o = g\beta_e m_s B_o \quad (\text{Eq 2.2})$$

$$E_{+1/2} = 1/2g\beta_e B_o \text{ and } E_{-1/2} = -1/2g\beta_e B_o \text{ therefore,}$$

$$\Delta E = E_{+1/2} - E_{-1/2} = 1/2g\beta_e B_o - (-1/2g\beta_e B_o) = g\beta_e B_o$$

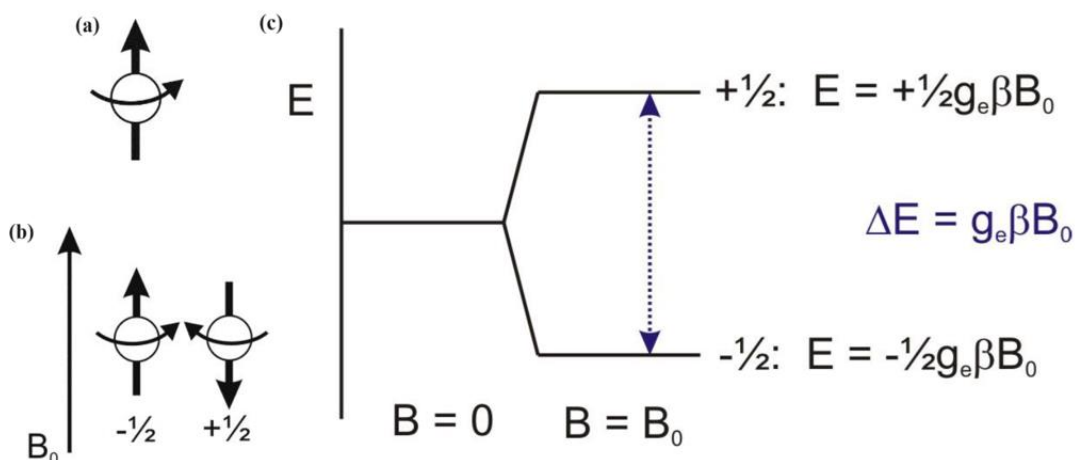


Figure 2.20 Effect on electronic spin to an applied magnetic field  $B_0$ . (a) single electron in a force free system (b) Zeeman effect caused by applied magnetic field  $B_0$  giving rise to spin orientation (c) Energy diagram corresponding to Zeeman effect and energy required for electronic transition. Figure was taken from [https://webhome.auburn.edu/~duinedu/epr/1\\_theory.pdf](https://webhome.auburn.edu/~duinedu/epr/1_theory.pdf) (Accessed on 28th May 2024).

When the applied frequency  $\nu$  is such that

$$\Delta E = g\beta_e B_0 = h\nu \quad (\text{Eq 2.3})$$

results in energy absorption and basic EPR spectroscopy is the detection of these absorptions. The frequency at which absorption takes place is denoted as the resonance (Larmor) frequency. Microwave resonance frequencies in the range between 2.8 to 42 GHz are observed for energy absorption of electron spin state with  $g = 2$  and  $B_0 = 0.1$  to 1.5 T. For use, microwave frequencies are divided to bands such as X-band  $\approx 9.5$  GHz, Q-Band  $\approx 34$  GHz, W-Band  $\approx 95$  GHz<sup>51</sup>. For this thesis work, X-band was used for CW-EPR experiments.

The microwave frequency is held constant, and the applied magnetic field is varied in EPR experiments. Energy absorption is observed when the resonance condition (Eq 2.3) is achieved. In general, EPR is conducted on a multitude of spins therefore the calculated value is the net magnetization (M) which is the net magnetization per unit volume. According to the Boltzmann Distribution, the relative populations of spins observed in the energy state  $\alpha$  corresponding to  $m_s = +1/2$  ( $n_\alpha$ ) and  $\beta$  corresponding to  $m_s = -1/2$  ( $n_\beta$ ) is given by,

$$\frac{n_\alpha}{n_\beta} = e^{-\frac{\Delta E}{kT}} \quad (\text{Eq 2.4})$$

where  $k$  is the Boltzmann constant ( $1.380649 \times 10^{-23}$  J/K), and  $T$  is the temperature. This will result in an excess polarization (P) given by,

$$P = \frac{n_\alpha - n_\beta}{n_\alpha + n_\beta} = \frac{1 - \exp(-\frac{\Delta E}{kT})}{1 + \exp(-\frac{\Delta E}{kT})} \quad (\text{Eq 2.5})$$

The equilibrium magnetization for a static magnetic field in the z-direction is,

$$M_o = \frac{1}{V} \sum_i \mu_i = \frac{1}{2} N \hbar \gamma_e P e_z \quad (\text{Eq 2.6})$$

where  $N$  is the total number of spins ( $n_\alpha + n_\beta$ ), and  $V$  is the sample volume. Furthermore, the presence of an external magnetic field can induce torque due to the magnetic moment. For a single spin, this can be represented by,

$$\hbar \frac{dS}{dt} = \mu \times B \quad (\text{Eq 2.7})$$

whereas for the complete set of spins, we can incorporate net magnetization (M) to obtain,

$$\hbar \frac{dM}{dt} = M \gamma_e \times B \quad (\text{Eq 2.8})$$



When the static magnetic field is applied along the z-direction, individual spins will be rotating at a precession frequency ( $\Omega_s$ ) equal to the resonance frequency ( $\omega_0$ ) and the bulk magnetization ( $M$ ) is static and is aligned along the magnetic field. Thus, it becomes time invariant and not detectable. This is known as “on resonance” (Figure 2.21a) where the bulk magnetization aligns with the static field. When there is a displacement in the magnetization vector from the z-axis, a detectable magnetic field occurs due to the offset resonance frequency ( $\omega_0$ ) and applied microwave frequency ( $\omega_{mw}$ ) deviating the precession frequency of the magnetization vector by  $\Omega_s = \omega_0 - \omega_{mw}$  factor. This is when a counterclockwise rotating coordinate system with the microwave frequency is introduced. This results in an “off resonance” condition (Figure 2.21b), where the bulk magnetization has non-zero magnitudes along the transverse (xy) axes. There are two relaxation effects perturbing the motion of the magnetization vector, the longitudinal relaxation which occurs due to the magnetization vector reaching thermal equilibrium denoted by  $T_1$ , and the transverse relaxation due to the loss of coherence in the transverse plane due to spin-spin interaction and is denoted by  $T_2$ .

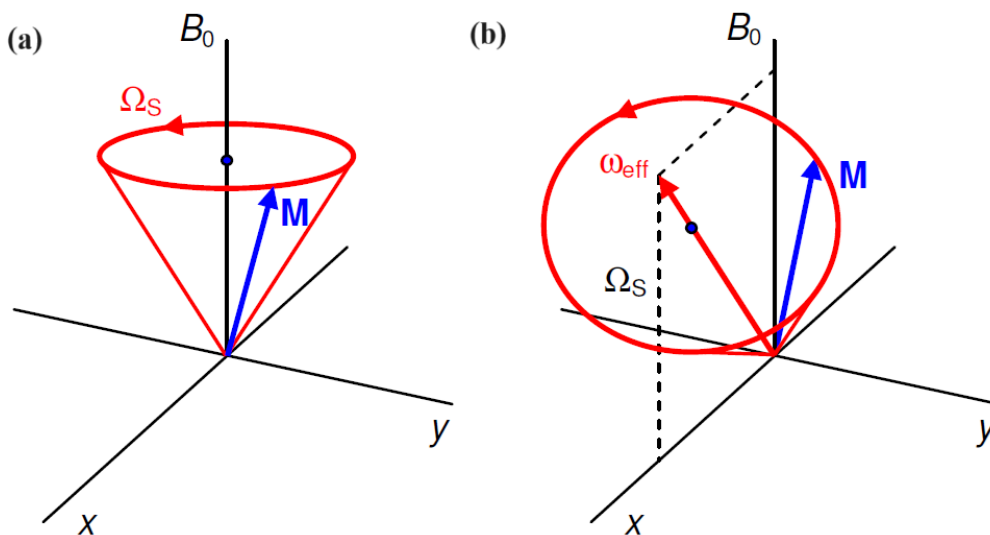


Figure 2.21 The precession of the magnetization vector ( $M$ ) along the rotating frame. (a) on resonance condition where free precession of  $M$  occurs along  $z$ -axis and bulk magnetization aligns with the static field. (b) off resonance condition where bulk magnetization resides in the transverse axes. Figure was taken from Junk, M. J. (2012). *Assessing the functional structure of molecular transporters by EPR spectroscopy*. Springer Science & Business Media.

#### 2.5.1.2 Anisotropy of $g$ value

The  $g$  value for an electron in an isolated atom is around 2.00232(5) which is remarkably close to the expected value. However, it can vary from species to species. The orbital angular momentum and the spin of the paramagnetic electron of a species contributes to its  $g$  value therefore information regarding electronic structure and symmetry can be obtained from  $g$  values. Deviations of the  $g$  value from 2.00232 can be observed when it is under an applied magnetic field and spin-orbit coupling between ground and excited states. Therefore,  $g$  is represented as a second-rank tensor. For every molecule with a paramagnetic center, a principal axis for measuring  $g$  factors can be defined. They are labelled as  $g_x$ ,  $g_y$ , and  $g_z$ . All  $g$ -anisotropy can be averaged out in the situation of a low viscosity solution, but if the paramagnetic molecules are fixed (in a single crystal), then deviations of  $g$ -factor can be observed as you change the orientation of the molecule. To further simplify the orientation dependence of  $g$ -tensor, we can use angular dependency of  $g$ -value to introduce two polar angles  $\theta$  and  $\phi$  where  $\theta$  represent the angle between applied magnetic field ( $B$ ) vector and  $z$ -axis of the molecule while  $\phi$  represent the angle between the projection of  $B$  vector on the  $xy$  plane and  $x$  axis<sup>52</sup>(Figure 2.22).

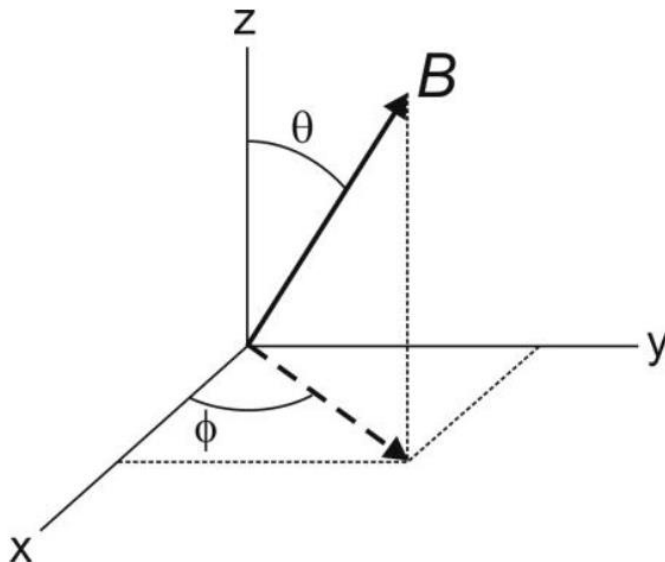


Figure 2.22 Applied magnetic field (B) orientation with respect to the orientation of the molecule containing paramagnetic center. Figure was taken from [https://webhome.auburn.edu/~duinedu/epr/1\\_theory.pdf](https://webhome.auburn.edu/~duinedu/epr/1_theory.pdf) (Accessed on 28th May 2024).

By using directional cosines, we can define directions using polar notations as

$$l_x = \sin(\theta)\cos(\phi), l_y = \sin(\theta)\sin(\phi), l_z = \cos(\theta)$$

using Eq 2.3, we can define anisotropic resonance due to Zeeman interaction for an electron spin  $S = \frac{1}{2}$  as,

$$B_{(res)} = \frac{h\nu}{\beta_e g(l_x, l_y, l_z)} \text{ where } g(l_x, l_y, l_z) = \sqrt{g_x^2 l_x^2 + g_y^2 l_y^2 + g_z^2 l_z^2} \quad (\text{Eq 2.9})$$

by introducing polar angles, we can obtain

$$g(l_x, l_y, l_z) = \sqrt{g_x^2 \sin^2 \theta \cos^2 \phi + g_y^2 \sin^2 \theta \sin^2 \phi + g_z^2 \cos^2 \theta} \quad (\text{Eq 2.10})$$

for an axial spectrum,  $g_x = g_y$ . Then Eq 2.10 becomes

$$g_{ax}(\theta) = \sqrt{g_{\perp}^2 \sin^2 \theta + g_{\parallel}^2 \cos^2 \theta} \quad (\text{Eq 2.11})$$

where perpendicular  $g_{\perp} = g_x = g_y$  and  $g_{\parallel} = g_z$ <sup>53</sup>.

### 2.5.1.3 Hyperfine interaction

In addition to the interaction between the free electron and the applied magnetic field, electron spins can also interact with a nearby nucleus with a magnetic moment or with another nearby electron spin. The interaction between an electron spin with the nucleus in which it originates from is known as a hyperfine interaction. Dipole-dipole interactions and Fermi contact are the cause of these interactions. If the interaction is between electron spin with the nearby nucleus is defined as a super hyperfine interaction. The interaction between electron spins of different atoms through dipole-dipole interactions is defined as a spin-spin interaction. A unique scenario in which overlapping spin orbitals exchange their electron spins is defined as Heisenberg exchange coupling.

In X-band, usually the hyperfine coupling contribution is around two orders of magnitude smaller than the Zeeman interaction. Therefore, according to Eq 2.3 the resonance condition can be modified as,

$$h\nu = g\beta_e B_0 + A'm_I \quad (\text{Eq 2.12})$$

where  $A'$  is measured in energy units ( $\text{cm}^{-1}$ ) and  $m_I$  is the magnetic quantum number of the nucleus. The hyperfine coupling constant was later defined as  $A = A'/\beta_e B_0$ . The selection rules for EPR transitions based on spin and magnetic quantum number are as follows.

$$\Delta m_S = 1 \quad \Delta m_I = 0$$

Since the number of nuclear levels is  $2I+1$  ( $I$  = nuclear spin number), there will be  $2I+1$  transitions for  $S = 1/2$ . For a resonance field ( $B_{(res)}$ ),

$$B_{(res)} = \left( \frac{h\nu}{g\beta_e} \right) - \sum_{m_I} A m_I \quad (\text{Eq 2.13})$$

in a scenario where the Zeeman interaction and the hyperfine interaction becomes anisotropic (Ex: Metalloproteins in fixed or fluidic environment), the resonance field becomes a function of the molecular orientation of the external magnetic field. Thus,

$$B_{(res)}(l_x, l_y, l_z) = \sum_{m_I} \{ [h\nu/g(l_x, l_y, l_z)\beta_e] - A(l_x, l_y, l_z, g_x, g_y, g_z)m_I \} \quad (\text{Eq 2.14})$$

$g(l_x, l_y, l_z)$  defined in Eq 2.10 and  $A(l_i, g_i)$  defined as

$$A(l_i, g_i) = g^{-2} \sqrt{l_x^2 g_x^4 A_x^2 + l_y^2 g_y^4 A_y^2 + l_z^2 g_z^4 A_z^2} \quad (\text{Eq 2.15})$$

using Eq 2.10 and Eq 2.15 with the addition of polar notations for directions, we can write,

$$A(\theta, \phi) = \frac{\sqrt{A_x^2 g_x^4 \sin^2 \theta \cos^2 \phi + A_y^2 g_y^4 \sin^2 \theta \sin^2 \phi + A_z^2 g_z^4 \cos^2 \theta}}{g_x^2 \sin^2 \theta \cos^2 \phi + g_y^2 \sin^2 \theta \sin^2 \phi + g_z^2 \cos^2 \theta} \quad (\text{Eq 2.16})$$

for fixed frequency, field swept spectra obtained by EPR spectroscopy.

For this thesis work, a spin label containing a paramagnetic spin on a nitroxide bond (N-O) was used. An unpaired electron on a nitroxide is influenced by the Zeeman interaction ( $\hat{H}_{EZ}$ ) and the hyperfine interaction ( $\hat{H}_{HF}$ ). Therefore, the spin Hamiltonian can be written as

$$\hat{H}_{NO} = \hat{H}_{EZ} + \hat{H}_{HF} \quad (\text{Eq 2.17})$$

Using the electron spin tensor ( $S$ ), nuclear spin tensor ( $I$ ), hyperfine coupling tensor ( $A$ ), we can rewrite Eq 2.17 as,

$$\hat{H}_{NO} = g \cdot \beta_e \cdot B_o \cdot S + A \cdot S \cdot I \quad (\text{Eq 2.18})$$

for a fast-rotating spin, the  $A$  and  $g$  tensors become isotropic. Therefore, Eq 2.18 is rewritten as,

$$\hat{H}_{\text{NO}} = g_{\text{iso}} \beta_e B_0 m_s + a_{\text{iso}} m_s m_I \quad (\text{Eq 2.19})$$

for a paramagnetic electron on a nitroxide bond,  $m_s = \pm 1/2$  and  $m_I = \pm 1, 0$  ( $I=1$  for  $^{14}\text{N}$  nucleus) contains three allowed transitions according to the selection rules (Figure 2.23). The resonance energies can be derived as,

$$\Delta E = h\nu = g_{\text{iso}} \beta_e B_0 + a_{\text{iso}} m_I \quad (\text{Eq 2.20})$$

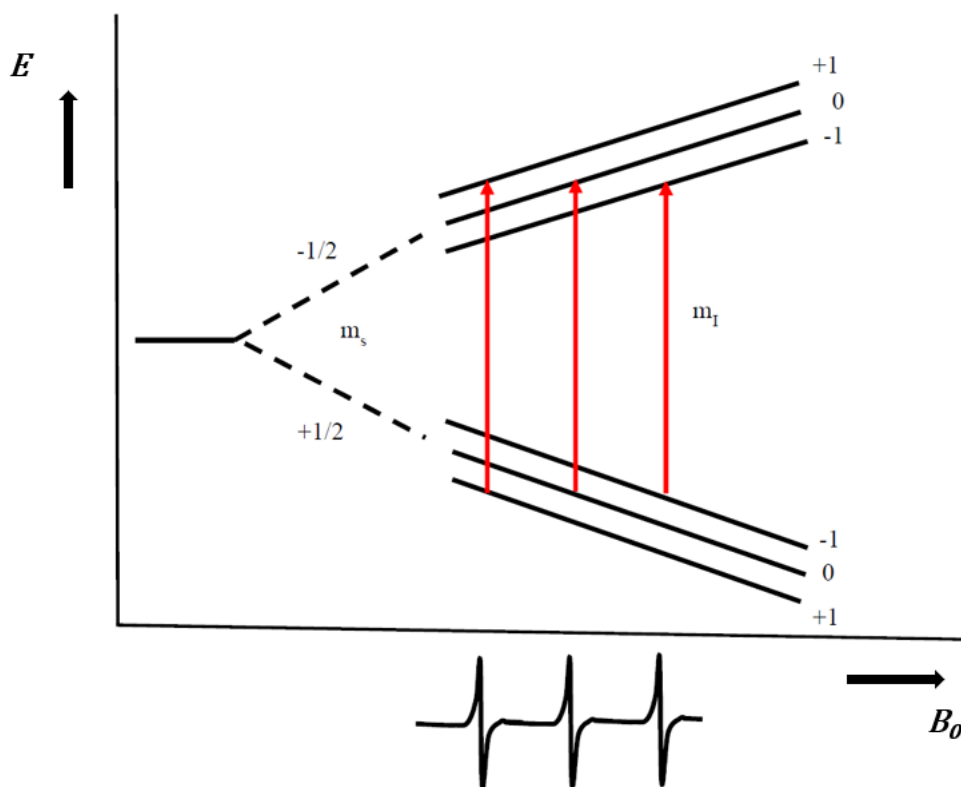


Figure 2.23 Energy diagram for nitroxide energy level splitting with  $m_s = \pm 1/2$  and  $m_I = \pm 1, 0$  due to Zeeman interaction and hyperfine coupling. The three allowed transitions between  $m_I = +1, 0$ , and  $-1$  is observed at low, central, and high magnetic fields, respectively. For high resolution signals, CW EPR signal is observed as the first derivative of the absorption spectra. Figure was taken from

Nilaweera, T. D. (2018). Exploring BtuB in Escherichia coli via a new direct spin labeling approach and electron paramagnetic resonance spectroscopy (Doctoral Thesis Dissertation). University of Virginia, Charlottesville, USA.

### 2.5.2 CW-EPR for detection of nitroxide

The  $2p_z$  orbital of the N atom in nitroxides is along the  $z$  axis while the N-O bond resides along the  $x$  axis (Figure 2.24a). The CW-EPR signal for nitroxides along the  $x$ ,  $y$ ,  $z$  axis is composed of three identical lines according to the transitions observed in Figure 2.23. Regardless of the number of hyperfine lines in the spectrum, they are all centered around the Zeeman transition therefore the  $g$  tensor can be calculated from the magnetic field corresponding to the central line. The hyperfine coupling tensor  $A$  can be calculated using the spacing between the spectrum lines.

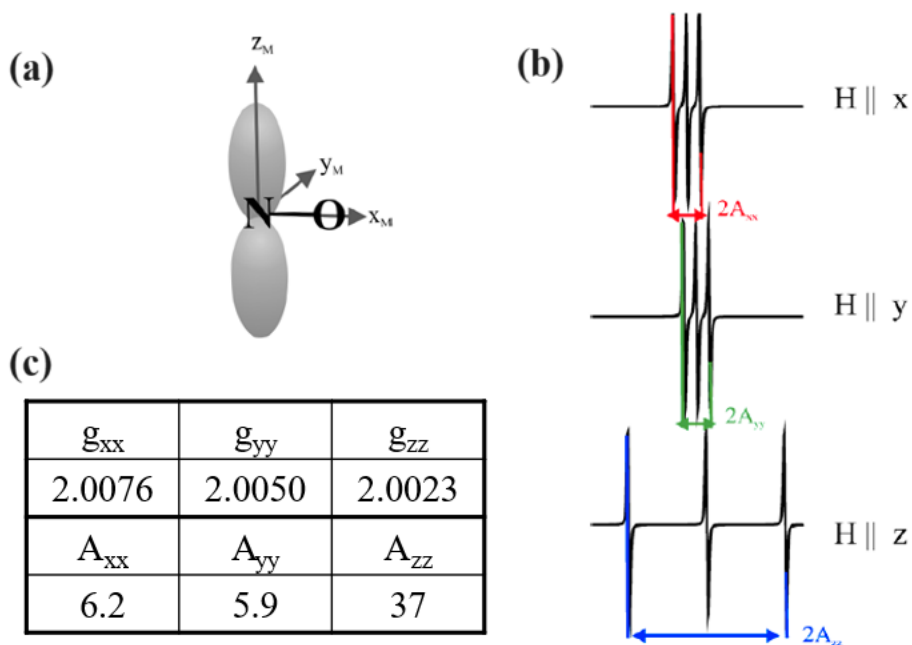


Figure 2.24 Spatial coordinates of the nitroxide bond and their corresponding CW-EPR spectra and calculated  $g$  and  $A$  tensors. (a) Spatial orientation indicates that the  $2p_z$  orbital of nitroxide

aligns with the z-axis and the N-O bond aligns with the x axis. (b) Observed CW-EPR signal along **x**, **y**, and **z** axis for nitroxide. (c) *A* and *g* tensor values calculated for a nitroxide site exposed to an aqueous environment. The figure was obtained from Columbus, L. M. (2001). Investigating backbone and side chain dynamics of [alpha]-helices in the nanosecond regime with site-directed spin labeling (Doctoral Thesis Dissertation). University of California, Los Angeles, USA.

Since the paramagnetic electron is located at the  $2p_z$  orbital of the N-atom with high probability, the largest hyperfine splitting due to nitrogen nucleus is observed for the z-axis (Figure 2.24b, c). The mobility of the spin label is dictated by the motion of the label with respect to the protein backbone, the rotational motion of the entire protein, and the local environment around the nitroxide bond. This is solely dependent upon the rotation diffusion. In the isotropic limit, the hyperfine interaction is averaged, and a single isotropic value ( $a_{\text{iso}}$ ) is defined with three EPR signals of equal height. In the rigid limit, rotation diffusion is prohibited therefore anisotropy in hyperfine interaction is observed. Between these two extreme limits, the time for rotation diffusion will impact the overall spectra. The parameter that dictates the motion of spins is the rotation correlation time ( $\tau_c$ ).  $\tau_c$  can be obtained by measuring the central line width of the spectra where small values ( $\tau_c < 1$  ns) indicate nitroxides with high degree in flexibility and small hyperfine coupling constants (Figure 2.25 Isotropic limit) whereas large  $\tau_c$  values will indicate a nitroxide present in a very restricted environment and large hyperfine coupling constants (Figure 2.25 Rigid limit)<sup>54</sup>.



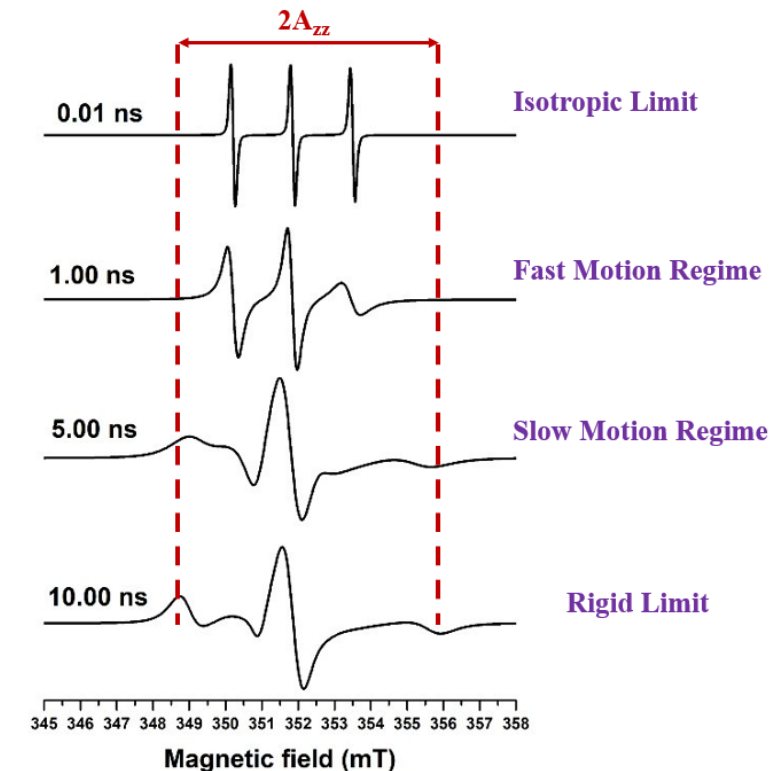


Figure 2.25 Simulated EPR spectra obtained at different rotation correlation times ( $\tau_c$ ). Smaller  $\tau_c$  values indicate nitroxides with fast rotational diffusion with an isotropic hyperfine coupling whereas a decrease in rotational diffusion with increasing  $\tau_c$  values will result in anisotropy of hyperfine coupling. Figure was obtained from Torricella, F., Pierro, A., Mileo, E., Belle, V., & Bonucci, A. (2021). Nitroxide spin labels and EPR spectroscopy: A powerful association for protein dynamics studies. *Biochimica et biophysica acta. Proteins and proteomics*, 1869(7), 140653.

The behavior of spin label can be strongly influenced by the local environment in which the label resides. The polarity of the solvent can affect the energetics of the single occupied molecular orbital (SOMO) and lowest unoccupied molecular orbital (LUMO), eventually affecting the  $g$  value and hyperfine coupling constants ( $A_{zz}$ ). This allows us to obtain information regarding

protein-protein interactions, structural and conformational dynamics of proteins through the nitroxide label (Figure 2.26)<sup>55,56</sup>.

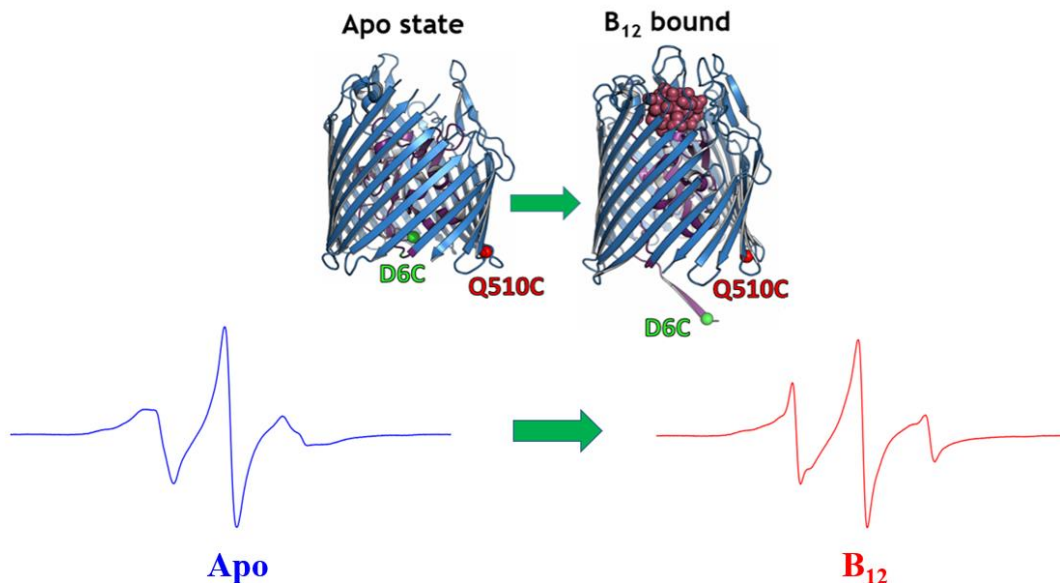


Figure 2.26 Experimental EPR spectra obtained for D6R1-Q510R1 BtuB. Primary difference between the two BtuB states (**apo** state [PDB ID 1NQE] and **B<sub>12</sub>** bound state [PDB ID 2GSK]) in the CW EPR spectra observed is due to D6R1 in the Ton box converting from a folded state inside the pore of the  $\beta$ -barrel domain to an unfolded state where nitroxide movement is no longer hindered therefore fast mobility of spin label is detected.

### 2.5.3 Pulse EPR experiments

#### 2.5.3.1 Laboratory and Rotating Frames for Pulse EPR

Pulse EPR experiments consist of a similar external static magnetic field ( $B_o$ ) along the z-axis of the laboratory frame. Therefore, the net magnetization ( $M$ ) due to spins is aligned with the external field at thermal equilibrium. The microwave source creates an additional magnetic field ( $B_I$ ) perpendicular to  $B_o$  which results in the precession of spins as well. In most cases,  $|B_I| \ll |B_o|$ .

Here, the spins are affected by both  $B_o$  and  $B_I$  resulting in simultaneous precession around both magnetic fields (Figure 2.27a). Furthermore, in contrast to CW-EPR experiments,  $B_I$  is not static. Thus, a rotating frame is utilized to observe our systems of interest where a synchronous rotation with a  $B_I$  component is executed. The coordinate system containing an angular velocity of  $\omega_0$  ( $\omega_0$  – microwave frequency) will have one  $B_I$  component static whereas components with  $2\omega_0$  can be neglected (Figure 2.27b). The rotating frame can be used to observe changes in  $\omega_0$  ( $\Delta\omega_0$ ) due to dipolar interactions and inhomogeneities<sup>57</sup>.

A  $B_I$  field created by applying a microwave source along the x-axis will result in the overall magnetization to precess about the x-axis (Figure 2.28a) with a frequency  $\omega_1$  where it is defined as the Rabi frequency.

$$\omega_1 = -\gamma B_1 \quad (\text{Eq 2.21})$$

We can also control the turn of M by eliminating the microwave frequency at distinct times. This process involves the use of microwave pulses where we can determine the angle of rotation for M defined as “*tip/flip angle*” to be,

$$\alpha = -\gamma | B_1 | t_p \quad (\text{Eq 2.22})$$

where  $t_p$  is the pulse length. Most commonly used tip angles are either  $\pi/2$  (90 °) or  $\pi$  (180 °). A  $\pi$  pulse can be obtained by extending the pulse length to twice as  $\pi/2$  pulse length (Figure 2.28b).

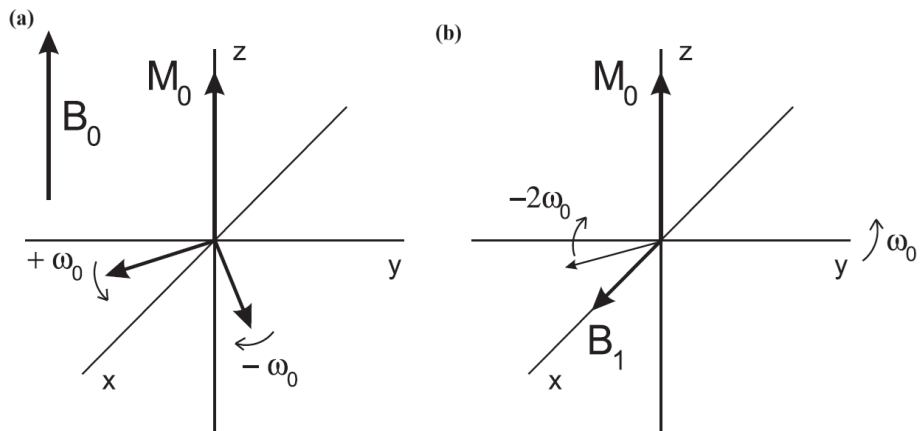


Figure 2.27 Microwave magnetic fields in (a) Laboratory (b) Rotational frames with angular frequency  $\omega_0$  for pulse EPR experiments. Figure was taken from <https://www.yumpu.com/en/document/read/45359546/e580-pulsedpdf> (Accessed on 3rd June 2024)

Pulse phases are defined based on the axis to which  $B_1$  is parallel to. If  $B_1$  is parallel to +x axis, it is defined as a +x pulse and a shift of microwave phase by  $90^\circ$  will result in shift of  $B_1$  to +y axis (+y pulse) and M to +x axis (Figure 2.29)<sup>58</sup>.

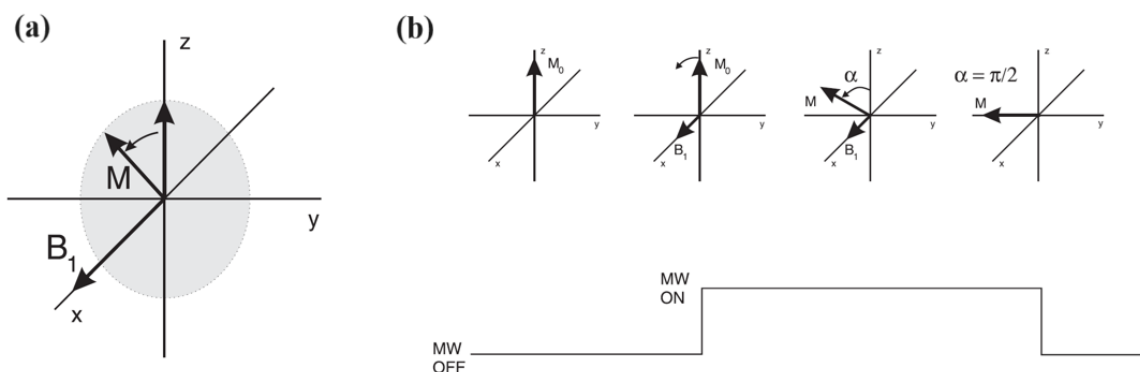


Figure 2.28 (a) Rotation of magnetization M due to  $B_1$  along x-axis (b) the effect of a  $\pi/2$  pulse on magnetization and its corresponding pulse shape. Figure was taken from

<https://www.yumpu.com/en/document/read/45359546/e580-pulsedpdf> (Accessed on 3rd June 2024)

Pulse experiments include a simultaneous excitation of a large frequency range with a single microwave pulse with high power at a given frequency  $\nu$ . By Fourier Transformation of the pulse shape within the limits of the linear response theory, the excitation profile of the pulse is determined where it correlates to a *sinc* function ( $\sin[x]/x$ ) for a rectangular pulse. The initial zero crossing from the central frequency is given by  $1/t_p$  and the area within dashed lines defined by  $\nu \pm \frac{1}{2} t_p$  is defined to contain uniform excitation (Figure 2.30). Thus, a reduction in pulse length results in the broadening of the excitation range<sup>59</sup>.

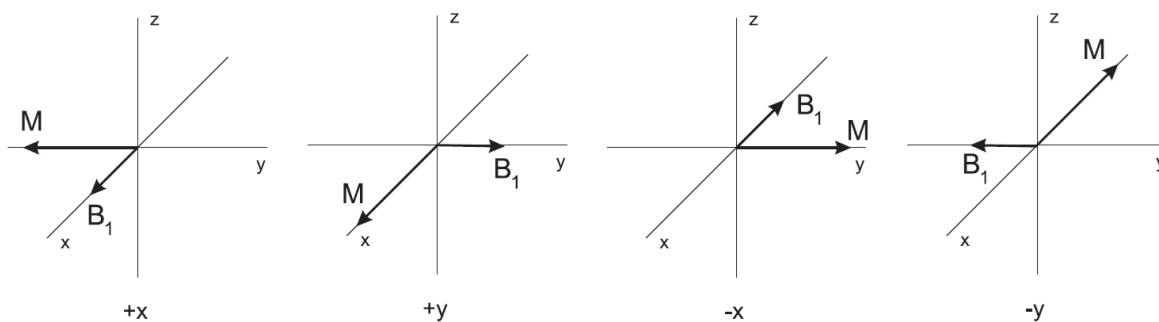


Figure 2.29 Pulse phases depending on the orientation of  $B_1$  and the corresponding orientation of  $M$ . Figure was taken from <https://www.yumpu.com/en/document/read/45359546/e580-pulsedpdf> (Accessed on 3rd June 2024)

An introduction of a  $\pi/2$  pulse will result in rotation of magnetization about the x-y plane at the Larmor frequency ( $\omega_0$ ) which can be clearly observed in the laboratory frame as the rotating frame would exhibit  $M$  to be static (Figure 2.31). The rotation of  $M$  induces currents and voltages inside the resonator where the maximum signal can be observed at the x-y plane. This signal is known as a Free Induction Decay (FID) and a rapid decay of this signal can be observed due to

spin interactions with the environment ultimately aligning the magnetization with the z-axis. There are two main types of relaxation effects that play a role during this process. They are Spin-Lattice Relaxation ( $T_1$ ) and Transverse Relaxation ( $T_2$ )<sup>57</sup>.

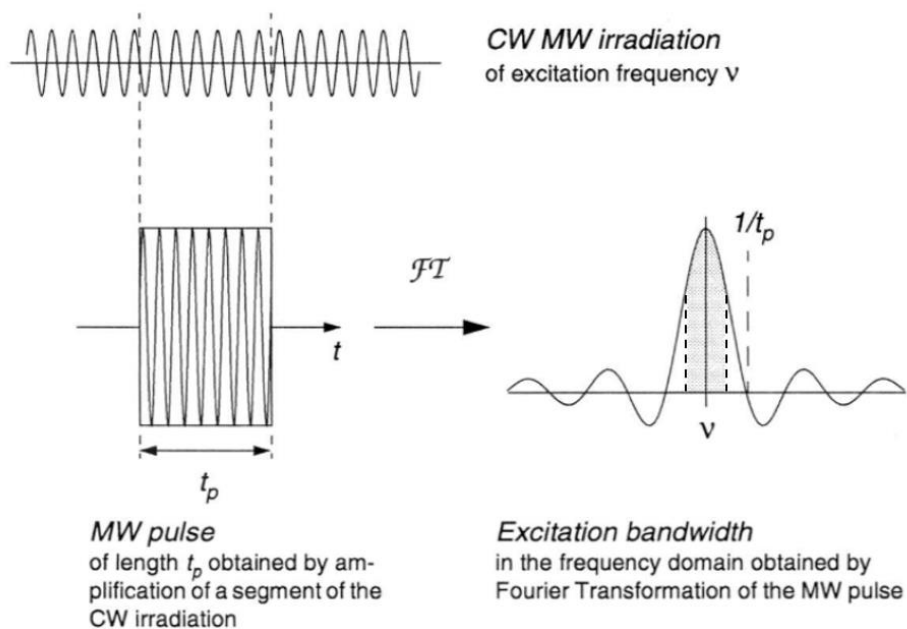


Figure 2.30 Microwave pulse length obtained by amplification of a segment of the CW microwave irradiation and its corresponding excitation bandwidth obtained through Fourier transformation. A homogeneous excitation is assumed in the area between the dashed lines in the excitation bandwidth defined by  $\nu \pm \frac{1}{2} t_p$ . Figure was taken from <https://epr.ethz.ch/education/basic-concepts-of-epr/cw-and-pulse-epr.html> (Accessed on 3rd June 2024).

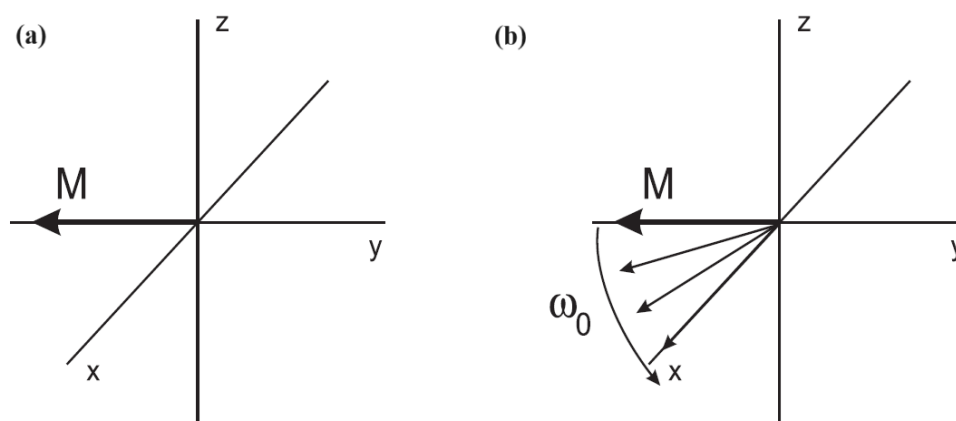


Figure 2.31 FID generation observed in (a) rotating frame (b) laboratory frame. Figure was taken from <https://www.yumpu.com/en/document/read/45359546/e580-pulsedpdf> (Accessed on 3rd June 2024)

### 2.5.3.2 Relaxation Effects of M through $T_1$ and $T_2$

#### 2.5.3.2.1 Spin-Lattice Relaxation Time ( $T_1$ )

According to Boltzmann statistics shown in Eq. 2.4, we observe higher number of magnetic moments to be present in the low energy parallel state at thermal equilibrium. An introduction of a  $\pi/2$  pulse will result in the net magnetization along z-axis to be zero which indicates equal magnetic moments present in both parallel and antiparallel states whereas a  $\pi$  pulse will result in M alignment along -z axis (also defined as an “inversion pulse”) indicating a high number of moments to be present in the high energy antiparallel state (Figure 2.32a). The rate at which net magnetization along z-axis ( $M_z$ ) reaches thermal equilibrium is defined as the Spin-Lattice relaxation time ( $T_1$ ) and it obeys the following equations depending on the type of pulse introduced (Figure 2.32b).

for a  $\pi/2$  pulse,

$$M_z(t) = M_0(1 - e^{-\frac{t}{T_1}}) \quad (\text{Eq 2.23})$$

And for a  $\pi$  pulse

$$M_z(t) = M_0(1 - 2 \cdot e^{-\frac{t}{T_1}}) \quad (\text{Eq 2.24})$$

where  $M_0$  is the initial magnetization along the z-axis.

Determination of  $T_1$  is crucial as it dictates the rate at which experiments can be repeated. The time between individual experiments defined as the Shot-Repetition Time (SRT) can be determined using  $T_1$  where  $t = SRT$  in Eq 2.23. Repetition of pulse experiments before net magnetization alignment with z-axis will result in the decrease of signal during FID. For reference, when  $SRT = 5 \times T_1$ , 99% of  $M_z$  will be recovered before the next experiment.

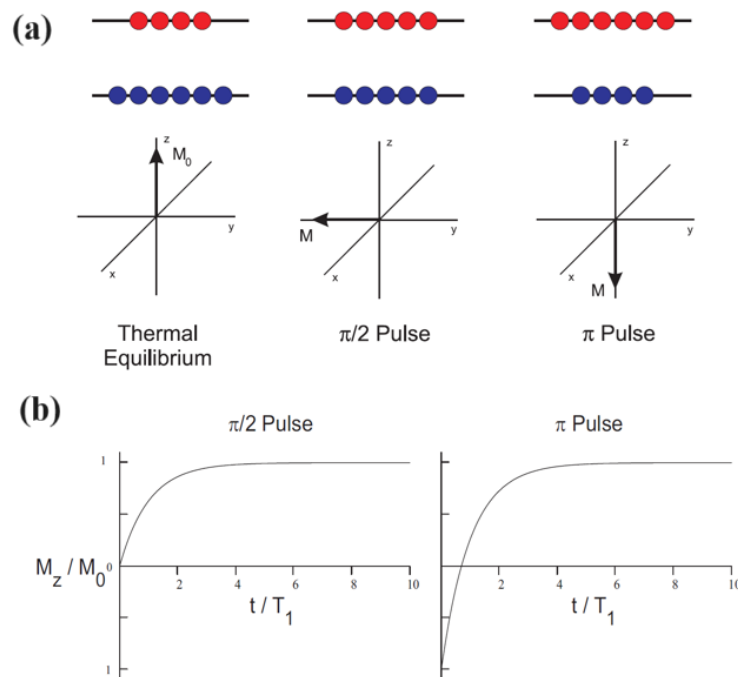


Figure 2.32 Spin-lattice relaxation effects net magnetization. (a) Population of magnetic moments in **parallel** and **anti-parallel** states and the population changes after  $\pi/2$  and  $\pi$  pulses. (b) recovery



of magnetization after  $\pi/2$  and  $\pi$  pulses. Figure was taken from <https://www.yumpu.com/en/document/read/45359546/e580-pulsedpdf> (Accessed on 3rd June 2024)

#### 2.5.3.2.2 Transverse Relaxation Time ( $T_2$ )

The time required for net magnetization to decay in the x-y plane is defined as the Transverse relaxation time ( $T_2$ ). The two fundamental processes accountable for this relaxation are homogeneous and inhomogeneous broadening. Lorentzian shape is exhibited for homogeneous broadening as the line shape is governed by the relaxation times whereas Gaussian shapes are quite common in inhomogeneous broadening as the line shape is governed by unresolved coupling. The overall signal is a collection of individual homogeneous broadening processes that are shifted in frequency because of different magnetic fields felt by the spins and the overlapping of multiple Lorentzian line shapes resulting in one broader gaussian line shape. During relaxation, the transverse magnetization “fans out” and the magnetization decreases until the random distribution of spin packets with different Larmour frequencies cancel each other (Figure 2.32). The decay of transverse magnetization is defined by a general exponential,

$$M_{-y}(t) = e^{-\frac{t}{T_2}} \quad (\text{Eq 2.25})$$

Where  $T_2$  is defined as the spin-spin relaxation time. A recording of  $M$  after a  $\pi/2$  pulse can be used to obtain the FID where the Fourier transform (FT) will provide the EPR spectrum of sample58.

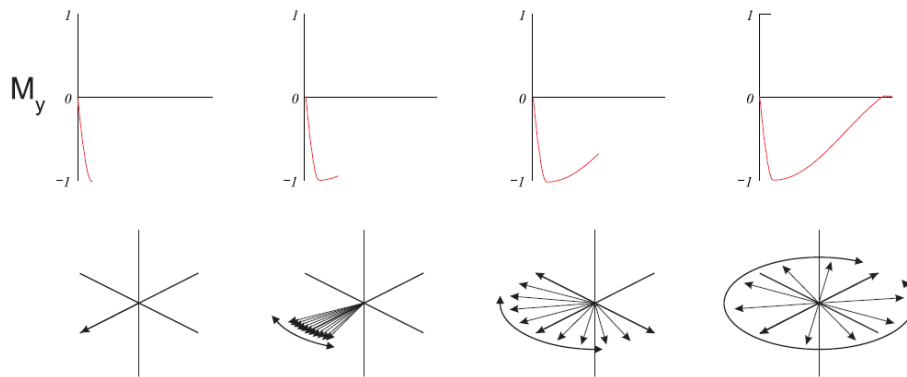


Figure 2.33 Transverse relaxation process where fanning out results in the decrease of net magnetization along x-y plane. Figure was taken from <https://www.yumpu.com/en/document/read/45359546/e580-pulsedpdf> (Accessed on 3rd June 2024)

### 2.5.3.3 Spin Echo and Relaxation

Application of a single  $\pi/2$  pulse will result in an FID with the decay of transverse magnetization according to spin-spin relaxation time ( $T_2$ ). In most scenarios, inhomogeneous broadening is a contributing factor for EPR signal so an additional secondary  $\pi$  pulse will assist in the recovery of the signal by refocusing the net magnetization. This resulting echo signal is defined as a Hahn Echo (Figure 2.34a, b).

The generation of an echo involves the initial  $\pi/2$  pulse resulting in a net magnetization aligned with the x-y plane where it fans out due to different frequencies in the EPR spectrum. Application of a  $\pi$  pulse flips the magnetization about the x-axis but the direction and speed of the magnetization is unaffected. Spin packets that have rotated faster away from the -y axis will be further away from +y axis after  $\pi$  pulse whereas spin packets rotated slower away from the -y axis will be closer to the +y axis (Figure 2.34b). Hence, all spin packets will eventually catch up at the

+y axis after the second pulse and they will de-phase once again. Therefore, a spin echo can be considered as a reverse FID followed by a normal FID. Hence, FT of second half (normal FID) will give the EPR spectra (Figure 2.34a).

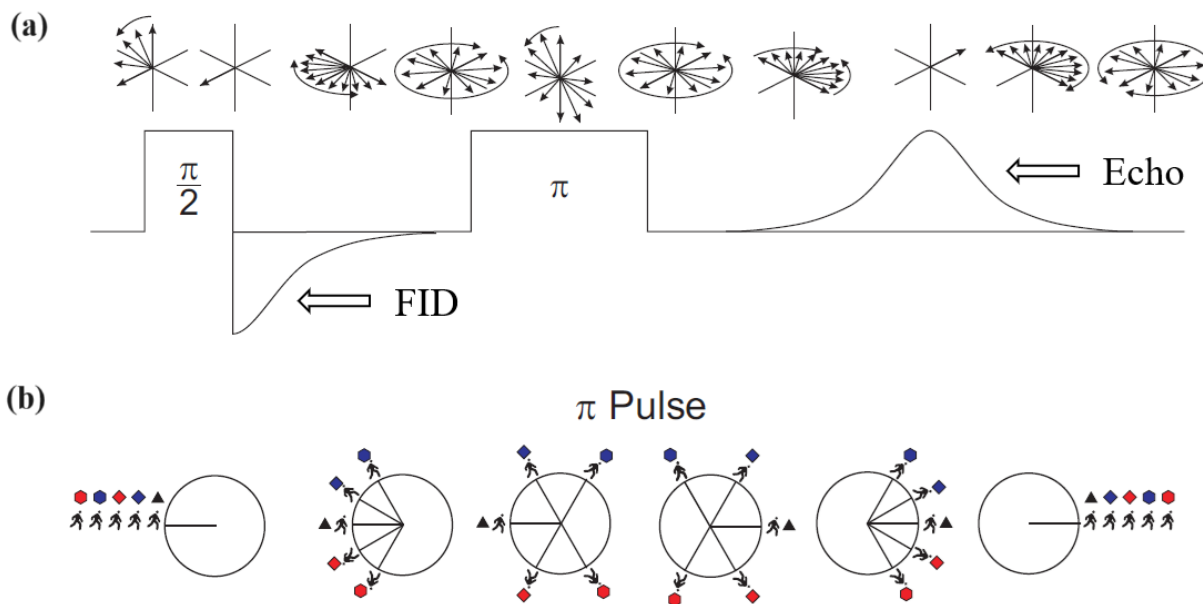


Figure 2.34 Behavior of magnetization in an echo experiment. (a) Pulse sequence for Hahn echo experiment where an initial  $\pi/2$  pulse followed by a  $\pi$  pulse result in rephasing of magnetization (b) refocusing of the magnetization by a  $\pi$  pulse during an echo experiment. Figure was taken from <https://www.yumpu.com/en/document/read/45359546/e580-pulsedpdf> (Accessed on 3rd June 2024)

Though an echo generation should be theoretically possible by increasing the time separation between  $\pi/2$  and  $\pi$  pulses ( $\tau$ ) (Figure 2.34a), the transverse relaxation of the net magnetization for long  $\tau$  results in an exponential decay of echo height. The relationship between echo height with the relaxation time is,

$$\text{Echo Height} \propto e^{-\frac{2\tau}{T_m}} \quad (\text{Eq 2.26})$$

Where  $T_m$  is the decay constant defined as Phase Memory Time. Several factors contribute to the phase memory time such as transverse relaxation ( $T_2$ ), spin diffusion, instantaneous diffusion and spectral diffusion due to molecular spin flip-flops, molecular rotation and molecular motion. Since normal FID begins  $2\tau$  time after  $\pi/2$  pulse, we can measure  $T_m$  by studying echo decay with increasing  $\tau$ <sup>58</sup>.

An echo can be generated with almost any two pulses. However more than two pulses are required for the generation of two special types of echoes, known as Stimulated echo and Refocused echo. Stimulated echo can be described using a Hahn echo experiment where the second  $\pi$  pulse is separated into two  $\pi/2$  pulses. The second  $\pi/2$  pulse will tip the de-phased magnetization towards the z-axis. This will result in the disappearance of the transverse magnetization but the longitudinal magnetization ( $M_z$ ) with frequency information of each spin moment is preserved. A third  $\pi/2$  pulse will tip the magnetization to x-y plane once again resulting in the rotation and refocusing of magnetization to create an echo. This methodology is commonly implemented in Electron Spin Echo Envelope Modulation (ESEEM) experiments (Figure 2.35a) which were not implemented in this thesis work.

A Refocused echo experiment can be explained where the second and third  $\pi/2$  pulses in a stimulated echo experiment is replaced with  $\pi$  pulses. During this pulse sequence, the initial  $\pi/2$  pulse and the secondary  $\pi$  pulse will generate a Hahn echo in which the transverse magnetization is focused but  $180^\circ$  ( $\pi$ ) out of phase with respect to the transverse magnetization right after the initial  $\pi/2$  pulse. After dephasing of magnetization, the second  $\pi$  pulse (overall third pulse) will refocus the transverse magnetization again generating an echo with opposite phase of Hahn echo,

and it will be in phase with original transverse magnetization after  $\pi/2$  pulse. Hence, the name refocused echo is given, and it is used for Double Electron-Electron Resonance (DEER) experiments (Figure 2.35b)<sup>58</sup>.

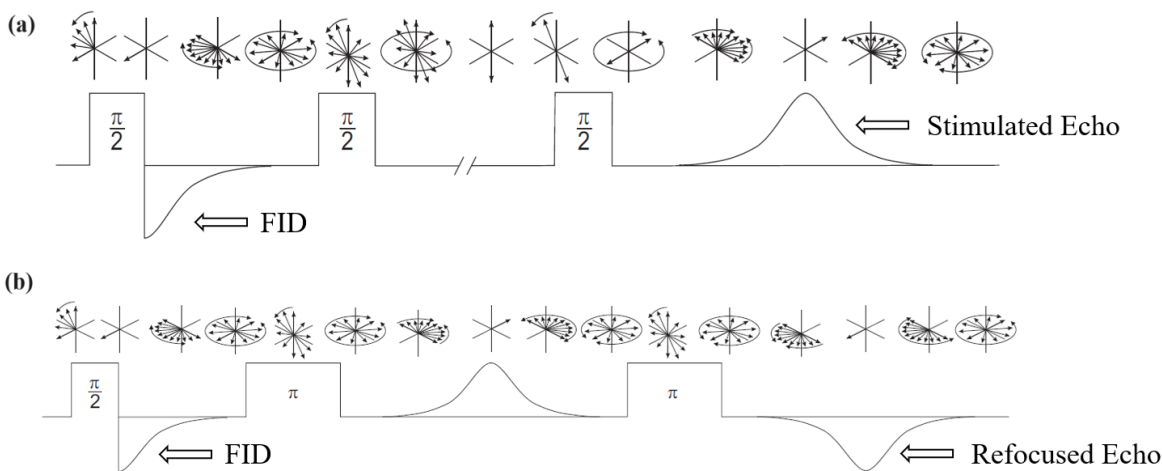


Figure 2.35 Pulse sequence and behavior of net magnetization in an (a) stimulated echo experiment (b) refocused echo experiment. Figure was taken from <https://www.yumpu.com/en/document/read/45359546/e580-pulsedpdf> (Accessed on 3rd June 2024)

#### 2.5.4 Double Electron-Electron Resonance (DEER) Spectroscopy

Double Electron-Electron Resonance (DEER) measures the dipolar coupling between electron spins to extract information on the distances between the two spins. Two paramagnetic species within close proximity can interact with each other due to dipolar and exchange interactions. These exchange interactions fade away significantly as the distance between the paramagnetic species increases and hence dipolar interactions become prominent where the species are considered as point dipoles. This interaction is dependent upon the applied magnetic

field, angle between the interspin vector, and the distance between the species (Figure 2.36). Thus, we can write the dipolar coupling frequency  $\omega_{dd}(r, \theta)$  as,

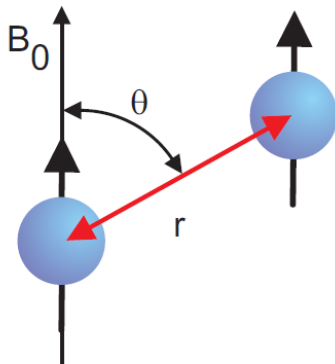


Figure 2.36 Dipolar interaction between two species with paramagnetic centers. Figure was taken from <https://www.yumpu.com/en/document/read/45359546/e580-pulsedpdf> (Accessed on 3rd June 2024)

$$\omega_{dd}(r, \theta) = \frac{\mu_0 \mu_B g_1 g_2}{2h} \cdot \frac{1}{r^3} \cdot (3 \cos^2 \theta - 1) \quad (\text{Eq 2.27})$$

where  $\mu_0$  is the permeability of vacuum,  $\mu_B$  is the Bohr magnetron,  $g_1$  and  $g_2$  are the g-values of the two species,  $h$  is the Planck constant,  $\theta$  is the interspecies angle, and  $r$  is the distance between the two species.

The angular dependence on dipolar coupling for a random orientation or spin pairs yields a dipolar spectrum known as a Pake pattern (Figure 2.37).

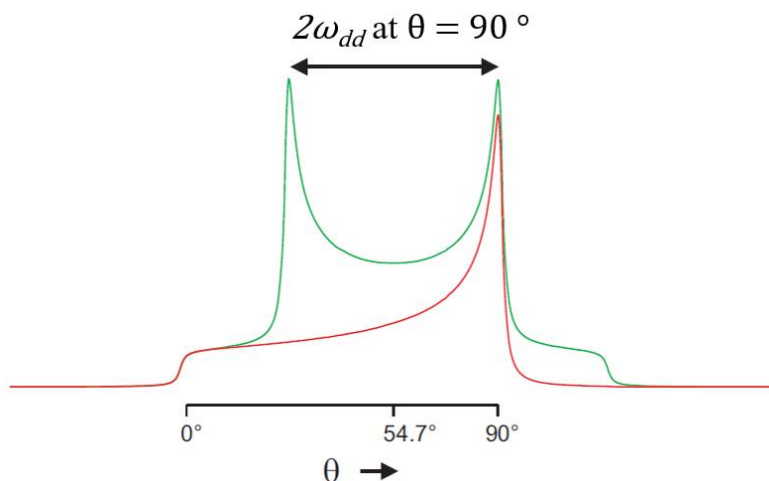


Figure 2.37 **Pake pattern** obtained from a FT of dipolar coupling due to paramagnetic nitroxide pair. The **single transition** is presented to emphasize the angular dependence on dipolar interactions. Figure was taken from <https://www.yumpu.com/en/document/read/45359546/e580-pulsedpdf> (Accessed on 3rd June 2024)

By obtaining the  $\omega_{dd}$ , we can determine  $r$  for a nitroxide pair with the following,

$$r = \sqrt[3]{\frac{52.16 \text{ MHz}}{\omega_{dd}(90^\circ)}} \text{ nm} \quad (\text{Eq 2.28})$$

#### 2.5.4.1 The DEER Experiment

DEER experiment requires two microwave frequencies, hereby denoted as observer frequency ( $\omega_A$ ) and pump frequency ( $\omega_B$ ) which is applied to the same EPR spectrum. In this instance, only pump frequency dependent changes in the EPR spectrum is considered as a DEER response whereas a constant spin echo would be observed in the absence of pump frequency. Spins that resonate with the observer frequency are named A spins and the spins that resonate with pump frequency are named B spins. Earlier experimental setup involved a three pulse DEER sequence involving two observer pulses and one pump pulse. The initial  $\pi/2$  pulse tips the magnetization to

the x-y plane followed by a  $\pi$  pump pulse to invert B spins and a refocusing  $\pi$  pulse to obtain the Hahn echo<sup>60</sup>. However, this pulse sequence involves the overlap of the  $\pi$  pump pulse with the observer  $\pi/2$  pulse at zero time ( $t = 0$ ) thus distorting the initial part of the trace, which is crucial to determine the modulation depth and zero time. The time limit in which the pump pulse and observer pulse overlap was defined as the “dead time.” This was overcome by introducing a pulse sequence which generates an electron spin echo to regain the initial magnetization where an addition of an extra observer  $\pi$  pulse between the observer  $\pi/2$  and pump  $\pi$  pulses result in the inversion of B spins by the pump pulse at zero time without any pulse overlap. Thus, the development of the “dead-time free” four (4) pulse DEER experiment has been able successfully address the necessary conditions required to obtain distance information between spins due to dipolar coupling without missing any data<sup>61</sup>. Since the introduction of the 4-pulse DEER sequence (Figure 2.38a), this technique has been widely used to measure distances ranging from 1.8 – 6 nm and even up to 8 nm in extreme cases to study structural and functional dynamics of membrane proteins<sup>62</sup> and soluble proteins<sup>63</sup>.

The 4-pulse sequence involves an initial Hahn echo generated with a  $\pi/2$  pulse which tips magnetization to the x-y plane followed by a  $\pi$  pulse to refocus the A spin magnetization at the observer frequency  $\omega_A$  at time  $2\tau_1$ . A pump  $\pi$  pulse with frequency  $\omega_B$  provided at a variable time  $t$  after the initial Hahn echo inverts a fraction ( $\lambda < 1$ ) of the subset of B spins coupled to A spins thereby modifying the magnetic field around the A spins (Figure 2.38b) by the electron-electron coupling frequency  $\omega_{ee}$  (Figure 2.38c). A final  $\pi$  pulse with frequency  $\omega_A$  refocuses the inhomogeneous broadening of A spin EPR line including hyperfine couplings, g-value dispersions, and dipolar coupling due to A spins interacting with inverted B spins. The resulting refocused Hahn echo generated at  $2(\tau_1 + \tau_2)$  is a coherence transfer echo oscillating at the dipolar coupling



frequency ( $\omega_{ee}$ )<sup>64,65</sup>. The change in frequency of A spins by  $\omega_{ee,i}$  leads to a phase gain given by  $\phi = \omega_{ee,i}t$  for  $\lambda_i$  fraction of net magnetization of A spins. Thus, the echo amplitude as a function of time can be written as,

$$v(t) = \prod_i \{1 - \lambda_i [1 - \cos(\omega_{ee,i}t)]\} \quad (\text{Eq 2.29})$$

and the product is for all B<sub>i</sub> spins that are potentially coupled to A spins. To obtain distance distributions through DEER experiments, additional assumptions are considered which simplifies Eq 2.29.

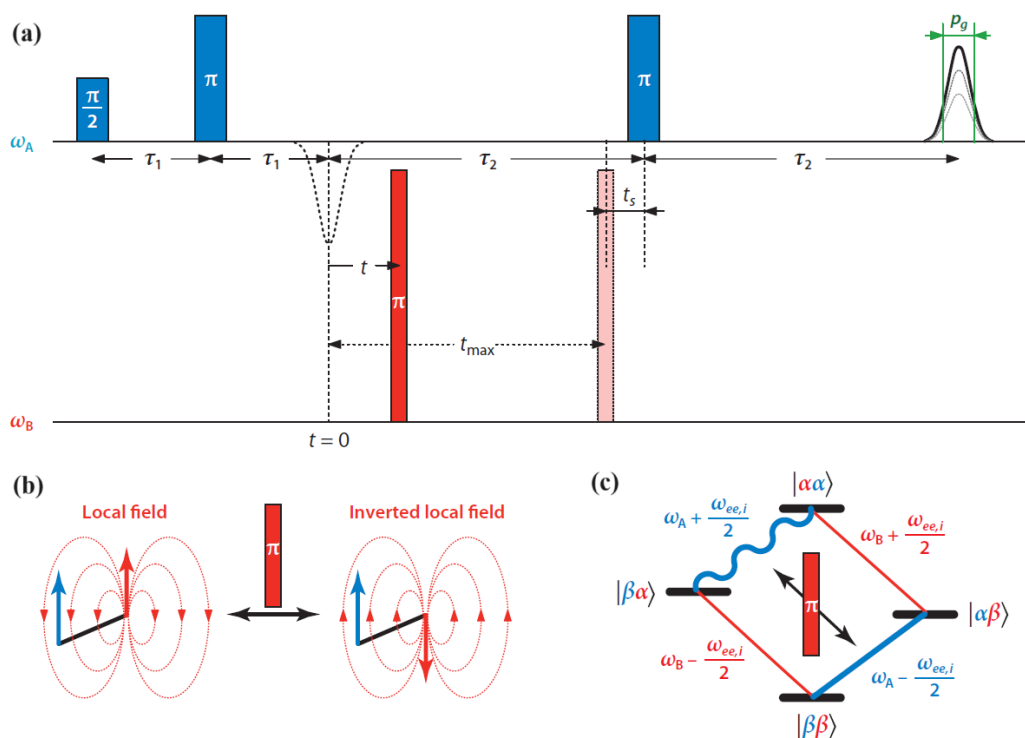


Figure 2.38 Fundamental principle of 4-pulse DEER Experiment. (a) Pulse sequence. **Pump** pulse time varies from  $t = 0$  to  $t_{max}$  and the echo intensity during the length  $p_g$  is measured.  $t_s$  is the minimum spacing between the  $\pi$  **pump** pulse and refocusing  $\pi$  **observer** pulse kept avoiding end artifacts of signal. (b) Change in local field due to pump pulse. Pump pulse of frequency  $\omega_B$  inverts the **B** spins thereby inverting the local field induced by **B** near **A** spins. (c) Energy diagram

indicating the change in coherence of **A** spins due to local field change by inversion of **B** spins is equal to  $\omega_{ee}$ . Figure was taken from Jeschke G. (2012). DEER distance measurements on proteins. *Annual review of physical chemistry*, 63, 419–446.

First assumption considers both spins to be quantized along the external magnetic field while neglecting exchange coupling between spins. This allows us to calculate  $\omega_{ee}$  as magnetic dipole-dipole coupling using Eq. 2.27 as

$$\omega_{ee, i} = \frac{C_i}{r_i^3} (1 - 3 \cos^2 \theta_i) \quad \text{where } C_i \propto g_A g_B \quad (\text{Eq 2.30})$$

(Noting that the extra negative sign when compared Eq 2.30 and Eq.2.27 is due to the pumping field being larger than the observer field. When calculating frequency,  $\Delta B = B_{observe} - B_{pump}$  therefore  $\Delta B$  becomes negative.)

Second assumption states that for a given spin A, there is only one spin B that is within the sensitive range of DEER. This assumes all B spins in other molecules to be distributed evenly in space. This simplifies homogeneous spatial distribution to a homogeneous distribution with fractional dimension denoted by D. This simplifies the data analysis process where  $D \approx 2$  can be assumed for membrane proteins imbedded in lipid liposomes and a  $D \approx 3$  can be assumed for soluble proteins or proteins in detergent.

Third assumption states that the dependency of  $\lambda_i$  and  $\omega_{ee,i}$  to  $\theta_i$  is neglected. Instead, an orientational average is considered. With these assumptions, Eq 2.29 simplifies to

$$V(t) = \{1 - \lambda [1 - \int_0^1 \cos(\frac{C_i}{r_i^3} (1 - 3 \cos^2 \theta_i) t) d\cos\theta]\} B(t) \quad (\text{Eq. 2.31})$$

where  $B(t) = e^{-c_B K_B t^{D/3}}$  and is defined as the background function.  $c_B$  is the concentration of B spins,  $K_B$  is the instantaneous diffusion strength of B spins and  $D$  is the fractional dimension.  $V(t)$  takes the form  $V(t) = F(t)B(t)$  when there are multiple B spins within sensitive DEER range where  $F(t)$  defined as “form factor” exhibit the product of all possible pairwise contributions.

The obtained DEER trace is a combination of spin pair interaction between the A spin and a B spin within the same molecule (intramolecular interactions) and between a B spin in a different molecule (intermolecular interactions). The time-domain signal  $V(t)$  consisting of form factor  $F(t)$  and background function  $B(t)$  is processed where  $V(t)$  is divided by  $B(t)$  to obtain  $F(t)$  (Figure 2.39a). The resulting  $F(t)$  appears as a damped oscillation where the frequency is inversely proportional to the cube of the mean distance between the A and B spins which is used to obtain distance distributions (Figure 2.39b,c). The width of the distance distribution has an inverse relationship with the decay of the oscillation<sup>66,67</sup>.

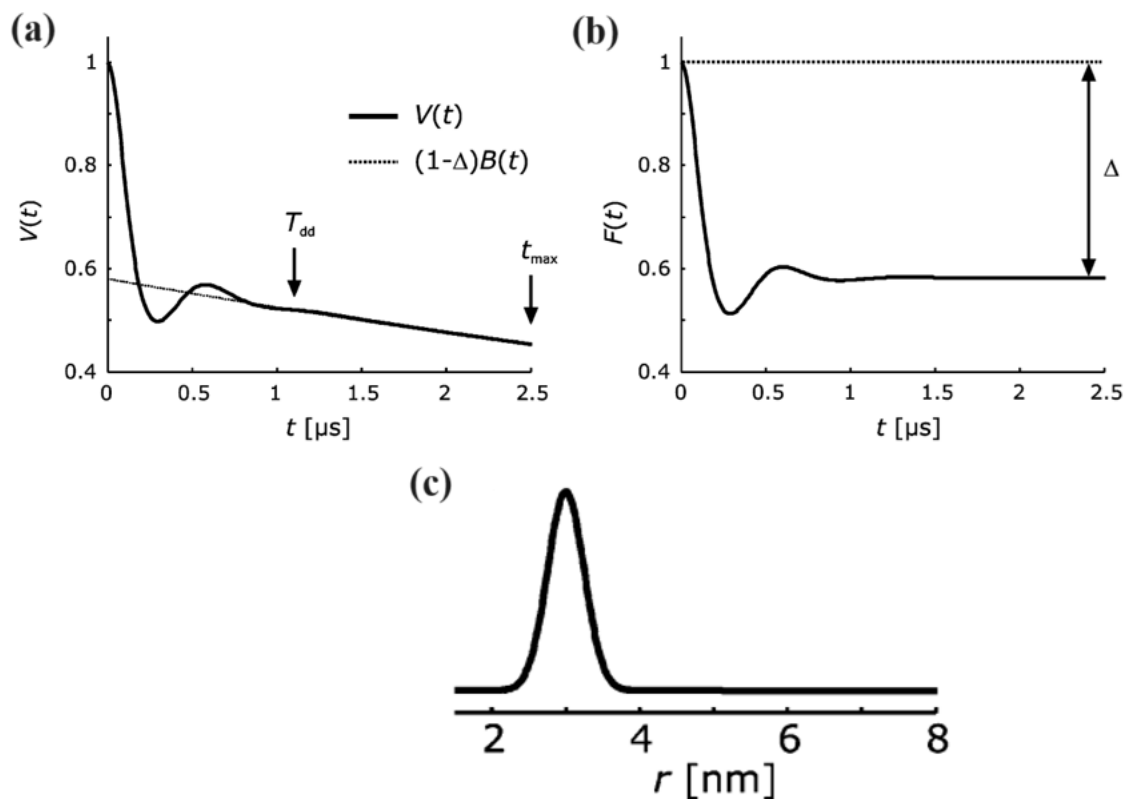


Figure 2.39 Separation of time domain trace  $V(t)$  to obtain form factor  $F(t)$  by removing background function  $B(t)$  to extract distance distribution data. (a) dipolar evolution data obtained until a time of  $t_{max}$  where the oscillation has decayed at time  $T_{dd}$  followed by fitting of background function (dash lines). (b) Form factor obtained by division of  $B(t)$  from  $V(t)$  and normalized to zero time where  $\Delta$  is the modulation depth. (c) Gaussian distance distribution obtained based on  $F(t)$ . Figure was taken from Jeschke, G., & Polyhach, Y. (2007). Distance measurements on spin-labelled biomacromolecules by pulsed electron paramagnetic resonance. *Physical chemistry chemical physics : PCCP*, 9(16), 1895–1910.

#### 2.5.4.2 Crucial factors for a successful DEER Experiment

Selection of optimum frequency for observer and pump pulses is very crucial in a successful DEER experiment. There are few criteria that must be satisfied, and these criteria can

vary based on the type of sample. One major criterion is that the observer and pump pulses should not overlap. Thus, the gap between these two pulses should be at least 50 MHz. The other criteria are optimizing DEER modulation and sensitivity. For this purpose, a field sweep EPR spectrum of the sample is obtained. For nitroxide, the maximum of the field sweep spectra can be used for either detection or pumping. For better modulation, it is found that pumping at the maximum provides high efficiency of spin inversion for dipolar coupling therefore the pump pulse is kept at the maximum intensity. For detection in a nitroxide system, it is preferable to use the low field edge as it differs to pump frequency by 65 MHz (satisfy overlap criteria), and it is of higher intensity than the high field edge (Figure 2.40)<sup>58</sup>.

A crucial fact is that the detected refocused echo will exponentially decay with the phase memory time ( $T_m$ ) after the first observer  $\pi/2$  pulse. With increasing distance between paramagnetic species, the dipolar oscillations in echo intensity become longer and the echo intensity decreases significantly. To overcome this, the pump pulse should be provided for a long-time frame to properly characterize and identify these oscillations.

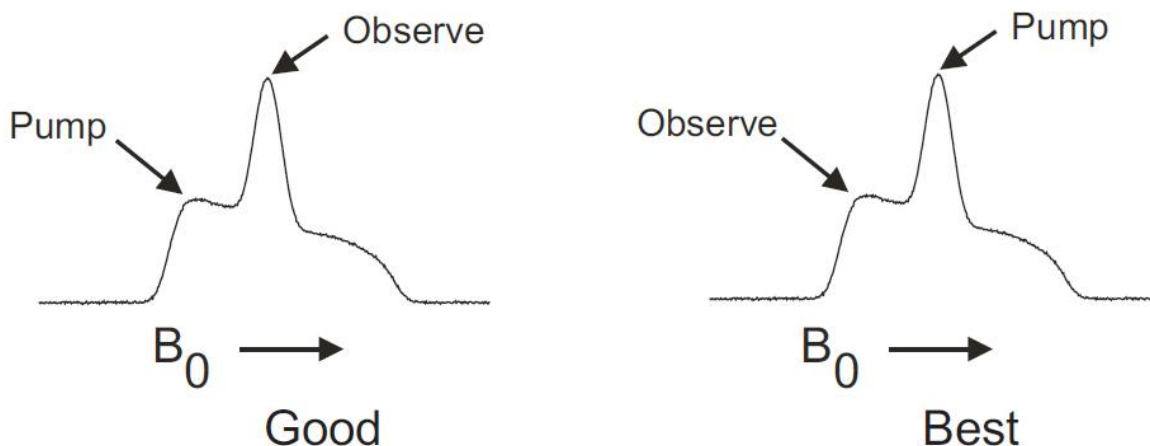


Figure 2.40 Possible positions for observer and pump pulses in the EPR spectra for nitroxide in DEER. Figure was taken from <https://www.yumpu.com/en/document/read/45359546/e580-pulsedpdf> (Accessed on 3rd June 2024)

Performing DEER experiments at lower temperature can also assist in detecting the refocused echo with higher sensitivity. A minimum  $T_m$  value of 0.5  $\mu\text{s}$  should be satisfied to detect the refocused echo. The rotation of the methyl groups commonly present in nitroxide spin labels strongly affects the  $T_m$  where the minimum condition is achieved at a temperature close to 120 K. To ensure long  $T_m$  values, experiments are performed below 90 K. However, this gives rise to another conundrum which is the increase of spin lattice relaxation time ( $T_1$ ). Low temperatures can increase relaxation times thus delaying the time in which the experiment can be repeated. To satisfy both parties, a temperature of 50 K is found to provide long  $T_m$  and short  $T_1$  values for DEER experiments.

Optimization of DEER modulation depth can be achieved by optimizing the pump pulse length through a nutation experiment. The observer and pump pulse frequencies are kept at an identical value, and a variable length pump pulse is applied before a Hahn echo detection at the observer frequency. The first minima of the oscillatory plot obtained with intensity vs pulse length gives the maximum inversion and thus the optimum pulse length for pump pulse.

As mentioned previously, two pulses are sufficient for the generation of an echo. Thus, we would assume that we would see multiple echoes in our 4-pulse system and require phase cycling to remove unwanted echoes. In the DEER experiment, the observer pulses are stationary, and the pump pulse is incoherent with the observer frequency therefore motion of pump pulse does not generate echoes. Though we assume no need of phase cycling, it is still performed to remove DC

offsets for simplification of data analysis. Furthermore, it assists in identifying the correct refocused echo by cancelling out all echoes except for first Hahn echo and the refocused echo.

Proper identification of data acquisition trigger time and integrator gate length ( $p_g$  in Figure 2.38a) is crucial to obtain optimum signal-to-noise ratio (SNR) for echo detection. These parameters are selected to satisfy the Davies criterion for echoes (Figure 2.41a).

Measures must be taken to ensure no overlap of observer and pump pulses by simultaneous application throughout the experiment as it can produce artifacts in the DEER signal. The two conditions that need to be avoided are the overlap of second observer ( $\pi$ ) pulse and the third observer ( $\pi$ ) pulse with the pump ( $\pi$ ) pulse (Figure 2.41b). To avoid the overlap with the second observer pulse, a delay ( $d3$ ) greater than the second observer pulse ( $p1$ ) is set before the beginning of the pump pulse. Avoiding the third observer pulse is tricky, but it can be achieved by selecting the number of points ( $sx$ ) for the DEER experiment such that,

$$sx < \frac{d1+d2-d3-p3}{d30} \quad (\text{Eq 2.32})$$

where  $sx$  is the number of points,  $d1+d2$  is the time between the second and third observer pulses,  $d3$  is the delay between second observe pulse and beginning of pump pulse,  $p3$  is the pump pulse length, and  $d30$  is the time resolution.

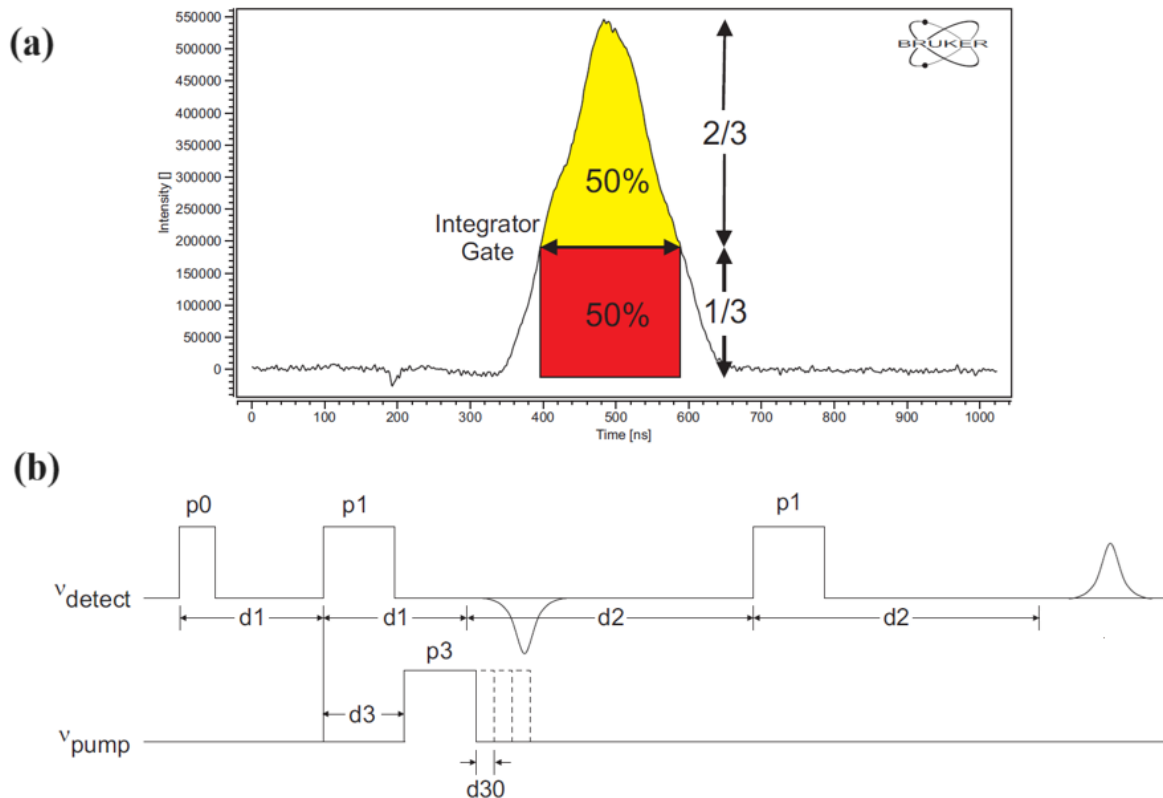


Figure 2.41 Optimum conditions for successful DEER experiment. (a) Davies Criterion for optimum S/N ratio (b) Pulse sequence with definitions to select optimum number of points. Figure was taken from <https://www.yumpu.com/en/document/read/45359546/e580-pulsedpdf> (Accessed on 3rd June 2024)



## 2.6 Reference

1. Khehra, N., Padda, I. S., & Swift, C. J. (2023). Polymerase Chain Reaction (PCR). In *StatPearls*. StatPearls Publishing.
2. Rychlik, W., Spencer, W. J., & Rhoads, R. E. (1990). Optimization of the annealing temperature for DNA amplification in vitro. *Nucleic acids research*, *18*(21), 6409–6412.
3. Lundberg, K. S., Shoemaker, D. D., Adams, M. W., Short, J. M., Sorge, J. A., & Mathur, E. J. (1991). High-fidelity amplification using a thermostable DNA polymerase isolated from *Pyrococcus furiosus*. *Gene*, *108*(1), 1–6.
4. Lu, L., Patel, H., & Bissler, J. J. (2002). Optimizing DpnI digestion conditions to detect replicated DNA. *BioTechniques*, *33*(2), 316–318.
5. de la Campa, A. G., Springhorn, S. S., Kale, P., & Lacks, S. A. (1988). Proteins encoded by the DpnI restriction gene cassette. Hyperproduction and characterization of the DpnI endonuclease. *The Journal of biological chemistry*, *263*(29), 14696–14702.
6. Green, M. R., & Sambrook, J. (2019). Analysis of DNA by agarose gel electrophoresis. *Cold Spring Harbor Protocols*, *2019*(1), pdb-top100388.
7. Green, M. R., & Sambrook, J. (2020). Recovery of DNA from low-melting-temperature agarose gels: organic extraction. *Cold Spring Harbor Protocols*, *2020*(3), pdb-prot100461.
8. <https://www.uniprot.org/>. Accessed on 21<sup>st</sup> May 2024
9. <https://web.expasy.org/translate/>. Accessed on 21<sup>st</sup> May 2024
10. <https://www.idtdna.com/pages/tools/oligoanalyzer?returnurl=%2Fcalc%2Falyzer>. Accessed on 21<sup>st</sup> May 2024

11. Klock, H. E., & Lesley, S. A. (2009). The Polymerase Incomplete Primer Extension (PIPE) method applied to high-throughput cloning and site-directed mutagenesis. *High Throughput Protein Expression and Purification: Methods and Protocols*, 91-103.
12. <https://clims4.genewiz.com/RegisterAccount/Login>. Accessed on 21<sup>st</sup> May 2024
13. <https://www.plasmidsaurus.com/>. Accessed on 21<sup>st</sup> May 2024
14. [https://assets.thermofisher.com/TFS-Assets/LSG/manuals/MAN0012888\\_Pfu\\_DNAPolymerase\\_ep0571\\_UG.pdf](https://assets.thermofisher.com/TFS-Assets/LSG/manuals/MAN0012888_Pfu_DNAPolymerase_ep0571_UG.pdf). Accessed on 22<sup>nd</sup> May 2024
15. Russel, D., & Sambrook, J. (2001). *Molecular cloning: a laboratory manual*. New.
16. Wycuff, D. R., & Matthews, K. S. (2000). Generation of an AraC-araBAD promoter-regulated T7 expression system. *Analytical biochemistry*, 277(1), 67-73.
17. *Document Connect*. (2024). Thermofisher.com. [https://www.thermofisher.com/document-connect/document-connect.html?url=https://assets.thermofisher.com/TFS-Assets%2FLSG%2Fmanuals%2FMAN0013117\\_GeneJET\\_Plasmid\\_Miniprep\\_UG.pdf](https://www.thermofisher.com/document-connect/document-connect.html?url=https://assets.thermofisher.com/TFS-Assets%2FLSG%2Fmanuals%2FMAN0013117_GeneJET_Plasmid_Miniprep_UG.pdf). Accessed on 22<sup>nd</sup> May 2024
18. <https://assets.thermofisher.com/TFS-Assets/BID/brochures/dna-purification-analysis-brochure.pdf>. Accessed on 22<sup>nd</sup> May 2024.
19. Lucena-Aguilar, G., Sánchez-López, A. M., Barberán-Aceituno, C., Carrillo-Ávila, J. A., López-Guerrero, J. A., & Aguilar-Quesada, R. (2016). DNA Source Selection for Downstream Applications Based on DNA Quality Indicators Analysis. *Biopreservation and biobanking*, 14(4), 264–270.

20. Crossley, B. M., Bai, J., Glaser, A., Maes, R., Porter, E., Killian, M. L., Clement, T., & Toohey-Kurth, K. (2020). Guidelines for Sanger sequencing and molecular assay monitoring. *Journal of veterinary diagnostic investigation : official publication of the American Association of Veterinary Laboratory Diagnosticians, Inc*, 32(6), 767–775.
21. Marx V. (2023). Method of the year: long-read sequencing. *Nature methods*, 20(1), 6–11.
22. Uematsu, M., & Baskin, J. M. (2023). Barcode-free multiplex plasmid sequencing using Bayesian analysis and nanopore sequencing. *bioRxiv : the preprint server for biology*, 2023.04.12.536413.
23. <https://www.snapgene.com/>. Accessed on 22<sup>nd</sup> May 2024
24. [https://blast.ncbi.nlm.nih.gov/Blast.cgi?PAGE=Proteins&PROGRAM=blastp&BLAST\\_PROGRAMS=blastp&PAGE\\_TYPE=BlastSearch&BLAST\\_SPEC=blast2seq&DATABASE=n/a&QUERY=&SUBJECTS=](https://blast.ncbi.nlm.nih.gov/Blast.cgi?PAGE=Proteins&PROGRAM=blastp&BLAST_PROGRAMS=blastp&PAGE_TYPE=BlastSearch&BLAST_SPEC=blast2seq&DATABASE=n/a&QUERY=&SUBJECTS=). Accessed on 22<sup>nd</sup> May 2024
25. Sanders E. R. (2012). Aseptic laboratory techniques: plating methods. *Journal of visualized experiments : JoVE*, (63), e3064.
26. Bykowski, T., & Stevenson, B. (2008). Aseptic technique. *Current protocols in microbiology, Appendix 4*, .
27. <https://goldbio.com/articles/article/understanding-competent-cells-for-bacterial-transformation#:~:text=To%20make%20chemically%20competent%20cells,move%20closer%20to%20the%20cell>. Accessed on 23<sup>rd</sup> May 2024
28. Froger, A., & Hall, J. E. (2007). Transformation of plasmid DNA into E. coli using the heat shock method. *Journal of visualized experiments : JoVE*, (6), 253.

29. Cadoret, F., Soscia, C., & Voulhoux, R. (2014). Gene transfer: transformation/electroporation. *Methods in molecular biology (Clifton, N.J.)*, 1149, 11–15.
30. Hubálek Z. (2003). Protectants used in the cryopreservation of microorganisms. *Cryobiology*, 46(3), 205–229.
31. Casasanta, M. A., & Slade, D. J. (2019). A Vector Suite for the Overexpression and Purification of Tagged Outer Membrane, Periplasmic, and Secreted Proteins in *E. coli*. *Methods in molecular biology (Clifton, N.J.)*, 1960, 123–138.
32. Miroux, B., & Walker, J. E. (1996). Over-production of proteins in *Escherichia coli*: mutant hosts that allow synthesis of some membrane proteins and globular proteins at high levels. *Journal of molecular biology*, 260(3), 289–298.
33. Danko, K., Lukasheva, E., Zhukov, V. A., Zgoda, V., & Frolov, A. (2022). Detergent-Assisted Protein Digestion-On the Way to Avoid the Key Bottleneck of Shotgun Bottom-Up Proteomics. *International journal of molecular sciences*, 23(22), 13903.
34. Butler, T. J., & Smith, S. M. (2023). Strategies for the Purification of Membrane Proteins. *Methods in molecular biology (Clifton, N.J.)*, 2699, 477–491.
35. Graeber, E., & Korkhov, V. M. (2020). Affinity Purification of Membrane Proteins. *Methods in molecular biology (Clifton, N.J.)*, 2127, 129–137.
36. Mitchell, S. F., & Lorsch, J. R. (2015). Protein Affinity Purification using Intein/Chitin Binding Protein Tags. *Methods in enzymology*, 559, 111–125.
37. dhikari, S., Manthena, P. V., Sajwan, K., Kota, K. K., & Roy, R. (2010). A unified method for purification of basic proteins. *Analytical biochemistry*, 400(2), 203–206.

38. Shen, H. H., Lithgow, T., & Martin, L. (2013). Reconstitution of membrane proteins into model membranes: seeking better ways to retain protein activities. *International journal of molecular sciences*, *14*(1), 1589–1607.
39. Majeed, S., Ahmad, A. B., Sehar, U., & Georgieva, E. R. (2021). Lipid Membrane Mimetics in Functional and Structural Studies of Integral Membrane Proteins. *Membranes*, *11*(9), 685.
40. Goddard, A. D., Dijkman, P. M., Adamson, R. J., dos Reis, R. I., & Watts, A. (2015). Reconstitution of membrane proteins: a GPCR as an example. *Methods in enzymology*, *556*, 405–424.
41. Chaffey, N. (2003). Alberts, B., Johnson, A., Lewis, J., Raff, M., Roberts, K. & Walter, P. *Molecular biology of the cell*. 4th edn.
42. Jeschke, G., & Polyhach, Y. (2007). Distance measurements on spin-labelled biomacromolecules by pulsed electron paramagnetic resonance. *Physical chemistry chemical physics : PCCP*, *9*(16), 1895–1910.
43. Fanucci, G. E., & Cafiso, D. S. (2006). Recent advances and applications of site-directed spin labeling. *Current opinion in structural biology*, *16*(5), 644–653.
44. Klare, J. P., & Steinhoff, H. J. (2009). Spin labeling EPR. *Photosynthesis research*, *102*(2-3), 377–390.
45. Klug, C. S., & Feix, J. B. (2008). Methods and applications of site-directed spin labeling EPR spectroscopy. *Methods in cell biology*, *84*, 617–658.

46. Kucher, S., Korneev, S., Tyagi, S., Apfelbaum, R., Grohmann, D., Lemke, E. A., Klare, J. P., Steinhoff, H. J., & Klose, D. (2017). Orthogonal spin labeling using click chemistry for in vitro and in vivo applications. *Journal of magnetic resonance (San Diego, Calif. : 1997)*, 275, 38–45.
47. Becker, C. F., Lausecker, K., Balog, M., Kálai, T., Hideg, K., Steinhoff, H. J., & Engelhard, M. (2005). Incorporation of spin-labelled amino acids into proteins. *Magnetic resonance in chemistry : MRC, 43 Spec no.*, S34–S39.
48. Cornish, V. W., Benson, D. R., Altenbach, C. A., Hideg, K., Hubbell, W. L., & Schultz, P. G. (1994). Site-specific incorporation of biophysical probes into proteins. *Proceedings of the National Academy of Sciences of the United States of America*, 91(8), 2910–2914.
49. Sahu, I. D., & Lorigan, G. A. (2018). Site-Directed Spin Labeling EPR for Studying Membrane Proteins. *BioMed research international*, 2018, 3248289.
50. Columbus, L., & Hubbell, W. L. (2002). A new spin on protein dynamics. *Trends in biochemical sciences*, 27(6), 288–295.
51. Junk, M. J. (2012). *Assessing the functional structure of molecular transporters by EPR spectroscopy*. Springer Science & Business Media.
52. [https://webhome.auburn.edu/~duinedu/epr/1\\_theory.pdf](https://webhome.auburn.edu/~duinedu/epr/1_theory.pdf). Accessed on 28th May 2024.
53. Hagen, W. R. (2008). *Biomolecular EPR spectroscopy*. CRC press.
54. Torricella, F., Pierro, A., Mileo, E., Belle, V., & Bonucci, A. (2021). Nitroxide spin labels and EPR spectroscopy: A powerful association for protein dynamics studies. *Biochimica et biophysica acta. Proteins and proteomics*, 1869(7), 140653.

55. Fanucci, G. E., Coggshall, K. A., Cadieux, N., Kim, M., Kadner, R. J., & Cafiso, D. S. (2003). Substrate-induced conformational changes of the periplasmic N-terminus of an outer-membrane transporter by site-directed spin labeling. *Biochemistry*, *42*(6), 1391–1400.
56. Columbus, L., Kálai, T., Jekő, J., Hideg, K., & Hubbell, W. L. (2001). Molecular motion of spin labeled side chains in alpha-helices: analysis by variation of side chain structure. *Biochemistry*, *40*(13), 3828–3846.
57. [https://www.researchgate.net/profile/Johann-Klare/publication/320871897\\_An\\_Introduction\\_to\\_Pulsed\\_EPR\\_Spectroscopy\\_-\\_A\\_lecture\\_held\\_at\\_the\\_3rd\\_Workshop\\_on\\_EPR\\_Spectroscopy\\_-\\_06-08112013\\_-\\_University\\_of\\_Osnabruck\\_Germany/links/5a0055970f7e9b62a14d2d6a/An-Introduction-to-Pulsed-EPR-Spectroscopy-A-lecture-held-at-the-3rd-Workshop-on-EPR-Spectroscopy-06-08112013-University-of-Osnabrueck-Germany.pdf](https://www.researchgate.net/profile/Johann-Klare/publication/320871897_An_Introduction_to_Pulsed_EPR_Spectroscopy_-_A_lecture_held_at_the_3rd_Workshop_on_EPR_Spectroscopy_-_06-08112013_-_University_of_Osnabruck_Germany/links/5a0055970f7e9b62a14d2d6a/An-Introduction-to-Pulsed-EPR-Spectroscopy-A-lecture-held-at-the-3rd-Workshop-on-EPR-Spectroscopy-06-08112013-University-of-Osnabrueck-Germany.pdf). Accessed on 3<sup>rd</sup> June 2024
58. Yumpu.com. (2024). *E580 Pulsed.pdf*. Yumpu.com. <https://www.yumpu.com/en/document/read/45359546/e580-pulsedpdf>. Accessed on 3<sup>rd</sup> June 2024
59. *CW and Pulse EPR*. (n.d.). Epr.ethz.ch. <https://epr.ethz.ch/education/basic-concepts-of-epr/cw-and-pulse-epr.html>. Accessed on 3<sup>rd</sup> June 2024
60. Milov, A. D., Ponomarev, A. B., & Tsvetkov, Y. D. (1984). Electron-electron double resonance in electron spin echo: Model biradical systems and the sensitized photolysis of decalin. *Chemical physics letters*, *110*(1), 67-72.

61. Bahrenberg, T., Jahn, S. M., Feintuch, A., Stoll, S., & Goldfarb, D. (2021). The decay of the refocused Hahn echo in double electron–electron resonance (DEER) experiments. *Magnetic Resonance*, 2(1), 161-173.
62. Jeschke, G., Wegener, C., Nietschke, M., Jung, H., & Steinhoff, H. J. (2004). Interresidual distance determination by four-pulse double electron-electron resonance in an integral membrane protein: the Na<sup>+</sup>/proline transporter PutP of Escherichia coli. *Biophysical journal*, 86(4), 2551–2557.
63. Borbat, P. P., McHaourab, H. S., & Freed, J. H. (2002). Protein structure determination using long-distance constraints from double-quantum coherence ESR: study of T4 lysozyme. *Journal of the American Chemical Society*, 124(19), 5304–5314.
64. Jeschke G. (2012). DEER distance measurements on proteins. *Annual review of physical chemistry*, 63, 419–446.
65. Pannier, M., Veit, S., Godt, A., Jeschke, G., & Spiess, H. W. (2011). Dead-time free measurement of dipole-dipole interactions between electron spins. 2000. *Journal of magnetic resonance (San Diego, Calif. : 1997)*, 213(2), 316–325.
66. Nilaweera, T. D. (2018). Exploring BtuB in Escherichia coli via a new direct spin labeling approach and electron paramagnetic resonance spectroscopy (Doctoral Thesis Dissertation). University of Virginia, Charlottesville, USA.
67. Nyenhuis, D. A. (2019). The Behavior of Spin-Labeled Mutants of the Escherichia coli Cobalamin Transporter BtuB Probed by EPR Spectroscopy in Native Environments (Doctoral Thesis Dissertation). University of Virginia, Charlottesville, USA.



## **Chapter 3: A disulfide chaperone knockout significantly enhances double spin labeling efficiency of BtuB for *in-vitro* pulse EPR spectroscopy**

### 3.1 Abstract

The outer membrane (OM) of Gram-negative bacteria contains several porins and transporters that are crucial for bacterial growth and survival. These transporters include TonB-dependent transporters (TBDTs) that facilitate the active uptake of trace metals and complex carbohydrates and are critical for the microbiome as well as the survival and virulence of many pathogens. During active transport, TBDTs couple with the trans-periplasmic protein, TonB and utilize energy from the inner membrane (IM) proton motive force. However, the exact mechanism of transport is not well understood. Recently, we have shown that it is possible to examine the structure of BtuB, the *E. coli* vitamin B<sub>12</sub> transporter, using Electron Paramagnetic Resonance (EPR) spectroscopy in intact cells. Distance measurements using pulse EPR require that pairs of labels be placed within BtuB, which was accomplished by site-directed spin labelling of cysteines. In cells, this required the use of a knockout of the Dsb system that functions to oxidize pairs of cysteines. Using a *dsbA*<sup>-</sup> strain, we have shown that the protein appears to have a different configuration *in-vivo* when compared to earlier work of reconstituted BtuB in liposomes. While comparing the *in-vivo* and *in-vitro* systems, we discovered that cysteine double mutants' *in-vitro* labeling efficiencies are poor when expressed in a wild-type strain. In contrast, we were able to efficiently spin label purified BtuB expressed in *dsbA*<sup>-</sup> strain. These results indicate that knocking out the Dsb system also promotes efficient double labeling for reconstituted membrane proteins that are isolated from the OM and facilitate the studies of BtuB in both *in-vivo* and *in-vitro* conditions<sup>1</sup>.

(Note: Portions of this chapter were published in the following research article and biophysical society (BPS) conference abstract: Wimalasiri, V. W., Jurczak, K. A., Wieliniec, M. K., Nilaweera, T. D., Nakamoto, R. K., & Cafiso, D. S. (2023). A disulfide chaperone knockout facilitates spin labeling and pulse EPR spectroscopy of outer membrane transporters. *Protein science : a publication of the Protein Society*, 32(7), e4704. Abstract obtained from Wimalasiri, V. W., Nilaweera, T. D., & Cafiso, D. S. (2021). Disulfide Chaperone Knockouts Facilitate Double Spin Labelling of an Outer Membrane Transporter For in Vitro EPR Studies. *Biophysical Journal*, 120(3), 72a-73a.)

### 3.2 Introduction

Gram-negative bacteria such as *Escherichia coli* (*E. coli*) consist of 2 membranes, namely outer membrane (OM) and inner membrane (IM). The OM is an asymmetric bilayer composed of phospholipids present in the inner leaflet and lipopolysaccharides (LPS) present in the outer leaflet with outer membrane proteins (OMPs). These two membranes provide robust, antibiotic resistant and adaptable properties, active transport, enzymatic activity and various critical functions required for bacterial survival<sup>3,4</sup>. Compounds greater than ~600 Da of molecular size cannot diffuse through the OM; therefore *E. coli* and other Gram-negative bacteria obtain their essential nutrients such as vitamin B<sub>12</sub>, carbohydrates, and metal complexes using active transporter proteins in the OM that have high affinity and unique specificity<sup>5,6</sup>. One such class is TonB-dependent transporters (TBDTs), which uptake essential nutrients by utilizing the proton motive force (PMF) present in the IM by coupling to IM protein complex TonB/ExbB/ExbD<sup>7</sup>. TBDTs are structurally homologous with the C-terminal folded into a 22-stranded  $\beta$ -barrel and the N-terminus forming a globular core-domain (plug domain) to occlude the interior of the barrel. The extracellular surface

of the  $\beta$ -barrel is composed of long loops, postulated to be crucial for substrate binding during active transport; whereas the periplasmic surface consist of short turns connecting the  $\beta$  sheets<sup>8</sup>. Even though a considerable number of studies on TBDTs have been carried out in non-native reconstituted systems, the mechanism of active transport of TBDTs is yet to be discovered.

Site-directed spin labeling (SDSL) coupled with EPR spectroscopy has evolved into a method that is widely used to examine structural and functional dynamics of soluble and membrane proteins. SDSL involves the attachment of a spin label through a specific residue (Ex: cysteine substitution DNA mutagenesis followed by modification of thiol through nitroxide spin labeling) followed by examination of the spin probe through EPR spectroscopy. This provides us with a plethora of information such as solvent accessibility, polarity index about the immediate environment, local secondary structure and protein-protein interactions (tertiary interactions), protein conformational changes<sup>9</sup>. In the presence of another paramagnetic center, distance measurements between the two centers can be obtained through pulse EPR techniques such as Double Electron-Electron Resonance (DEER)<sup>10</sup>. This has been previously used to study conformational and structural changes of TBDTs such as ferric citrate transporter FecA<sup>11</sup>, ferrichrome transporter FhuA<sup>12</sup>, and most importantly on the cobalamin transporter BtuB<sup>13,14</sup> *in-vitro* in membrane reconstituted reconstituted systems. TBDT has never been reconstituted as it requires the OMP interaction with the IM TonB coupled with ExbB/ExbD complex simultaneously. This led us to develop EPR methods that could be applied to *in-vivo* systems so that changes in protein structure and dynamics could be examined in the native environment where proteins are known to be active. This also allows us to gain insight to structural changes that may be present in an *in-vivo* energized system but are not observed in the isolated systems.

DEER spectroscopy of OMPs over expressed in the intact bacteria has provided valuable knowledge regarding the regulation of protein structure by the native outer membrane. It has been observed that structural heterogeneity and gating movements in the extracellular loops of BtuB that are observed in isolated systems<sup>15</sup> are absent in the intact cell<sup>16</sup>. Furthermore, structural transitions have been observed within the plug domain of BtuB in the intact cell, that are not observed for the protein in a purified and phospholipid reconstituted bilayer<sup>17</sup>. Moreover, the *in-vivo* system allows us to study the important TBDT-TonB interactions involved in active transport. However, spin labeling OMPs in the intact cell may be very challenging, since periplasmic label sites are prone to rapid reduction due to the reducing environment, whereas isolated systems will retain the attached spin label and provide good signal to noise ratio in EPR experiments.

In intact *Escherichia coli* (*E. coli*), outer membrane proteins typically have zero or an even number of cysteines<sup>18</sup>. BtuB lacks cysteines and single cysteines that are incorporated into BtuB can be efficiently spin labeled *in-vivo* using the K12-derived strain RK5016<sup>19</sup>. However, when pairs of cysteines are incorporated into BtuB and the protein is expressed in RK5016 under conditions where the cell viability is maintained, *in-vivo* labeling of BtuB does not occur, and this is a direct consequence of the presence of a periplasmic disulfide oxidation (Dsb) system that functions to cross-link pairs of cysteines (see Figure 3.1). Labeling can be performed on pairs of cysteines in BtuB *in-vivo* using an *E. coli* strain deficient in the activity of either DsbA or DsbB<sup>2,19</sup>.

In this work, we show that for *in-vitro* preparations of BtuB, where the protein is purified and reconstituted into phospholipid vesicles, the use of a DsbA minus strain enhances overall labeling efficiency, indicating that double spin labeling even on the purified isolate protein is improved using a Dsb deficient strain. Evidence for BtuB-BtuB interactions that had previously

been seen only in cells is seen in membrane reconstituted BtuB that is obtained from the DsbA minus strain, and this is likely a result of the enhanced labeling efficiency.

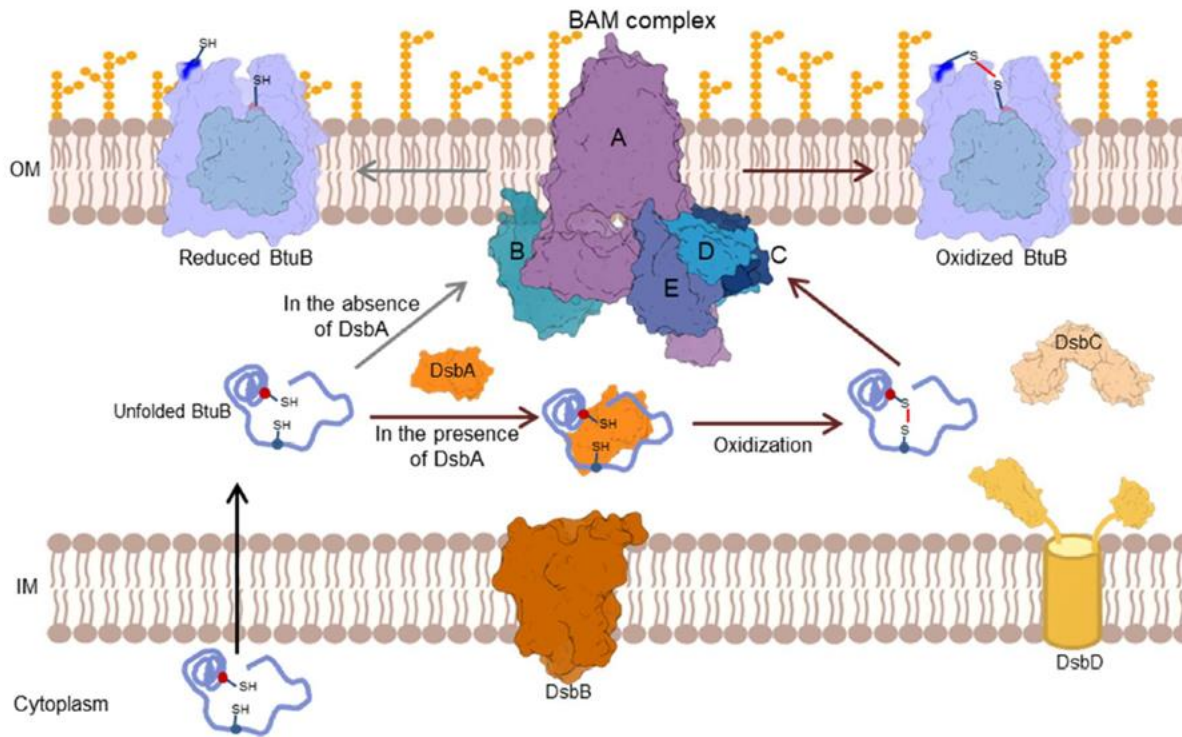


Figure 3.1 The disulfide bond formation system responsible for crosslinking pairs of cysteine residues in OMPs before reaching the OM. Electrons are extracted from unfolded BtuB containing free thiols by DsbA which is delivered to DsbB in the IM, and ultimately transported into the electron transport chain in the IM. This process in turn re-oxidizes thiols in DsbA for function. OMPs that have disulfides that require isomerization, DsbC acts as an isomerase for function which is re-energized by DsbD in the IM. Unfolded BtuB after interacting with the Dsb system is then folded and inserted into the OM at the BAM complex. Figure was obtained from Nilaweera, T. D., Nyenhuis, D. A., Nakamoto, R. K., & Cafiso, D. S. (2019). Disulfide Chaperone Knockouts Enable In Vivo Double Spin Labeling of an Outer Membrane Transporter. *Biophysical journal*, 117(8), 1476–1484.

### 3.3. Materials and Methods

#### 3.3.1 Cell lines and plasmids

For the vitamin B<sub>12</sub> transporter, BtuB, the pAG1 plasmid with WT *btuB* gene and the *E. coli* strain RK5016 (*-argH*, *-btuB*, *-metE*) was obtained from late Professor Robert Kadner, University of Virginia. Both wild-type and mutant *dsb E. coli* strains were obtained from the Coli Genetic Stock Center (Yale University, New Haven, CT). Strain RI89 carries the WT Dsb system (*araD139 Δ(araABC-leu)7679 galU galK Δ(lac)X74 rpsL thi phoR Δara714 leu+*), whereas strain RI90 carries the *dsbA* null mutation system (*araD139 Δ(araABC-leu) 7679 galU galK Δ(lac)X74 rpsL thi phoR Δara714 leu +dsbA:: Kanr*)<sup>2</sup>.

#### 3.3.2 PCR mutagenesis and OMP expression

BtuB double cysteine mutations (V90C-T188C, D6C-Q510C) were generated using site-directed mutagenesis and polymerase incomplete primer extension<sup>20</sup> followed by DNA sequencing verification (Genewiz, South Plainfield, NJ). The *btuB* containing plasmids were transformed into both RK5016 and *dsbA*<sup>-</sup> strains.

A single colony was used to inoculate Luria-Bertani (LB) media and prepare a glycerol stock which was stored at -80 °C. For BtuB, precultures of Minimal Media (100 mM phosphate buffer, 8 mM (NH<sub>4</sub>)<sub>2</sub>SO<sub>4</sub>, 2 mM sodium citrate, 100 mg/mL ampicillin, 0.2% w/v glucose, 150 mM thiamine, 3 mM MgSO<sub>4</sub>, 300 mM CaCl<sub>2</sub>, 0.01% w/v methionine, 0.01% w/v arginine) were inoculated using the glycerol stock and later used to inoculate the main culture. An initial overnight preculture growth was followed by an 8 hr main culture growth. For BtuB, an initial 8 hr preculture growth was also followed by an overnight main culture growth for the RK5016 strain<sup>2</sup>.

### 3.3.3 OM and reconstituted BtuB sample preparation

An intact OM preparation is obtained from the total cell membrane fraction using a standard procedure<sup>6</sup>. This involves treating the cell membrane fraction with 1% sarkosyl to remove the inner membrane, and then pelleting the OM and removal of the sarkosyl by centrifugation. For measurements made in the OM preparation, the preparation was spin labeled at this stage<sup>19</sup>. For protein that was to be purified, the OM preparation was solubilized with OG as described previously, and 5 mL of the solubilized OM sample then was treated with 100  $\mu$ L of 22 mM MTSL [(1-oxyl-2,2,5,5-tetramethylpyrroline-3-methyl) methanethiosulfonate] followed by incubation for 2–3 hr at room temperature (RT)<sup>19</sup>. Spin labeled BtuB was purified using ion-exchange chromatography as described previously<sup>13</sup>. For some samples, BtuB was taken through two purification steps and treated with DTT following the first purification as described previously<sup>6</sup>. Briefly, the solubilized OM sample underwent an initial ion-exchange followed by treatment of the BtuB fraction with 6 mM dithiothreitol (DTT) at RT for 30 min. The sample then underwent a buffer exchange into 25 mM Tris, 17 mM OG to remove excess DTT. These samples were then treated with 100  $\mu$ L of 22 mM MTSL at RT for 2–4 hr followed by a second ion-exchange to purify BtuB from other OMPs and to remove excess MTSL<sup>6</sup>. Purified BtuB were quantified using the Bradford Assay<sup>21, 22</sup>.

The purified and spin-labeled BtuB samples were reconstituted into 1-palmitoyl-2-oleoyl-sn-glycero-3-phosphocholine (POPC) vesicles by the addition of OG/POPC (10:1) mixed micelles to the purified BtuB samples at a protein: lipid ration of 1:25. The samples were then dialyzed against six 4 L dialysis buffer changes (10 mM HEPES, 128 mM NaCl, and 1 mM EDTA at pH 6.5) at 10–12 hr intervals<sup>2, 6, 23</sup>.

### 3.3.4 EPR Measurements

For CW-EPR measurements, 5  $\mu\text{L}$  sample with 1  $\mu\text{L}$  dialysis buffer was loaded into 0.84 x 0.6 mm<sup>2</sup> quartz capillaries and used as apo sample whereas 5  $\mu\text{L}$  sample with 1  $\mu\text{L}$  of 1 mM Vitamin B<sub>12</sub> was used as the substrate bound sample. EPR spectra were recorded at room temperature at X-band using a Bruker EMX spectrometer (Billerica, MA) with an ER 4123D dielectric resonator using a sweep width of 100 gauss (G), a modulation amplitude of 1 G, and 2 mW incident microwave power. Data were collected as additive averages of 10 scans and were normalized by their second integral. For DEER, a 16  $\mu\text{L}$  sample with 4  $\mu\text{L}$  of concentrated d-glycerol was loaded into 1.1 x 1.6 mm<sup>2</sup> quartz capillaries (VitroCom, Mountain Lakes, NJ). 2  $\mu\text{L}$  of 1 mM Vitamin B<sub>12</sub> was added for samples with substrate. All DEER experiments were performed on a Bruker E580 spectrometer operating at Q-band (Bruker BioSpin, Billerica, MA) with the following hardware: Bruker EN5107D2 dielectric resonator, Bruker SpinJet-AWG, and a 300 W TWT amplifier (Applied Systems Engineering, Benbrook, TX). Experiments were run at 50 K using the standard dead-time free 4-pulse DEER experiment, with a 10 ns  $\pi/2$  pulse and 20 ns  $\pi$  pulses. All pulses were rectangular. The separation between observe and pump frequencies was 75 MHz. Acquisition times for most samples typically ranged from 10 to 15 hr<sup>2</sup>.

### 3.3.5 Data processing

All DEER data were processed with DeerAnalysis<sup>24</sup> using the DEERNet routine<sup>25</sup>. Simulated distance distributions were generated using the software package Multiscale Modeling of Macromolecules (MMM) and the default rotamer library<sup>26,27</sup>. Protein structure images were generated using Pymol<sup>2, 28</sup>.



## 3.4 Results

### 3.4.1 Expression in *dsbA*<sup>-</sup> strain improves the labeling efficiency of BtuB *in-vitro*

Figure 3.2 shows a series of EPR spectra obtained from phospholipid reconstituted BtuB at two pairs of sites, D6R1-Q510R1 on the periplasmic surface (see Figure 3.2c) and V90R1-T188R1 on the extracellular surface (see Figure 3.2d). The reconstituted BtuB proteoliposomes from which these spectra are obtained all contain equivalent levels of protein, where the reconstitution is performed in an identical manner. As indicated, BtuB was labeled and purified from *E. coli* preparations that were grown for different time periods and under different conditions in the RK5016 strain; BtuB was also labeled and purified from a strain where the thiol disulfide oxidoreductase, DsbA, was not functional. As a result, the differences in signal intensity seen in Figure 3.2 reflect differences in labeling efficiency by the MTSL reagent<sup>2</sup>.

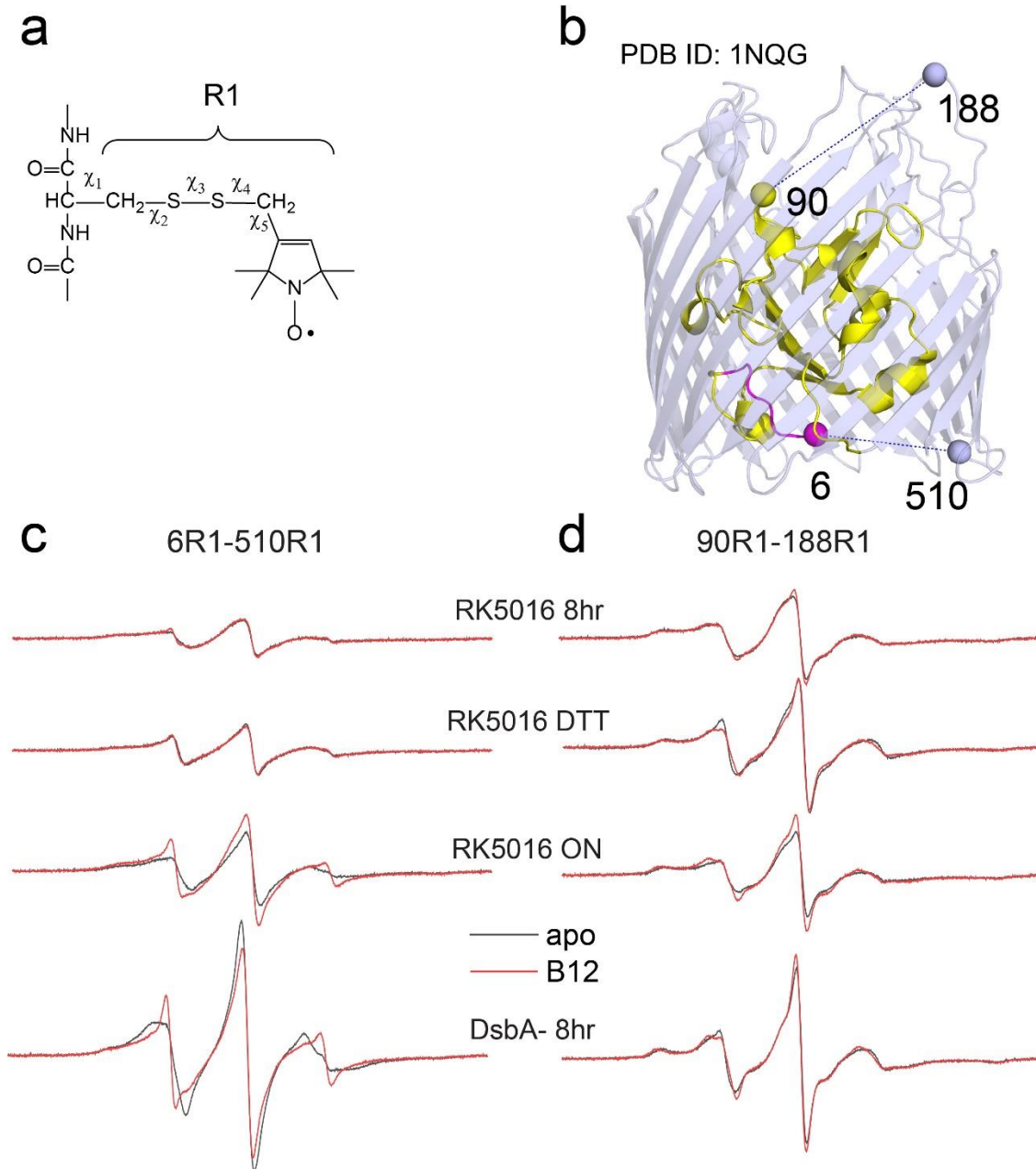


Figure 3.2 The use of DsbA deficient strain improves the relative labeling efficiency of BtuB in a phospholipid reconstituted preparation. (a) For EPR measurements, free cysteines are labeled using a conventional MTSL spin label to generate the side chain R1. In (b) crystal structure of BtuB (PDB ID: 1NQG) with sites labeled on the extracellular and periplasmic surfaces of BtuB shown as spheres. The periplasmic energy coupling Ton box is shown in magenta. In (c) are shown the EPR spectra obtained from D6R1-Q510R1 on the periplasmic interface where BtuB is

overexpressed in either the RK5016 strain or a *dsbA*<sup>-</sup> strain. The RK5016 strain was grown either for 8 hr or overnight (ON). In one case BtuB was taken through an initial ion-exchange purification and was subjected to DTT treatment and a buffer exchange. The protein was then spin labeled and taken through a second ion-exchange purification prior to reconstitution. Each reconstituted preparation includes the same quantity of BtuB and POPC. In (d) are shown the EPR spectra for the V90R1-T188R1 spin pair for BtuB that was expressed under the same conditions as shown in (c)<sup>2</sup>.

For the D6R1-Q510R1 pair (see Figure 3.2c) the 8 hr growth (top trace) yields relatively weak EPR signals that undergo an increase in amplitude of about 30% when the sample is treated with 6 mM DTT treatment prior to labeling. Site D6 in BtuB located in the N-terminal Ton box, an energy coupling segment that is known from previous *in-vitro* work to undergo a substrate-induced unfolding<sup>6, 13</sup>; however, the slight improvement in signal intensity with DTT treatment fails to yield clear evidence for a substrate-induced unfolding of the Ton box (apo and B<sub>12</sub>-bound traces are in gray and red, respectively). This earlier work was performed on *E. coli* that were grown for an extended time, and we repeated the measurement using BtuB produced from cells grown overnight. With overnight growth, the EPR signal amplitudes are increased and the substrate-induced change in the Ton box is now apparent in the EPR spectrum. However, if the cells are grown for 8 hr in the *dsbA*<sup>-</sup> strain, so that pairs of cysteines are not enzymatically oxidized in the periplasm by the Dsb system<sup>29</sup>, there is an approximately 6-fold increase in the amplitude of the resulting EPR signals relative to the 8 hr growth once the protein is purified and reconstituted. The EPR signals from the V90R1-T188R1 spin pair (see Figure 3.2d) are also improved upon expression in the *dsbA*<sup>-</sup> strain, although the increase in signal intensity is not as dramatic, in this case showing a 2-fold enhancement in signal intensity relative to equivalent levels

of protein obtained from the standard RK5016 strain. In addition to facilitating the labeling of BtuB in intact *E. coli*<sup>19</sup>, the data in Figure 3.2 indicate that the Dsb system impacts the labeling of purified and membrane reconstituted BtuB. We speculate that the improved signal intensities observed when the growth time for the RK5016 strain is extended is due to the culture entering a stationary phase, where cell growth is balanced by cell death and lysis. Cell lysis produces conditions that are reducing, and this may act to reduce oxidized cysteine pairs and increase their reactivity toward the MTSL reagent. Extended cell growth times and expression of BtuB may also compromise the Dsb system and allow some cysteine pairs to escape oxidation in the periplasm<sup>2</sup>.

### 3.4.2 Expression in *dsbA*<sup>-</sup> strain improves pulse EPR signals for labelled BtuB in both reconstituted and OM preparations

In addition to improving the quality of the CW EPR spectra obtained from purified BtuB, the use of the DsbA deficient strain also improves DEER signals obtained from reconstituted or OM preparations. Shown in Figure 3.3a are examples of DEER data obtained using the *dsbA*<sup>-</sup> strain for the D6R1-Q510R1 spin pair. Both the purified as well as the OM preparation yield similar dipolar evolutions and similar distance distributions. In these corrected DEER data, there appears to be a long but poorly defined long-distance component. This component resembles an intermolecular component that was observed previously in cells<sup>30</sup>, although the exact position and width of this longer distance is not well defined due to the relatively short echo times in these experiments. In this previous work, this long-distance component was consistent with the formation of strings of BtuB monomers that are thought to drive the formation of OMP islands<sup>23</sup>. This feature had not previously been observed in reconstituted systems where protein was expressed from a strain with an intact Dsb system. As shown in Figure 3.3b, when expressed with

a functional Dsb system, reconstituted or OM samples of labeled BtuB are noticeably poorer than those lacking an active Dsb system<sup>2</sup>.

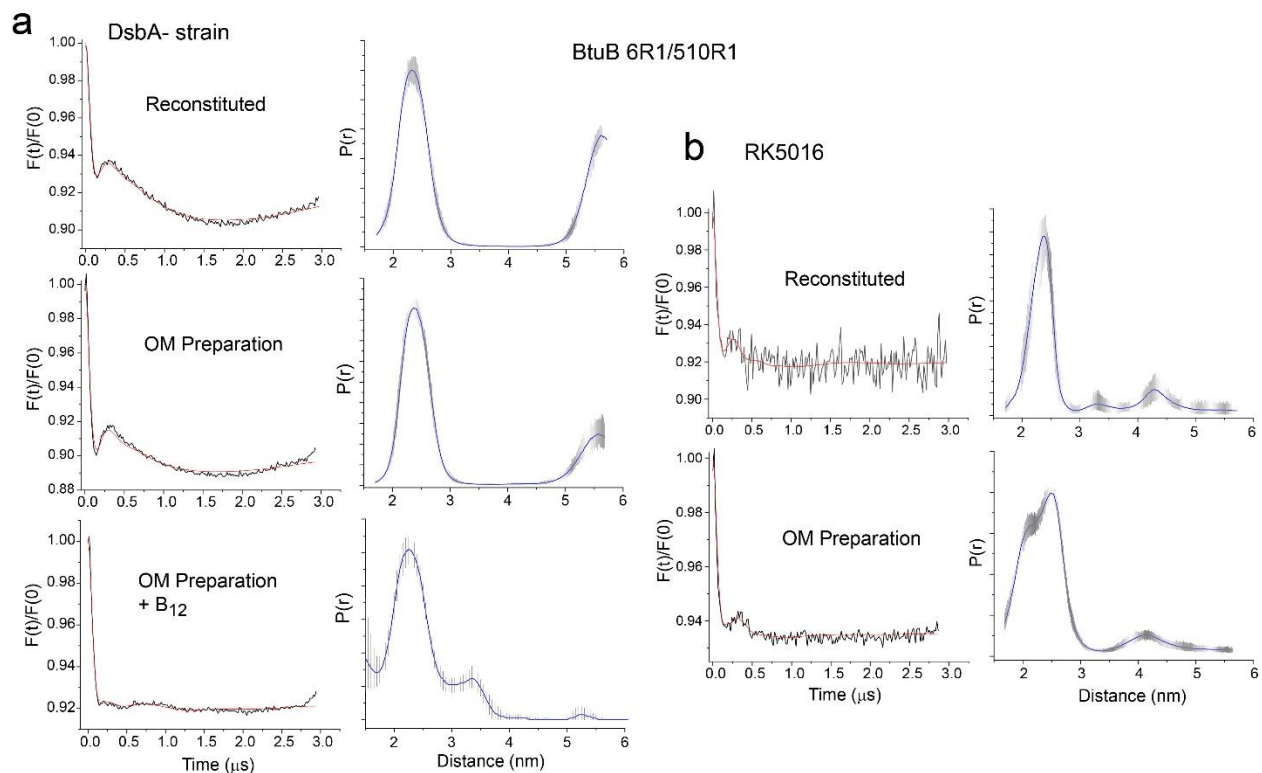


Figure 3.3 DEER data from purified reconstituted protein or an outer-membrane preparation are improved using a DsbA deficient strain. In (a) DEER data obtained for BtuB labeled at sites D6 and Q510 when isolated from a *dsbA*<sup>-</sup> strain following an 8 hr growth and reconstituted into POPC bilayers or obtained from an OM preparation. Data are shown in the apo state for BtuB in the reconstituted state (top), from the OM preparation (middle) and in the OM preparation following vitamin B<sub>12</sub> addition (bottom). In (b) DEER data obtained from BtuB produced from an 8 h growth in RK5016 when labeled at sites D6 and Q510 in either the reconstituted vesicle preparation or OM preparation in the apo state. All distance distributions were obtained using DEERNet, except for the bottom panel in (a) where Tikhonov regularization and a validation procedure were used (see Section 3.3)<sup>2</sup>.

### 3.5 Discussion

The efficient *in-vivo* spin labeling of pairs of cysteine residues in the vitamin B<sub>12</sub> transporter, BtuB, was previously shown to require the use of an E. coli strain deficient in the thiol disulfide oxidoreductase, DsbA, or the DsbA oxidase, DsbB<sup>19</sup>. In the present work, we demonstrate that *in-vitro* EPR measurements on BtuB that is purified and reconstituted into bilayers is dramatically improved by the production of the protein in a *dsbA*<sup>-</sup> strain. We expect that both *in-vivo* and *in-vitro* labeling of pairs of cysteines may either require or be improved by the use of a *dsbA*<sup>-</sup> strain for a range of outer-membrane proteins<sup>2</sup>.

In previous work, it was possible to incorporate pairs of spin labels into BtuB and FecA in purified, reconstituted preparations<sup>6, 11</sup>, and in outer membrane preparations<sup>15</sup> using conventional E. coli K12-derived strains having a functional Dsb system. But often, obtaining adequate DEER data required some additional manipulations of the sample. For example, our first attempts to incorporate pairs of cysteines into BtuB<sup>6</sup> required a protocol for labeling that involved two ion-exchange purifications with a DTT treatment after the first purification prior to spin labeling. The dramatic improvement seen here for the labeling of sites D6 and Q510 on the periplasmic interface of BtuB when the *dsbA*<sup>-</sup> strain is used (see Figure 3.2c) suggests that even in the purified, reconstituted system some significant level of internally disulfide cross-linked BtuB is present when a wild-type strain is used for protein production. As seen in Figure 3.2c, performing an overnight growth combined with DTT treatment improves the signal, but not to the same extent seen by the use of the *dsbA*<sup>-</sup> strain. It should be noted that the signal improvement obtained *in-vitro* using the *dsbA*<sup>-</sup> strain was greatest for the pair of sites tested on the periplasmic surface of BtuB (see Figure 3.2c)<sup>2</sup>.

There was less improvement for the pair of sites on extracellular surface (see Figure 3.2d). We do not presently understand the basis for this difference, but it may reflect the ability of the Dsb system to oxidize certain pairs of cysteine residues, perhaps because of the local protein dynamics or structure at these sites. However, overall spin labeling efficiency at the extracellular surface has also improved with the use of the *dsbA*<sup>-</sup> strain where an increase in modulation depth was observed. Furthermore, a substrate induced conformational shift from a primary distance component near 3 nm is converted to a secondary state at a shorter distance indicating an upward shift of substrate binding loop 3 (SB3) containing V90 towards the substrate (see Supplementary Figure S3.1) and was previously observed *in-vivo*<sup>19</sup>. In previous whole cell measurements on BtuB, we demonstrated that long-distances that appear in the distance distribution around 6 nm have an intermolecular origin<sup>30</sup> and are likely due to specific BtuB-BtuB interactions. These interactions are the basis for the formation of string-like oligomers termed OMP islands<sup>23</sup>, which play a role in the turnover and movement of outer membrane proteins to the bacterial poles. Previously, we found no evidence for these intermolecular BtuB interactions in reconstituted systems, but they appear to be present in a reconstituted system (see Figure 3.3a), when BtuB is expressed in a *dsbA*<sup>-</sup> strain. This observation is consistent with the idea that with an intact Dsb system, a significant level of protein is internally cross-linked; and as a result, the protein population may not be well-labeled. In the intact cell, the long distances observed for BtuB were consistent with the presence of a single LPS molecule interacting between each pair of BtuB monomers however BtuB-BtuB interactions in the absence of interacting LPS is also possible. This would not be expected to be the case for reconstituted BtuB, but additional measurements with extended echo times in the DEER experiment will be required to make this determination and accurately resolve the distance<sup>2</sup>.

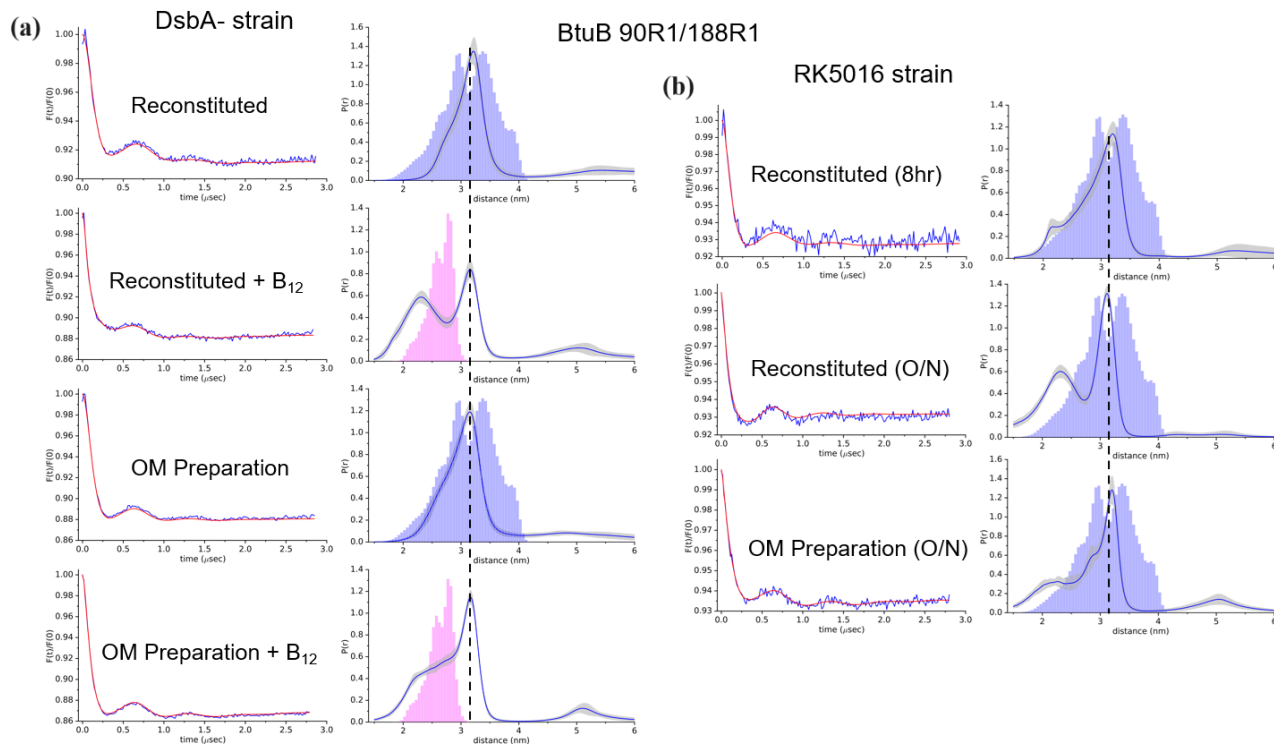
In summary, we provide evidence that the expression of an outer-membrane protein in a strain where the Dsb system is inhibited facilitates the efficient spin labeling pairs of cysteines both *in-vivo* and *in-vitro*. BtuB, expression in a *dsbA*<sup>-</sup> strain dramatically improved the efficiency and quality of the EPR data obtained *in-vitro*. This improved labeling efficiency also revealed the presence of intermolecular BtuB-BtuB interactions that had not been previously observed in a reconstituted membrane environment<sup>2</sup>.

### 3.6 Future directions

The *dsbA*<sup>-</sup> strain significantly enhanced the spin labeling efficiency of BtuB thereby allowing us to observe possible BtuB-BtuB intermolecular interactions using DEER spectroscopy in isolated systems which was not observed before. However, the distance distributions observed cannot be accepted with great confidence as the data acquisition time is smaller ( $d_2 \sim 3.1$  to  $3.4 \mu\text{s}$ ). To further clarify these distance distributions, data acquisition time should be increased ( $d_2 > 5 \mu\text{s}$  recommended) to accurately resolve distance distributions above 5 nm. Also, single cysteine mutation in BtuB is sufficient for distance distributions obtained through intermolecular interactions as it was observed *in-vivo*<sup>30</sup>. Thus, the use of standard K-12 strain RK5016 is possible since single cysteine cannot undergo disulfide crosslinking in the presence of the Dsb system. Furthermore, a comparison between BtuB spin labeling efficiencies in RK5016 and *dsbA*<sup>-</sup> strain for single cysteine mutation will allow us to gain insight regarding the relationship between BtuB expression and spin labeling efficiencies between different *E. coli* strains.

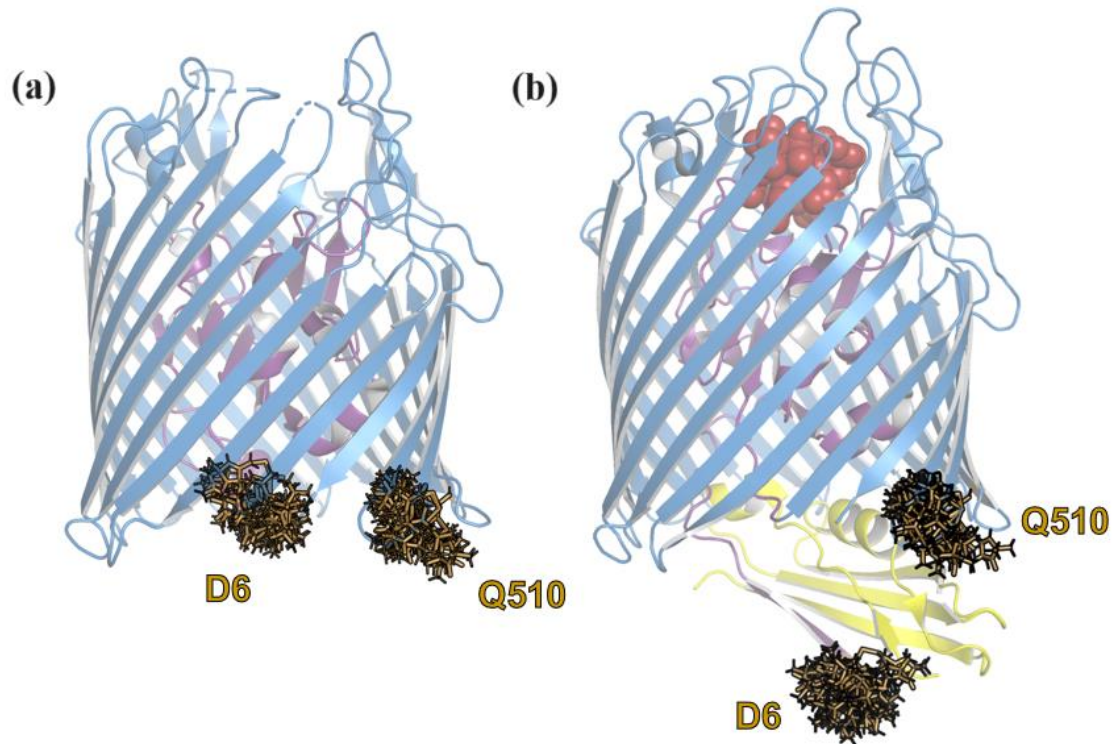


### 3.7 Supplementary information

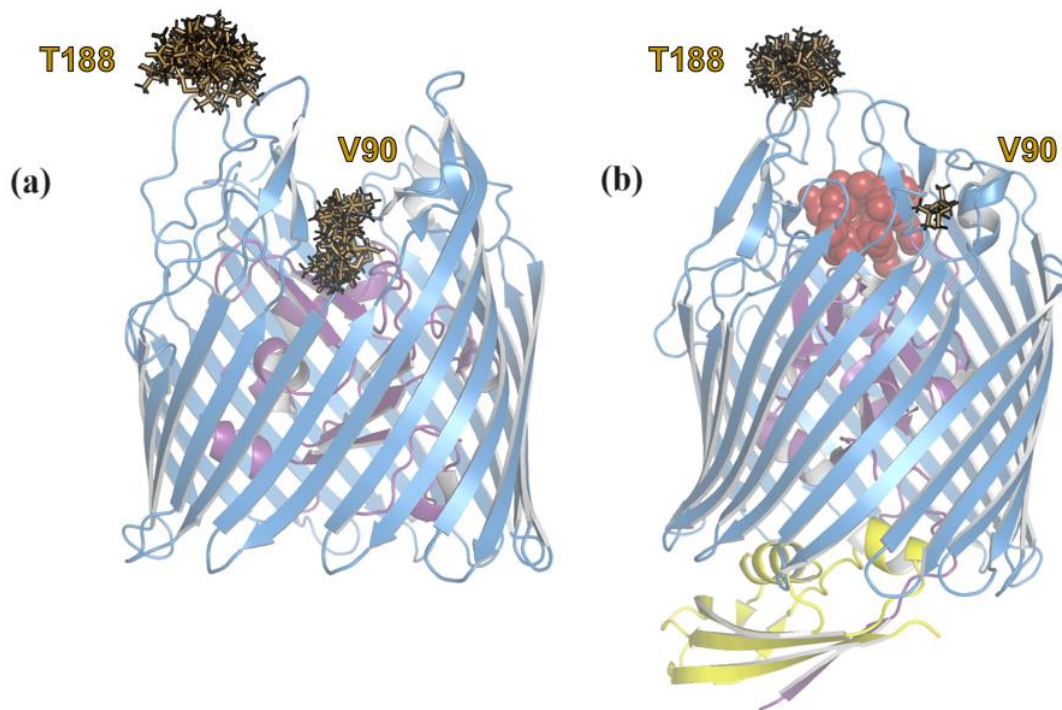


Supplementary Figure S3.1 V90R1-T188R1 DEER data from purified reconstituted protein or an outer-membrane preparation are improved using a DsbA deficient strain. In (a) DEER data obtained for BtuB labeled at sites V90 and T188 when isolated from a *dsbA*<sup>-</sup> strain following an 8 hr growth and reconstituted into POPC bilayers or obtained from an OM preparation. Data are shown in the apo state for BtuB in the reconstituted state (top), B<sub>12</sub> bound state for BtuB in the reconstituted state (2<sup>nd</sup> from top), apo state for BtuB from the OM preparation (3<sup>rd</sup> from top) and in the OM preparation following vitamin B<sub>12</sub> addition (bottom). In (b) DEER data obtained from BtuB produced from an 8 hr growth-based reconstitution in RK5016 (top) when labeled at sites V90 and T188 in either the reconstituted vesicle preparation or OM preparation in the apo state with an O/N growth (middle and bottom respectively). All distance distributions were obtained using DEERNet. One primary distance near 3 nm is seen in the apo state, but a second state at a shorter distance appears with substrate addition. The predictions from the apo and substrate bound

crystal structures (PDB ID: 1NQG and 2GSK, respectively) are shown as blue and pink histograms.



Supplementary Figure S3.2 Substrate induced unfolding of the BtuB Ton box observed in crystal structures. (a) Apo state (PDB ID 1NQG) and (b) B<sub>12</sub> (brick red) and TonB C-terminal (yellow) bound (PDB ID 2GSK) of BtuB with possible rotamers available for R1 spin label (brown) at residues D6 and Q510 in the plug domain (dark purple) and barrel domain (blue), respectively.



Supplementary Figure S3.3 Substrate induced conformational changes of plug domain (dark purple) of BtuB observed in crystal structures. (a) Apo state (PDB ID 1NQG) and (b) B<sub>12</sub> (brick red) and TonB C-terminal (yellow) bound (PDB ID 2GSK) of BtuB with possible rotamers available for R1 spin label (brown) at residues V90 and T188 in the plug domain and barrel domain (blue), respectively. Substrate docking induces an unfolding of a helix conformation near site V90 resulting in a motion towards substrate. Number of possible R1 rotamers at V90 are reduced due to the docking of substrate.

### 3.8 References

1. Wimalasiri, V. W., Nilaweera, T. D., & Cafiso, D. S. (2021). Disulfide Chaperone Knockouts Facilitate Double Spin Labelling of an Outer Membrane Transporter For in Vitro EPR Studies. *Biophysical Journal*, *120*(3), 72a-73a.
2. Wimalasiri, V. W., Jurczak, K. A., Wieliniec, M. K., Nilaweera, T. D., Nakamoto, R. K., & Cafiso, D. S. (2023). A disulfide chaperone knockout facilitates spin labeling and pulse EPR spectroscopy of outer membrane transporters. *Protein science : a publication of the Protein Society*, *32*(7), e4704.
3. Nikaido H. (2003). Molecular basis of bacterial outer membrane permeability revisited. *Microbiology and molecular biology reviews : MMBR*, *67*(4), 593–656.
4. Nagle, J. F., & Tristram-Nagle, S. (2000). Structure of lipid bilayers. *Biochimica et biophysica acta*, *1469*(3), 159–195.
5. Balusek, C., & Gumbart, J. C. (2016). Role of the Native Outer-Membrane Environment on the Transporter BtuB. *Biophysical journal*, *111*(7), 1409–1417.
6. Xu, Q., Ellena, J. F., Kim, M., & Cafiso, D. S. (2006). Substrate-dependent unfolding of the energy coupling motif of a membrane transport protein determined by double electron-electron resonance. *Biochemistry*, *45*(36), 10847–10854.
7. Krewulak, K. D., & Vogel, H. J. (2011). TonB or not TonB: is that the question?. *Biochemistry and cell biology = Biochimie et biologie cellulaire*, *89*(2), 87–97.

8. Hickman, S. J., Cooper, R. E. M., Bellucci, L., Paci, E., & Brockwell, D. J. (2017). Gating of TonB-dependent transporters by substrate-specific forced remodelling. *Nature communications*, *8*, 14804.
9. Hubbell, W. L., Cafiso, D. S., & Altenbach, C. (2000). Identifying conformational changes with site-directed spin labeling. *Nature structural biology*, *7*(9), 735–739.
10. eschke G. (2012). DEER distance measurements on proteins. *Annual review of physical chemistry*, *63*, 419–446.
11. Mokdad, A., Herrick, D. Z., Kahn, A. K., Andrews, E., Kim, M., & Cafiso, D. S. (2012). Ligand-induced structural changes in the Escherichia coli ferric citrate transporter reveal modes for regulating protein-protein interactions. *Journal of molecular biology*, *423*(5), 818–830.
12. Sarver, J. L., Zhang, M., Liu, L., Nyenhuis, D., & Cafiso, D. S. (2018). A Dynamic Protein-Protein Coupling between the TonB-Dependent Transporter FhuA and TonB. *Biochemistry*, *57*(6), 1045–1053.
13. Fanucci, G. E., Coggshall, K. A., Cadieux, N., Kim, M., Kadner, R. J., & Cafiso, D. S. (2003). Substrate-induced conformational changes of the periplasmic N-terminus of an outer-membrane transporter by site-directed spin labeling. *Biochemistry*, *42*(6), 1391–1400.
14. Merianos, H. J., Cadieux, N., Lin, C. H., Kadner, R. J., & Cafiso, D. S. (2000). Substrate-induced exposure of an energy-coupling motif of a membrane transporter. *Nature structural biology*, *7*(3), 205–209.
15. Sikora, A., Joseph, B., Matson, M., Staley, J. R., & Cafiso, D. S. (2016). Allosteric Signaling Is Bidirectional in an Outer-Membrane Transport Protein. *Biophysical journal*, *111*(9), 1908–1918.

16. Nyenhuis, D. A., Nilaweera, T. D., & Cafiso, D. S. (2020). Native Cell Environment Constrains Loop Structure in the *Escherichia coli* Cobalamin Transporter BtuB. *Biophysical journal*, *119*(8), 1550–1557.
17. Nilaweera, T. D., Nyenhuis, D. A., & Cafiso, D. S. (2021). Structural intermediates observed only in intact *Escherichia coli* indicate a mechanism for TonB-dependent transport. *eLife*, *10*, e68548.
18. Dutton, R. J., Boyd, D., Berkmen, M., & Beckwith, J. (2008). Bacterial species exhibit diversity in their mechanisms and capacity for protein disulfide bond formation. *Proceedings of the National Academy of Sciences of the United States of America*, *105*(33), 11933–11938.
19. Nilaweera, T. D., Nyenhuis, D. A., Nakamoto, R. K., & Cafiso, D. S. (2019). Disulfide Chaperone Knockouts Enable In Vivo Double Spin Labeling of an Outer Membrane Transporter. *Biophysical journal*, *117*(8), 1476–1484.
20. Klock, H. E., & Lesley, S. A. (2009). The Polymerase Incomplete Primer Extension (PIPE) method applied to high-throughput cloning and site-directed mutagenesis. *Methods in molecular biology (Clifton, N.J.)*, *498*, 91–103.
21. Bradford M. M. (1976). A rapid and sensitive method for the quantitation of microgram quantities of protein utilizing the principle of protein-dye binding. *Analytical biochemistry*, *72*, 248–254.
22. Sedmak, J. J., & Grossberg, S. E. (1977). A rapid, sensitive, and versatile assay for protein using Coomassie brilliant blue G250. *Analytical biochemistry*, *79*(1-2), 544–552.
23. Rassam, P., Copeland, N. A., Birkholz, O., Tóth, C., Chavent, M., Duncan, A. L., Cross, S. J., Housden, N. G., Kaminska, R., Seger, U., Quinn, D. M., Garrod, T. J., Sansom, M. S., Piehler, J.,

- Baumann, C. G., & Kleanthous, C. (2015). Supramolecular assemblies underpin turnover of outer membrane proteins in bacteria. *Nature*, *523*(7560), 333–336.
24. Jeschke, G., Chechik, V., Ionita, P., Godt, A., Zimmermann, H., Banham, J., ... & Jung, H. (2006). DeerAnalysis2006—a comprehensive software package for analyzing pulsed ELDOR data. *Applied magnetic resonance*, *30*, 473-498.
25. Worswick, S. G., Spencer, J. A., Jeschke, G., & Kuprov, I. (2018). Deep neural network processing of DEER data. *Science advances*, *4*(8), eaat5218.
26. Jeschke, G. (2018). MMM: A toolbox for integrative structure modeling. *Protein Science*, *27*(1), 76-85.
27. Polyhach, Y., Bordignon, E., & Jeschke, G. (2011). Rotamer libraries of spin labelled cysteines for protein studies. *Physical chemistry chemical physics : PCCP*, *13*(6), 2356–2366.
28. DeLano, W. L. (2002). Pymol: An open-source molecular graphics tool. *CCP4 Newsl. Protein Crystallogr*, *40*(1), 82-92.
29. Landeta, C., Boyd, D., & Beckwith, J. (2018). Disulfide bond formation in prokaryotes. *Nature microbiology*, *3*(3), 270-280.
30. Nyenhuis, D. A., Nilaweera, T. D., Niblo, J. K., Nguyen, N. Q., DuBay, K. H., & Cafiso, D. S. (2020). Evidence for the Supramolecular Organization of a Bacterial Outer-Membrane Protein from In Vivo Pulse Electron Paramagnetic Resonance Spectroscopy. *Journal of the American Chemical Society*, *142*(24), 10715–10722.

## **Chapter 4: A disulfide chaperone knockout facilitates efficient double spin labeling of ferric citrate transporter FecA for *in-vivo* pulse EPR spectroscopy**

### 4.1 Abstract

The outer membrane (OM) of Gram-negative bacteria such as *Escherichia coli* (*E. coli*) contains a fascinating class of active transport proteins that are TonB-dependent. These TonB dependent transporters (TBDTs) function in the uptake of trace nutrients such as iron, vitamin B<sub>12</sub> as well as carbohydrates. TBDTs are essential for the success of many pathogens and for the proper functioning of the human microbiome. TBDTs obtain the energy for active transport from the inner membrane (IM) proton motive force (PMF) by coupling with the IM protein complex TonB/ExbB/ExbD. Although many high-resolution structures for TBDTs are known, the molecular mechanism by which TBDTs function has not been elucidated.

Previous research has shown that it is possible to examine the dynamics and structure of double spin labeled mutants of the cobalamin transporter BtuB in cells, utilizing a knockout strain. It has also been shown that BtuB behaves differently *in-vivo* than it does in a purified, reconstituted membrane system, yielding information on the transport mechanism. Analyzing TBDTs and other outer-membrane proteins in a whole cell system can give us valuable insight into how these proteins function in their natural environment. Here, we extend these *in-vivo* measurements to FecA, the *E. coli* ferric citrate transporter. As seen for BtuB, pairs of cysteines cannot be labeled when the protein is present in a standard expression strain. However, incorporating plasmids that permit an arabinose induced expression of FecA into a strain defective in the thiol disulfide oxidoreductase, DsbA, enables efficient spin-labeling and pulse EPR of FecA in cells. A comparison of the measurements made on FecA in cells with measurements made in reconstituted



phospholipid bilayers suggests that the cellular environment alters the behavior of the extracellular loops of FecA<sup>1</sup>.

(Note: Portions of this chapter have been published in: Wimalasiri, V. W., Jurczak, K. A., Wieliniec, M. K., Nilaweera, T. D., Nakamoto, R. K., & Cafiso, D. S. (2023). A disulfide chaperone knockout facilitates spin labeling and pulse EPR spectroscopy of outer membrane transporters. *Protein science : a publication of the Protein Society*, 32(7), e4704.)

## 4.2 Introduction

Active transport in the outer membrane (OM) of Gram-negative bacteria is facilitated by a family of proteins that bind to and obtain energy from the inner membrane (IM) protein TonB<sup>2</sup>. These TonB-dependent transporters (TBDTs) are responsible for the acquisition of trace nutrients, such as iron, nickel, and vitamin B<sub>12</sub>, as well as the uptake of carbohydrates. TonB-dependent transporters are critical for the success of many pathogens<sup>3,4</sup>, and they are essential for the proper functioning of the human microbiome<sup>5</sup>. Although numerous crystal structures have been obtained for this family of transporters<sup>6</sup>, the molecular mechanisms by which they function are poorly understood<sup>1,7</sup>.

Site-directed spin labeling when combined with EPR spectroscopy is a powerful and sensitive method that can reveal structural changes and conformational exchange in membrane transport proteins<sup>8</sup>. This approach has been used to examine structural transitions and conformational exchange in BtuB, the *Escherichia coli* TonB-dependent vitamin B<sub>12</sub> transporter<sup>9,10</sup>, as well as other *E. coli* TBDTs such as the ferric citrate transporter, FecA<sup>11,12</sup>, the ferrichrome transporter FhuA<sup>13</sup> and the ferric enterobactin receptor, FepA<sup>14,15</sup>. Most of this work

has been performed *in-vitro* on detergent purified and membrane reconstituted protein. Because transport requires an interaction between the transporter in the OM and TonB in the IM, transport has never been reconstituted, and one issue with the *in-vitro* experiments on BtuB and other TBDTs is that the function of the transporter has never been established<sup>1</sup>.

It is possible to perform continuous wave (CW) EPR on TBDTs *in-vivo*<sup>14</sup>, and more recently pulse EPR measurements have been conducted *in-situ* on BtuB when it is over-expressed in intact bacteria<sup>16</sup>. Measurements on the intact cell have the advantage that they can be carried out on a transport protein that is known to be functional and where it is present in its native environment. Remarkably, this outer membrane environment appears to modify protein structure and behavior. For example, in isolated OM preparations<sup>17</sup> or reconstituted phospholipid bilayers<sup>18</sup>, the extracellular loops of BtuB sample a wide range of conformations in the apo state and undergo a gating motion with substrate addition; however, in the cell, loop conformations are restricted, and substrate is not observed to modulate the extracellular loops<sup>19</sup>. Different behaviors are also observed in the core region of BtuB. For example, structural changes in the core region of the protein that could mediate transport are observed in the cell but not observed in reconstituted phospholipid membranes<sup>20</sup>. Compared to measurements made in cells, measurements in purified reconstituted systems do have the advantage that they generally yield spectra with better signal to noise and lower levels of non-specific labeling. They also enable the characterization of protein-protein interactions between BtuB and fragments of the inner-membrane machinery<sup>1, 21</sup>.

Pulse EPR experiments, such as double electron-electron resonance (DEER), provide information on the distances and distance distributions between pairs of spin labels<sup>22</sup>. This is most easily performed on proteins through the covalent modification of pairs of reactive cysteine residues that have been engineered into the protein. In intact *Escherichia coli*, outer membrane

proteins typically have zero or an even number of cysteines<sup>23</sup>. The ferric citrate transporter FecA lacks cysteines and single cysteines that are incorporated into FecA can be efficiently spin labeled *in-vivo* using the standard BL21(DE3) strain. However, FecA cannot be efficiently double spin-labeled in the commonly used BL21(DE3) strain but can be efficiently double-labeled when it is expressed in a DsbA minus strain (Figure 3.1 in Chapter 3). Excellent CW and pulse EPR data are obtained from FecA in cells with minimal background labeling. The initial data suggest that extracellular loop 8, which is seen to undergo large movements by crystallography upon substrate binding<sup>24</sup>, samples two states in cells with substrate addition, suggesting that the environment used for crystallography has trapped one state. Work comparing the results obtained in cells with data obtained in a purified phospholipid reconstituted membrane indicates that FecA, like BtuB, behaves differently in the cell than it does in the purified reconstituted environment<sup>1</sup>.

## 4.3 Materials and Methods

### 4.3.1 Cell lines and plasmids

For the ferric citrate transporter, FecA, the pIS711 plasmid carrying the WT *fecA* gene downstream of the phage T7 gene 10 promoter, was generously provided by Volkmar Braun (University of Tübingen, Tübingen, Germany). The pTARA plasmid was purchased from Addgene (Watertown, MA), and was used to control FecA expression levels. The pTARA plasmid harbors the phage T7 RNA polymerase gene under control of the araBAD promoter. Both wild-type and mutant *dsb E. coli* strains were obtained from the Coli Genetic Stock Center (Yale University, New Haven, CT). Strain RI89 carries the WT Dsb system (*araD139 Δ(araABC-leu)7679 galU galK Δ(lac)X74 rpsL thi phoR Δara714 leu+*), whereas strain RI90 carries the *dsbA* null mutation system (*araD139 Δ(araABC-leu) 7679 galU galK Δ(lac)X74 rpsL thi phoR Δara714 leu +dsbA:: Kanr*). FecA was

also expressed in the standard *E. coli* strain BL21(DE3), which lacks outer membrane porins such as OmpA, OmpC, and LamB<sup>1, 25</sup>.

#### 4.3.2 PCR mutagenesis and OMP expression

FecA double cysteine mutations (Q528C-T666C, K12C-N256C, T70C-N256C) were constructed using site-directed mutagenesis and verified by DNA sequencing (Genewiz, South Plainfield, NJ). The fecA containing plasmids were transformed into either BL21(DE3), the *dsbA*<sup>-</sup> strain, or the *dsbA*<sup>-</sup> strain with a previously incorporated pTARA plasmid.

A single colony was used to inoculate Luria-Bertani (LB) media and prepare a glycerol stock which was stored at 80 °C. For BtuB, precultures of Minimal Media (100 mM phosphate buffer, 8 mM (NH<sub>4</sub>)<sub>2</sub>SO<sub>4</sub>, 2mM sodium citrate, 100 mg/mL ampicillin, 0.2% w/v glucose, 150 mM thiamine, 3 mM MgSO<sub>4</sub>, 300 mM CaCl<sub>2</sub>, 0.01% w/v methionine, 0.01% w/v arginine) were inoculated using the glycerol stock and later used to inoculate the main culture. For FecA, a preculture of Luria-Bertani (LB) with appropriate antibiotics was inoculated using the glycerol stock and later was used to inoculate the main culture in Minimal Media. FecA was overexpressed by induction with 0.5 mM IPTG at OD<sub>600</sub> of 0.5–0.6 for 5 hr at 37 °C. In both cases, an initial overnight preculture growth was followed by an 8 hr main culture growth. The pTARA mediated expression was induced at OD<sub>600</sub> of 0.1 by adding arabinose up to final concentration of 0.1% w/v<sup>1</sup>.

#### 4.3.3 OM and reconstituted FecA sample preparation

An intact OM preparation is obtained from the total cell membrane fraction using a standard procedure<sup>10</sup>. This involves treating the cell membrane fraction with 1% sarkosyl to remove the inner membrane, and then pelleting the OM and removal of the sarkosyl by centrifugation. For measurements made in the OM preparation, the preparation was spin labeled

at this stage<sup>26</sup>. For protein that was to be purified, the OM preparation was solubilized with OG as described previously, and 5 mL of the solubilized OM sample then was treated with 100  $\mu$ L of 22 mM MTSL [(1-oxyl-2,2,5,5-tetramethylpyrroline-3-methyl) methanethiosulfonate] followed by incubation for 2–3 hr at room temperature (RT)<sup>20</sup>. Spin labeled FecA was purified using ion-exchange chromatography as described previously<sup>9, 27</sup>. The purified FecA was quantified using the Bradford Assay<sup>28, 29</sup>.

The purified and spin-labeled BtuB samples were reconstituted into 1-palmitoyl-2-oleoyl-sn-glycero-3-phosphocholine (POPC) vesicles by the addition of OG/POPC (10:1) mixed micelles to the purified FecA samples at a protein: lipid ration of 1:25. The samples were then dialyzed against six 4 L dialysis buffer changes (10 mM HEPES, 128 mM NaCl, and 1 mM EDTA at pH 6.5) at 10–12 hr intervals<sup>1, 10, 30, 31</sup>.

#### 4.3.4 Whole cell spin labeling of FecA

For spin labeling FecA in cells, an identical protocol to that used for BtuB in cells was followed<sup>20,32</sup> where pTARA mediated expression was induced at an OD<sub>600</sub> of 0.1 by adding L-arabinose to a final concentration of 0.1% w/v. Briefly, cells were grown until early log phase and harvested at OD<sub>600</sub> of 0.3. Cells were resuspended in 100 mM HEPES (pH 7.0) containing 2.5% (w/v) glucose followed by MTSL spin labelling at RT for 30 mins with a label concentration of 0.02 mg/mL as described previously<sup>20,32</sup>. Spin labeled cells went through two washing steps in 100 mM HEPES with 2.5% (w/v) glucose to remove any excess spin label and were then immediately used for EPR<sup>1</sup>.

#### 4.3.5 EPR Measurements

For CW-EPR measurements, 5  $\mu$ L sample with 1  $\mu$ L dialysis buffer was loaded into 0.84 x 0.6 mm<sup>2</sup> quartz capillaries and used as apo sample whereas 5  $\mu$ L sample with 1  $\mu$ L of 1 mM

Vitamin B<sub>12</sub> was used as the substrate bound sample. EPR spectra were recorded at room temperature at X-band using a Bruker EMX spectrometer (Billerica, MA) with an ER 4123D dielectric resonator using a sweep width of 100 gauss (G), a modulation amplitude of 1 G, and 2 mW incident microwave power. Data were collected as additive averages of 10 scans and were normalized by their second integral. For DEER, a 16  $\mu$ L sample with 4  $\mu$ L of concentrated d-glycerol was loaded into 1.1 x 1.6 mm<sup>2</sup> quartz capillaries (VitroCom, Mountain Lakes, NJ). 2  $\mu$ L of 1 mM Vitamin B<sub>12</sub> was added for samples with substrate. All DEER experiments were performed on a Bruker E580 spectrometer operating at Q-band (Bruker BioSpin, Billerica, MA) with the following hardware: Bruker EN5107D2 dielectric resonator, Bruker SpinJet-AWG, and a 300 W TWT amplifier (Applied Systems Engineering, Benbrook, TX). Experiments were run at 50 K using the standard dead-time free 4-pulse DEER experiment, with a 10 ns  $\pi/2$  pulse and 20 ns  $\pi$  pulses. All pulses were rectangular. The separation between observe and pump frequencies was 75 MHz. Acquisition times for most samples typically ranged from 10 to 15 hr<sup>l</sup>.

#### 4.3.6 Data processing

All DEER data were processed with DeerAnalysis<sup>33</sup> using the DEERNet routine<sup>34</sup>. Simulated distance distributions were generated using the software package MMM and the default rotamer library<sup>35, 36</sup>. Protein structure images were generated using Pymol<sup>l, 37</sup>.

(Note: I would like to acknowledge Ms. Kinga Aleksandra Jurczak for optimization of dual plasmid (pTARA and pIS711) transformation to *dsbA*- strain and final arabinose % (w/v) for optimum induction of pTARA for FecA overexpression)

## 4.4 Results

### 4.4.1 The use of a DsbA deficient strain facilitates double spin-labeling of FecA *in-vivo*

In Chapter 3, we demonstrated that BtuB could not be efficiently double labeled *in-vivo* when expressed in the standard K12-derived RK5016 strain<sup>26</sup>. For the iron transporter, FecA, attempts to label the protein when produced in BL21(DE3) or in RI89 (with a functional Dsb system) failed to produce a measurable spectrum *in-vivo*. Shown in Figure 4 are EPR spectra obtained from FecA where we attempted to label two sites (Q528C and T666C) in the 8–11 extracellular loops of FecA (see Figure 4.1a). Shown in Figure 4.1b is the EPR spectrum obtained when we attempted to label the Q528C-T666C cysteine pair *in-vivo* using a strain with an active Dsb system (RI89). As seen, essentially no signal can be detected<sup>1</sup>.

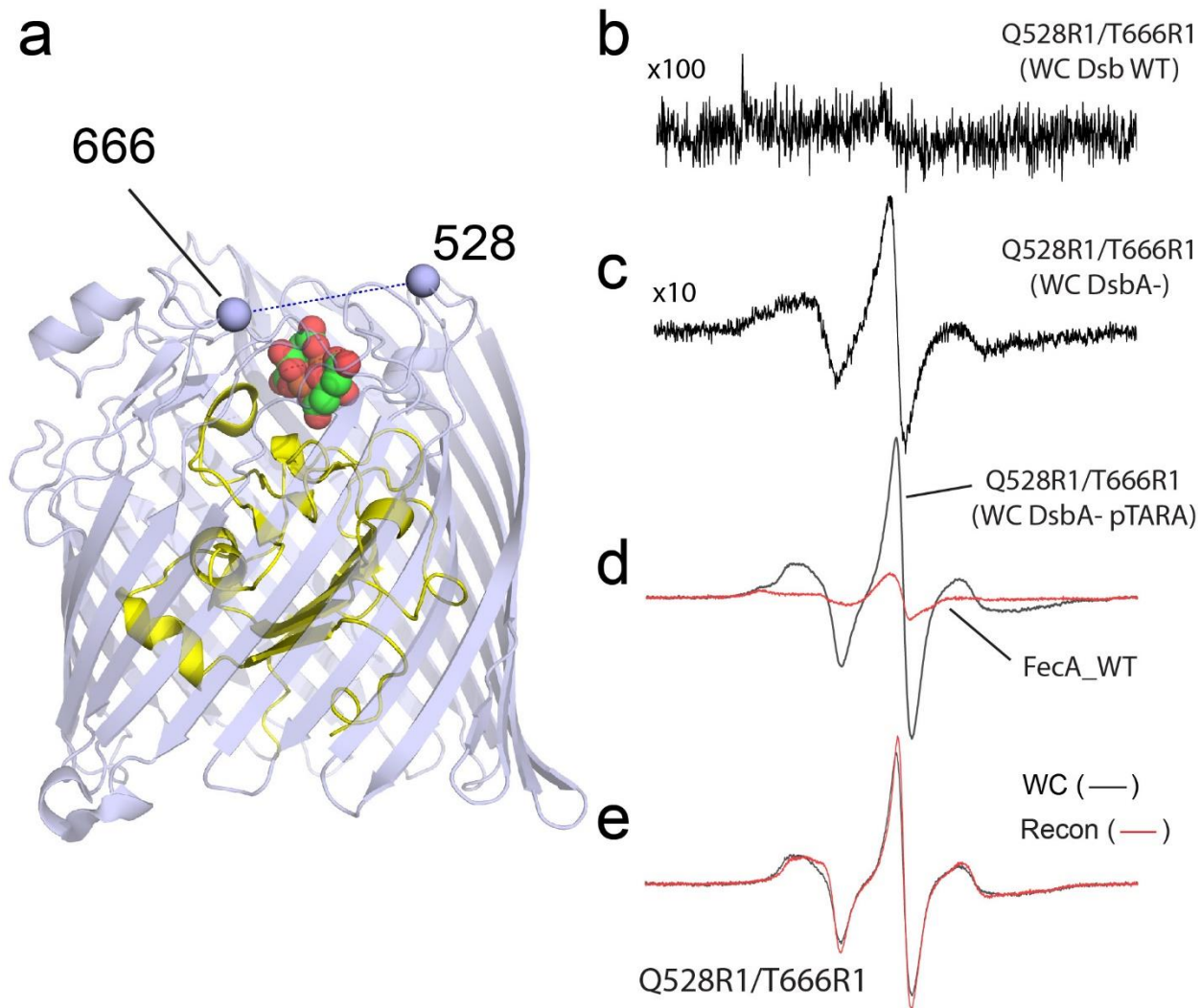


Figure 4.1 Double spin labeling of FecA *in-vivo* requires a DsbA deficient strain. Shown in (a) crystal structure of FecA bound to ferric citrate (PDB ID: 1KMP) with the Ca carbons of sites 528 (loop 8) and 666 (loop 11) shown as spheres. In (b) *in-vivo* EPR spectrum obtained using strain RI89 with an intact Dsb system; and (c) EPR spectrum obtained from a *dsbA*<sup>-</sup> strain lacking induction by T7 polymerase. The relative receiver gains used in (b) and (c) are indicated. In (d) is the EPR spectrum obtained *in-vivo* for Q528R1/T666R1 using the *dsbA*<sup>-</sup> strain RI90 along with the pTARA plasmid and arabinose induction of the T7 polymerase. The background signal obtained when WT FecA is expressed is also shown (red trace). Shown in (e) is a comparison of



the EPR spectra obtained from Q528R1/T666R1 *in-vivo* and in a reconstituted preparation. In (e), the background signal has been subtracted from the *in-vivo* spectrum.

When we repeated the labeling using the *dsbA*<sup>-</sup> strain having an inactive DsbA system, a measurable signal was obtained and is shown in Figure 4.1c. Although FecA is under the control of a T7 promoter and requires the T7 polymerase (which is not present in the *dsbA*<sup>-</sup> strain), there is apparently enough expression of FecA to allow some labeling and the acquisition of an EPR spectrum. However, when the T7 polymerase is expressed from the pTARA plasmid (see Figure 4.2) upon addition of arabinose, the labeling of FecA is dramatically elevated and a relatively noise-free EPR spectrum is obtained (see Figure 4.1d). The level of labeled FecA in cells is clearly improved over the case where the T7 polymerase is not being induced (see Figure 4.1c) and obviously much better than the strain having a functional Dsb system (see Figure 4.1b). Also shown on the same scale is the background signal obtained when WT FecA (lacking any cysteines) is expressed (red trace). A comparison between the Q666R1-T666R1 spectra obtained in a purified reconstituted system versus the intact cell is shown in Figure 4.1e. In this case, there are minor differences in the spectra, but the motion of the labels and hence the environment around the labels in these two preparations is very similar<sup>l</sup>.

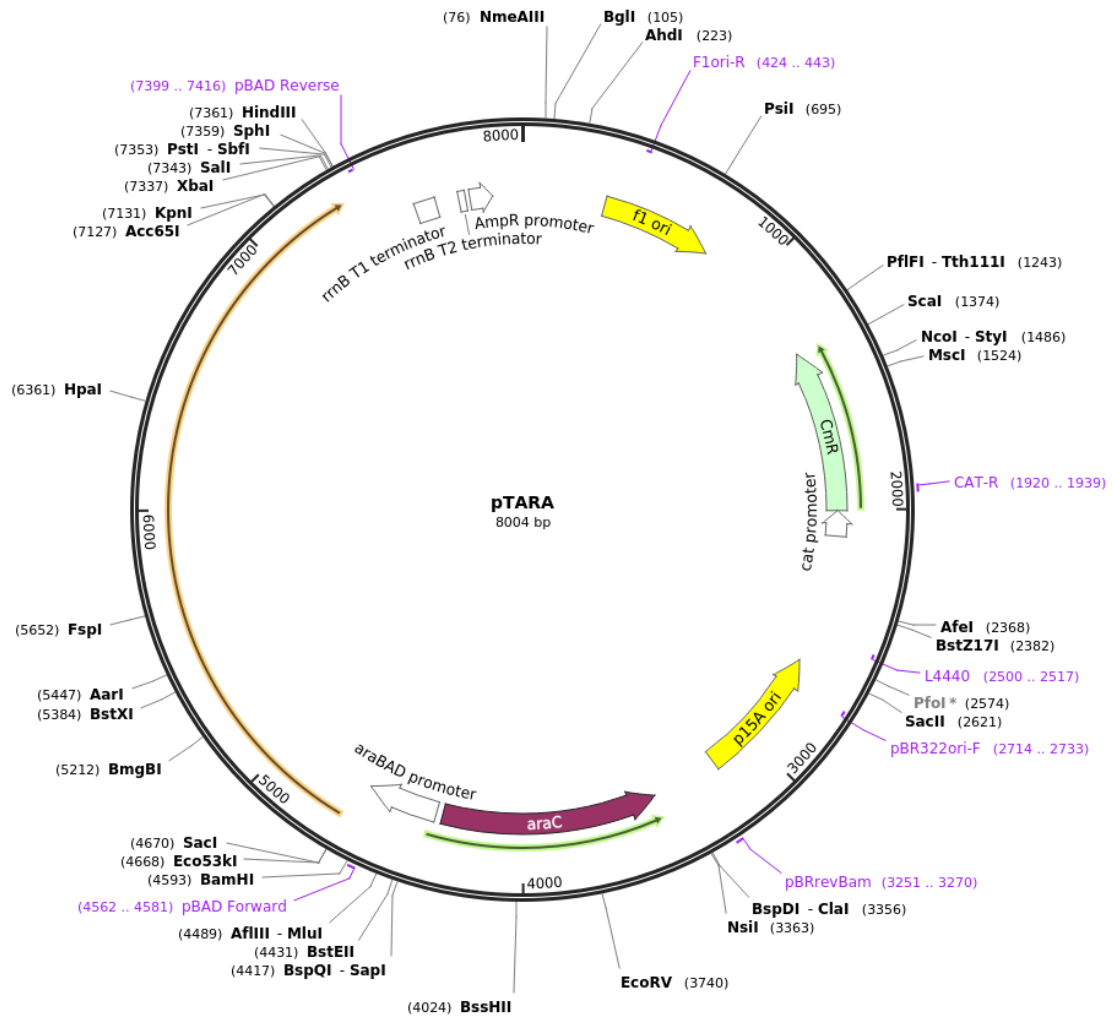


Figure 4.2 Plasmid map of pTARA harboring the phage T7 RNA Polymerase (T7 RNAP) gene. It also contains chloramphenicol resistant (CmR) gene and the T7 RNAP expression is regulated by the araBAD - araC promoter. Figure was taken from <https://www.addgene.org/31491/>. Accessed on 22<sup>nd</sup> May 2024

#### 4.4.2 DEER signals from FecA *in-situ* reveal the presence of a conformational gating in an extracellular loop

Without inducing the expression of FecA, a measurable signal was obtained from the cell preparation (see Figure 4.1c) and we were able to run pulse EPR on this sample and acquire a dipolar evolution (DEER signal) for FecA in the *dsbA*<sup>-</sup> strain. The data are shown in Figure 4.3a and yield a major distance component near 3.1 nm for the Q528R1-T666R1 spin pair. However, without the induction of FecA expression, the levels of labeled FecA are low, the dipolar DEER signal is noisy, and the data required an acquisition period of 24 h<sup>1</sup>.

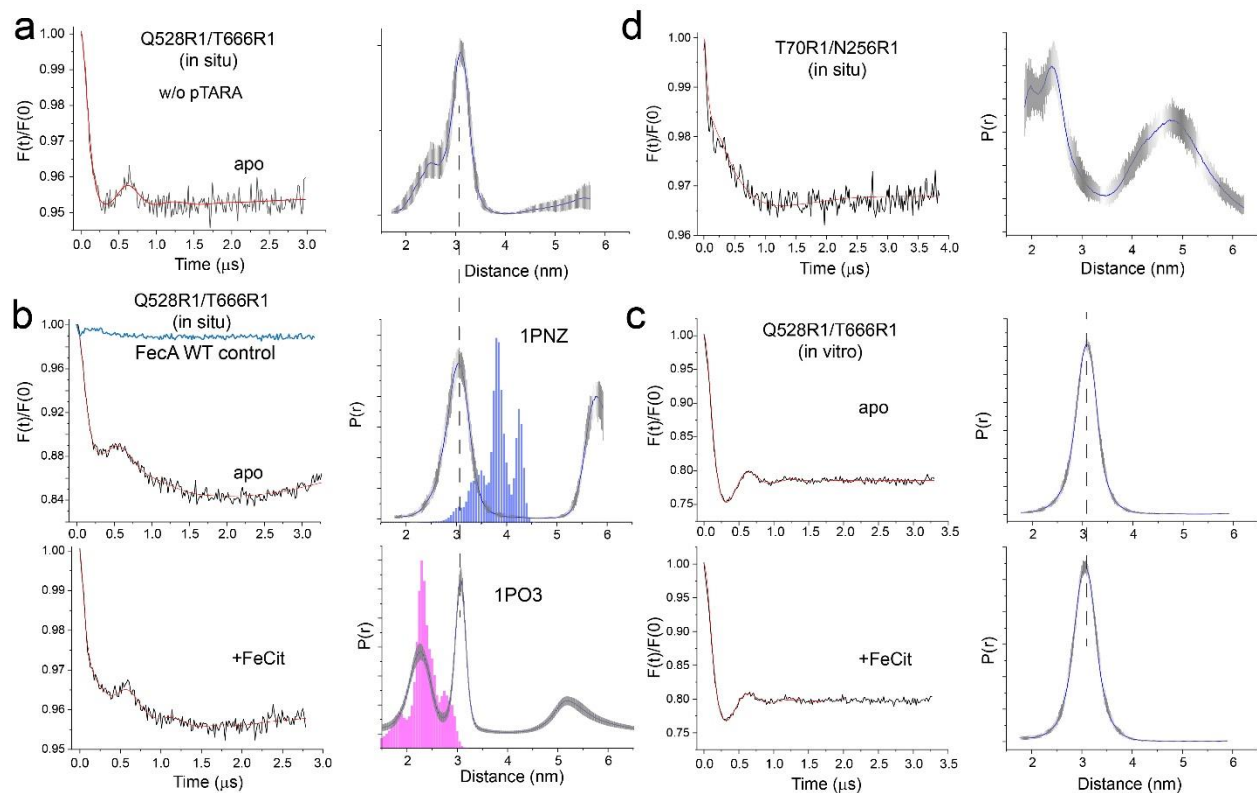


Figure 4.3 Conformational gating in the 8/11 extracellular loops is dependent upon environment. Shown in (a) is a DEER trace obtained in cells for the Q528C-T666C double mutant of FecA in the *dsbA*<sup>-</sup> strain without induction by the pTARA plasmid. Shown in (b) are DEER traces in the apo and ferric citrate bound states for the Q528R1-T666R1 spin pair when FecA expression in the

*dsbA*<sup>-</sup> strain is induced by arabinose using the pTARA plasmid. Also shown is a DEER trace (blue line) obtained when WT FecA is expressed, and cells are taken through the same spin labeling procedure. One primary distance near 3 nm is seen in the apo state, but a second state at a shorter distance appears with ferric citrate addition. The predictions from the apo and substrate bound crystal structures (PDB ID: 1PNZ and 1PO3, respectively) are shown as blue and magenta histograms. In (c) are the apo and ferric citrate bound states of the 8/11 loops for the purified protein obtained from the *dsbA*<sup>-</sup> strain with the pTARA plasmid reconstituted into POPC vesicles. Shown in (d) are data from the periplasmic surface of FecA in cells where one label is in the Ton box (site 70), and a second is located on the periplasmic surface of the barrel (site 256).

The data are dramatically improved when FecA expression is induced by expression of T7 polymerase using the pTARA plasmid. Shown in Figure 4.3b are DEER data obtained for FecA Q528R1-T666R1 in the apo and substrate bound forms when FecA expression is induced by arabinose. As noted above (see Figure 4.1d, red trace) there is some background labeling when WT FecA lacking any cysteines is induced and labeled in the *dsbA*<sup>-</sup> strain; however, this background signal fails to produce a measurable dipolar signal (see Figure 4.3b, top panel, blue trace)<sup>1</sup>.

As seen in Figure 4.3b, in the apo state one well-defined peak near 3 nm is obtained that also shows up in both the apo as well as the substrate bound forms. There is also a low frequency component in the background corrected DEER signal that may be due to a long-distance component (in the 5–6 nm range). It is poorly resolved in terms of width and position, but it resembles the intermolecular peak seen previously for BtuB in intact cells<sup>1, 31</sup>.

The predicted distance distributions from the apo and ferric citrate bound crystal structures are shown in Figure 4.3b (blue and magenta histograms, respectively). In the apo state, there are

distance components in the prediction arising from label rotamers that overlap with the experimental distance at 3.1 nm, but the center of the distribution is approximately 8 or 9 Å longer than the experimental distance. For the ferric citrate bound state, the crystal structure predicts a shorter distance near 2.4 nm, and the center of that distribution agrees well with experimentally measured distance. However, the original distance component at 3 nm is still present in the substrate bound form. Unlike the crystal structure where there is a well-defined state for the 8–11 loops in the substrate bound state, these data suggest that both more open and closed states are simultaneously present in the substrate bound form. Although more work is needed to examine the loops in FecA, this result indicates that there may be an equilibrium between these conformations in the ligand bound state<sup>l</sup>.

The use of the *dsbA*<sup>-</sup> strain also improved the data obtained from reconstituted samples, and Figure 4c shows data obtained from FecA (Q528R1-T666R1) expressed in the *dsbA*<sup>-</sup> strain with arabinose induction using pTARA and purified in detergent by ion exchange. There are some notable differences in the *in-vitro* data compared with the whole cell (*in-situ*) sample. Although the peak near 3 nm is present in the reconstituted preparation in the apo state, there is no evidence for a movement or gating of the 8–11 loops with the addition of substrate (see Figure 4.3c). In addition, there is no evidence for a long-distance component, which also appears to be absent from the signal obtained in cells without the induction of FecA expression (Figure 4.3a)<sup>l</sup>.

Finally, as was the case for BtuB<sup>26</sup>, the *dsbA*<sup>-</sup> strain appears to facilitate the labeling of the periplasmic surface of FecA in cells (Figure 4d). The data are of noticeably poorer quality than that from the extracellular surface, but we expect that deuteration of the sample will improve data quality and permit an examination of the position of the FecA Ton box and transcriptional regulatory domain in cells<sup>l</sup>.

## 4.5 Discussion

In the present work, we demonstrate that a strain deficient in DsbA activity is necessary to double-label cysteines in the extracellular loops of the *E. coli* ferric citrate transporter, FecA, in cells. We have also observed efficient double spin labeling of BtuB *in-vivo*<sup>26</sup> and *in-vitro*<sup>1</sup>. Thus, we can expect that both *in-vivo* and *in-vitro* labeling of pairs of cysteines may either require or be improved by the use of a *dsbA*<sup>-</sup> strain for a range of outer-membrane proteins<sup>1</sup>.

In previous work, it was possible to incorporate pairs of spin labels into BtuB and FecA in purified, reconstituted preparations<sup>10,12</sup>, and in outer membrane preparations<sup>17</sup> using conventional *E. coli* K12-derived strains having a functional Dsb system. But often, obtaining adequate DEER data required some additional manipulations of the sample. Finally, it is interesting to note that evidence for longer distances, like those seen for BtuB, appears for FecA expressed and double labeled in whole cells. However, unlike BtuB, the data obtained from FecA in the reconstituted system using the *dsbA*<sup>-</sup> strain shows no evidence for an extended distance (see Figure 4.3c). Although additional work is needed to establish the presence and source of this distance component, this preliminary data suggests that the nature of the interactions between these OMPs may differ, and that the FecA-FecA interaction may require components in the native outer membrane (perhaps LPS), whereas BtuB-BtuB interactions do not<sup>31</sup>.

The substrate-dependent loop movements observed here in FecA (see Figure 4.3b) suggest that like BtuB<sup>20</sup>, conformational changes in the extracellular loops of FecA are altered by the native environment. The crystal structures of FecA<sup>24</sup> reveal substantial changes in the positions of loops 7 and 8 upon the addition of substrate. These large movements are thought to be important for the high affinity of ferric citrate to the transporter, and for effectively trapping and preventing the release of the substrate back into extracellular space. However, the data shown in Figure 4.3b

indicate that while there is a substrate-induced shift in loop position in cells consistent with the crystal structure (see Supplementary Figure S4.1), the 8–11 interloop distance seen for the apo state persists and is in fact the dominant configuration. Although more work is necessary to determine the nature of these conformations, the two populations seen by DEER likely reflect an equilibrium between the two conformational states. If this is the case, the free energy difference between these two states is small and the loops may not be functioning to trap the substrate. Remarkably, the FecA 8–11 loop distance does not change with substrate addition when the protein is reconstituted into POPC (see Figure 4.3b), indicating that the structural change seen in cells is dependent upon components that are absent in the reconstituted system.

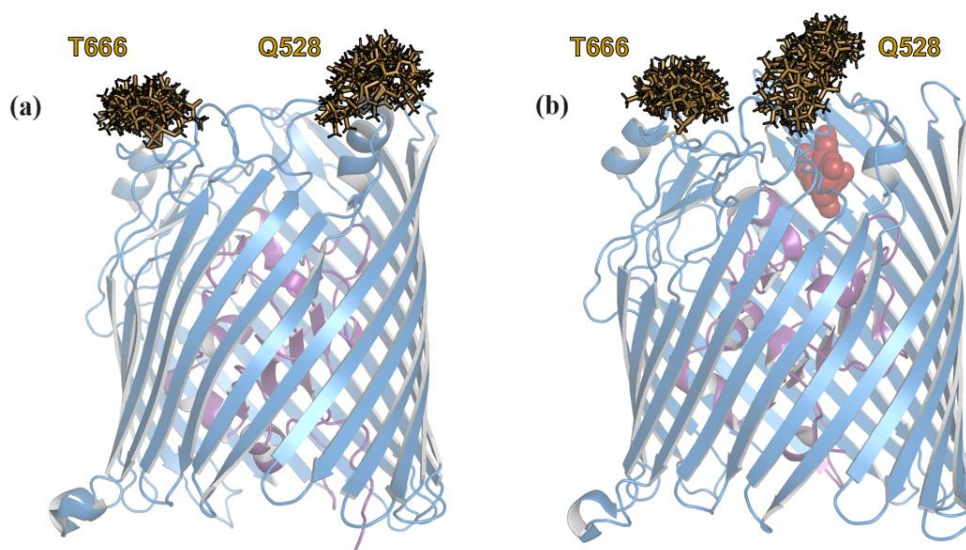
In summary, we provide evidence that the expression of an outer-membrane protein in a strain where the Dsb system is inhibited facilitates the efficient spin labeling pairs of cysteines both *in-vivo* and *in-vitro*. For FecA, it was not possible to label the extracellular loops in cells unless a *dsbA*<sup>-</sup> strain was used, and measurements in cells show evidence for substrate-dependent changes in loop structure that are not observed in a purified reconstituted phospholipid membrane.

#### 4.6 Future directions

The *dsbA*<sup>-</sup> strain coupled with pTARA enhanced the double spin labeling efficiency of FecA thereby allowing us to observe conformational dynamics using DEER spectroscopy in intact systems which was not achieved previously. However, the intermolecular FecA-FecA interactions were not observed in the isolated system as we observed for BtuB<sup>1</sup>. To further explore the molecular organization of FecA, single labeled and reconstituted FecA should be examined at longer DEER acquisition times ( $d_2 > 5 \mu\text{s}$ ), which will provide distance distributions originating from intermolecular interactions as it was observed for BtuB *in-vivo*<sup>31</sup>. Furthermore, further experiments with variable spin label concentrations to optimize periplasmic spin labeling are

required to obtain EPR data that will provide insight into periplasmic dynamics of FecA. To avoid the necessity of carrying out a 2-plasmid transformation (introduction of pTARA to *dsbA* followed by pIS711 containing *fecA*), the *fecA* gene can be inserted to a plasmid vector which consist of the T7 RNAP (Ex: pTrc99a<sup>38</sup> plasmid encoding T7 RNAP inducible by IPTG) therefore plasmid transformation efficiency and dual plasmid compatibility would not be a factor in FecA expression.

#### 4.7 Supplementary information



Supplementary Figure S4.1 Substrate induced conformational changes of extracellular loops of FecA observed in crystal structures. (a) Apo state (PDB ID 1PNZ) and (b) Ferric Citrate (brick red) bound (PDB ID 1PO3) FecA with possible rotamers available for R1 spin label (brown) at residues Q528 and T666 in the extracellular loops of the barrel domain (blue). Crystal structures indicate a substrate induced gating motion of the loops where an unfolding of a helix conformation near site Q528 (loop 7 or L7) followed by  $\sim 11$  Å translation towards the center of the barrel domain.



#### 4.8 References

1. Wimalasiri, V. W., Jurczak, K. A., Wieliniec, M. K., Nilaweera, T. D., Nakamoto, R. K., & Cafiso, D. S. (2023). A disulfide chaperone knockout facilitates spin labeling and pulse EPR spectroscopy of outer membrane transporters. *Protein science : a publication of the Protein Society*, 32(7), e4704.
2. Noinaj, N., Guillier, M., Barnard, T. J., & Buchanan, S. K. (2010). TonB-dependent transporters: regulation, structure, and function. *Annual review of microbiology*, 64, 43–60.
3. Braun V. (2001). Iron uptake mechanisms and their regulation in pathogenic bacteria. *International journal of medical microbiology : IJMM*, 291(2), 67–79.
4. Klebba, P. E., Newton, S. M. C., Six, D. A., Kumar, A., Yang, T., Nairn, B. L., Munger, C., & Chakravorty, S. (2021). Iron Acquisition Systems of Gram-negative Bacterial Pathogens Define TonB-Dependent Pathways to Novel Antibiotics. *Chemical reviews*, 121(9), 5193–5239.
5. Bolam, D. N., & van den Berg, B. (2018). TonB-dependent transport by the gut microbiota: novel aspects of an old problem. *Current opinion in structural biology*, 51, 35–43.
6. Pollet, R. M., Martin, L. M., & Koropatkin, N. M. (2021). TonB-dependent transporters in the Bacteroidetes: Unique domain structures and potential functions. *Molecular microbiology*, 115(3), 490–501.
7. Ratliff, A. C., Buchanan, S. K., & Celia, H. (2022). The Ton Motor. *Frontiers in microbiology*, 13, 852955.
8. Hubbell, W. L., López, C. J., Altenbach, C., & Yang, Z. (2013). Technological advances in site-directed spin labeling of proteins. *Current opinion in structural biology*, 23(5), 725–733.

9. Fanucci, G. E., Coggs, K. A., Cadieux, N., Kim, M., Kadner, R. J., & Cafiso, D. S. (2003). Substrate-induced conformational changes of the periplasmic N-terminus of an outer-membrane transporter by site-directed spin labeling. *Biochemistry*, *42*(6), 1391–1400.
10. Xu, Q., Ellena, J. F., Kim, M., & Cafiso, D. S. (2006). Substrate-dependent unfolding of the energy coupling motif of a membrane transport protein determined by double electron-electron resonance. *Biochemistry*, *45*(36), 10847–10854.
11. Kim, M., Fanucci, G. E., & Cafiso, D. S. (2007). Substrate-dependent transmembrane signaling in TonB-dependent transporters is not conserved. *Proceedings of the National Academy of Sciences of the United States of America*, *104*(29), 11975–11980.
12. Mokdad, A., Herrick, D. Z., Kahn, A. K., Andrews, E., Kim, M., & Cafiso, D. S. (2012). Ligand-induced structural changes in the Escherichia coli ferric citrate transporter reveal modes for regulating protein-protein interactions. *Journal of molecular biology*, *423*(5), 818–830.
13. Sarver, J. L., Zhang, M., Liu, L., Nyenhuis, D., & Cafiso, D. S. (2018). A Dynamic Protein-Protein Coupling between the TonB-Dependent Transporter FhuA and TonB. *Biochemistry*, *57*(6), 1045–1053.
14. Jiang, X., Payne, M. A., Cao, Z., Foster, S. B., Feix, J. B., Newton, S. M., & Klebba, P. E. (1997). Ligand-specific opening of a gated-porin channel in the outer membrane of living bacteria. *Science (New York, N.Y.)*, *276*(5316), 1261–1264.
15. Klug, C. S., Eaton, S. S., Eaton, G. R., & Feix, J. B. (1998). Ligand-induced conformational change in the ferric enterobactin receptor FepA as studied by site-directed spin labeling and time-domain ESR. *Biochemistry*, *37*(25), 9016–9023.

16. Joseph, B., Jaumann, E. A., Sikora, A., Barth, K., Prisner, T. F., & Cafiso, D. S. (2019). In situ observation of conformational dynamics and protein ligand-substrate interactions in outer-membrane proteins with DEER/PELDOR spectroscopy. *Nature protocols*, *14*(8), 2344–2369.
17. Sikora, A., Joseph, B., Matson, M., Staley, J. R., & Cafiso, D. S. (2016). Allosteric Signaling Is Bidirectional in an Outer-Membrane Transport Protein. *Biophysical journal*, *111*(9), 1908–1918.
18. Kim, M., Xu, Q., Murray, D., & Cafiso, D. S. (2008). Solutes alter the conformation of the ligand binding loops in outer membrane transporters. *Biochemistry*, *47*(2), 670–679.
19. Nyenhuis, D. A., Nilaweera, T. D., & Cafiso, D. S. (2020). Native Cell Environment Constrains Loop Structure in the Escherichia coli Cobalamin Transporter BtuB. *Biophysical journal*, *119*(8), 1550–1557.
20. Nilaweera, T. D., Nyenhuis, D. A., & Cafiso, D. S. (2021). Structural intermediates observed only in intact *Escherichia coli* indicate a mechanism for TonB-dependent transport. *eLife*, *10*, e68548.
21. Freed, D. M., Horanyi, P. S., Wiener, M. C., & Cafiso, D. S. (2010). Conformational exchange in a membrane transport protein is altered in protein crystals. *Biophysical journal*, *99*(5), 1604–1610.
22. Jeschke G. (2012). DEER distance measurements on proteins. *Annual review of physical chemistry*, *63*, 419–446.
23. Dutton, R. J., Boyd, D., Berkmen, M., & Beckwith, J. (2008). Bacterial species exhibit diversity in their mechanisms and capacity for protein disulfide bond formation. *Proceedings of the National Academy of Sciences of the United States of America*, *105*(33), 11933–11938.

24. Yue, W. W., Grizot, S., & Buchanan, S. K. (2003). Structural evidence for iron-free citrate and ferric citrate binding to the TonB-dependent outer membrane transporter FecA. *Journal of molecular biology*, 332(2), 353–368.
25. Prilipov, A., Phale, P. S., Van Gelder, P., Rosenbusch, J. P., & Koebnik, R. (1998). Coupling site-directed mutagenesis with high-level expression: large scale production of mutant porins from *E. coli*. *FEMS microbiology letters*, 163(1), 65–72.
26. Nilaweera, T. D., Nyenhuis, D. A., Nakamoto, R. K., & Cafiso, D. S. (2019). Disulfide Chaperone Knockouts Enable In Vivo Double Spin Labeling of an Outer Membrane Transporter. *Biophysical journal*, 117(8), 1476–1484.
27. Cogshall, K. A., Cadieux, N., Piedmont, C., Kadner, R. J., & Cafiso, D. S. (2001). Transport-defective mutations alter the conformation of the energy-coupling motif of an outer membrane transporter. *Biochemistry*, 40(46), 13964–13971.
28. Bradford, M. M. (1976). A rapid and sensitive method for the quantitation of microgram quantities of protein utilizing the principle of protein-dye binding. *Analytical biochemistry*, 72(1-2), 248-254.
29. Sedmak, J. J., & Grossberg, S. E. (1977). A rapid, sensitive, and versatile assay for protein using Coomassie brilliant blue G250. *Analytical biochemistry*, 79(1-2), 544-552.
30. Rassam, P., Copeland, N. A., Birkholz, O., Tóth, C., Chavent, M., Duncan, A. L., Cross, S. J., Housden, N. G., Kaminska, R., Seger, U., Quinn, D. M., Garrod, T. J., Sansom, M. S., Piehler, J., Baumann, C. G., & Kleanthous, C. (2015). Supramolecular assemblies underpin turnover of outer membrane proteins in bacteria. *Nature*, 523(7560), 333–336.
31. Nyenhuis, D. A., Nilaweera, T. D., Niblo, J. K., Nguyen, N. Q., DuBay, K. H., & Cafiso, D. S. (2020). Evidence for the Supramolecular Organization of a Bacterial Outer-Membrane Protein

from In Vivo Pulse Electron Paramagnetic Resonance Spectroscopy. *Journal of the American Chemical Society*, 142(24), 10715–10722.

32. Landeta, C., Boyd, D., & Beckwith, J. (2018). Disulfide bond formation in prokaryotes. *Nature microbiology*, 3(3), 270–280.

33. Jeschke, G., Chechik, V., Ionita, P., Godt, A., Zimmermann, H., Banham, J., ... & Jung, H. (2006). DeerAnalysis2006—a comprehensive software package for analyzing pulsed ELDOR data. *Applied magnetic resonance*, 30, 473-498.

34. Worswick, S. G., Spencer, J. A., Jeschke, G., & Kuprov, I. (2018). Deep neural network processing of DEER data. *Science advances*, 4(8), eaat5218.

35. Jeschke, G. (2018). MMM: A toolbox for integrative structure modeling. *Protein Science*, 27(1), 76-85.

36. Polyhach, Y., Bordignon, E., & Jeschke, G. (2011). Rotamer libraries of spin labelled cysteines for protein studies. *Physical chemistry chemical physics : PCCP*, 13(6), 2356–2366.

37. DeLano, W. L. (2002). Pymol: An open-source molecular graphics tool. *CCP4 Newsl. Protein Crystallogr*, 40(1), 82-92.

38. <https://www.novoprolabs.com/vector/Vgezdmobt> (Accessed on 13th June 2024).

## **Chapter 5: The Role of a Conserved Ionic Lock in Transport by the Outer Membrane Cobalamin Transporter BtuB using pulse EPR spectroscopy**

### 5.1 Abstract

Gram-negative bacteria such as *Escherichia coli* (*E. coli*) take up nutrients such as vitamin B12, iron, and carbohydrates through a family of outer-membrane TonB-dependent transporters (TBDTs). These TBDTs are essential for the success of many pathogens as well as for the proper function of the human microbiome, and they obtain energy from the inner-membrane (IM) proton motive force by coupling to the IM protein TonB. Although numerous high-resolution structures of different TBDTs have been determined, the molecular mechanism of transport remains uncharacterized.

The *E. coli* Vitamin B12 transporter BtuB is highly allosteric. EPR spectroscopy has shown that the binding of substrate to the extracellular surface shifts the equilibrium of an energy coupling segment termed the Ton box towards an extended or disordered state. This may make the Ton box available for coupling with the IM protein TonB. Disrupting a conserved ionic lock (D316/R14) between the protein beta-barrel and the core of the protein eliminates this substrate-dependent coupling and shifts the Ton box equilibrium towards an unfolded state. In the present work, we have used pulse EPR spectroscopy to compare the conformational state of the Ton box induced by substrate with that produced by mutation of the conserved ionic lock. These measurements were carried out both in OM preparations and lipid reconstitution systems, since allostery in this protein is known to be modulated by the native membrane environment. The data show that mutating the ionic lock produces a more extended state of the Ton box than does substrate, and that this state can be mimicked by the binding of a C-terminal fragment of TonB, suggesting a mechanism of transport.

## 5.2 Introduction

*E. coli* and other Gram-negative bacteria consist of an asymmetric outer membrane (OM) composed of phospholipids and lipopolysaccharides (LPS) that are crucial to survive variable environmental conditions<sup>1</sup>. This OM inhibits passage for crucial co-factors for bacterial nutrition, thus a unique class of transporter proteins reside in the OM for uptake of these trace nutrients with high affinity. The energy for active transport is acquired by coupling to the inner membrane (IM) protein TonB which in turn is coupled with the proton motive force (PMF) sensitive ExbB/ExbD complex in the IM. Hence, these outer membrane proteins (OMPs) are known as TonB-dependent transporters (TBDTs)<sup>2</sup>. Crystal structures elucidated for the Cobalamin (Vitamin B<sub>12</sub>) transporter BtuB<sup>3</sup> and the iron transporters FecA<sup>4</sup>, FhuA<sup>5</sup>, and FepA<sup>6</sup> exhibit similar architecture where the C-terminus is folded into a 22-stranded antiparallel  $\beta$ -barrel and the N-terminus folded into a plug domain and occlude the interior of the barrel. TBDT function is mediated by an interaction between the C-terminus of TonB and a highly conserved N-terminal segment of the OMP known as Ton box. The conformation of the Ton box is also known to be substrate dependent<sup>7,8</sup>. However, the overall mechanism of active transport is yet to be elucidated. Furthermore, the substrate dependent transmembrane signaling resulting in the TonB-Ton box interaction is also unclear.

Numerous crystal structures obtained for FhuA do not resolve the Ton box region in either the presence or absence of substrate, whereas the Ton box of FecA is resolved for apo state but not resolved in the presence of ferric citrate. BtuB crystal structures indicate slight changes in Ton box configuration in the presence of substrate. Early advancements in site-directed spin labeling (SDSL) coupled with continuous wave electron paramagnetic resonance (CW-EPR) spectroscopy on BtuB indicated a substrate specific disordering of Ton box<sup>9</sup>. Pulse EPR measurements between the Ton box and the periplasmic turns indicate a 20 – 30 Å shift towards the periplasmic space

upon substrate binding. Furthermore, double electron-electron resonance (DEER) data indicated the presence of an equilibrium between unfolded and folded states of the Ton box<sup>10</sup>. The combination of CW and DEER data suggests that the substrate induced unfolding of Ton box will promote association with TonB through as an early step in active transport. High resolution crystal structure obtained for BtuB in complex with a C-terminal fragment of TonB show that the Ton box must extend, and that the interaction occurs through an edge-to-edge  $\beta$ -sheet interaction between Ton box and TonB but does not exhibit as dramatic an extension of the Ton box as observed by EPR<sup>11</sup>. This contrast in Ton box conformation between crystallography and EPR data is presumed to be due to the different osmolytes and buffers utilized during the crystallization process<sup>12</sup>.

The crystal structure of BtuB:TonB complex does not reveal any significant changes to the majority of the core domain. In this conformation, the core domain will block substrate transport, and it is proposed that TonB exerts a mechanical force on the core domain by means of pulling<sup>13,14</sup> or rotation<sup>15</sup> thereby altering the folding of the core domain and permitting substrate transport. However, a more dynamic behavior of TonB when bound to FhuA<sup>16</sup> is observed in EPR experiments, where four to five residues of the Ton box are unstructured in the presence of TonB. This makes a rotation mechanism unlikely as it would not be possible to transmit torque through this unstructured region. Molecular dynamics (MD) simulations<sup>13</sup> and atomic force microscopy (AFM) based pulling experiments<sup>14</sup> indicate that a significant portion of the N-terminus of the core domain may be unfolded to allow for passage of substrate. In these studies, the C-terminus of the core domain remains static, which is consistent with site-specific denaturation experiments on BtuB<sup>17</sup>.

CW EPR experiments in combination with a two-mutant cycle analysis show that an ionic interaction between R14 in the core domain and D316 in the barrel domain contribute about 2



kcal/mole to the stability of the Ton box. Mutating either or both residues allows the Ton box to become disordered and presumably extend into the periplasmic space in the absence of substrate (see Figure 5.1a,b)<sup>18</sup>. Also, recent advancements in SDSL has allowed us to study BtuB in the intact cell with the assistance of an *E. coli* strain containing the knockout of the disulfide bond oxidase *dsbA* or its inner-membrane electron acceptor *dsbB*<sup>19</sup>. Pulse EPR measurements obtained from the periplasmic surface of BtuB in the *dsbA* null strain are difficult because of the rapid reduction of spin label, but the data do allow the evaluation of distance distributions. Surprisingly, the distributions obtained from the intact cell do not reveal the expected substrate dependent disordering of the Ton box (as observed in isolated reconstituted systems), but instead indicate that the Ton box is largely unfolded. Further pulse experiments have been made in this thesis to study the dynamics of the BtuB core domain by making measurements from the extracellular surface when the R14-D316 ionic lock is disrupted<sup>20</sup>. In addition, pulse EPR has been used to examine the BtuB Ton box in isolated reconstituted systems and OM preparations when the R14-D316 ionic interaction is disrupted. The configuration of the Ton box has also been examined in the presence of the C-terminal fragment of TonB.

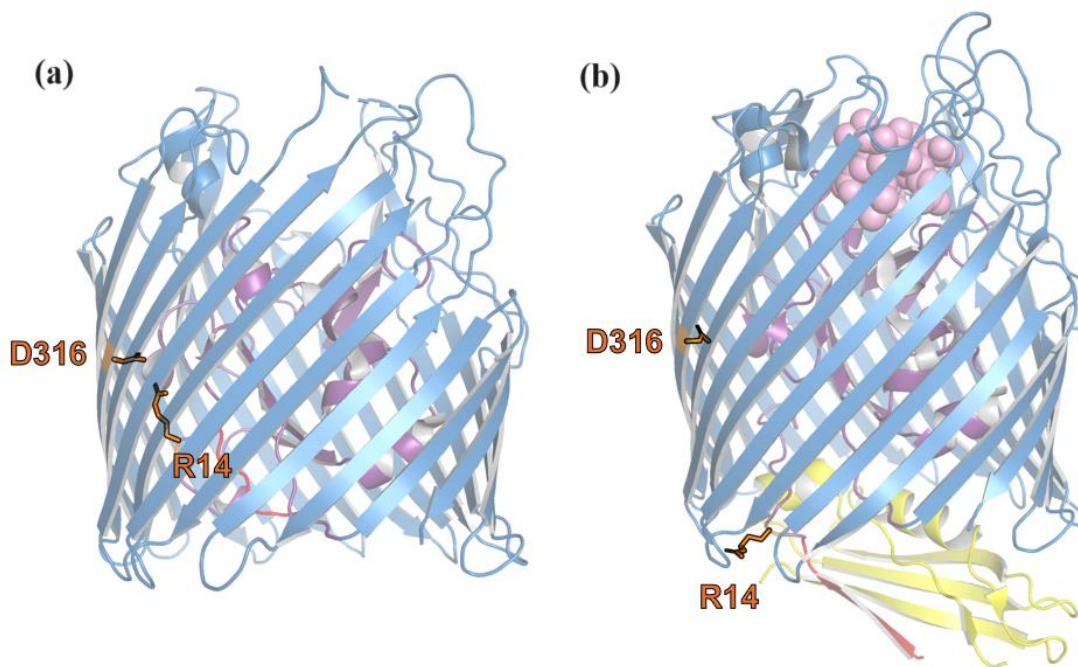


Figure 5.1 The crystal structures of BtuB with the R14-D316 ionic interaction. (a) Apo state (PDB ID 1NQG) exhibit ionic interaction between Arg14 (R14) in the core domain (purple) and Asp316 (D316) in the barrel domain (blue). In this structure, the two side-chains are separated by approximately 5 Å. (b) B<sub>12</sub> (pink) and TonB C-terminus (yellow) bound state (PDB ID 2GSK) indicates that the separation increases to approximately 25 Å. BtuB Ton box (residues 6–12) are highlighted in red.

In the present work, we investigate the BtuB Ton box in apo and substrate bound states, when the R14-D316 ionic lock is disrupted, and in the presence of the purified TonB C-terminal fragment using the dead-time free four pulse DEER measurement. The DEER experiment generates a dipolar echo that is modulated by the frequency of the dipolar interaction between spin pairs introduced through SDSL. DEER can be used to measure distances up to 8 nm<sup>21</sup>. Spin pairs were introduced to BtuB between the Ton box (positions 6 and 10)(see Figure 5.2) and the

periplasmic turns (positions 305 and 510)(see Figure 5.2) and the R14-D316 ionic interaction was disrupted through an alanine mutation on residue D316 (D316A) of the barrel domain. The CW EPR data obtained from BtuB reconstituted in liposomes indicates that the Ton box undergoes an unfolding when the R14-D316 ionic lock is disrupted regardless of the presence of substrate. The DEER data are consistent with the disordering observed in CW EPR studies for BtuB in isolated in OM preparations. Interestingly, the Ton box appears to be extended in the absence of substrate when TonB C-terminal fragment is bound as was observed previously in the intact cell<sup>19</sup>. Therefore, we propose that the extent of Ton box unfolding is much larger when the R14-D316 ionic lock is disrupted, or TonB C-terminal fragment is introduced than with substrate addition. Furthermore, the binding of TonB to BtuB Ton box is likely to mimic the disruption of the R14-D316 ionic lock between the core and barrel domains.

## 5.3 Materials and Methods

### 5.3.1 Cell lines and plasmids

For the vitamin B<sub>12</sub> transporter, BtuB, the pAG1 plasmid with WT *btuB* gene and the *E. coli* strain RK5016 (*-argH*, *-btuB*, *-metE*) was obtained from late Professor Robert Kadner, University of Virginia. The TonB fragment with a 6X His tag lacking the N-terminal domain and a portion of the periplasmic domain (residues 103-239)(TonB C-term) was generously provided by Prof. Robert K. Nakamoto, University of Virginia. Mutant *dsb E. coli* strains were obtained from the Coli Genetic Stock Center (Yale University, New Haven, CT). Strain RI90 carries the *dsbA* null mutation system (*araD139 Δ(araABC-leu) 7679 galU galK Δ(lac)X74 rpsL thi phoR Δara714 leu +dsbA:: Kanr*). *E. coli* strain T7 express *LysY/I<sup>q</sup>* competent cells were obtained from New England Biolabs (Ipswich, MA).

### 5.3.2 PCR mutagenesis and OMP expression

BtuB double cysteine mutations (D6C-I305C, D6C-Q510C, V10C-Q510C) and ionic lock disruption mutations (D6C-I305C-D316A, D6C-Q510C-D316A, V10C-Q510C-D316A) were generated using site-directed mutagenesis and polymerase incomplete primer extension<sup>22</sup> followed by DNA sequencing verification (Genewiz, South Plainfield, NJ and Plasmidsaurus, Eugene, OR). The *btuB* containing plasmids were transformed into *dsbA*<sup>-</sup> strains.

A single colony was used to inoculate Luria-Bertani (LB) media and prepare a glycerol stock which was stored at -80 °C. For BtuB, precultures of Minimal Media (100 mM phosphate buffer, 8 mM (NH<sub>4</sub>)<sub>2</sub>SO<sub>4</sub>, 2 mM sodium citrate, 100 mg/mL ampicillin, 0.2% w/v glucose, 150 mM thiamine, 3 mM MgSO<sub>4</sub>, 300 mM CaCl<sub>2</sub>, 0.01% w/v methionine, 0.01% w/v arginine) were inoculated using the glycerol stock and later used to inoculate the main culture. An initial overnight preculture growth was followed by an 8 hr main culture growth<sup>23</sup>.

### 5.3.3 OM and reconstituted BtuB sample preparation

An intact OM preparation is obtained from the total cell membrane fraction using a standard procedure<sup>9, 10</sup>. This involves treating the cell membrane fraction with 1% sarkosyl to remove the inner membrane, and then pelleting the OM and removal of the sarkosyl by centrifugation. For measurements made in the OM preparation, the preparation was spin labeled at this stage<sup>19</sup>. For protein that was purified, the OM preparation was solubilized with OG as described previously, and 5 mL of the solubilized OM sample then was treated with 100 µL of 22 mM MTSL [(1-oxyl-2,2,5,5-tetramethylpyrroline-3-methyl) methanethiosulfonate] followed by incubation for 2 - 3 hr at room temperature (RT)<sup>19</sup>. Spin labeled BtuB was purified using ion-exchange chromatography as described previously<sup>9</sup>. Purified BtuB was quantified using the Bradford Assay<sup>24, 25</sup>.

The purified and spin-labeled BtuB samples were reconstituted into 1-palmitoyl-2-oleoyl-sn-glycero-3-phosphocholine (POPC) vesicles by the addition of OG/POPC (10:1), and the mixed micelles were added to the purified BtuB samples at a protein: lipid ratio of 1:25. The samples were then dialyzed against six 4 L dialysis buffer changes (10 mM HEPES, 128 mM NaCl, and 1 mM EDTA at pH 6.5) at 10–12 hr intervals<sup>10, 26, 27</sup>.

#### 5.3.4 C-terminus TonB expression and purification

TonB was expressed and purified as described previously<sup>16</sup>. Plasmid containing 6X His tagged TonB C-term was transformed into *LysY/I<sup>q</sup>* cells and was grown in 2XYT media at 37 °C. Cells were induced with 0.5 mM IPTG at OD<sub>600</sub> of 0.7 – 0.8 and were grown for additional 6 hr at 20 °C and then pelleted by centrifugation.

TonB purification was performed on ice to avoid proteolysis. The cell pellet was resuspended in resuspension buffer<sup>16</sup> with protease inhibitors aprotinin, leupeptin and AEBSF and DTT. Cells were disrupted using a French Press followed by centrifugation to obtain the supernatant. The supernatant was then loaded to a nickel column containing equilibration buffer<sup>16</sup> and was washed with 3 column volumes of equilibration buffer. Column was then treated with 5mL of a 100 mM imidazole buffer<sup>16</sup> to remove non-specific proteins, and bound protein (TonB) was eluted with 25 mL elution buffer<sup>16</sup>. Fractions containing TonB were identified using protein gel electrophoresis and the pure fractions were pooled. A 3 kDa molecular weight cut off (MWCO) was used to concentrate the pooled fractions to obtain a 1.5 mL solution of TonB with a concentration of approximately 350 μM. Quantification was done using the Bradford Assay for TonB just as BtuB.

### 5.3.5 EPR Measurements

For CW-EPR measurements, 5  $\mu\text{L}$  sample with 1  $\mu\text{L}$  dialysis buffer was loaded into 0.84 x 0.6  $\text{mm}^2$  quartz capillaries and used as apo sample, whereas 5  $\mu\text{L}$  sample with 1  $\mu\text{L}$  of 1 mM Vitamin B<sub>12</sub> was used as the substrate bound sample. EPR spectra were recorded at room temperature at X-band using a Bruker EMX spectrometer (Billerica, MA) with an ER 4123D dielectric resonator. A sweep width of 100 gauss (G) was used with a modulation amplitude of 1 G, and 2 mW incident microwave power. Data were collected as additive averages of 10 scans and were normalized by their second integral. For DEER, a 16  $\mu\text{L}$  sample with 4  $\mu\text{L}$  of concentrated d-glycerol was loaded into 1.1 x 1.6  $\text{mm}^2$  quartz capillaries (VitroCom, Mountain Lakes, NJ). 2  $\mu\text{L}$  of 1 mM Vitamin B<sub>12</sub> and 4  $\mu\text{L}$  of purified TonB (~ 350  $\mu\text{M}$ ) was added for samples with substrate and with TonB, respectively. All samples underwent 6 - 7 freeze thaw cycles to ensure substrate and TonB access to all BtuB in the sample. All DEER experiments were performed on a Bruker E580 spectrometer operating at Q-band (Bruker BioSpin, Billerica, MA) with the following hardware: Bruker EN5107D2 dielectric resonator or Bridge12 B12TQLP Q-Band loop-gap resonator, Bruker SpinJet-AWG, and a Bruker 10 W solid state amplifier. Experiments were run at 50 K using the standard dead-time free 4-pulse DEER experiment, with a 14 or 16 ns  $\pi/2$  pulse and 28 or 32 ns  $\pi$  pulses, respectively. All pulses were rectangular. The separation between observe and pump frequencies was 75 MHz. Acquisition times for most samples typically ranged from 12 to 20 hr.

### 5.3.6 Data processing

All DEER data were processed with DeerAnalysis<sup>28</sup> using the DEERNet routine<sup>29</sup>. Simulated distance distributions were generated using the software package Multiscale Modeling

of Macromolecules (MMM) and the default rotamer library<sup>30,31</sup>. Protein structure images were generated using Pymol<sup>32</sup>.

## 5.4 Results

### 5.4.1 Disruption of the R14-D316 ionic lock results in a substrate independent extension of the BtuB Ton box in isolated reconstituted systems

Figure 5.2 represents CW-EPR spectra obtained from reconstituted BtuB preparations of spin labeled cysteine pairs introduced to the periplasmic surface of BtuB. Site D6 and V10 from the BtuB Ton box was paired with sites I305 and Q510 from the periplasmic turns to create D6R1-I305R1, D6R1-Q510R1, and V10R1-Q510R1 spin pairs (see Figure 5.2b,c top row). Reconstitution was performed for all three spin pairs with similar protein levels and phospholipids in an identical manner. BtuB was purified and spin labelled using an *E. coli dsbA*<sup>-</sup> growth allowing the availability of introduced cysteines for crosslinking with MTSL reagent during labeling step. The difference in signal intensity observed for some spin pairs in Figure 5.2c is due to unavoidable variability during CW-EPR sample preparation.

D6 and V10 are located in the BtuB N-terminal energy coupling segment termed the Ton box, which undergoes a substrate-induced unfolding previously observed *in-vitro*<sup>10, 23</sup>, whereas I305 and Q510 are located in the periplasmic turns and remain static. Thus, the changes in CW-EPR observed under different conditions will be solely due to the structural and functional dynamics of the Ton box. As observed, the apo state of all three spin pairs yield broader EPR spectra with hindered spin label dynamics due to the native fold of BtuB Ton box inside the barrel domain. The introduction of substrate (Vitamin B<sub>12</sub>) results in the unfolding of the Ton box followed by extension into the periplasmic direction of BtuB. The resulting extension facilitates a

free environment for spin label tumbling thus, an increase in spin label dynamics where narrow resonance peaks are observed (see Figure 5.2c top row).

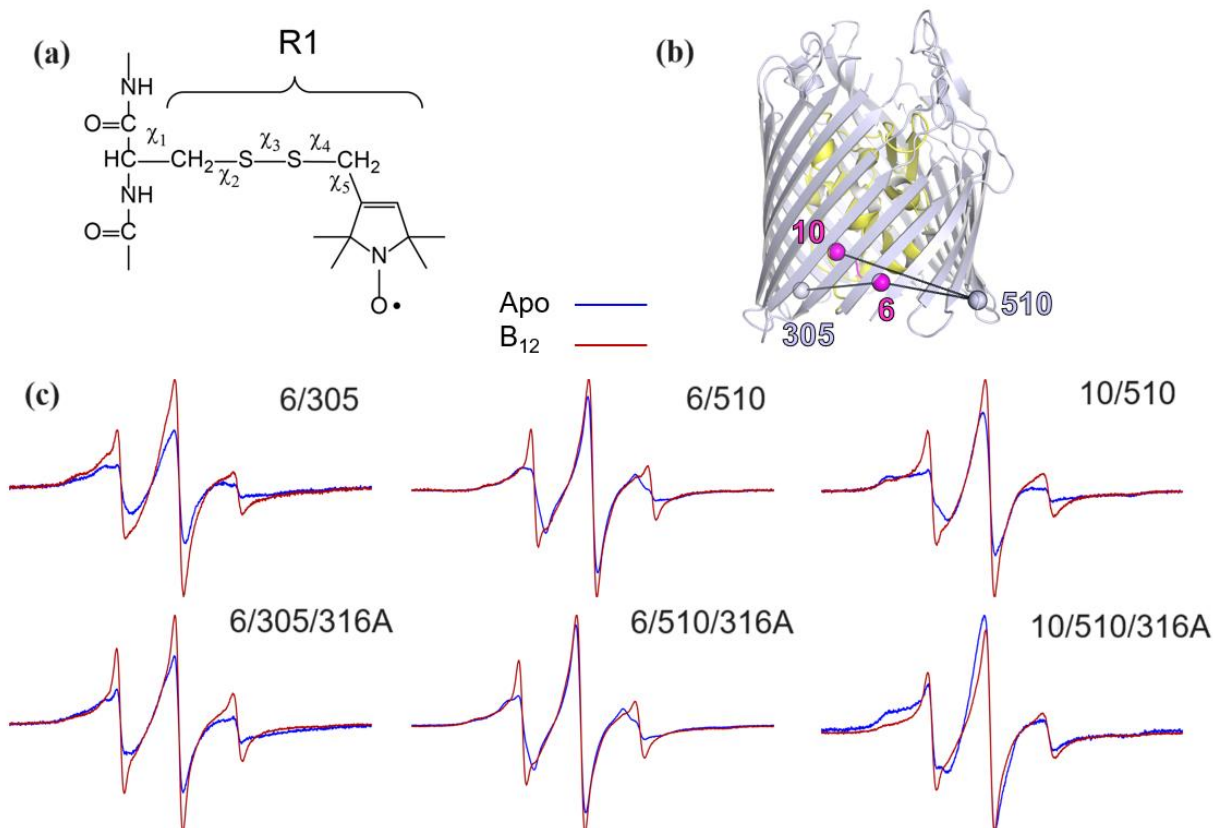


Figure 5.2 The cleavage of R14-D316 ionic lock results in extension of BtuB Ton box in a phospholipid reconstituted preparation. (a) For EPR measurements, free cysteines are labeled using a conventional MTSL spin label to generate the side chain R1<sup>23</sup>. In (b) crystal structure of BtuB (PDB ID: 1NQG) with sites labeled on the periplasmic surface and Ton box of BtuB shown as spheres. The periplasmic energy coupling Ton box is shown in magenta. In (c) are shown the CW-EPR spectra obtained from D6R1-I305R1, D6R1-Q510R1, and V10R1-Q510R1 (top row) and D6R1-I305R1-D316A, D6R1-Q510R1-D316A, V10R1-Q510R1-D316A (bottom row) on the periplasmic interface where BtuB is overexpressed in a *dsbA*<sup>-</sup> strain.



The extension of Ton box is a transmembrane signaling event that was observed previously, where substrate binding induces a partial disengagement of an ionic lock between R14 in the core domain and D316 in the barrel domain<sup>18</sup>. Conversion of D316 to A316 (D316A) permanently cleaves this ionic lock allowing the Ton box to freely shift into the periplasmic surface. Phospholipid reconstitutions done for all three spin pairs with the additional D316A mutation (D6R1-I305R1-D316A, D6R1-Q510R1-D316A, V10R1-Q510R1-D316A) demonstrate the release of Ton box for all three spin pairs as indicated by a narrowing of EPR spectra for BtuB in the apo state (see Figure 5.2c bottom row) when this ionic lock is mutated (see Figure 5.2c top row). B<sub>12</sub> addition results in further unfolding of Ton box indicated by sharper and less broadened EPR spectra observed for spin pairs with a disrupted ionic lock.

5.4.2 Pulse EPR indicates that the Ton box of BtuB in OM preparations undergoes a greater extension in the presence of the ionic lock mutant, or the binding of TonB, than that seen in reconstituted preparations

In addition to CW-EPR spectra, DEER data were obtained for D6R1-I305R1 and D6R1-I305R1-D316A BtuB spin pairs in OM and reconstituted preparations. As observed in Figure 5.3a, the OM preparation of D6R1-I305R1 yielded a remarkably similar distance distribution which agrees well with the predicted distance distributions obtained for the spin pair in crystal structures using MMM. The addition of substrate results in the extension of Ton box for a limited spin population. Addition of the C-terminal fragment of TonB to OM preparations resulted in a more dramatic extension of the Ton box with distances up to 5 nm with respect to the periplasmic turn containing site 305 (Figure 5.3b). Surprisingly, the binding of TonB alone resulted in a greater extension of the Ton box than that seen for substrate addition, suggesting that substrate binding and TonB binding are not equivalent in their ability to unfold the N-terminus<sup>7, 9, 10, 14, 18</sup>. A behavior

similar to TonB binding was also observed in the presence of ionic lock disruption (D316A) as seen in Figure 5.4a, indicating that the effect of ionic lock on the Ton box extension is equivalent to that seen for TonB binding in a non-energized isolated system. However, when BtuB is purified and reconstituted into liposomes, such transitions are not obvious. The distance distributions obtained for D6R1-I305R1-D316A in the reconstituted system (see Figure 5.4b) show distributions matching the predicted distance distributions obtained from the allowed label rotamers (see Supplementary Figure S5.5) calculated using MMM. However, both reconstituted states exhibit a possible intermolecular distance component which was also observed in previous studies<sup>23</sup>.

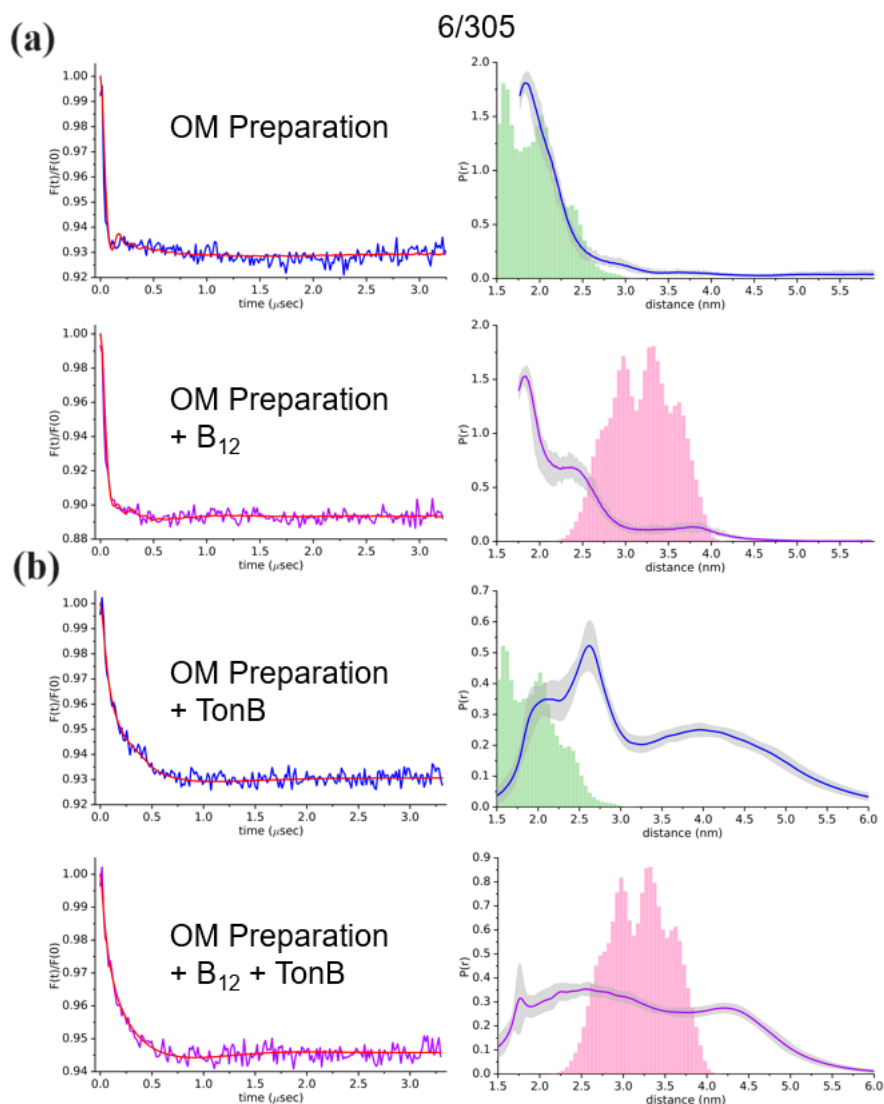


Figure 5.3 DEER data of D6R1-I305R1 obtained from an outer-membrane preparation. For all conditions, data are shown in the apo (blue trace) and B<sub>12</sub> bound (purple trace) states of BtuB. (a) DEER data obtained for BtuB labeled at sites D6 and I305 obtained from an OM preparation. (b) DEER data obtained for BtuB D6R1-I305R1 obtained from an OM preparation in the presence of C-terminal TonB fragment. All distance distributions were obtained using DEERNet. The predictions from the apo and substrate bound crystal structures (PDB ID: 1NQG and 2GSK, respectively) are shown as green and pink histograms, respectively.

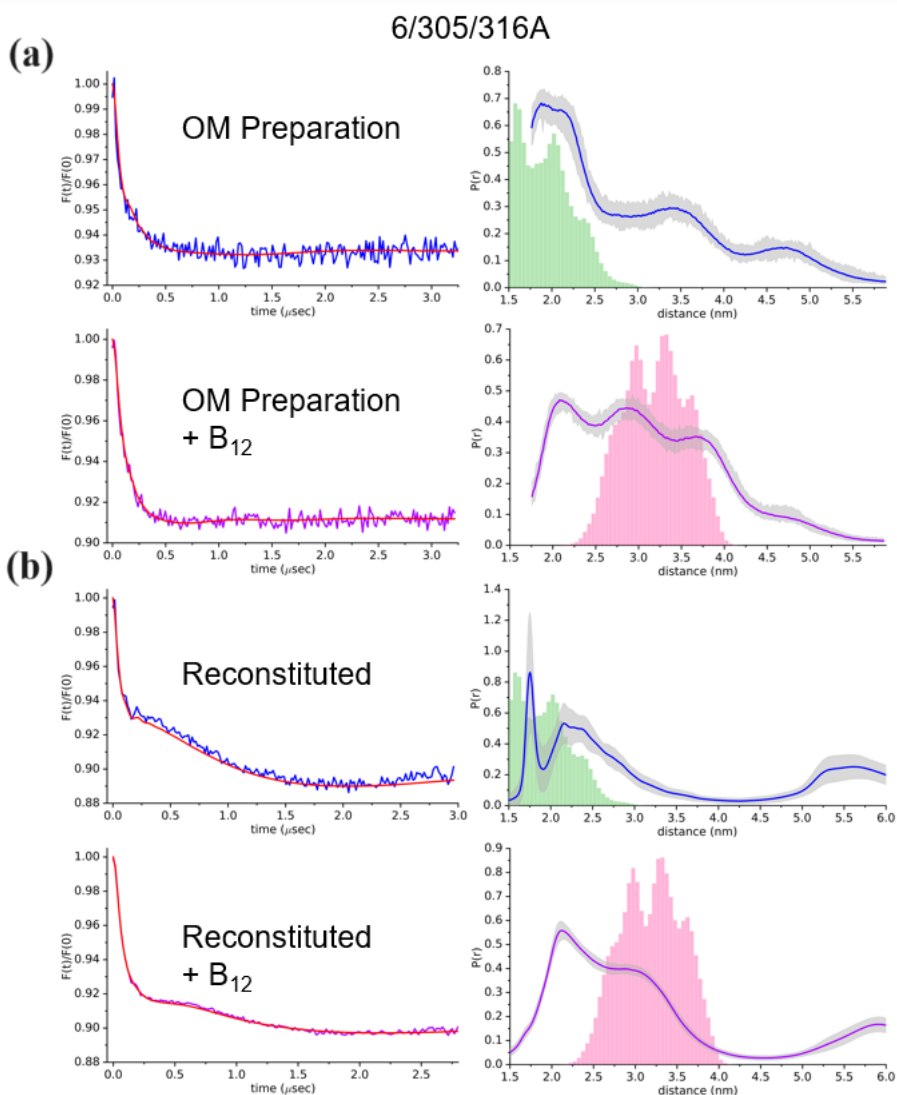


Figure 5.4 DEER data of D6R1-I305R1-D316A obtained from purified reconstituted protein or an outer-membrane preparation. For all conditions, data are shown in the apo (blue trace) and B<sub>12</sub> bound (purple trace) states of BtuB. (a) DEER data obtained for BtuB labeled at sites D6 and I305 with the alanine mutation at D316 obtained from an OM preparation. (b) DEER data obtained for BtuB D6R1-I305R1-D316A reconstituted into POPC bilayers. All distance distributions were obtained using DEERNet. The predictions from the apo and substrate bound crystal structures (PDB ID: 1NQG and 2GSK, respectively) are shown as green and pink histograms, respectively.

Similar Ton box behavior was observed between the D6R1-Q510R1 and D6R1-Q510R1-D316A spin pairs (see Supplementary Figure S5.1, S5.2, S5.6) indicating that these conformational dynamics remain consistent under given experimental conditions. Examination of V10R1-Q510R1 and V10-Q510R1-D316A spin pairs (see Supplementary Figure S5.3, S5.4, S5.7) yielded distance distributions indicating a similar behavior to what was observed for D6 spin pairs.

## 5.5 Discussion

In previous work, spin pairs incorporated into the BtuB N-terminal energy coupling segment known as Ton box and periplasmic turns shows a substrate dependent conformational shift where the Ton box extends into the periplasmic space upon substrate binding<sup>10</sup>. DEER data obtained for these pairs required additional labeling steps due to the presence of the native disulfide bond formation (Dsb) system crosslinking mutated cysteine pairs. Recently, we have observed higher efficiency of BtuB double spin labelling with the assistance of an *E. coli* strain deficient in disulfide oxidase *dsbA* under both *in-vitro*<sup>23</sup> and *in-vivo*<sup>19</sup> conditions. DEER data obtained for BtuB periplasmic spin pairs expressed in the *dsbA*- strain under different experimental conditions exhibit novel conformations that was previously not observed *in-vitro*.

This study focuses on the dynamics of the BtuB Ton box under different experimental conditions. It is our intention to identify the constituents that are crucial for initial signaling process of BtuB function, believed to be the Ton box extension upon substrate binding and interaction with TonB. It is also observed that the binding of substrate disengages a crucial ionic lock between R14 in the core domain and D316 in the barrel domain allowing the Ton box to extend into the periplasmic space (see Figure 5.1)<sup>18,20</sup>. For this study, two sites of BtuB Ton box (D6 and V10) along with two sites of BtuB periplasmic turns (I305 and Q510) were selected to create three spin pairs (BtuB D6R1-I305R1, D6R1-Q510R1, and V10R1-Q510R1). To disrupt the ionic lock between core and barrel domain of BtuB, an alanine mutation to D316 in the barrel domain was introduced to all three spin pairs (BtuB D6R1-I305R1-D316A, D6R1-Q510R1-D316A, and V10R1-Q510R1-D316A).

The CW-EPR spectra obtained for all three spin pairs indicated a substrate induced conformational change where addition of vitamin B<sub>12</sub> resulted in the disordering of Ton box. The R1 spin label EPR spectra is extremely sensitive to the backbone motion and possible steric contacts arising at a location where the label is present. The switch from a broader spectrum in the apo state to a motionally narrowed spectrum in the B<sub>12</sub> bound state (see Figure 5.2c top row) is indicative of unfolded Ton box where an unrestrained environment allows motional averaging of the nitroxide magnetic interactions. In this instance, disruption of the ionic lock allowed a small fraction of spin population to shift to an unfolded Ton box configuration in the apo state, which is seen as a narrow feature in the relatively broad low field resonance (see Figure 5.2c bottom row). Previous studies have shown that the disruption of ionic lock resulted in a dramatic unfolding of Ton box using site V10 in the reconstituted system<sup>18</sup>, which is also observed prominently in the V10-Q510 spin pair compared to D6-I305 and D6-Q510 spin pairs. However, it is important to

understand that the EPR spectra obtained here is a combination of R1 motions present in all labeled sites.

It is important to point out that there exists an equilibrium between substrate bound and unbound states when vitamin B<sub>12</sub> is introduced to BtuB samples<sup>9, 10, 18, 23</sup>. Thus, DEER experiments performed on BtuB in the presence of substrate always contain distance components corresponding to both states. D6R1-I305R1 BtuB in OM preparations indicated a slight extension of Ton box in the presence of substrate (see Figure 5.3a) in agreement with the predicted distance distributions obtained through MMM simulations, whereas OM preparation of D6R1-I305R1-D316A BtuB exhibit a continuously unfolded Ton box regardless of substrate (see Figure 5.4a) as seen previously in CW EPR experiments on the reconstituted preparations of BtuB Ton box<sup>18</sup>. The Ton box extension spans more than the previously observed 20 - 30 Å<sup>10</sup> indicating the unfolding of the BtuB N-terminus at least up to 15 residues<sup>10</sup> or possibly even more. Interestingly, in OM preparations, addition of the TonB C-terminal fragment to BtuB having an intact ionic lock resulted in an unexpected discovery where a similar dramatic extension of Ton box was observed independent of substrate or the presence of D6R1-I305R1-D316A mutant alone (see Figure 5.3b). We believe that this is a direct result of the extremely high affinity of TonB towards BtuB (nanomolar range)<sup>33</sup> that will break the R14-D316 ionic lock and allow Ton box unfolding. The release of free energy of TonB-Ton box interaction was sufficient for significant extension of the N-terminus of BtuB, possibly up to 35 – 40 Å.

However, it was interesting to observe that for D6R1-I305R1-D316A BtuB reconstituted in POPC liposomes, such significant extension was not observed for apo state. However, a small population of spin pairs does exhibit distance distributions around 3 nm indicative of a partially unfolded Ton box (see Figure 5.4b). This distance component aligns with distance components

predicted through MMM for the BtuB:TonB complex<sup>11</sup>. We do not understand the foundation behind the diversity of distance distributions obtained through separate BtuB preparations. However, previous studies through steered molecular dynamics simulations (SMD) have shown that the force required for BtuB N-terminal extension towards periplasmic surface is around 15% less in an asymmetric membrane such as Gram-negative OM compared to a symmetric membrane and that it is also dependent upon the LPS interaction with the extracellular loops<sup>34</sup>. Therefore, the release of Ton box from the interior of the barrel domain in a symmetric membrane such as that obtained in a POPC reconstitution without LPS can differ from a partially asymmetric membrane such as an OM preparation that does contain LPS. The separate long-distance distribution observed for reconstituted BtuB around 5.5 – 6.0 nm might be due to intermolecular BtuB-BtuB interactions observed through efficient double spin labeling in the *dsbA*<sup>-</sup> strain<sup>23</sup>. This was also observed *in-vivo*<sup>27</sup> where these BtuB-BtuB interactions allow the formation of string-like oligomers known as outer membrane protein (OMP) islands, which assist the cells in membrane protein clearance by driving them to the poles of the cell.<sup>26</sup> Surprisingly, this distance component was present for all three reconstituted preparations.

DEER data obtained for D6R1-Q510R1 BtuB and D6R1-Q510R1-D316A BtuB show a similar pattern as to what was observed for D6R1-I305R1 BtuB and D6R1-I305R1-D316A BtuB, indicating that these structural transitions are reproducible (see Supplementary Figure S5.1, S5.2). Previous studies of D6R1-Q510R1 BtuB in the intact cell indicated a permanent unfolding of the Ton box in intact cells<sup>19</sup> (see Supplementary Figure S5.8). Unexpectedly, we can observe similar distance distributions for the same spin pair in the presence of TonB or with the disruption of ionic lock in the isolated system. Therefore, we can assume that we would be able to observe Ton box dynamics seen in the intact cell in an isolated preparation with the assistance of the IM protein

TonB. Unexpectedly, V10R1-Q510R1 BtuB and V10-Q510R1-D316A BtuB presented with a unique scenario. The predicted distance distributions obtained through MMM using possible rotamers indicate a movement of V10 towards Q510 during the interaction between TonB (PDB ID 2GSK) (see Supplementary Figure S5.7). This is due to V10 being buried in the lumen of the barrel domain and displaced from the periplasmic turns. As the BtuB N-terminal domain begins to extend towards the periplasmic space, V10 shift will align its position with the plane of the periplasmic turn site Q510, providing a short distance component between the two sites. Next, the continuous unfolding of the Ton box will allow V10 to be below the plane of site Q510, thus allowing us to observe longer distance distributions between the spins. Regardless, TonB addition (see Supplementary Figure S5.3b) or disruption of the ionic lock (see Supplementary Figure S5.4a) resulted in distance distributions up to 4.0 – 4.5 nm which may indicate a significant unfolding of BtuB N-terminus as observed for D6 spin pairs.

Currently, the sequential steps involved in TonB-dependent transport are not known, but it is apparent that both substrate and TonB will be bound to BtuB at some stage in transport. This will result in the cleavage of R14-D316 ionic lock. Experimental data indicate that substantial unfolding of the Ton box will occur upon TonB binding or ionic lock disruption. These data suggest that the free energy of binding TonB to BtuB ( $K_d$  in nanomolar range) is sufficient for this unfolding, and that it can be mimicked by ionic lock disruption. Previous studies have indicated that breaking the ionic lock allows for large structural changes in the C-terminus of the core domain upon substrate binding in the cell<sup>20</sup>. However, isolated preparations do not exhibit such changes due to the absence of energy driven processes such as ATP hydrolysis or PMF. Therefore, the observation that there can be a considerable extension of the Ton box without any mechanical action of TonB on BtuB (for example, pulling or rotating) suggests that the free energy of binding



of TonB to BtuB may be sufficient for a structural rearrangement of the core domain that allows substrate passage.

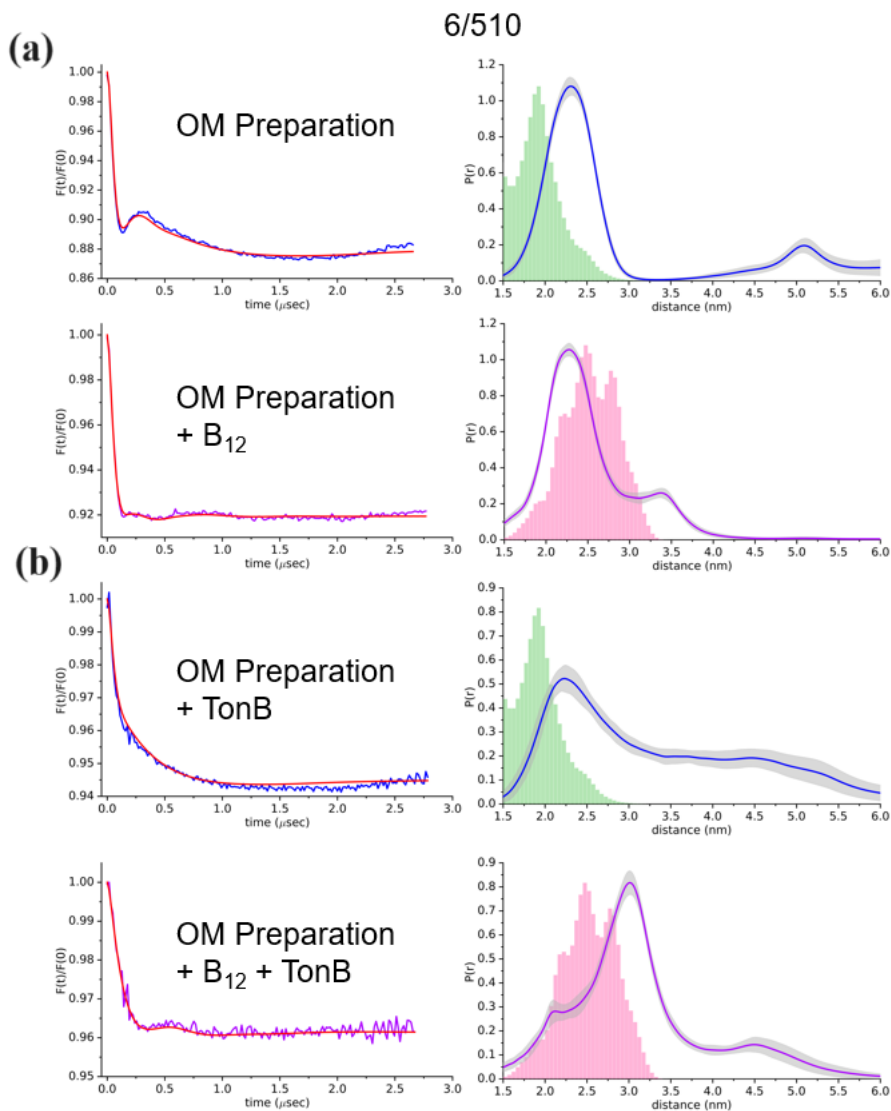
In summary, we have provided evidence that the BtuB Ton-box undergoes irreversible unfolding up to 35 – 40 Å towards the periplasmic space when the crucial R14-D316 ionic lock between the core and barrel domains is disrupted. We show that this unfolding is substrate independent, and that a similar unfolding behavior is observed for BtuB when the ionic lock is intact and TonB is bound. Thus, the binding of TonB can be mimicked by disruption of the ionic lock. We further postulate that this behavior is significant in the OM preparation where the constituents of the native membrane are present and that it is feasible to observe the conformational dynamics seen in the intact cell to in an isolated system, provided that the necessary OM constituents are present.

## 5.6 Future Directions

The disruption of the R14-D316 ionic lock resulted in a substrate independent extension of the BtuB N-terminus up to about 40 Å in isolated OM preparations which was not observed previously. Furthermore, a similar behavior was observed when C-terminal domain of TonB was introduced in place of ionic lock mutations in isolated OM preparations. However, there is a difference in the distance distributions obtained for lipid reconstituted systems when compared to OM preparations. This should be further studied to identify possible membrane contribution towards BtuB structural dynamics. To investigate these contributions, DEER distance distributions should be made with BtuB inserted in POPC:LPS lipid mixtures to clarify the contributions of LPS towards BtuB function. Generally, POPC lipids create well sealed liposomes and this can prevent the interaction between BtuB and TonB when TonB is introduced externally. Following reconstitution, BtuB is randomly oriented in POPC vesicles, and multiple freeze thaw cycles are

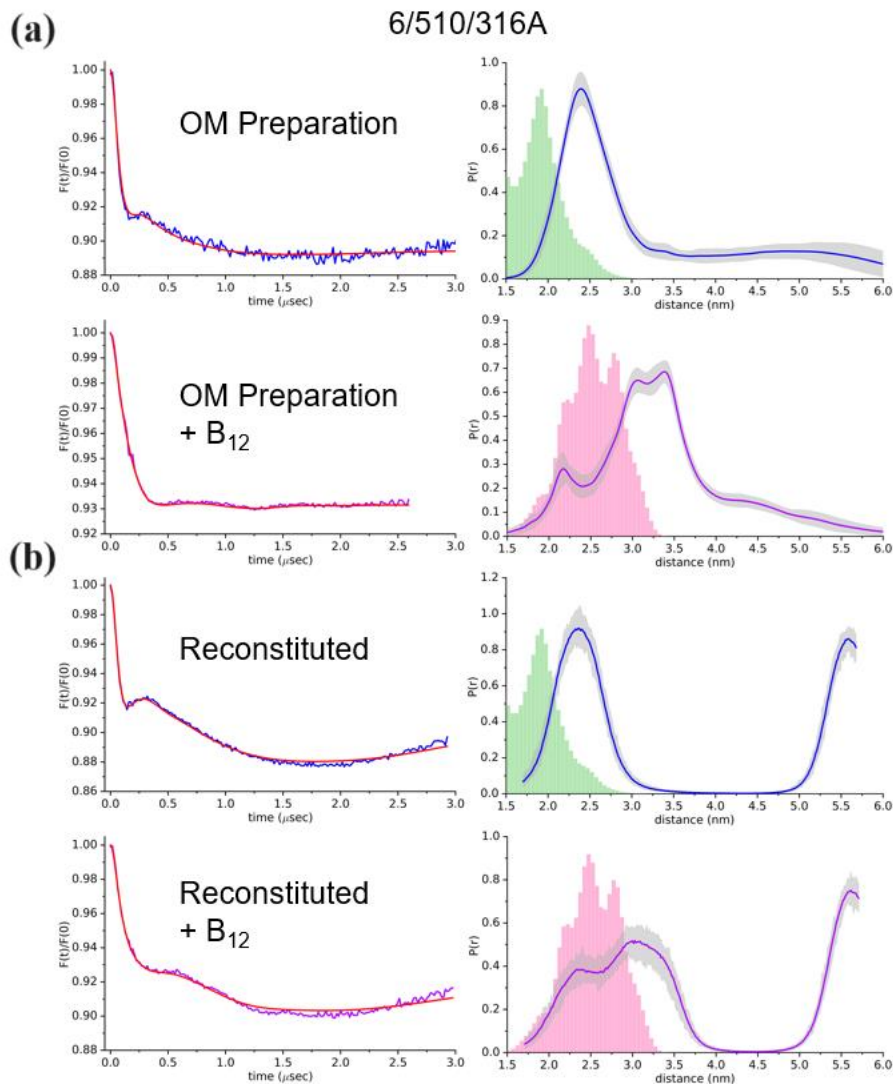
required to ensure that TonB interacts with the Ton box. Reconstitution in a lipid that creates a leaky bilayer such as DLPC, will help this interaction take place. Also, the conformational dynamics at site V10 of the Ton box should be studied with a periplasmic turn mutation that is far away from Ton box during its unfolded state to effectively examine the position and orientation of Ton box during unfolding. Finally, incorporation of molecular dynamics (MD) simulations with the restraints obtained through DEER can provide further insight into the extent of Ton box unfolding which seems to vary upon substrate binding, TonB binding, and with ionic lock disruption<sup>35</sup>.

## 5.7 Supplementary Information



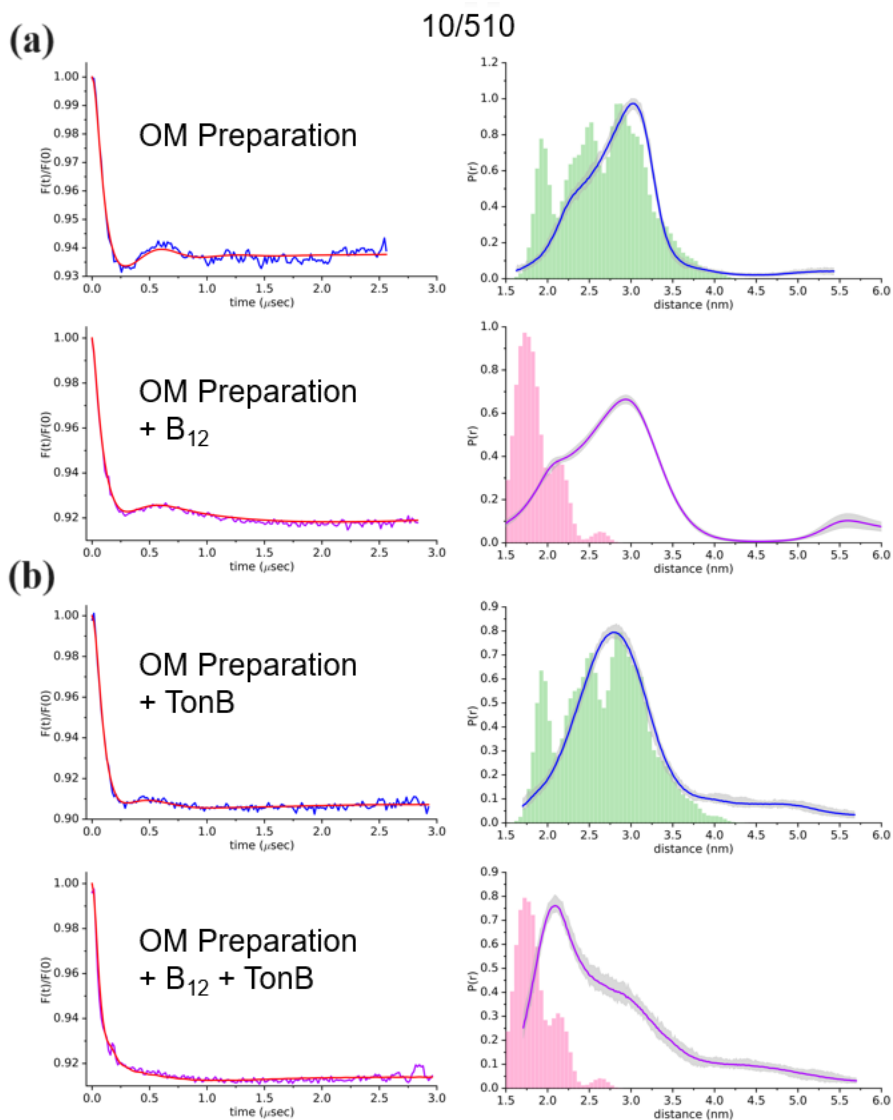
Supplementary Figure S5.1 DEER data for D6R1-Q510R1 obtained from an outer-membrane preparation. For all conditions, data are shown in the apo (blue trace) and B<sub>12</sub> bound (purple trace) states of BtuB. (a) DEER data obtained for BtuB labeled at sites D6 and Q510 obtained from an OM preparation. (b) DEER data obtained for BtuB D6R1-Q510R1 obtained from an OM preparation in the presence of C-terminal TonB fragment. All distance distributions were obtained

using DEERNet. The predictions from the apo and substrate bound crystal structures (PDB ID: 1NQG and 2GSK, respectively) are shown as green and pink histograms, respectively.



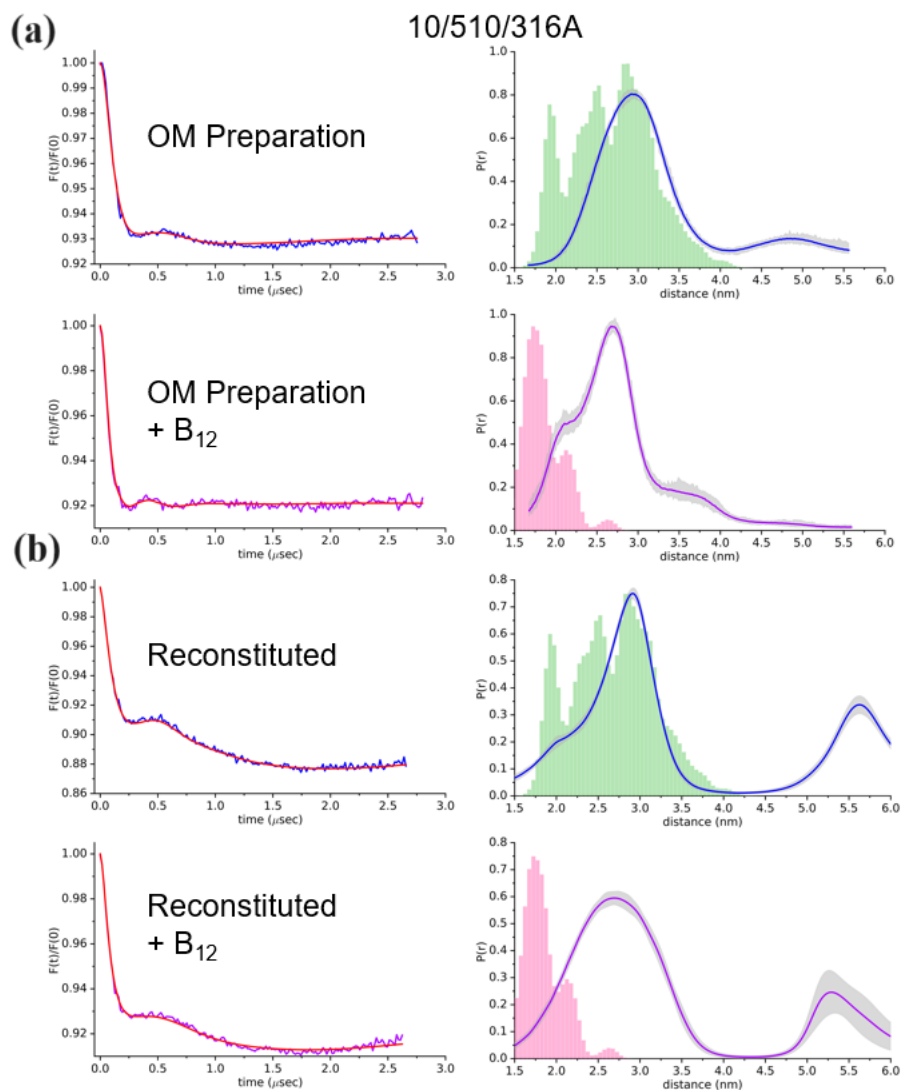
Supplementary Figure S5.2 DEER data for D6R1-Q510R1-D316A obtained from purified reconstituted protein or an outer-membrane preparation. For all conditions, data are shown in the apo (blue trace) and B<sub>12</sub> bound (purple trace) states of BtuB. (a) DEER data obtained for BtuB labeled at sites D6 and Q510 with the alanine mutation at D316 obtained from an OM preparation. (b) DEER data obtained for BtuB D6R1-Q510R1-D316A reconstituted into POPC bilayers. All

distance distributions were obtained using DEERNet. The predictions from the apo and substrate bound crystal structures (PDB ID: 1NQG and 2GSK, respectively) are shown as green and pink histograms, respectively.



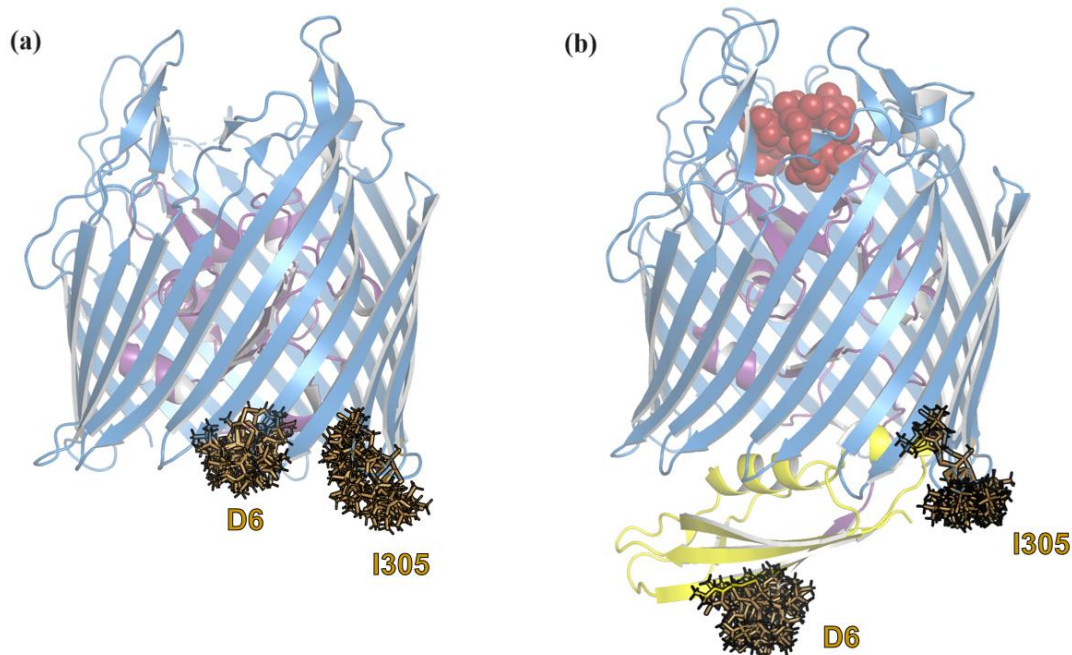
Supplementary Figure S5.3 DEER data for V10R1-Q510R1 obtained from an outer-membrane preparation. For all conditions, data are shown in the apo (blue trace) and B<sub>12</sub> bound (purple trace) states of BtuB. (a) DEER data obtained for BtuB labeled at sites V10 and Q510 obtained from an OM preparation. (b) DEER data obtained for BtuB V10R1-Q510R1 obtained from an OM

preparation in the presence of C-terminal TonB fragment. All distance distributions were obtained using DEERNet. The predictions from the apo and substrate bound crystal structures (PDB ID: 1NQG and 2GSK, respectively) are shown as green and pink histograms, respectively.

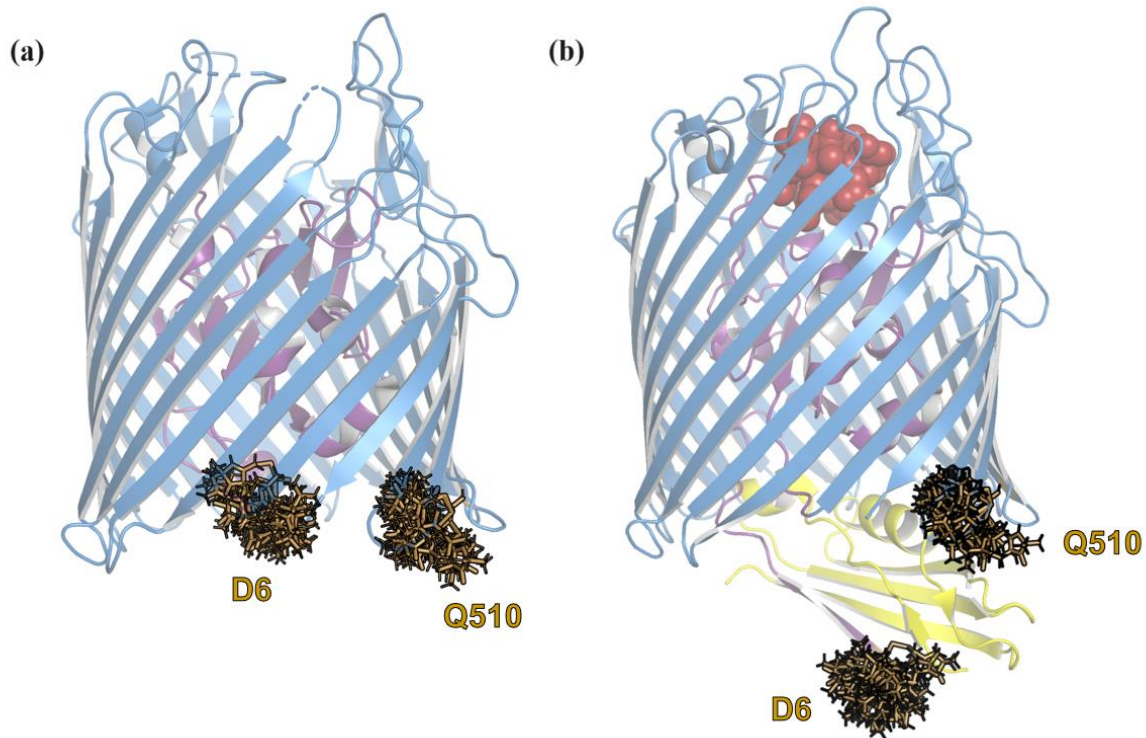


Supplementary Figure S5.4 DEER data for V10R1-Q510R1-D316A obtained from purified reconstituted protein or an outer-membrane preparation. For all conditions, data are shown in the apo (blue trace) and B<sub>12</sub> bound (purple trace) states of BtuB. (a) DEER data obtained for BtuB labeled at sites V10 and Q510 with the alanine mutation at D316 obtained from an OM preparation.

(b) DEER data obtained for BtuB V10R1-Q510R1-D316A reconstituted into POPC bilayers. All distance distributions were obtained using DEERNet. The predictions from the apo and substrate bound crystal structures (PDB ID: 1NQG and 2GSK, respectively) are shown as green and pink histograms, respectively.

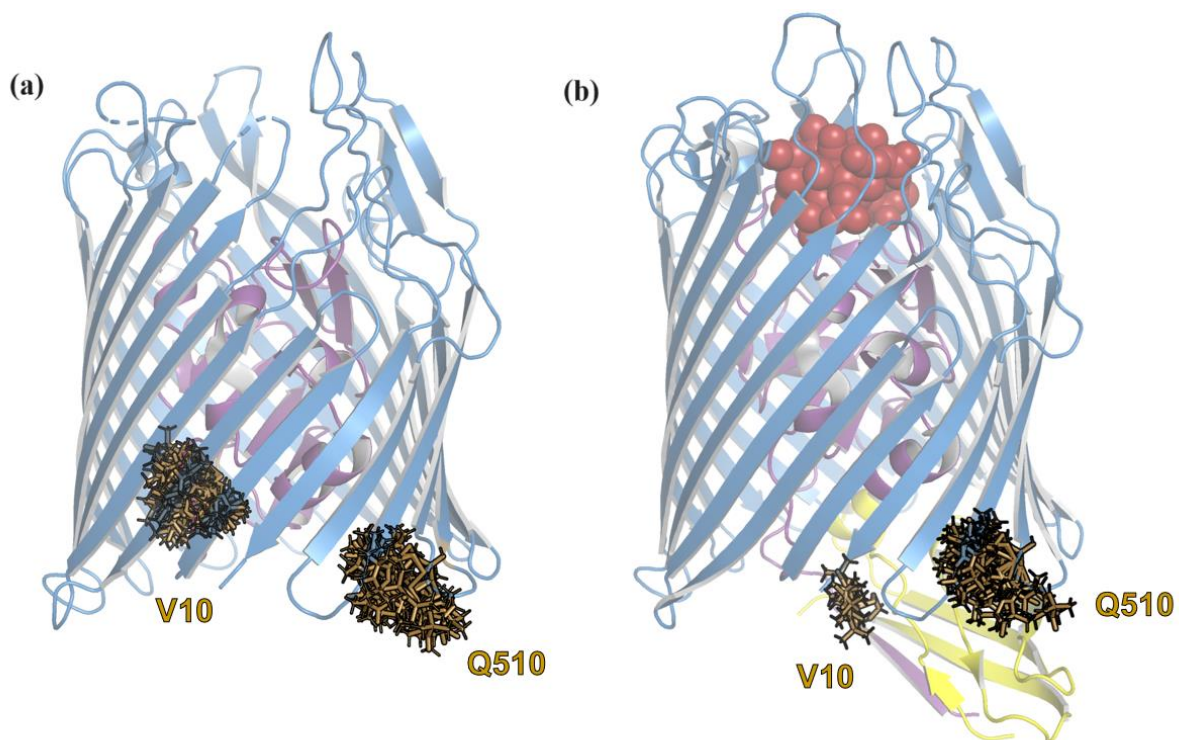


Supplementary Figure S5.5 Substrate induced conformational changes of plug domain (dark purple) of BtuB observed in crystal structures. (a) Apo state (PDB ID 1NQG) and (b) B<sub>12</sub> (brick red) and TonB C-terminal (yellow) bound (PDB ID 2GSK) of BtuB with possible rotamers available for R1 spin label (brown) at residues D6 and I305 in the plug domain and barrel domain (blue), respectively. Substrate docking induces an unfolding of Ton box towards the periplasmic surface.



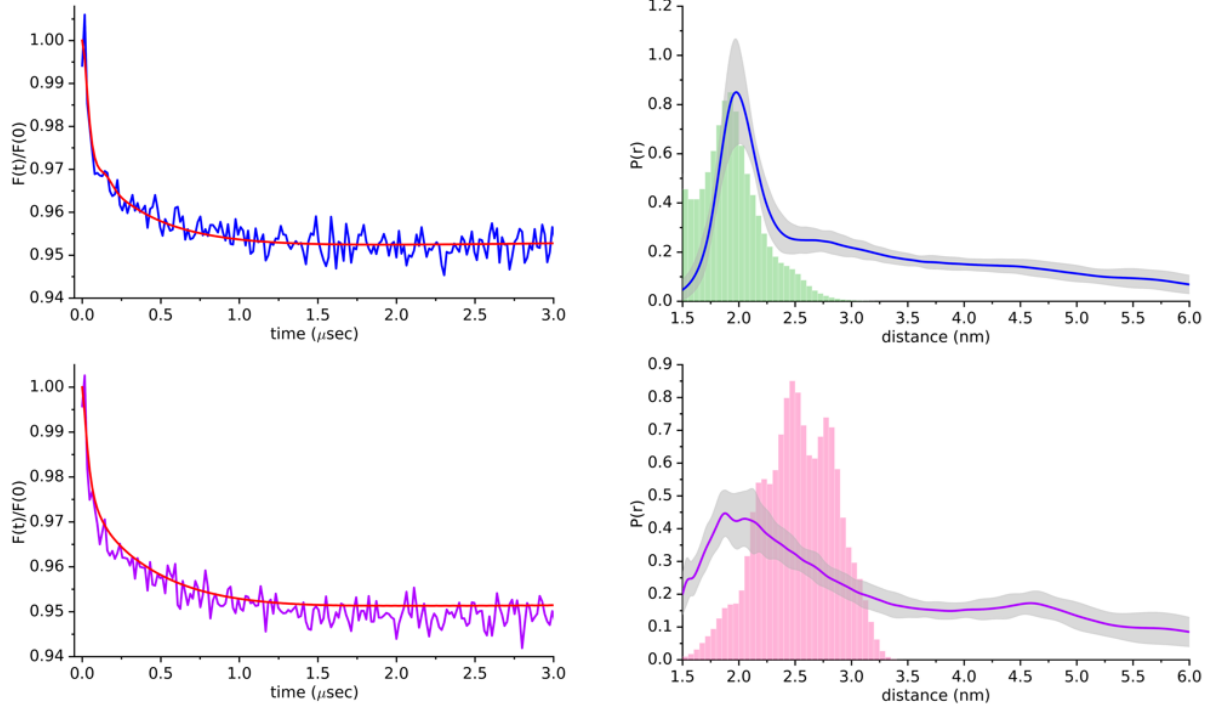
Supplementary Figure S5.6 Substrate induced conformational changes of plug domain (dark purple) of BtuB observed in crystal structures. (a) Apo state (PDB ID 1NQG) and (b) B<sub>12</sub> (brick red) and TonB C-terminal (yellow) bound (PDB ID 2GSK) of BtuB with possible rotamers available for R1 spin label (brown) at residues D6 and Q510 in the plug domain and barrel domain (blue), respectively. Substrate docking induces an unfolding of Ton box towards the periplasmic surface.





Supplementary Figure S5.7 Substrate induced conformational changes of plug domain (dark purple) of BtuB observed in crystal structures. (a) Apo state (PDB ID 1NQG) and (b) B<sub>12</sub> (brick red) and TonB C-terminal (yellow) bound (PDB ID 2GSK) of BtuB with possible rotamers available for R1 spin label (brown) at residues V10 and Q510 in the plug domain and barrel domain (blue), respectively. Substrate docking induces an unfolding of Ton box towards the periplasmic surface. Number of R1 rotamers at V10 is reduced due to C-term TonB interaction with Ton box.

6/510



Supplementary Figure S5.8 DEER data D6R1-Q510R1 obtained in the intact cell. Data are shown in the apo (blue trace) and B<sub>12</sub> bound (purple trace) states of BtuB. All distance distributions were obtained using DEERNet. The predictions from the apo and substrate bound crystal structures (PDB ID: 1NQG and 2GSK, respectively) are shown as green and pink histograms, respectively. BtuB seems to maintain a continuously unfolded Ton box under *in-vivo* conditions (Note: This is a repeated experiment of a study done previously<sup>19</sup>).

## 5.8 References

1. Nikaido H. (2003). Molecular basis of bacterial outer membrane permeability revisited. *Microbiology and molecular biology reviews : MMBR*, 67(4), 593–656.
2. Noinaj, N., Guillier, M., Barnard, T. J., & Buchanan, S. K. (2010). TonB-dependent transporters: regulation, structure, and function. *Annual review of microbiology*, 64, 43–60.
3. Chimento, D. P., Mohanty, A. K., Kadner, R. J., & Wiener, M. C. (2003). Substrate-induced transmembrane signaling in the cobalamin transporter BtuB. *Nature structural biology*, 10(5), 394–401.
4. Ferguson, A. D., Chakraborty, R., Smith, B. S., Esser, L., van der Helm, D., & Deisenhofer, J. (2002). Structural basis of gating by the outer membrane transporter FecA. *Science (New York, N.Y.)*, 295(5560), 1715–1719.
5. Locher, K. P., Rees, B., Koebnik, R., Mitschler, A., Moulinier, L., Rosenbusch, J. P., & Moras, D. (1998). Transmembrane signaling across the ligand-gated FhuA receptor: crystal structures of free and ferrichrome-bound states reveal allosteric changes. *Cell*, 95(6), 771–778.
6. Buchanan, S. K., Smith, B. S., Venkatramani, L., Xia, D., Esser, L., Palnitkar, M., Chakraborty, R., van der Helm, D., & Deisenhofer, J. (1999). Crystal structure of the outer membrane active transporter FepA from Escherichia coli. *Nature structural biology*, 6(1), 56–63.
7. Cadieux, N., Phan, P. G., Cafiso, D. S., & Kadner, R. J. (2003). Differential substrate-induced signaling through the TonB-dependent transporter BtuB. *Proceedings of the National Academy of Sciences of the United States of America*, 100(19), 10688–10693.

8. Cadieux, N., & Kadner, R. J. (1999). Site-directed disulfide bonding reveals an interaction site between energy-coupling protein TonB and BtuB, the outer membrane cobalamin transporter. *Proceedings of the National Academy of Sciences of the United States of America*, *96*(19), 10673–10678.
9. Fanucci, G. E., Coggs, K. A., Cadieux, N., Kim, M., Kadner, R. J., & Cafiso, D. S. (2003). Substrate-induced conformational changes of the periplasmic N-terminus of an outer-membrane transporter by site-directed spin labeling. *Biochemistry*, *42*(6), 1391–1400.
10. Xu, Q., Ellena, J. F., Kim, M., & Cafiso, D. S. (2006). Substrate-dependent unfolding of the energy coupling motif of a membrane transport protein determined by double electron-electron resonance. *Biochemistry*, *45*(36), 10847–10854.
11. Shultis, D. D., Purdy, M. D., Banchs, C. N., & Wiener, M. C. (2006). Outer membrane active transport: structure of the BtuB:TonB complex. *Science (New York, N.Y.)*, *312*(5778), 1396–1399.
12. Fanucci, G. E., Lee, J. Y., & Cafiso, D. S. (2003). Spectroscopic evidence that osmolytes used in crystallization buffers inhibit a conformation change in a membrane protein. *Biochemistry*, *42*(45), 13106–13112.
13. Gumbart, J., Wiener, M. C., & Tajkhorshid, E. (2007). Mechanics of force propagation in TonB-dependent outer membrane transport. *Biophysical journal*, *93*(2), 496–504.
14. Hickman, S. J., Cooper, R. E. M., Bellucci, L., Paci, E., & Brockwell, D. J. (2017). Gating of TonB-dependent transporters by substrate-specific forced remodelling. *Nature communications*, *8*, 14804.

15. Klebba P. E. (2016). ROSET Model of TonB Action in Gram-Negative Bacterial Iron Acquisition. *Journal of bacteriology*, *198*(7), 1013–1021.
16. Sarver, J. L., Zhang, M., Liu, L., Nyenhuis, D., & Cafiso, D. S. (2018). A Dynamic Protein-Protein Coupling between the TonB-Dependent Transporter FhuA and TonB. *Biochemistry*, *57*(6), 1045–1053.
17. Flores Jiménez, R. H., & Cafiso, D. S. (2012). The N-terminal domain of a TonB-dependent transporter undergoes a reversible stepwise denaturation. *Biochemistry*, *51*(17), 3642–3650.
18. Lukasik, S. M., Ho, K. W., & Cafiso, D. S. (2007). Molecular basis for substrate-dependent transmembrane signaling in an outer-membrane transporter. *Journal of molecular biology*, *370*(5), 807–811.
19. Nilaweera, T. D., Nyenhuis, D. A., Nakamoto, R. K., & Cafiso, D. S. (2019). Disulfide Chaperone Knockouts Enable In Vivo Double Spin Labeling of an Outer Membrane Transporter. *Biophysical journal*, *117*(8), 1476–1484.
20. Nilaweera, T. D., Nyenhuis, D. A., & Cafiso, D. S. (2021). Structural intermediates observed only in intact *Escherichia coli* indicate a mechanism for TonB-dependent transport. *eLife*, *10*, e68548.
21. Jeschke G. (2012). DEER distance measurements on proteins. *Annual review of physical chemistry*, *63*, 419–446.
22. Klock, H. E., & Lesley, S. A. (2009). The Polymerase Incomplete Primer Extension (PIPE) method applied to high-throughput cloning and site-directed mutagenesis. *Methods in molecular biology (Clifton, N.J.)*, *498*, 91–103.

23. Wimalasiri, V. W., Jurczak, K. A., Wieliniec, M. K., Nilaweera, T. D., Nakamoto, R. K., & Cafiso, D. S. (2023). A disulfide chaperone knockout facilitates spin labeling and pulse EPR spectroscopy of outer membrane transporters. *Protein science : a publication of the Protein Society*, 32(7), e4704.
24. Bradford M. M. (1976). A rapid and sensitive method for the quantitation of microgram quantities of protein utilizing the principle of protein-dye binding. *Analytical biochemistry*, 72, 248–254.
25. Sedmak, J. J., & Grossberg, S. E. (1977). A rapid, sensitive, and versatile assay for protein using Coomassie brilliant blue G250. *Analytical biochemistry*, 79(1-2), 544–552.
26. Rassam, P., Copeland, N. A., Birkholz, O., Tóth, C., Chavent, M., Duncan, A. L., Cross, S. J., Housden, N. G., Kaminska, R., Seger, U., Quinn, D. M., Garrod, T. J., Sansom, M. S., Piehler, J., Baumann, C. G., & Kleanthous, C. (2015). Supramolecular assemblies underpin turnover of outer membrane proteins in bacteria. *Nature*, 523(7560), 333–336.
27. Nyenhuis, D. A., Nilaweera, T. D., Niblo, J. K., Nguyen, N. Q., DuBay, K. H., & Cafiso, D. S. (2020). Evidence for the Supramolecular Organization of a Bacterial Outer-Membrane Protein from In Vivo Pulse Electron Paramagnetic Resonance Spectroscopy. *Journal of the American Chemical Society*, 142(24), 10715–10722.
28. Jeschke, G., Chechik, V., Ionita, P., Godt, A., Zimmermann, H., Banham, J., ... & Jung, H. (2006). DeerAnalysis2006—a comprehensive software package for analyzing pulsed ELDOR data. *Applied magnetic resonance*, 30, 473-498.
29. Worswick, S. G., Spencer, J. A., Jeschke, G., & Kuprov, I. (2018). Deep neural network processing of DEER data. *Science advances*, 4(8), eaat5218.

30. Jeschke, G. (2018). MMM: A toolbox for integrative structure modeling. *Protein Science*, 27(1), 76-85.
31. Polyhach, Y., Bordignon, E., & Jeschke, G. (2011). Rotamer libraries of spin labelled cysteines for protein studies. *Physical chemistry chemical physics : PCCP*, 13(6), 2356–2366.
32. DeLano, W. L. (2002). Pymol: An open-source molecular graphics tool. *CCP4 Newsl. Protein Crystallogr*, 40(1), 82-92.
33. Freed, D. M., Lukasik, S. M., Sikora, A., Mokdad, A., & Cafiso, D. S. (2013). Monomeric TonB and the Ton box are required for the formation of a high-affinity transporter-TonB complex. *Biochemistry*, 52(15), 2638–2648.
34. Balusek, C., & Gumbart, J. C. (2016). Role of the Native Outer-Membrane Environment on the Transporter BtuB. *Biophysical journal*, 111(7), 1409–1417.
35. Hays, J. M., Cafiso, D. S., & Kasson, P. M. (2019). Hybrid Refinement of Heterogeneous Conformational Ensembles Using Spectroscopic Data. *The journal of physical chemistry letters*, 10(12), 3410–3414.

## **Chapter 6: Structural intermediates observed for TonB dependent Cobalamin**

### **Transporter BtuB indicating a possible transport mechanism**

#### 6.1 Abstract

The outer membrane (OM) of Gram-negative bacteria such as *Escherichia coli* (*E. coli*) contain a fascinating class of active transport proteins that are TonB-dependent. These TonB dependent transporters (TBDTs) function in the uptake of trace nutrients such as iron, vitamin B<sub>12</sub> as well as carbohydrates. TBDTs are essential for the success of many pathogens and for the proper functioning of the human microbiome. TBDTs obtain the energy for active transport from the inner membrane (IM) proton motive force (PMF) by coupling with the IM protein complex TonB/ExbB/ExbD. Although many high-resolution structures for TBDTs are known, the molecular mechanism by which TBDTs function has not been elucidated.

We have examined the structure and substrate-induced conformation transitions for the *E. coli* Cobalamin (vitamin B<sub>12</sub>) transporter BtuB using Electron Paramagnetic Resonance (EPR) spectroscopy both *in-vivo* and *in-vitro*. One dramatic structural change previously observed from *in-vivo* work involves a 2 nm shift of an extracellular substrate binding loop towards the periplasm, which is only seen when the R14-D316 ionic lock is disrupted<sup>1</sup>. Although this transition has been examined in intact cells and in reconstituted proteoliposomes, it has not been characterized in an OM preparation or from the periplasmic surface of BtuB in a purified reconstituted membrane. The transition has not been observed in reconstituted systems; however, measurements in reconstituted membranes were performed in the absence of TonB, a crucial cofactor for TonB-dependent transport. Here we provide evidence for this structural change in several different types of preparations of BtuB. Surprisingly, although this structural transition is not observed in reconstituted preparations, it is clearly present in OM isolations with the disruption of R14-D316



ionic lock or with the addition of TonB. This work illustrates the importance of the native membrane environment for the function of these outer membrane proteins (OMPs), and also demonstrates that these structural transitions can be observed *in-vitro* provided that IM constituents crucial for TBDTs function are present.

## 6.2 Introduction

*E. coli* and other Gram-negative bacteria consist of an extra outer membrane (OM) apart from the plasma membrane which separates cell from its surrounding environment. This OM is asymmetric where the inner leaflet is primarily composed of phospholipids and the outer leaflet primarily composed of lipopolysaccharides (LPS). The OM creates a barrier that helps with bacterial survival under harsh environmental conditions, and the OM enables bacterial virulence<sup>2</sup>. As a result, the uptake of many nutrients and crucial cofactors require membrane proteins imbedded in the OM. The OM consists of porins which can uptake compounds with size less than 600 Da whereas high affinity active transporters are responsible for efficient acquisition of nutrients greater than 600 Da. There are no energy driven processes such as ATP hydrolysis or the presence of a proton motive force (PMF) in the OM. To drive active transport these transport proteins interact with the IM protein TonB, which is coupled to the ExbB/ExbD complex and the PMF for energy transfer during active transport. Thus, these active transporters in the OM are designated as TonB-dependent transporters<sup>3</sup>.

TBDTs have a conserved architecture where the C-terminus forms barrel domain with 22 antiparallel  $\beta$ -strands and the N-terminus resides within the barrel for form a core domain (plug domain) and occludes the barrel. The  $\beta$ -strands are linked by short turns on the periplasmic surface (periplasmic turns) whereas they are linked by long and variable loops on the extracellular surface (extracellular loops). A highly conserved segment near the N-terminus termed the Ton box interacts

with the C-terminal domain of TonB during transport<sup>4,5</sup>. The substrates that are transported through the TBDTs are large and there is no obvious permeation pathway<sup>6</sup> through the barrel domain; as a result, it is believed that a significant conformational rearrangement, such as partial or full removal of the plug domain, is required for substrate transport<sup>7</sup>. However, numerous high-resolution crystal structures obtained for multiple TBDTs such as FecA<sup>8</sup>, FhuA<sup>9</sup>, FepA<sup>10</sup> and BtuB<sup>11</sup> do not provide evidence for such structural transitions of the core domain. Thus, the actual mechanism of TBDTs is yet to be elucidated.

Early applications of site-directed spin labeling (SDSL) and electron paramagnetic resonance (EPR) spectroscopy to BtuB indicate that there is a transmembrane allosteric event, where the binding of substrate unfolds the Ton box and extends it into the periplasmic space. This structural change may function to promote a coupling between BtuB and TonB<sup>12, 13</sup>. High resolution structures obtained for the C-terminal domain of TonB in complex with BtuB<sup>5</sup> and FhuA<sup>4</sup> show the Ton box extending from the core domain to make an edge-to-edge  $\beta$ -sheet interaction with the C-terminal domain; however, in these structures, the remainder of the core domain is unchanged following the binding of the TonB fragment. As a result of these structures, it has been proposed that TonB, which is coupled to the energized IM through ExbB/ExbD, exerts a mechanical force on the TBDTs to induce unfolding of the transporter core domain. There are two models for this mechanical force that were initially proposed. In one, TonB rotates while interacting with the Ton box thereby promoting an unfolding of the core<sup>14</sup>; justification for this model comes in part from homology between the ExbB/ExbD complex with the flagellar motor MotAB in the IM<sup>15</sup>. However, EPR studies on the ferrichrome transporter FhuA in complex with TonB indicate the presence of multiple residues in the Ton box that are unstructured, thus a transfer of torque to the core domain seems unlikely<sup>16</sup>. The other model involves a pulling motion, and

TonB when coupled to the Ton box is proposed to directly pull on the N-terminus of the transporter and unfold a portion of the core domain. This model seems to have more support and it has been tested through steered molecular dynamics simulations (SMD)<sup>17</sup> and atomic force microscopy (AFM)<sup>18</sup>. These studies indicate that pulling the N-terminus of BtuB unfolds the first 73 residues on the N-terminal side of the core, forming a channel and allowing substrate to pass through the barrel. The C-terminal side of the BtuB core domain is conserved and is not believed to unfold. Denaturation experiments coupled with EPR spectroscopy for the BtuB N-terminus, also provides some support for this proposal<sup>19</sup>.

Most of the structural work for BtuB has been performed under partially or fully purified membrane systems where the native conditions of the cell are absent. Since TonB-dependent transport has never been reconstituted, it has not been possible to confirm that TBDTs are active in these *in-vitro* conditions. Recent work using SDSL-EPR has permitted the study of BtuB in the intact cell where over-expressed BtuB is known to be active<sup>20, 21</sup>. This was done with the assistance of a knockout strain of the periplasmic bacterial disulfide bond formation (Dsb) system, responsible for crosslinking pairs of cysteines in OMPs<sup>20</sup>. The knockout of either the periplasmic disulfide oxidase *dsbA* or *dsbB*<sup>22</sup>, the IM protein responsible for re-energizing *dsbA*, allows pairs of cysteines incorporated through mutagenesis to remain in a reduced state for spin labeling. Double electron-electron resonance (DEER) studies carried out on the extracellular surface of BtuB using an *E. coli* strain deficient in *dsbA* demonstrates that there are substrate dependent changes of substrate binding loop 3 (SB3) observed *in-situ*, that cannot be observed in isolated preparations<sup>21</sup>. Additional measurements made when the R14-D316 ionic lock is disrupted, provide evidence for a larger conformational change in SB3 *in-situ* that is not observed in

reconstituted preparations<sup>1</sup>. This involves an approximately 2 nm movement of SB3 towards the periplasmic surface when substrate is added.

In the present work, we investigate the movement of SB3 with respect to the periplasmic turns in both apo and substrate bound states, with the disruption of R14-D316 ionic lock, and in the presence of a purified TonB C-terminal fragment. We make use of the dead-time free four pulse DEER measurement. The DEER measurement generates a dipolar echo that is modulated at the frequency of the dipolar interaction between spin pairs. DEER can be used to measure distances and distance distributions between spin pairs up to 8 nm while distances up to 10 nm are achievable in deuterated soluble proteins<sup>23</sup>. In this work, spin pairs were introduced into BtuB between SB3 (position 90)(see Figure 6.1) and the periplasmic turns (positions 305 and 510)(see Figure 6.1). The R14-D316 ionic interaction was disrupted in both these spin pairs by creating a mutant where the aspartic acid residue at position 316 in the barrel was substituted with alanine (mutant D316A). CW EPR data from BtuB in reconstituted in liposomes does not reveal any substrate dependent conformational shifts, and slight changes in the spectra are observed upon mutating the R14-D316 ionic lock. However, DEER measurements performed on OM preparations indicate large conformational changes for SB3 when the ionic lock is disrupted or when the C-terminal TonB fragment is added. A small component at a short distance appears that is consistent with SB3 shifting closer towards the periplasmic surface of BtuB. Previous studies on isolated preparations did not indicate such distance populations with substrate addition while *in-vivo* studies of BtuB with ionic lock disruption did not exhibit SB3 shift towards the periplasmic surface in the absence of substrate<sup>1</sup>. However, this study indicates that the shift of SB3 towards the periplasmic surface in OM preparations takes place along with a significant Ton box extension when the ionic lock is disrupted, and it can be substrate independent. As shown earlier (see Chapter 5), a significant

extension of the Ton box occurs when the R14-D316 ionic lock is disrupted in the presence of substrate. Furthermore, a similar movement of SB3 is observed upon the binding of TonB to BtuB, which is likely to mimic the disruption of the R14-D316 ionic lock between the core and barrel domains (see Chapter 5). It is important to note that these structural transitions in SB3 are not observed when BtuB is reconstituted into liposomes, suggesting that the OM environment and its constituents are important for facilitating these structural transitions.

## 6.3 Materials and Methods

### 6.3.1 Cell lines and plasmids

For the vitamin B<sub>12</sub> transporter, BtuB, the pAG1 plasmid with WT *btuB* gene and the *E. coli* strain RK5016 (*-argH*, *-btuB*, *-metE*) was obtained from late Professor Robert Kadner, University of Virginia. The TonB fragment with a 6X His tag lacking the N-terminal domain and a portion of the periplasmic domain (residues 103-239)(TonB C-term) was generously provided by Prof. Robert K. Nakamoto, University of Virginia. Mutant *dsb E. coli* strain were obtained from the Coli Genetic Stock Center (Yale University, New Haven, CT). Strain RI90 carries the *dsbA* null mutation system (*araD139 Δ(araABC-leu) 7679 galU galK Δ(lac)X74 rpsL thi phoR Δara714 leu +dsbA:: Kanr*). *E. coli* strain T7 express *LysY/I<sup>q</sup>* competent cells were obtained from New England Biolabs (Ipswich, MA).

### 6.3.2 PCR mutagenesis and OMP expression

BtuB double cysteine mutations (V90C-I305C, V90C-Q510C) and ionic lock disruption mutations (V90C-I305C-D316A, V90C-Q510C-D316A) were generated using site-directed mutagenesis and polymerase incomplete primer extension<sup>24</sup> followed by DNA sequencing verification (Genewiz, South Plainfield, NJ and Plasmidsaurus, Eugene, OR). The *btuB* containing plasmids were transformed into *dsbA*<sup>-</sup> strains.

A single colony was used to inoculate Luria-Bertani (LB) media and prepare a glycerol stock which was stored at -80 °C. For BtuB, precultures of Minimal Media (100 mM phosphate buffer, 8 mM (NH<sub>4</sub>)<sub>2</sub>SO<sub>4</sub>, 2 mM sodium citrate, 100 mg/mL ampicillin, 0.2% w/v glucose, 150 mM thiamine, 3 mM MgSO<sub>4</sub>, 300 mM CaCl<sub>2</sub>, 0.01% w/v methionine, 0.01% w/v arginine) were inoculated using the glycerol stock and later used to inoculate the main culture. An initial overnight preculture growth was followed by an 8 hr main culture growth<sup>25</sup>.

### 6.3.3 OM and reconstituted BtuB sample preparation

An intact OM preparation is obtained from the total cell membrane fraction using a standard procedure<sup>12, 26</sup>. This involves treating the cell membrane fraction with 1% sarkosyl to remove the inner membrane, and then centrifugation to collect the OM and remove of the sarkosyl. For measurements made in the OM preparation, the preparation was spin labeled at this stage<sup>21</sup>. For protein that was to be purified, the OM preparation was solubilized with OG as described previously, and 5 mL of the solubilized OM sample then was treated with 100 µL of 22 mM MTSL [(1-oxyl-2,2,5,5-tetramethylpyrroline-3-methyl) methanethiosulfonate] followed by incubation for 2 - 3 hr at room temperature (RT)<sup>25</sup>. Spin labeled BtuB was purified using ion-exchange chromatography as described previously<sup>26</sup>. The yield of purified BtuB was quantitated using the Bradford Assay<sup>27, 28</sup>.

The purified and spin-labeled BtuB samples were reconstituted into 1-palmitoyl-2-oleoyl-sn-glycero-3-phosphocholine (POPC) or 1,2-dilauroyl-sn-glycero-3-phosphocholine (DLPC) vesicles by the addition of OG/POPC and OG/DLPC (10:1) mixed micelles to the purified BtuB samples at a protein: lipid ration of 1:25. The samples were then dialyzed against six 4 L dialysis buffer changes (10 mM HEPES, 128 mM NaCl, and 1 mM EDTA at pH 6.5) at 10–12 hr intervals<sup>12, 29, 30</sup>.

#### 6.3.4 C-terminal TonB fragment (103-239) expression and purification

TonB was expressed and purified as described previously<sup>16</sup>. A plasmid containing the 6X His tagged TonB C-term was transformed into *LysY/T<sup>q</sup>* cells and was grown in 2XYT media at 37 °C. Cells were induced with 0.5 mM IPTG at OD<sub>600</sub> of 0.7 – 0.8 and were grown for additional 6 hr at 20 °C and then collected by centrifugation.

TonB purification was performed on ice to avoid proteolysis. The cell pellet was resuspended in resuspension buffer<sup>16</sup> with protease inhibitors aprotinin, leupeptin and AEBSF and DTT. The cells were disrupted using French Press followed by centrifugation to obtain the supernatant. The supernatant was then loaded to a nickel column containing equilibration buffer<sup>16</sup> and was washed with 3 column volumes of equilibration buffer. The column was then treated with 5mL of a 100 mM imidazole buffer<sup>16</sup> to remove non-specific proteins and bound protein (TonB) was eluted with 25 mL elution buffer<sup>16</sup>. Fractions containing TonB were identified using protein gel electrophoresis and the pure fractions were pooled. A 3 kDa molecular weight cut off (MWCO) was used to concentrate the pooled fractions to obtain a 1.5 mL solution of TonB with a concentration of approximately 350 μM. Quantification TonB was performed using the Bradford Assay in a manner similar to that used for BtuB.

#### 6.3.5 EPR Measurements

For CW-EPR measurements, 5 μL sample with 1 μL dialysis buffer was loaded into 0.84 x 0.6 mm<sup>2</sup> quartz capillaries and used as apo sample whereas 5 μL sample with 1 μL of 1 mM Vitamin B<sub>12</sub> was used as the substrate bound sample. EPR spectra were recorded at room temperature at X-band using a Bruker EMX spectrometer (Billerica, MA) with an ER 4123D dielectric resonator using a sweep width of 100 gauss (G), a modulation amplitude of 1 G, and 2 mW incident microwave power. Data were collected as additive averages of 10 scans and were

normalized by their second integral. For DEER, a 16  $\mu\text{L}$  sample with 4  $\mu\text{L}$  of concentrated d-glycerol was loaded into 1.1 x 1.6  $\text{mm}^2$  quartz capillaries (VitroCom, Mountain Lakes, NJ). 2  $\mu\text{L}$  of 1 mM Vitamin B<sub>12</sub> and 4  $\mu\text{L}$  of purified TonB ( $\sim 350 \mu\text{M}$ ) was added for samples with substrate and with TonB, respectively. All samples underwent 6 - 7 freeze thaw cycles to ensure substrate and TonB access to all BtuB in the sample. All DEER experiments were performed on a Bruker E580 spectrometer operating at Q-band (Bruker BioSpin, Billerica, MA) with the following hardware: Bruker EN5107D2 dielectric resonator or Bridge12 B12TQLP Q-Band loop-gap resonator, Bruker SpinJet-AWG, and a Bruker 10 W solid state amplifier. Experiments were run at 50 K using the standard dead-time free 4-pulse DEER experiment, with a 14 or 16 ns  $\pi/2$  pulse and 28 or 32 ns  $\pi$  pulses, respectively. All pulses were rectangular. The separation between observe and pump frequencies was 75 MHz. Acquisition times for most samples typically ranged from 12 to 20 hr.

### 6.3.6 Data processing

All DEER data were processed with DeerAnalysis<sup>31</sup> using the DEERNet routine<sup>32</sup>. Simulated distance distributions were generated using the software package Multiscale Modeling of Macromolecules (MMM) and the default rotamer library<sup>33,34</sup>. Protein structure images were generated using Pymol<sup>35</sup>.

## 6.4 Results

### 6.4.1 Disruption of the R14-D316 ionic lock produces minimal changes in the EPR spectra of SB3 in isolated reconstituted systems

Figure 6.1 represents a combination of CW-EPR spectra obtained from reconstituted BtuB preparations of spin labeled cysteine pairs introduced across BtuB. Site V90 residing on the substrate binding loop 3 (SB3) from the BtuB extracellular side was coupled with sites I305 and



Q510 from the periplasmic turns to construct V90R1-I305R1 and V90R1-Q510R1 spin pairs (see Figure 6.1b,c top row). Reconstitution was performed for both spin pairs in an identical manner. BtuB was purified and spin labelled using an *E. coli dsbA*<sup>-</sup> growth making the introduced cysteines available for reaction with the MTSL reagent during labeling. The difference in signal intensity observed for some spin pairs in Figure 6.1c might be due to unavoidable variability during sample preparation for CW-EPR.

Previous CW-EPR spectra of V90 present in the apex of BtuB SB3 from the extracellular surface of the core domain are identical between apo and substrate (Vitamin B<sub>12</sub>) bound states either *in-vivo*<sup>1</sup> or *in-vitro* in a reconstituted preparation (see Chapter 3, Figure 3.2). Furthermore, the environment around sites I305 and Q510 in the periplasmic turns is not expected to change upon substrate addition. As a result, significant changes in the CW-EPR signals are not expected under the different experimental conditions used during this work. As observed, both apo and substrate bound states of both spin pairs show broadened spectra where the label dynamics are hindered due to the native fold of BtuB core domain. The introduction of substrate (Vitamin B<sub>12</sub>) results in the loss of spin label rotamers for site 90 according to the crystal structures (see Supplementary Figure S6.3 and S6.4), but no significant change in spin label dynamics is observed experimentally. Also, the EPR spectra exhibit two modes of motion due to the two spin labels attached to BtuB. Through qualitative comparison of the EPR spectra of each individual spin label in BtuB through previous studies<sup>1, 12</sup>, we can assume that the EPR spectra obtained is a collective contribution of both attached spin labels.

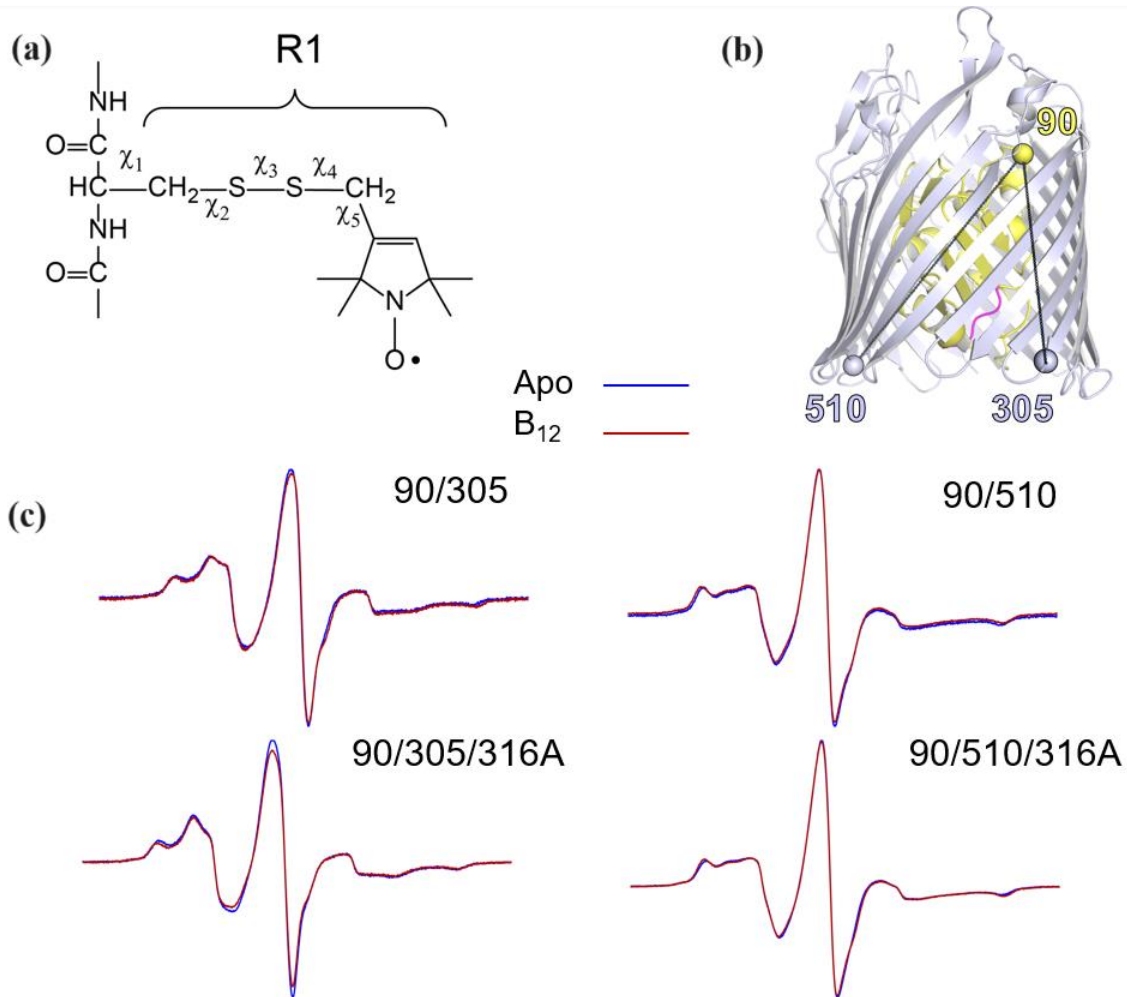


Figure 6.1 The cleavage of R14-D316 ionic lock exhibit minute structural changes of BtuB in a phospholipid reconstituted preparation. (a) For EPR measurements, free cysteines are labeled using a conventional MTSL spin label to generate the side chain R1<sup>25</sup>. In (b) crystal structure of BtuB (PDB ID: 1NQG) with sites labeled on the extracellular (yellow) and periplasmic surfaces (blue-white) of BtuB shown as spheres. The periplasmic energy coupling Ton box is shown in magenta. In (c) are shown the CW-EPR spectra obtained from V90R1-I305R1 and V90R1-Q510R1 (top row) and V90R1-I305R1-D316A and V90R1-Q510R1-D316A (bottom row) where BtuB is overexpressed in a *dsbA*<sup>-</sup> strain.

Previously, it was observed that an irreversible extension of the Ton box can be induced by disengaging an ionic lock between R14 in the core domain and D316 in the barrel domain<sup>36</sup>. Conversion of D316 to A316 (D316A) permanently disrupts this ionic lock allowing a population of the Ton box to shift into the periplasmic space. Presumably, the Ton box extension will create a cavity that may allow SB3 to shift towards the periplasmic space. This may be facilitated by the lower side chain density in this region of the protein interior<sup>l</sup>. However, phospholipid reconstitutions done for both spin pairs with the additional D316A mutation (V90R1-I305R1-D316A and V90R1-Q510R1-D316A) did not indicate changes in EPR spectra apart from a subtle change in line-shape for V90R1-I305R1 with the disruption of ionic lock (see Figure 6.1c bottom row) in the lower field. Due to the fact that site 90 in SB3 remains in tertiary contact during these experimental conditions, and the fact that the change in SB3 occurs for only a small fraction of the total spins, the change may be difficult to detect by CW-EPR spectrum.

6.4.2 Pulse EPR signals observed for OM preparations indicate novel conformations for SB3 not observed in reconstituted preparations when the R14-D316 ionic lock is disrupted or when TonB is bound

In addition to CW-EPR spectra, pulse EPR measurements were made on the V90R1-I305R1 and V90R1-I305R1-D316A spin pairs in OM and reconstituted preparations. As observed in Figure 6.2a, DEER signals obtained for the OM preparation of V90R1-I305R1 yield a distance distribution agreeing very well with the predicted distance distributions obtained using MMM for the spin pair in crystal structures. The addition of substrate did not indicate a significant shift of SB3 from its primary distance distribution around 4.5 nm, but a slight increase in spin population was observed around 5.5 – 6.0 nm matching the predicted distance distributions. Surprisingly, the addition of TonB C-terminal fragment to OM preparation resulted in the occurrence of a short

distance signal around 2 nm with respect to the periplasmic turns of BtuB for a limited spin population (around 9% of the overall signal) as seen in Figure 6.2b. This may be direct evidence for the shift of SB3 towards periplasmic surface of BtuB, which was previously observed *in-vivo*.<sup>1</sup> A similar distance distribution is seen when the C-terminal domain of TonB is bound and the ionic lock is disrupted (D316A), see Figure 6.3a, indicating that the TonB-dependent Ton box unfolding in a non-energized isolated system is equivalent to breaking the ionic lock, and that the movement of SB3 towards periplasmic surface may open a pathway for substrate permeation.

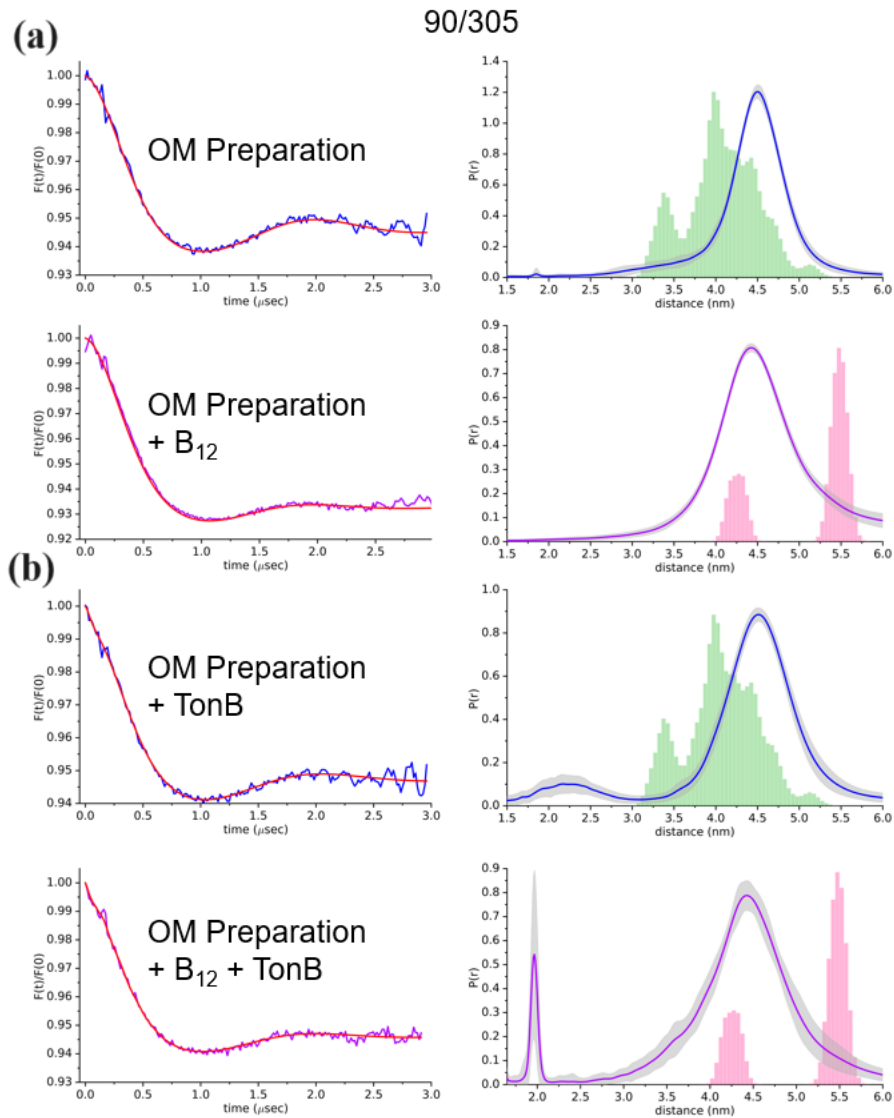


Figure 6.2 DEER data for V90R1-I305R1 obtained from an outer-membrane preparation. For all conditions, data are shown in the apo (blue trace) and B<sub>12</sub> bound (purple trace) states of BtuB. (a) DEER data obtained for BtuB labeled at sites V90 and I305 obtained from an OM preparation. (b) DEER data obtained for BtuB V90R1-I305R1 obtained from an OM preparation in the presence of C-terminal TonB fragment. All distance distributions were obtained using DEERNet. The predictions from the apo and substrate bound crystal structures (PDB ID: 1NQG and 2GSK, respectively) are shown as green and pink histograms, respectively.

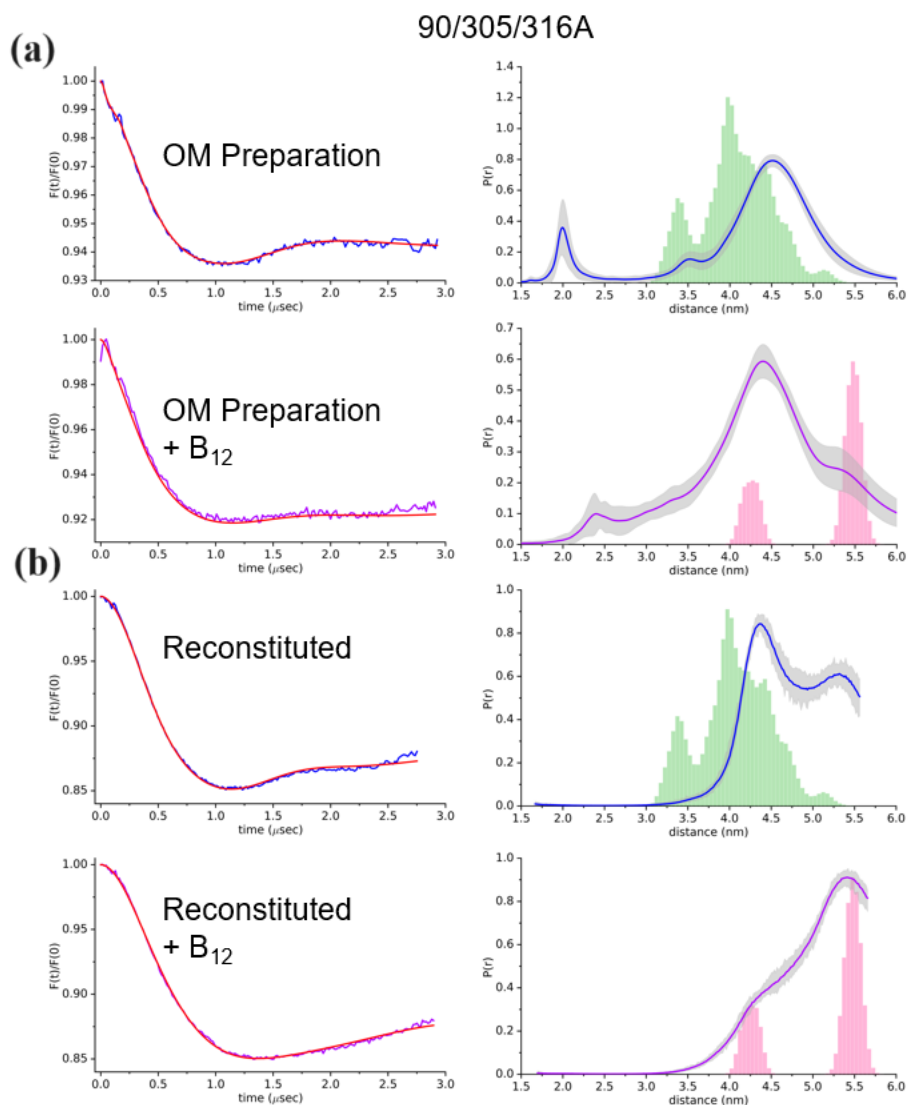


Figure 6.3 DEER data for V90R1-I305R1-D316A obtained from purified reconstituted protein or an outer-membrane preparation. For all conditions, data are shown in the apo (blue trace) and B<sub>12</sub> bound (purple trace) states of BtuB. (a) DEER data obtained for BtuB labeled at sites V90 and I305 with the alanine mutation at D316 obtained from an OM preparation. (b) DEER data obtained for BtuB V90R1-I305R1-D316A reconstituted into POPC bilayers. All distance distributions were obtained using DEERNet. The predictions from the apo and substrate bound crystal structures (PDB ID: 1NQG and 2GSK, respectively) are shown as green and pink histograms, respectively.

When BtuB is purified and reconstituted into liposomes, the transitions seen in the OM preparation are not observed. The distance distributions obtained for V90R1-I305R1-D316A in the reconstituted system (see Figure 6.3b) show distributions matching the predicted distributions determined from the allowed label rotamers (see Supplementary Figure S6.3) using MMM, and no evidence is seen for a shift of SB3 towards the periplasm as observed for OM preparations. However, a unique interconversion between two rotamer states is observed in the reconstituted system at distances around 4.5 nm and 5.5 nm with substrate addition (see Figure 6.3b and Figure 6.3a). A similar behavior is also observed for the reconstituted system with TonB addition (see Figure 6.4b). Interestingly, distance distributions obtained for BtuB reconstituted in DLPC vesicles demonstrated a singular component around 4.5 nm which remained unaffected by substrate addition (see Figure 6.5).

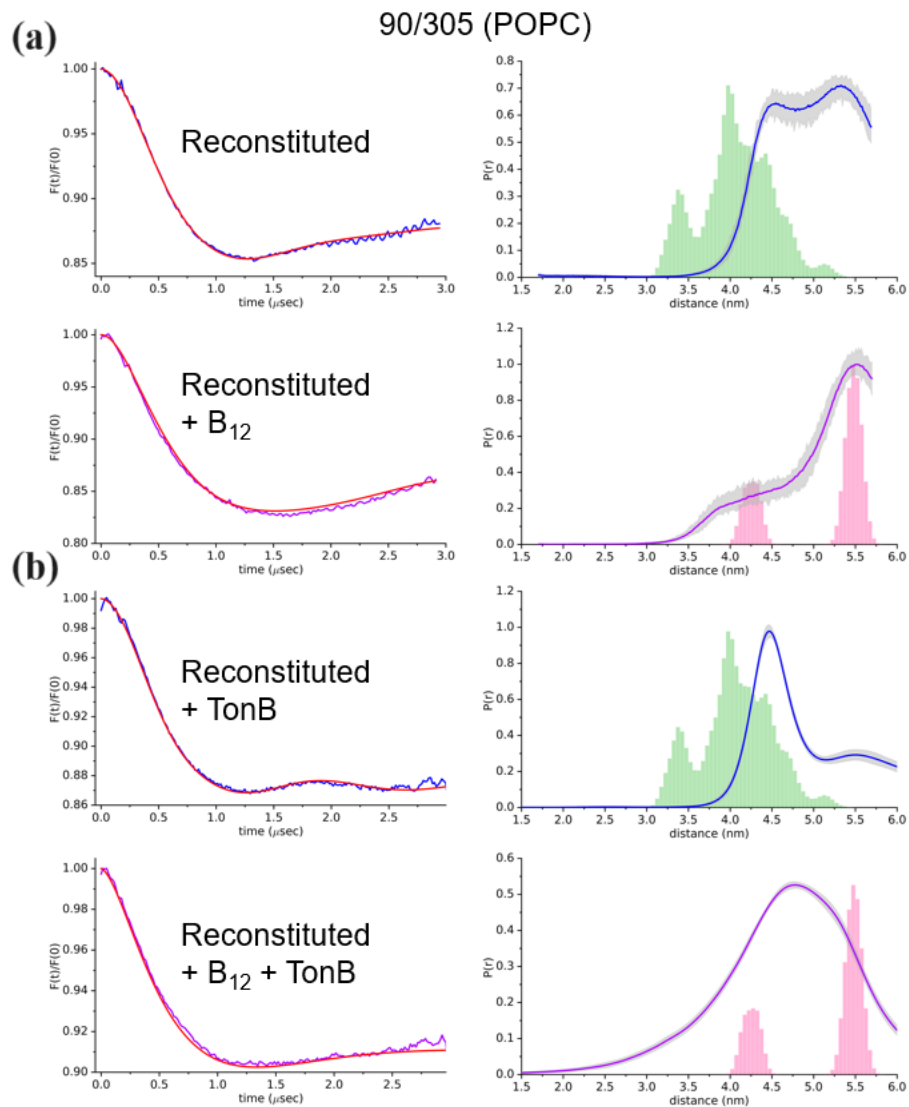


Figure 6.4 DEER data for V90R1-I305R1 obtained from purified reconstituted protein in POPC liposomes. For all conditions, data are shown in the apo (blue trace) and B<sub>12</sub> bound (purple trace) states of BtuB. (a) DEER data obtained for BtuB V90R1-I305R1 reconstituted into POPC bilayers. (b) DEER data obtained for BtuB V90R1-I305R1 reconstituted into POPC bilayers in the presence of C-terminal TonB fragment. All distance distributions were obtained using DEERNet. The predictions from the apo and substrate bound crystal structures (PDB ID: 1NQG and 2GSK, respectively) are shown as green and pink histograms, respectively.

## 90/305 (DLPC)

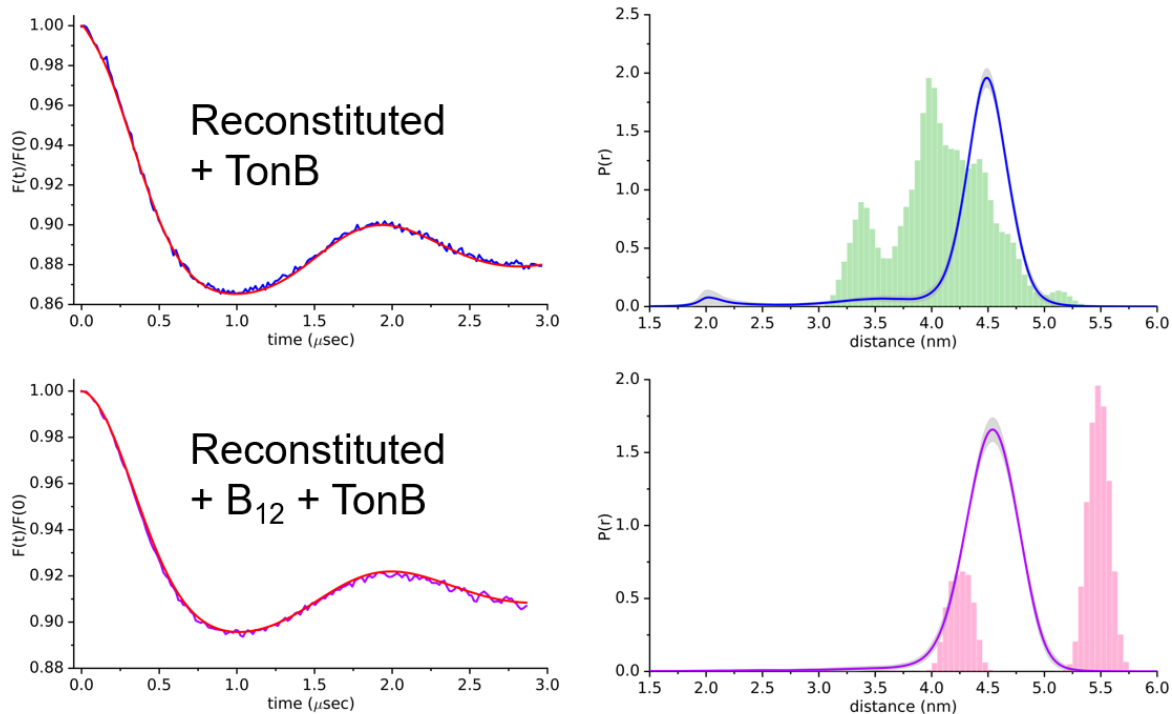


Figure 6.5 DEER data for V90R1-I305R1 obtained from purified reconstituted protein in DLPC liposomes. For all conditions, data are shown in the apo (blue trace) and B<sub>12</sub> bound (purple trace) states of BtuB. DEER data obtained for BtuB V90R1-I305R1 reconstituted into DLPC bilayers with TonB C-terminal fragment. All distance distributions were obtained using DEERNet. The predictions from the apo and substrate bound crystal structures (PDB ID: 1NQG and 2GSK, respectively) are shown as green and pink histograms, respectively.

A similar behavior of SB3 was also observed for the V90R1-Q510R1 and V90R1-Q510R1-D316A spin pairs indicating that these conformational dynamics are also seen with other spin pairs under the same experimental conditions (see Supplementary Figure S6.1, S6.2). Examination of both V90R1-Q510R1 with TonB addition and V90-Q510R1-D316A in the OM preparation revealed the presence of short distance components in the distributions, consistent with the



outward movement measured from site 188 in loop 2 (L2) in the intact cell<sup>1</sup>, while V90-Q510R1-D316A reconstituted into POPC liposomes provides distributions that agree well with the distributions predicted from the protein crystal structures and the allowed rotamers (see Supplementary Figure S6.4). The inter-conversion between possible rotamer states is the opposite of what was observed for V90R1-I305R1 where distance distribution around 4.5 nm increases while distance distribution around 5.5 nm decreases (see Supplementary Figure S6.1, S6.2 pink histograms) with substrate addition.

## 6.5 Discussion

In previous work, spin pairs incorporated into site V90 in SB3 of the BtuB core domain and site T188 on L2 show a substrate dependent conformational shift *in-vivo* towards L2 when titrated with Vitamin B<sub>12</sub><sup>1</sup>. This was assumed to be due to the unfolding of a helical turn followed by a movement in SB3 loop<sup>11</sup> as L2 remains relatively static upon substrate addition *in-vivo*<sup>37</sup>. DEER data obtained for these spin pairs with the disruption of R14-D316 ionic lock between core and barrel domain *in-vivo* resulted in a more dramatic substrate-dependent shift of SB3, where SB3 moves towards the periplasmic surface. This transition was not observed in reconstituted systems<sup>1</sup>.

The present study focuses on the dynamics of SB3 with respect to the BtuB periplasmic turns under varied experimental conditions in an isolated OM preparation. Our objective is to identify the factors that allow SB3 to extend towards the periplasmic space. Previous studies have observed this shift of SB3 in the intact cell<sup>1</sup>. We assume that it is possible to observe a similar shift in an isolated OM preparation from the periplasmic surface if either the R14-D316 ionic lock is disrupted or the C-terminal TonB fragment is introduced. For this purpose, site V90 at the apex of SB3 in the BtuB core domain along with two sites on the BtuB periplasmic turns (I305 and Q510)

were selected to create two spin pairs (BtuB V90R1-I305R1 and V90R1-Q510R1). To disrupt the ionic lock between core and barrel domain of BtuB, an alanine mutation to D316 in the barrel domain was introduced into both spin pairs (BtuB V90R1-I305R1-D316A and V90R1-Q510R1-D316A).

The CW-EPR spectra obtained for both spin pairs did not indicate any substantial changes upon substrate binding. In both cases, the R1 spin label at site V90 at SB3 remains in tertiary contact within the interior of BtuB, and disruption of the ionic lock does not result in any substantial changes in the EPR spectrum except for a minute change in the lower field of V90R1-I305R1 spin pair (see Figure 6.1c top left and bottom left spectra). Previous studies using scintillation proximity assays have also shown that the Ton box-TonB interaction results in a higher retention of Vitamin B<sub>12</sub> within BtuB binding site and that site V90 located in the substrate binding site is essential<sup>38</sup>. This is assumed to be the initial step in substrate permeation. Hence, the substantial shift of SB3 could result in strong retention or capturing of substrate to BtuB for transport.

It is not clear why a more native environment is necessary to observe changes in the conformation of SB3; however, studies of BtuB using MD simulation have shown that LPS may play an important role. For example, in the presence of LPS there is a reduction in the interaction energy between R14 and D316. Furthermore, LPS also alters the state of SB3 where a helical form is present when BtuB is reconstituted in a symmetric membrane (POPC reconstitution), and an extended form of SB3 when reconstituted in an asymmetric membrane with LPS<sup>39</sup>.

It should be noted that the EPR spectra obtained here are a combination of R1 motions present from both labeled sites. Both sites I305 and Q510 are unperturbed by disruption of the ionic lock or by substrate addition whereas site 90 experiences similar tertiary contacts within the

BtuB core and barrel domains under both conditions. CW-EPR is sensitive to motions in the nano-second (ns) time scale, thus changes in the motion on much slower time scales (longer than 10s of ns) might not be observed through conventional EPR methods<sup>39</sup>. Thus, it is not necessarily surprising that changes in CW-EPR signals are not observed in a liposome reconstitution.

As mentioned previously in Chapter 5, even though Vitamin B<sub>12</sub> binds to BtuB with high affinity<sup>40</sup>, there is an equilibrium between conformational states exhibited by the Ton box and by SB3, even when substrate is fully bound, and DEER experiments performed on BtuB in the presence of substrate will contain distance components associated with apo and ligand bound states. For the BtuB label pair, V90R1-I305R1 in OM preparations, there is a primary distance distribution around 4.5 nm which was retained upon substrate addition. However, there is an increase in a longer distance around 5.5 nm. Pulse EPR measurements indicate that there is a substrate induced unfolding of the helix attached to SB3 followed by slight shift of SB3 towards site T188 in loop 2 (L2) (see Chapter 3, Supplementary Figure S3.1) in the reconstituted system but was more prominent when observed *in-vivo*<sup>1</sup>. Site I305 remains static upon substrate addition, apart from the loss of possible rotamer representation for I305 as seen in the crystal structure. The addition of substrate and the TonB C-terminal domain results in the extension of Ton box<sup>5</sup> thus resulting in two primary rotamer representations for I305 (see Supplementary Figure S6.3) with rotamers facing inward and outward of the barrel domain. It is likely that the extension of the Ton box creates a water filled cavity that may be occupied by rotamers of I305R1. These are observed by MMM as shown above (see Figure 6.2, 6.3, 6.4, and 6.5 pink histograms).

The DEER distances for the OM preparation agree well with the predicted distance distributions obtained through MMM (see Figure 6.2a). An important observation made in this study is a significant structural change for SB3 when the C-terminal domain of TonB is introduced

to an OM preparation of V90R1-I305R1 (see Figure 6.2b). A similar observation was made when the crucial ionic lock between R14 and D316 was disrupted to create V90R1-I305R1-D316A BtuB (see Figure 6.3a) where a short distance around 2.0 – 2.5 nm was observed between site V90 and the periplasmic turn site I305 independent of substrate. This distance corresponds to SB3 extending 2 – 2.5 nm towards the periplasmic surface, a change that was only observed *in-vivo* with substrate addition and disruption of the ionic lock<sup>l</sup>. Interestingly, this behavior was not observed in POPC liposome reconstitutions (see Figure 6.3b), but a unique conformational interchange between two rotamer states was observed as is indicated through predicted distance distributions obtained through MMM. Given the level of overexpression of BtuB and the native copy number of TonB, there are insufficient TonB to bind all the available BtuB. The number of BtuB occupied by TonB may be at most about 5 or 6 percent. Thus, *in-vivo* most of the BtuB will not be bound to TonB in the intact cell. Hence, observing this particular SB3 shift in the intact cell with limited TonB concentrations might be challenging. However, by adding excess TonB in isolated OM preparations, all the available BtuB will be interacting with TonB. This may be why we observe conformational shifts in the presence of TonB regardless of substrate addition.

For purified BtuB labeled at V90R1-I305R1 in POPC liposomes, there are two primary conformational states around 4.5 nm and 5.5 nm in the absence (see Figure 6.4a) and presence (see Figure 6.4b) of TonB, indicating that TonB addition does not significantly perturb the initial reconstituted system. It is important to mention that the orientation of BtuB reconstituted into liposomes is random. Therefore, it is crucial that substrate and TonB should be able to access both inner and outer environments of the liposomes for effective Ton box-TonB binding. Unfortunately, liposomes constructed through POPC are well-sealed and permeation of large protein fragment such as the C-terminal TonB might be difficult even if subjected to freeze-thaw cycles. To

overcome this potential issue, BtuB was reconstituted into a DLPC liposome where DLPC creates a leakier membrane than POPC. However, DEER data obtained for DLPC liposomes with TonB (see Figure 6.5) indicate no perturbation of SB3 upon substrate or TonB binding where the inter-conversion between two states of SB3 have coalesced into a single distance around 4.5 nm. This may be an indication that the configuration of SB3 may be altered when reconstituted into liposomes with different lipid composition, but more studies needs to be done to verify it. Though BtuB with periplasmic surface facing outward would have access to TonB, the DEER distribution consists of a primary distance component around 4.5 nm consistent with the predicted distributions in all reconstituted preparations. Although we currently do not understand the reason behind BtuB being significantly unaffected by TonB in liposomes, it is assumed that protein accessibility and membrane environment has a contribution towards this behavior as observed previously through steered molecular dynamics (SMD) simulations<sup>41</sup>.

Further DEER data obtained for V90R1-Q510R1 BtuB and V90R1-Q510R1-D316A BtuB show a similar pattern as that observed for V90R1-I305R1 BtuB and V90R1-I305R1-D316A BtuB indicating that these structural transitions are reproducible (see Supplementary Figure S6.1, S6.2). The short distances around 2 nm that are seen for the V90R1-Q510R1 spin pair in the apo state (see Supplementary Figure S6.1a) have a high uncertainty, indicating that the distance may or may not be present. However, these short distances are clearly seen upon TonB addition or with the ionic lock mutation. Therefore, the movement of SB3 that is seen in the intact cell seems to be reproduced in an isolated preparation provided that the IM protein TonB is added or that the ionic lock between R14 and D316 is broken.

Currently, the steps involved in TonB-dependent transport are not fully elucidated, but it is apparent that both substrate and TonB are bound to BtuB during a certain stage in transport

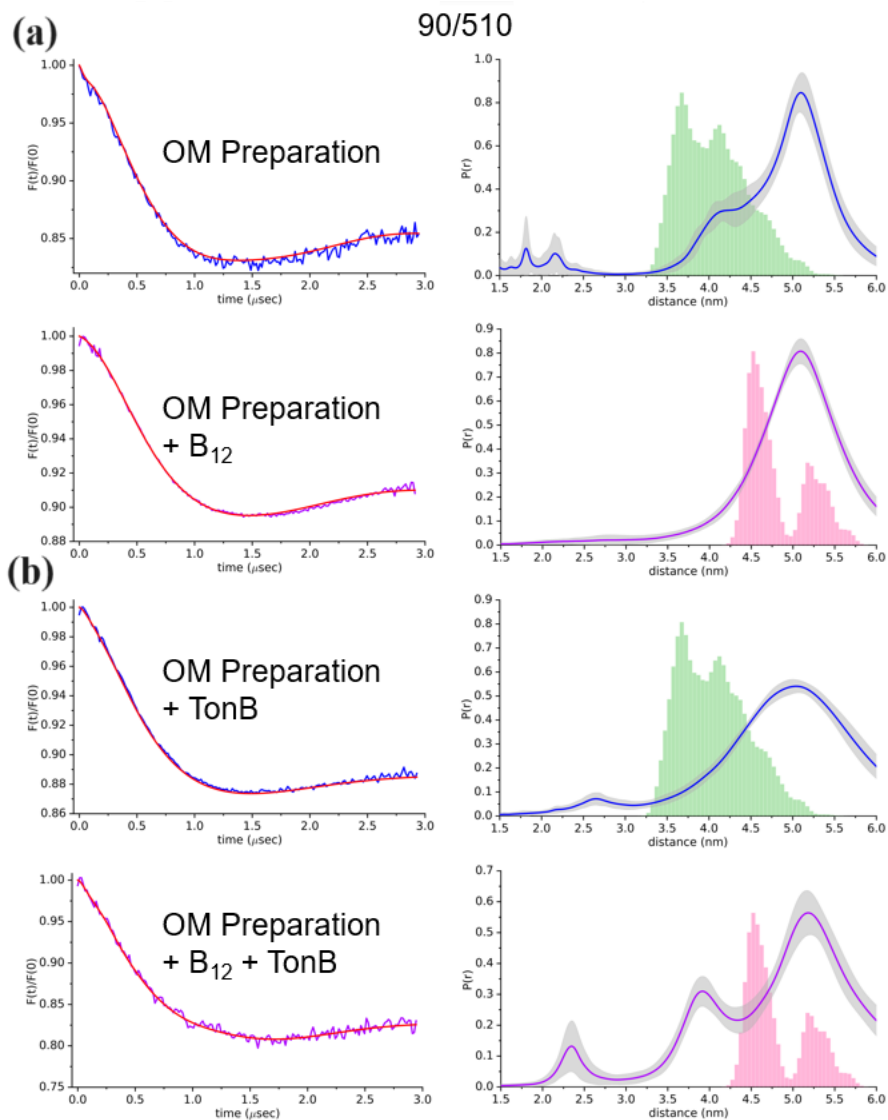
resulting in the breaking of the R14-D316 ionic lock. Experimental data indicate that substantial unfolding of the Ton box due to TonB binding or disruption of the ionic lock disruption will shift SB3 towards the periplasmic surface of BtuB. This suggests that the free energy of binding TonB to BtuB due to their high affinity towards each other ( $K_d$  in nanomolar range<sup>42</sup>) is sufficient for this shift. Previous studies have indicated that upon cleaving the ionic lock, distance distributions indicate that SB3 is migrating towards the periplasmic surface upon substrate binding in the cell<sup>l</sup>. This shift was not observed in isolated OM preparations until the TonB C-terminal domain was introduced. Therefore, the observation of this dramatic shift of SB3 without any possible mechanical action of TonB upon BtuB (by means of pulling or rotating), suggests that the free energy derived from the binding of TonB alone is sufficient to rearrange the core domain and allow substrate passage.

In summary, we have provided evidence that the disruption of the crucial R14-D316 ionic lock between the core and barrel domains from the periplasmic side results in a downward shift of SB3 around 2.0 – 2.5 nm towards the periplasmic surface. We show that this shift can be substrate independent provided that the C-terminal fragment of TonB is bound to BtuB in an OM preparation. Furthermore, such behavior is not observed when BtuB is reconstituted in liposomes, and some feature of the native membrane preparation is likely important. Our work also suggests that the binding of TonB mimics the disruption of the ionic lock, and that this binding event may be an important step in substrate transport. This behavior is only observed *in-vitro* in an OM preparation where the constituents of the native membrane are present and where a component of the IM protein TonB has been added.

## 6.6 Future Directions

The disruption of the R14-D316 ionic lock resulted in a downward shift of SB3 by about 2.0–2.5 nm towards the periplasmic surface in isolated OM preparations which was not previously observed. Furthermore, a similar behavior was observed when either the C-terminal domain of TonB was introduced or when the ionic lock was mutated in isolated OM preparations. However, there is a difference in distance distributions obtained for lipid reconstituted systems where this downward shift of SB3 is not observed. This should be further studied to identify the likely contribution that the membrane makes towards BtuB core dynamics. To investigate this contribution, DEER distance distributions can be made with BtuB inserted in POPC:LPS or DLPC:LPS lipid mixture to clarify the LPS contribution to BtuB function in isolated systems. Previous studies have shown that TonB access to the OM ferrichrome transporter FhuA in a DLPC reconstituted system was possible when lipid:protein is around 500:1<sup>16</sup>. However, this study was done with DLPC:BtuB of 25:1 to keep the lipid:protein identical to POPC liposome reconstitution. Therefore, to ensure TonB access to both inner and outer environments, an optimized DLPC liposome reconstitution system with DLPC:BtuB of 500:1 along with multiple freeze-thaw cycles and *E. coli* LPS should be used to ensure a complete interaction of TonB C-terminal domain with the BtuB periplasmic surface. Another approach could be to reconstitute BtuB in lipid nano-discs so that the periplasmic surface is always available for effective TonB binding when C-terminal TonB fragment is added externally. Finally, further DEER studies with spin pairs between periplasmic turn and SB3 from both sides of site V90 to obtain further restraints to identify the extent of SB3 shift is recommended. This data and *in-vivo* data<sup>1</sup> will enable an accurate modeling of the SB3 motion and will provide insight into BtuB substrate transport mechanism.

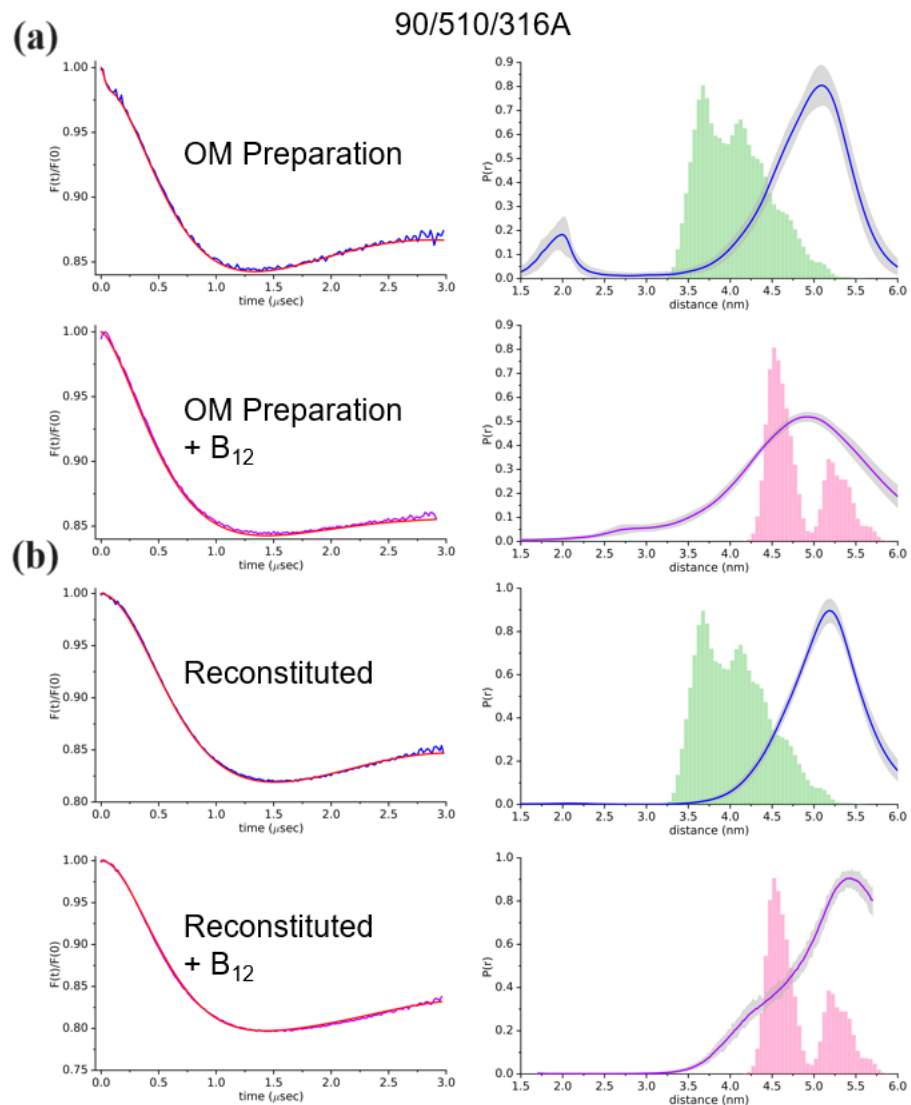
## 6.7 Supplementary Information



Supplementary Figure S6.1 DEER data for V90R1-Q510R1 obtained from an outer-membrane preparation. For all conditions, data are shown in the apo (blue trace) and B<sub>12</sub> bound (purple trace) states of BtuB. (a) DEER data obtained for BtuB labeled at sites V90 and Q510 obtained from an OM preparation. (b) DEER data obtained for BtuB V90R1-Q510R1 obtained from an OM preparation in the presence of C-terminal TonB fragment. All distance distributions were obtained

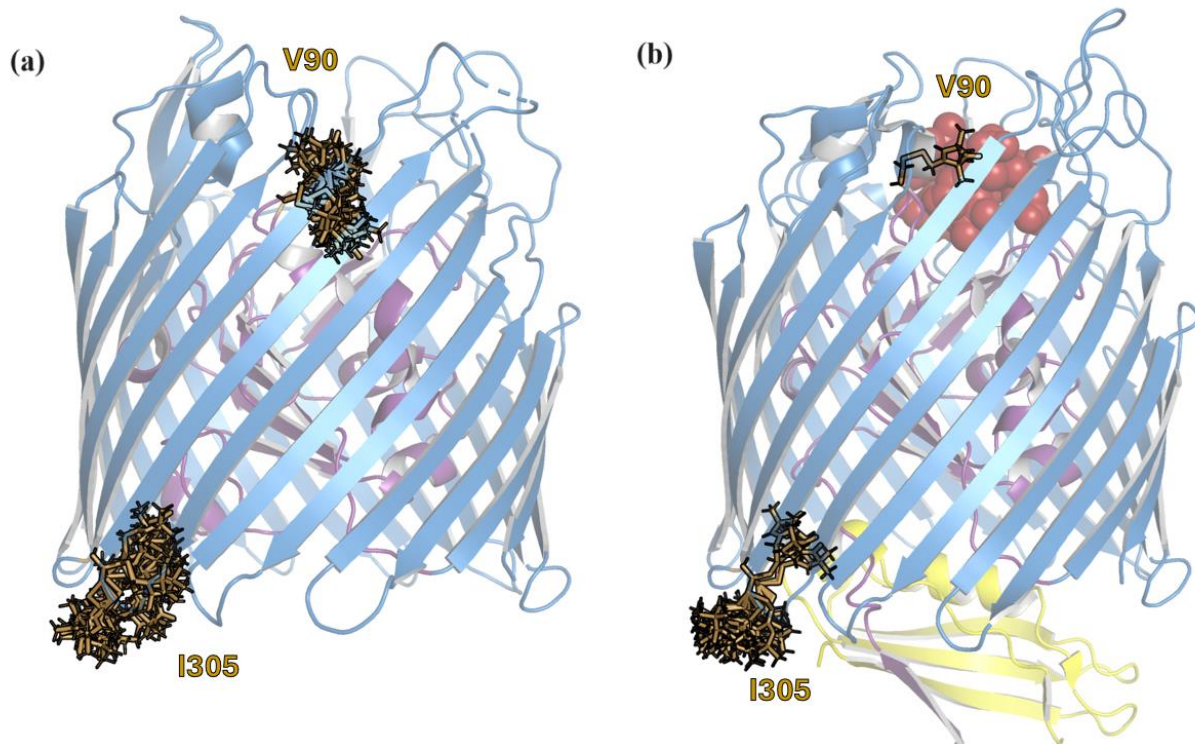


using DEERNet. The predictions from the apo and substrate bound crystal structures (PDB ID: 1NQG and 2GSK, respectively) are shown as green and pink histograms, respectively.

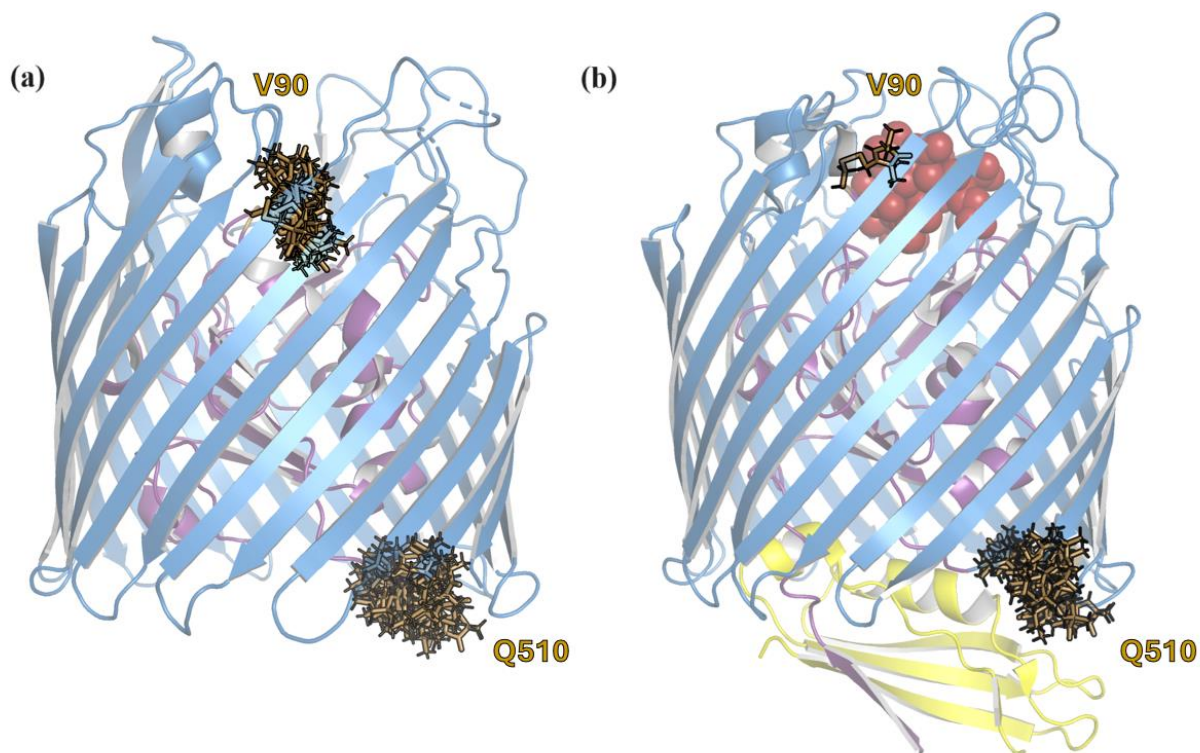


Supplementary Figure S6.2 DEER data for V90R1-Q510R1-D316A obtained from purified reconstituted protein or an outer-membrane preparation. For all conditions, data are shown in the apo (blue trace) and B<sub>12</sub> bound (purple trace) states of BtuB. (a) DEER data obtained for BtuB labeled at sites V90 and Q510 with the alanine mutation at D316 obtained from an OM preparation. (b) DEER data obtained for BtuB V90R1-Q510R1-D316A reconstituted into POPC bilayers. All

distance distributions were obtained using DEERNet. The predictions from the apo and substrate bound crystal structures (PDB ID: 1NQG and 2GSK, respectively) are shown as green and pink histograms, respectively.



Supplementary Figure S6.3 Substrate induced conformational changes of plug domain (dark purple) of V90R1-I305R1 BtuB observed in crystal structures. (a) Apo state (PDB ID 1NQG) and (b) B<sub>12</sub> (brick red) and TonB C-terminal (yellow) bound (PDB ID 2GSK) of BtuB with possible rotamers available for R1 spin label (brown) at residues V90 and I305 in the plug domain and barrel domain (blue), respectively.



Supplementary Figure S6.4 Substrate induced conformational changes of plug domain (dark purple) of V90R1-Q510R1 BtuB observed in crystal structures. (a) Apo state (PDB ID 1NQG) and (b) B<sub>12</sub> (brick red) and TonB C-terminal (yellow) bound (PDB ID 2GSK) of BtuB with possible rotamers available for R1 spin label (brown) at residues V90 and Q510 in the plug domain and barrel domain (blue), respectively.

## 6.8 References

1. Nilaweera, T. D., Nyenhuis, D. A., & Cafiso, D. S. (2021). Structural intermediates observed only in intact *Escherichia coli* indicate a mechanism for TonB-dependent transport. *eLife*, *10*, e68548.
2. Nikaido H. (2003). Molecular basis of bacterial outer membrane permeability revisited. *Microbiology and molecular biology reviews : MMBR*, *67*(4), 593–656.
3. Noinaj, N., Guillier, M., Barnard, T. J., & Buchanan, S. K. (2010). TonB-dependent transporters: regulation, structure, and function. *Annual review of microbiology*, *64*, 43–60.
4. Pawelek, P. D., Croteau, N., Ng-Thow-Hing, C., Khursigara, C. M., Moiseeva, N., Allaire, M., & Coulton, J. W. (2006). Structure of TonB in complex with FhuA, *E. coli* outer membrane receptor. *Science (New York, N.Y.)*, *312*(5778), 1399–1402.
5. Shultis, D. D., Purdy, M. D., Banchs, C. N., & Wiener, M. C. (2006). Outer membrane active transport: structure of the BtuB:TonB complex. *Science (New York, N.Y.)*, *312*(5778), 1396–1399.
6. Faraldo-Gómez, J. D., & Sansom, M. S. (2003). Acquisition of siderophores in gram-negative bacteria. *Nature reviews. Molecular cell biology*, *4*(2), 105–116.
7. Chimento, D. P., Kadner, R. J., & Wiener, M. C. (2005). Comparative structural analysis of TonB-dependent outer membrane transporters: implications for the transport cycle. *Proteins*, *59*(2), 240–251.
8. Ferguson, A. D., Chakraborty, R., Smith, B. S., Esser, L., van der Helm, D., & Deisenhofer, J. (2002). Structural basis of gating by the outer membrane transporter FecA. *Science (New York, N.Y.)*, *295*(5560), 1715–1719.

9. Locher, K. P., Rees, B., Koebnik, R., Mitschler, A., Moulinier, L., Rosenbusch, J. P., & Moras, D. (1998). Transmembrane signaling across the ligand-gated FhuA receptor: crystal structures of free and ferrichrome-bound states reveal allosteric changes. *Cell*, *95*(6), 771–778.
10. Buchanan, S. K., Smith, B. S., Venkatramani, L., Xia, D., Esser, L., Palnitkar, M., Chakraborty, R., van der Helm, D., & Deisenhofer, J. (1999). Crystal structure of the outer membrane active transporter FepA from *Escherichia coli*. *Nature structural biology*, *6*(1), 56–63.
11. Chimento, D. P., Mohanty, A. K., Kadner, R. J., & Wiener, M. C. (2003). Substrate-induced transmembrane signaling in the cobalamin transporter BtuB. *Nature structural biology*, *10*(5), 394–401.
12. Xu, Q., Ellena, J. F., Kim, M., & Cafiso, D. S. (2006). Substrate-dependent unfolding of the energy coupling motif of a membrane transport protein determined by double electron-electron resonance. *Biochemistry*, *45*(36), 10847–10854.
13. Kim, M., Fanucci, G. E., & Cafiso, D. S. (2007). Substrate-dependent transmembrane signaling in TonB-dependent transporters is not conserved. *Proceedings of the National Academy of Sciences of the United States of America*, *104*(29), 11975–11980.
14. Klebba P. E. (2016). ROSET Model of TonB Action in Gram-Negative Bacterial Iron Acquisition. *Journal of bacteriology*, *198*(7), 1013–1021.
15. Ratliff, A. C., Buchanan, S. K., & Celia, H. (2022). The Ton Motor. *Frontiers in microbiology*, *13*, 852955.

16. Sarver, J. L., Zhang, M., Liu, L., Nyenhuis, D., & Cafiso, D. S. (2018). A Dynamic Protein-Protein Coupling between the TonB-Dependent Transporter FhuA and TonB. *Biochemistry*, *57*(6), 1045–1053.
17. Gumbart, J., Wiener, M. C., & Tajkhorshid, E. (2007). Mechanics of force propagation in TonB-dependent outer membrane transport. *Biophysical journal*, *93*(2), 496–504.
18. Hickman, S. J., Cooper, R. E. M., Bellucci, L., Paci, E., & Brockwell, D. J. (2017). Gating of TonB-dependent transporters by substrate-specific forced remodelling. *Nature communications*, *8*, 14804.
19. Flores Jiménez, R. H., & Cafiso, D. S. (2012). The N-terminal domain of a TonB-dependent transporter undergoes a reversible stepwise denaturation. *Biochemistry*, *51*(17), 3642–3650.
20. Joseph, B., Jaumann, E. A., Sikora, A., Barth, K., Prisner, T. F., & Cafiso, D. S. (2019). In situ observation of conformational dynamics and protein ligand-substrate interactions in outer-membrane proteins with DEER/PELDOR spectroscopy. *Nature protocols*, *14*(8), 2344–2369.
21. Nilaweera, T. D., Nyenhuis, D. A., Nakamoto, R. K., & Cafiso, D. S. (2019). Disulfide Chaperone Knockouts Enable In Vivo Double Spin Labeling of an Outer Membrane Transporter. *Biophysical journal*, *117*(8), 1476–1484.
22. Landeta, C., Boyd, D., & Beckwith, J. (2018). Disulfide bond formation in prokaryotes. *Nature microbiology*, *3*(3), 270–280.
23. Jeschke G. (2012). DEER distance measurements on proteins. *Annual review of physical chemistry*, *63*, 419–446.

24. Klock, H. E., & Lesley, S. A. (2009). The Polymerase Incomplete Primer Extension (PIPE) method applied to high-throughput cloning and site-directed mutagenesis. *Methods in molecular biology (Clifton, N.J.)*, 498, 91–103.
25. Wimalasiri, V. W., Jurczak, K. A., Wieliniec, M. K., Nilaweera, T. D., Nakamoto, R. K., & Cafiso, D. S. (2023). A disulfide chaperone knockout facilitates spin labeling and pulse EPR spectroscopy of outer membrane transporters. *Protein science : a publication of the Protein Society*, 32(7), e4704.
26. Fanucci, G. E., Cogshall, K. A., Cadieux, N., Kim, M., Kadner, R. J., & Cafiso, D. S. (2003). Substrate-induced conformational changes of the periplasmic N-terminus of an outer-membrane transporter by site-directed spin labeling. *Biochemistry*, 42(6), 1391–1400.
27. Bradford M. M. (1976). A rapid and sensitive method for the quantitation of microgram quantities of protein utilizing the principle of protein-dye binding. *Analytical biochemistry*, 72, 248–254.
28. Sedmak, J. J., & Grossberg, S. E. (1977). A rapid, sensitive, and versatile assay for protein using Coomassie brilliant blue G250. *Analytical biochemistry*, 79(1-2), 544–552.
29. Rassam, P., Copeland, N. A., Birkholz, O., Tóth, C., Chavent, M., Duncan, A. L., Cross, S. J., Housden, N. G., Kaminska, R., Seger, U., Quinn, D. M., Garrod, T. J., Sansom, M. S., Piehler, J., Baumann, C. G., & Kleanthous, C. (2015). Supramolecular assemblies underpin turnover of outer membrane proteins in bacteria. *Nature*, 523(7560), 333–336.
30. Nyenhuis, D. A., Nilaweera, T. D., Niblo, J. K., Nguyen, N. Q., DuBay, K. H., & Cafiso, D. S. (2020). Evidence for the Supramolecular Organization of a Bacterial Outer-Membrane Protein from In Vivo Pulse Electron Paramagnetic Resonance Spectroscopy. *Journal of the American Chemical Society*, 142(24), 10715–10722.

31. Jeschke, G., Chechik, V., Ionita, P., Godt, A., Zimmermann, H., Banham, J., ... & Jung, H. (2006). DeerAnalysis2006—a comprehensive software package for analyzing pulsed ELDOR data. *Applied magnetic resonance*, *30*, 473-498.
32. Worswick, S. G., Spencer, J. A., Jeschke, G., & Kuprov, I. (2018). Deep neural network processing of DEER data. *Science advances*, *4*(8), eaat5218.
33. Jeschke, G. (2018). MMM: A toolbox for integrative structure modeling. *Protein Science*, *27*(1), 76-85.
34. Polyhach, Y., Bordignon, E., & Jeschke, G. (2011). Rotamer libraries of spin labelled cysteines for protein studies. *Physical chemistry chemical physics : PCCP*, *13*(6), 2356–2366.
35. DeLano, W. L. (2002). Pymol: An open-source molecular graphics tool. *CCP4 Newsl. Protein Crystallogr*, *40*(1), 82-92.
36. Lukasik, S. M., Ho, K. W., & Cafiso, D. S. (2007). Molecular basis for substrate-dependent transmembrane signaling in an outer-membrane transporter. *Journal of molecular biology*, *370*(5), 807–811.
37. Nyenhuis, D. A., Nilaweera, T. D., & Cafiso, D. S. (2020). Native Cell Environment Constrains Loop Structure in the Escherichia coli Cobalamin Transporter BtuB. *Biophysical journal*, *119*(8), 1550–1557.
38. Mills, A., Le, H. T., & Duong, F. (2016). TonB-dependent ligand trapping in the BtuB transporter. *Biochimica et biophysica acta*, *1858*(12), 3105–3112.
39. Grosskopf, J. D., Sidabras, J. W., Altenbach, C., Anderson, J. R., Mett, R. R., Strangeway, R. A., ... & Lerch, M. T. (2024). A pressure-jump EPR system to monitor millisecond conformational exchange rates of spin-labeled proteins. *bioRxiv*.



40. Pieńko, T., & Trylska, J. (2020). Extracellular loops of BtuB facilitate transport of vitamin B12 through the outer membrane of *E. coli*. *PLoS computational biology*, *16*(7), e1008024.
41. Balusek, C., & Gumbart, J. C. (2016). Role of the Native Outer-Membrane Environment on the Transporter BtuB. *Biophysical journal*, *111*(7), 1409–1417.
42. Freed, D. M., Lukasik, S. M., Sikora, A., Mokdad, A., & Cafiso, D. S. (2013). Monomeric TonB and the Ton box are required for the formation of a high-affinity transporter-TonB complex. *Biochemistry*, *52*(15), 2638–2648.

## **Significance of the Research**

TonB-dependent transporters (TBDTs) are a fascinating class of active transporters present in Gram negative bacterial outer membrane (OM) responsible for the uptake of trace nutrients greater than 600 Da against a concentration gradient. They are all composed of a similar architecture where the C-terminus is folded into a 22 antiparallel  $\beta$ -stranded barrel and the N-terminus is folded into a core/plug domain which occludes the interior of the barrel domain. These transporters couple with TonB which is coupled with the proton motive force (PMF) sensitive ExbB/ExbD motif present in the inner membrane (IM) during active transport through a highly conserved N-terminal segment in the transporter protein known as Ton box<sup>1</sup>. However, overall mechanism of active transport is yet to be elucidated. A unique behavior of these transporters is that they exhibit allosteric behavior<sup>2</sup>. It is also important to understand that transport has never been reconstituted for this protein transport system. Currently, there are two proposed models for TonB-dependent transport where both models involve mechanical force exerted on TBDTs through TonB using the TonB Ton box interaction. These two models are the pulling model<sup>3</sup> and the rotating model<sup>4</sup>. The pulling model states that TonB introduces a pulling motion to allow unfolding of the TBDT core domain sufficient for substrate passage. The rotating model based on the similarities between ExbB/ExbD complex and the flagellar motor system present in the IM states that TonB exerts a rotational motion to the core domain to facilitate partial unfolding of core domain for substrate transport. By utilizing the findings of this thesis, we intend to critically evaluate the proposed models in order to gain deeper understanding of TBDT function and possibly propose a possible novel mechanism.

The first two chapters of this thesis was based on optimizing spin labeling efficiencies of BtuB (Chapter 3) and FecA (Chapter 4) to be able to study the structural and functional dynamics using Continuous Wave (CW) and Pulse Electron Paramagnetic Resonance (EPR) spectroscopy<sup>5</sup>. It was identified that the use of a knockout strain of the disulfide bond formation (Dsb) system, particularly the disulfide bond oxidase (*dsbA*) allowed BtuB and FecA to retain their mutated cysteines in thiol form to be reactive with the paramagnetic nitroxide spin label through disulfide bond formation. We were able to exhibit efficient BtuB spin labeling *in-vitro* and FecA spin labeling *in-vivo* through CW-EPR and Double Electron-Electron Resonance (DEER) experiments<sup>5</sup>.

In Chapter 5, we intended to further evaluate the extent of BtuB Ton box unfolding upon the disruption of R14-D316 ionic lock between core and barrel domain via D316A mutation or through the addition of C-terminal TonB fragment. Previous studies of BtuB has shown a 20 – 30 Å expansion of the Ton box upon substrate (Vitamin B<sub>12</sub>) addition observed through DEER experiments<sup>6</sup>. Utilizing isolated OM preparations, it was observed that the BtuB Ton box undergoes irreversible extension up to 35 – 40 Å upon disruption of R14-D316 ionic lock. A similar extension in the presence of intact ionic lock was observed when C-terminal TonB fragment was bound to BtuB Ton box. Surprisingly, this extension was observed in the absence of substrate. Previous studies have shown the Ton box extension of 20 – 30 Å represent the unfolding of up to 15 residues of the N-terminus of BtuB<sup>6</sup>. Therefore, it is possible to assume much more substantial unfolding of the Ton box occurs upon TonB binding or R14-D316 ionic lock disruption in isolated preparations.

In Chapter 6, we intended to observe a novel conformational shift that was observed *in-vivo* where the substrate binding loop 3 (SB3) extends about 20 Å into the periplasmic space upon

R14-D316 ionic lock disruption in isolated BtuB preparations<sup>7</sup>. By introducing cysteine mutations across BtuB through one site of SB3 and another site in one periplasmic turn, nitroxide spin labeled OM isolations were obtained. DEER experiments performed with the disruption of the R14-D316 ionic lock indicated a downward shift of SB3 up to 20 – 25 Å, verifying the periplasmic shift of SB3 observed *in-vivo*. Furthermore, the addition of C-terminal TonB fragment with an intact R14-D316 ionic lock yielded a similar result. As observed for BtuB Ton box extension in Chapter 5, this shift was observed in the absence of substrate. These experimental data suggest that the binding of TonB can be possibly mimicked by the disruption of R14-D316 ionic lock and that TonB binding is crucial step in overall transport process. Also, it is crucial to mention that this behavior was only observed in OM preparations where the constituents of the native membrane is present.

When comparing currently proposed models for TBDT transport with the experimental data obtained through DEER experiments in OM preparations, it is vital to mention that the constituents of the native membrane (lipopolysaccharides) (LPS) has a role in TBDT function. Previous studies have indicated the role of LPS in loop function as well the energetics between R14-D316 ionic lock during substrate binding<sup>8</sup>. However, when we consider the DEER experimental data, it is important to understand that these experiments were conducted in a system where native energetics (PMF) is absent. Therefore, the structural transitions that are present are solely due to free energy derived through TonB binding. BtuB has extremely high affinity towards TonB (Kd in nm range)<sup>9</sup> thus the resulting free energy of binding may induce substantial structural transitions of the BtuB core domain. The substantial extension of Ton box upon C-terminal TonB fragment binding observed in Chapter 5 suggests that the initial unfolding of Ton box may not require a pulling or rotating force through TonB. The discovery of SB3 downward shift towards

the periplasmic space upon substrate binding when R14-D316 ionic lock is disrupted or C-terminal TonB fragment bound suggest that the hollow cavity created inside the barrel domain upon Ton box unfolding is sufficient for SB3 to shift into periplasmic space allowing the substrate for initial permeation into the barrel domain. This may act as the initial steps during active transport. Previous *in-vivo* preparations of BtuB indicated a continuously extended Ton box regardless of substrate which contradicts isolated reconstituted preparations where the binding of substrate induces a transmembrane signaling event resulting in the extension of the BtuB Ton box<sup>10</sup>. It is likely that cells deprived of Vitamin B<sub>12</sub> are rapidly accumulating substrate through BtuB and that substrate binding immediately signals Ton box to be bound with TonB to initiate transport. Crystal structures of TonB C-terminal domain has shown that TonB tends to dimerize therefore it is plausible that TonB remains in a dimerized state in the apo states of TBDTs<sup>11</sup>. Upon substrate binding, Ton box may induce the dimeric state of TonB to convert into a monomeric state allowing Ton box to be bound to TonB and initiate transport. After transport is completed, TonB may disengage from Ton box and convert back to its stable dimeric state. Recent crystal structures have indicated a possible interaction of TonB periplasmic domain with periplasmic domains of ExbD dimer<sup>12</sup>. Therefore, a potential mechanical force can be transferred to TonB through ExbB/ExbD complex allowing TonB to unfold core domain of TBDTs through TonB Ton box interaction. However, the experimental data of BtuB presented in this thesis suggest that the free energy-based core unfolding has a substantial impact on substrate permeation and may only require minimum force exertion to achieve active transport.


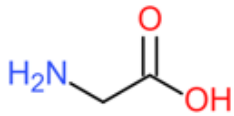
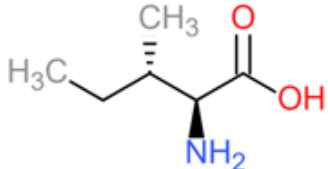
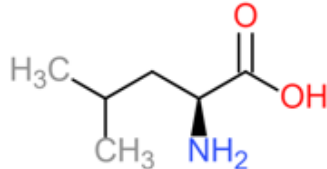
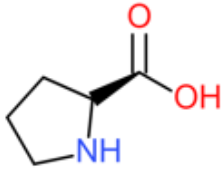

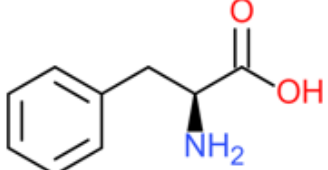
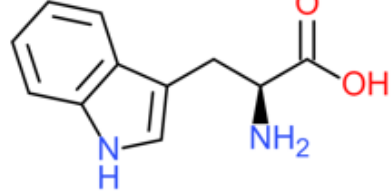
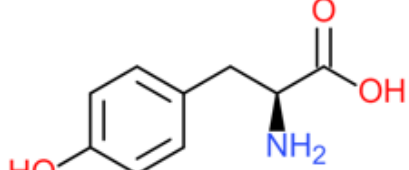
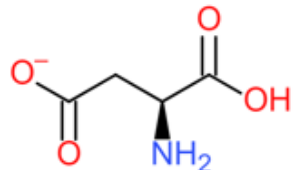
## References

1. Noinaj, N., Guillier, M., Barnard, T. J., & Buchanan, S. K. (2010). TonB-dependent transporters: regulation, structure, and function. *Annual review of microbiology*, *64*, 43–60.
2. Sikora, A., Joseph, B., Matson, M., Staley, J. R., & Cafiso, D. S. (2016). Allosteric Signaling Is Bidirectional in an Outer-Membrane Transport Protein. *Biophysical journal*, *111*(9), 1908–1918.
3. Hickman, S. J., Cooper, R. E. M., Bellucci, L., Paci, E., & Brockwell, D. J. (2017). Gating of TonB-dependent transporters by substrate-specific forced remodelling. *Nature communications*, *8*, 14804.
4. Klebba P. E. (2016). ROSET Model of TonB Action in Gram-Negative Bacterial Iron Acquisition. *Journal of bacteriology*, *198*(7), 1013–1021.
5. Wimalasiri, V. W., Jurczak, K. A., Wieliniec, M. K., Nilaweera, T. D., Nakamoto, R. K., & Cafiso, D. S. (2023). A disulfide chaperone knockout facilitates spin labeling and pulse EPR spectroscopy of outer membrane transporters. *Protein science : a publication of the Protein Society*, *32*(7), e4704.
6. Xu, Q., Ellena, J. F., Kim, M., & Cafiso, D. S. (2006). Substrate-dependent unfolding of the energy coupling motif of a membrane transport protein determined by double electron-electron resonance. *Biochemistry*, *45*(36), 10847–10854.
7. Nilaweera, T. D., Nyenhuis, D. A., & Cafiso, D. S. (2021). Structural intermediates observed only in intact *Escherichia coli* indicate a mechanism for TonB-dependent transport. *eLife*, *10*, e68548.

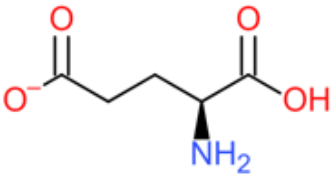
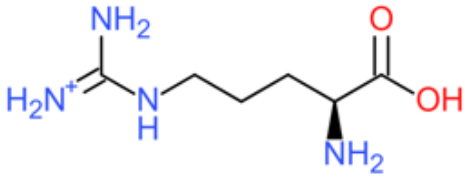
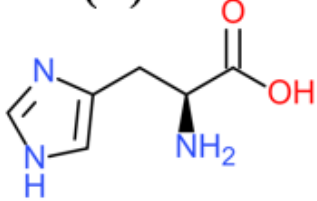
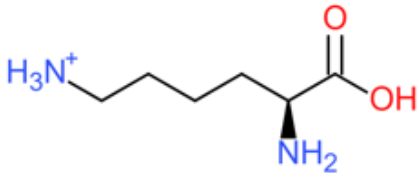
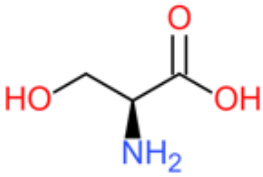
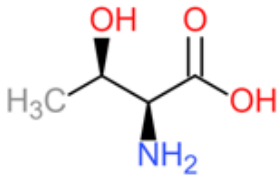
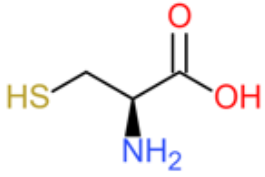
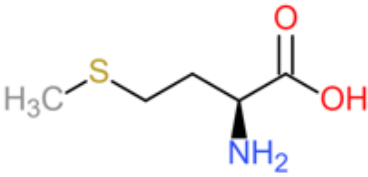
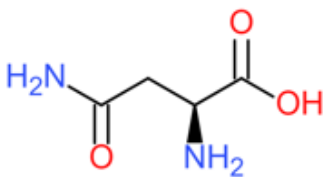
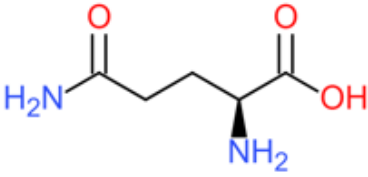
8. Balusek, C., & Gumbart, J. C. (2016). Role of the Native Outer-Membrane Environment on the Transporter BtuB. *Biophysical journal*, *111*(7), 1409–1417.
9. Freed, D. M., Lukasik, S. M., Sikora, A., Mokdad, A., & Cafiso, D. S. (2013). Monomeric TonB and the Ton box are required for the formation of a high-affinity transporter-TonB complex. *Biochemistry*, *52*(15), 2638–2648.
10. Nilaweera, T. D., Nyenhuis, D. A., Nakamoto, R. K., & Cafiso, D. S. (2019). Disulfide Chaperone Knockouts Enable In Vivo Double Spin Labeling of an Outer Membrane Transporter. *Biophysical journal*, *117*(8), 1476–1484.
11. Sauter, A., Howard, S. P., & Braun, V. (2003). In vivo evidence for TonB dimerization. *Journal of bacteriology*, *185*(19), 5747-5754.
12. Zinke, M., Lejeune, M., Mechaly, A., Bardiaux, B., Boneca, I. G., Delepelaire, P., & Izadi-Pruneyre, N. (2024). Ton motor conformational switch and peptidoglycan role in bacterial nutrient uptake. *Nature Communications*, *15*(1), 331.

## Appendix

### Appendix 1 – Standard Amino Acids

<p><b>Alanine (A)</b></p>  <p><i>GCT, GCC, GCA, GCG</i></p>	<p><b>Glycine (G)</b></p>  <p><i>GGT, GGC, GGA, GGG</i></p>
<p><b>Isoleucine (I)</b></p>  <p><i>ATT, ATC, ATA</i></p>	<p><b>Leucine (L)</b></p>  <p><i>CTT, CTC, CTA, CTG, TTA, TTG</i></p>
<p><b>Proline (P)</b></p>  <p><i>CCT, CCC, CCA, CCG</i></p>	<p><b>Valine (V)</b></p>  <p><i>GTT, GTC, GTA, GTG</i></p>
<p><b>Phenylalanine (F)</b></p>  <p><i>TTT, TTC</i></p>	<p><b>Tryptophan (W)</b></p>  <p><i>TGG</i></p>
<p><b>Tyrosine (Y)</b></p>  <p><i>TAT, TAC</i></p>	<p><b>Aspartic Acid (D)</b></p>  <p><i>GAT, GAC</i></p>



<p><b>Glutamic Acid (E)</b></p>  <p><i>GAA, GAG</i></p>	<p><b>Arginine (R)</b></p>  <p><i>CGT, CGC, CGA, CGG, AGA, AGG</i></p>
<p><b>Histidine (H)</b></p>  <p><i>CAT, CAC</i></p>	<p><b>Lysine (K)</b></p>  <p><i>AAA, AAG</i></p>
<p><b>Serine (S)</b></p>  <p><i>TCT, TCC, TCA, TCG, AGT, AGC</i></p>	<p><b>Threonine (T)</b></p>  <p><i>ACT, ACC, ACA, ACG</i></p>
<p><b>Cysteine (C)</b></p>  <p><i>TGT, TGC</i></p>	<p><b>Methionine (M)</b></p>  <p><i>ATG</i></p>
<p><b>Asparagine (N)</b></p>  <p><i>AAT, AAC</i></p>	<p><b>Glutamine (Q)</b></p>  <p><i>CAA, CAG</i></p>

Appendix 2 – *E. coli* wild type BtuB, FecA, and TonB sequences

2.1 *E. coli* wild type BtuB amino acid sequence (Uniprot ID P06129)<sup>1</sup>

10	20	30	40	50
<b>MIKKASLLTA</b>	<b>CSVTAFSAWA</b>	QDTSPDTLVV	TANRFEQPRS	TVLAPTTVVT
60	70	80	90	100
RQDIDRWQST	SVNDVLRRLP	GVDITQNGGS	GQLSSIFIRG	TNASHVLVLI
110	120	130	140	150
DGVRLNLAGV	SGSADLSQFP	IALVQRVEYI	RGPRSAVYGS	DAIGGVVNII
160	170	180	190	200
TTRDEPGTEI	SAGWGSNSYQ	NYDVSTQQQL	GDKTRVTLLG	DYAHTHGYDV
210	220	230	240	250
VAYGNTGTQA	QTDNDGFLSK	TLYGALAHNF	TDAWSGFVRG	YGYDNRTNYD
260	270	280	290	300
AYYSPGSPLL	DTRKLYSQSW	DAGLRYNGEL	IKSQLITSYS	HSKDYNYPH
310	320	330	340	350
YGRYDSSATL	DEMKQYTVQW	ANNVIVGHGS	IGAGVDWQKQ	TTTPGTGYVE
360	370	380	390	400
DGYDQRNTGI	YLTGLQQVGD	FTFEGAARSD	DNSQFGRHGT	WQTSAGWEFI
410	420	430	440	450
EGYRFIASYG	TSYKAPNLGQ	LYGFYGNPNL	DPEKSKQWEG	AFEGLTAGVN
460	470	480	490	500
WRISGYRNDV	SDLIDYDDHT	LKYYNEGKAR	IKGVEATANF	DTGPLTHTVS
510	520	530	540	550
YDYVDARNAI	TDTPLLRRAK	QQVKYQLDWQ	LYDFDWGITY	QYLGTRYDKD
560	570	580	590	600
YSSYPYQTVK	MGGVSLWDLA	VAYPVTSHLT	VRGKIANLFD	KDYETVYGYQ
610				
TAGREYTLTG	SYTF			

*E. coli* complete BtuB amino acid sequence contains the N-terminus **translocation signaling domain** (residues **1 – 20**)

2.2 *E. coli* wild type FecA amino acid sequence (Uniprot ID P13036)<sup>1</sup>

10	20	30	40	50
<b>MTPLRVFRKT</b>	<b>TPLVNTIRLS</b>	<b>LLPLAGLSFS</b>	<b>AFAAQVNIAP</b>	GSLDKALNQY
60	70	80	90	100
AAHSGFTLSV	DASLTRGKQS	NGLHGDYDVE	SGLQQLLDGS	GLQVKPLGNN
110	120	130	140	150
SWTLEPAPAP	KEDALTVVGD	WLGDARENDV	FEHAGARDVI	RREDFAKTGA
160	170	180	190	200
TTMREVLNRI	PGVSAPENNG	TGSHDLAMNF	GIRGLNPRLA	SRSTVLMDCI

210	220	230	240	250
PVPFAPYQGP	QLSLAPVSLG	NMDAIDVVRG	GGAVRYGPQS	VGGVNVFVTR
260	270	280	290	300
AIPQDFGIEA	GVEGQLSPTS	SQNNPKETHN	LMVGGTADNG	FGTALLYSGT
310	320	330	340	350
RGSDWREHSA	TRIDDLMLKS	KYAPDEVHTF	NSLLQYYDGE	ADMPPGGLSRA
360	370	380	390	400
DYDADRWQST	RPYDRFWGRR	KLASLGYQFQ	PDSQHKFNIQ	GFYTQTLRSG
410	420	430	440	450
YLEQGKRITL	SPRNYWVRGI	EPRYSQIFMI	GPSAHEVGVG	YRYLNESTHE
460	470	480	490	500
MRYYTATSSG	QLPSGSSPYD	RDTRSGTEAH	AWYLDDKIDI	GNWTITPGMR
510	520	530	540	550
FEHIESYQNN	AITGTHEEVS	YNAPLPALNV	LYHLTDSWNL	YANTEGSFGT
560	570	580	590	600
VQYSQIGKAV	QSGNVEPEKA	RTWELGTRYD	DGALTAEMGL	FLINFNNQYD
610	620	630	640	650
SNQTNDTVTA	RGKTRHTGLE	TQARYDLGTL	TPTLDNVSIIY	ASYAYVNAEI
660	670	680	690	700
REKGDYGNL	VPFSPKHKGT	LGVDYKPGNW	TFNLNSDFQS	SQFADNANTV
710	720	730	740	750
KESADGSTGR	IPGFMLWGAR	VAYDFGPQMA	DLNLAFGVKN	IFDQDYFIRS
760	770			
YDDNNKGIYA	GQPRTLMOG	SLKF		

*E. coli* complete FecA amino acid sequence contains the N-terminus **translocation signaling domain** (residues **1 – 33**)

2.3 *E. coli* wild type TonB amino acid sequence (Uniprot ID P02929)<sup>1</sup>

10	20	30	40	50
<b>MTLDLPRRFP</b>	<b>WPTLLSVCIH</b>	<b>GAVVAGLLYT</b>	<b>SVHQVIELPA</b>	PAQPISVTMV
60	70	80	90	100
TPADLEPPQA	VQPPPEPVVE	PEPEPEPIPE	PPKEAPVVIE	KPKPKPKPKP
110	120	130	140	150
KPVKKVQEQP	KRDVKPVESR	PASPFENTAP	ARLTSSTATA	ATSKPVTVA
160	170	180	190	200
SGPRALSRNQ	PQYPARAQAL	RIEQVKVKF	DVTPDGRVDN	VQILSAKPAN
210	220	230		
MFEREVKNAM	RRWRYEPGKP	GSGIVVNILF	KINGTTEIQ	

*E. coli* complete TonB amino acid sequence contains the **transmembrane helical signal anchor** (residues **1 – 32**)

Appendix 3 – *E. coli* BtuB and FecA mutations

3.1 BtuB Mutations

<b>Mutation</b>	<b>Protein</b>	<b>T<sub>m</sub> of primers (Forward Primer, Reverse Primer) (°C)</b>	<b>Annealing Temperature Range (°C)</b>
D6C	BtuB	(67.3, 69.1)	60 – 69
V10C	BtuB	(66.6, 66.6)	65 – 69
V90C	BtuB	(68.8, 68.8)	61 – 68
T188C	BtuB	(67.3, 66.1)	63 – 69
I305C	BtuB	(64.7, 68.0)	64 – 68
Q510C	BtuB	(64.6, 64.6)	64 – 67
D316A	BtuB	(69.0, 69.0)	63 – 69

Table 3.1 *E. coli* BtuB primers with their corresponding melting temperatures (T<sub>m</sub>) and PCR annealing temperatures

3.2 FecA Mutations

<b>Mutation</b>	<b>Protein</b>	<b>T<sub>m</sub> of primers (Forward Primer, Reverse Primer) (°C)</b>	<b>Annealing Temperature Range (°C)</b>
Q528C	FecA	(69.1, 69.1)	64 – 70
T666C	FecA	(69.3, 69.3)	64 – 70
T70C	FecA	(66.7, 66.7)	63 – 69
N256C	FecA	(69.5, 69.5)	64 – 70

Table 3.2 *E. coli* FecA primers with their corresponding melting temperatures (T<sub>m</sub>) and PCR annealing temperatures

## References

1. UniProt Consortium T. (2018). UniProt: the universal protein knowledgebase. *Nucleic acids research*, 46(5), 2699.
2. Owczarzy, R., Tataurov, A. V., Wu, Y., Manthey, J. A., McQuisten, K. A., Almabrazi, H. G., Pedersen, K. F., Lin, Y., Garretson, J., McEntaggart, N. O., Sailor, C. A., Dawson, R. B., & Peek, A. S. (2008). IDT SciTools: a suite for analysis and design of nucleic acid oligomers. *Nucleic acids research*, 36(Web Server issue), W163–W169.

## **Disclaimer**

The Figures used for Chapter 1 and Chapter 2 of this thesis were obtained from open access research journals, instrument manuals, online webpages and PhD thesis dissertations of particular individuals. The resources used to obtain the images has been cited in the figure caption and permission was obtained from the original authors of the thesis dissertations.